# High Performance Amplifier Topologies Implemented With a Micro-machined Vibrating Capacitor

by

Akin Adeniyi Aina

S.B. (Massachusetts Institute of technology) 1997
M.Eng (Massachusetts Institute of technology) 1997

Submitted to the Department of Electrical Engineering and Computer Science
in Partial Fulfillment of the Requirements for the Degree of

Doctor of Philosophy In Electrical Engineering and Computer Science

At the
Massachusetts Institute of technology
June 2003





Signature of Author.....
Department of Electrical Engineering and Computer Science
May 2, 2003

Certified by.....
Timothy Denison
Design Engineer
Thesis Supervisor

Certified by.....
Steven Leeb
Associate Professor of Electrical Engineering
Thesis Supervisor

Accepted by.....
Arthur C. Smith
Chairman, Committee on Graduate Students
Department of Electrical Engineering and Computer Science

# HIGH PERFORMANCE AMPLIFIER TOPOLOGIES IMPLEMENTED WITH A MICRO-MACHINED VIBRATING CAPACITOR

by

AKIN ADENIYI AINA

Submitted to the Department of Electrical Engineering and Computer Science
on May 2, 2003 in partial fulfillment of the
requirements for the Degree of Doctor of Philosophy in
Electrical Engineering and Computer Science

## ABSTRACT

In this work, the design of a MEMS based differential amplifier is investigated. The goal of this investigation is to design, fabricate and characterize a differential amplifier whose performance is based on a physically coupled, but electrically isolated fully differential mechanical transconductor input stage that is fabricated using SOI-MEMS technology.

The MEMS sensor will act as a vibrating capacitor input stage. It will provide galvanic isolation and up-modulation of the input signal as it vibrates. The galvanic isolation facilitates low-leakage inputs and a very wide input common mode voltage range. The up-modulation provides a means for achieving a low input referred offset voltage and low-noise via the use of correlated double sampling or chopper stabilization.

At the system level, this amplifier consists of two major loops: the drive loop and a sense loop. The drive loop includes half of the MEMS structure along with some electronics and provides a means of moving the beam at a constant frequency. The drive loop's design was facilitated by describing function analysis. The drive loop vibrated the beam at its mechanical resonance because at that frequency, the displacement of the beam is maximized for a given electrostatic force and consequently, the sensitivity of the amplifier is maximized. The sense loop includes the other half of the beam and some electronics whose role is to process the differential input signal applied at the MEMS structure's inputs. Common-mode rejection is performed by the mechanical transconductor, while the sense loop's crossover frequency sets the signal bandwidth.

The performance of the amplifier agreed very well with hand calculations and simulations. The noise performance was dominated by the total noise at the preamplifier's input. The noise performance achieved in this design was 55 $\mu V/\sqrt{Hz}$, which is higher than that of other high performance amplifiers. Based on the analytical model created for the amplifier, a noise level of 450 $nV/\sqrt{Hz}$ can be achieved when the circuitry is fully integrated with the sensor.

Thesis Supervisors: Timothy Denison, Steven Leeb

Titles: Design Engineer, Professor of Electrical Engineering

# TABLE OF CONTENTS

# LIST OF FIGURES

# LIST OF TABLES

# ACKNOWLEDGEMENTS

The list of acknowledgements for this work must begin with my family and friends, without whose undying support, the completion of this work would not have been possible. I must also thank my academic advisor, Professor S. B. Leeb, whose guidance and nudging (read: kick in the pants) led me and kept me moving forward through the unclear and sometimes uncharted territory of the Ph.D. process.

In addition, I'd like to extend sincere thanks my thesis committee -- Dr. T. A. Denison, Prof. S. B. Leeb and Prof. J. K. Roberge -- for taking their time to review this dissertation. I'd like to thank Halston Taylor and the MIT Men's Varsity Track & Field team for providing an outlet for the stress and frustrations associated with this dissertation.

I'd also like to thank Analog Devices Inc. for granting me virtually unlimited access to their facilities, expertise and experience in the design of MEMS devices. More specifically, I'd like to thank Sam Fuller and Frank Weigold for the financial support of my thesis work, Craig Core for his generous grant of fabrication resources, Thomas Chen for keeping my layouts realizable and more importantly, for supervising the fabrication of my design, Tom Kelly, David Whitley & Steve Lewis for lending me their design expertise and their endurance of my incessant questions, Al Lima for providing laboratory support and well-needed comic relief, Jinbo Kuang and Bill Crocker for their assistance with the mechanical modeling of the sensor, and O.C. Wambu for always

having a patch or workaround for Cadence limitations. I'd like to thank all of the Micro-machined Products Division of Analog Devices Inc. for their unmentioned, but not insignificant, contributions to this thesis.

Lastly, I'd like to offer my deepest appreciation and gratitude to Tim Denison, without whom the idea for this work would not have been conceived. His undying support, guidance and most importantly, friendship carried me through this dissertation. For that, in addition to the countless favors he cashed in to expedite the process, I owe him an unrepayable debt and therefore, I dedicate this work to him.

# 1 INTRODUCTION

This thesis involves the design, fabrication and characterization of a fully differential parametric amplifier (para-amp) that can be configured for use as either a low-leakage amplifier, or as a galvanically isolated differential amplifier. The performance of this design is based on a physically coupled, but electrically isolated fully differential mechanical transconductor fabricated using silicon-on-insulator micro-electromechanical structures (SOI-MEMS) technology and a fully differential feedback loop. The transconductor's galvanically isolated inputs allow the amplifier to be applied as an isolation amplifier. Some of the amplifier design and testing along with its fabrication was done at the Micromachined Products Division of Analog Devices, Inc. in Cambridge, Massachusetts. The mechanical transconductor will be part of a differential amplifier that is designed to have low input leakage currents (< 1 pA), low input voltage offset (1 mV), wide common-mode range (±150 V), and moderate input noise (≤55 $\frac{\mu V}{\sqrt{Hz}}$).

One of the important tradeoffs made in order to achieve the wide common-mode range possible with this design is the system bandwidth. The system bandwidth will be limited by the resonant frequency of the mechanical transconductor (< 100 kHz). At first glance, low system bandwidth may seem like a severe limitation. However, a few kilohertz of bandwidth, in addition to the specifications mentioned above, is well-suited for a variety of applications including pH meters, thermocouples and ion gauges.

This thesis focuses on the design of a differential amplifier with galvanically isolated inputs. The rest of this chapter motivates the characteristics desired in an ideal amplifier, presents typical characteristics of high-performance amplifiers, and an overview of common isolation techniques. Amplifier design considerations and their imperfections will also be discussed. This overview will provide a context for the work described in this thesis.

## 1.1 HIGH PERFORMANCE AMPLIFIER OVERVIEW

### 1.1.1 IDEAL AMPLIFIERS

Important performance metrics for gauging the performance of an amplifier include: open-loop gain, bandwidth, common-mode rejection ratio, input common-mode range, leakage currents, and input referred offset voltage. Moreover, an *ideal*, high performance amplifier would have:

- Infinite open-loop gain so it has zero error between input and output when placed in a unity gain feedback configuration
- Infinite bandwidth so it can process signals spanning the entire frequency spectrum
- Infinite common-mode rejection ratio so it only responds to the differential component of the input signal
- Infinite input common-mode range so that the amplifier can still properly amplify the differential component of the input signal regardless of the amplitude of the common-mode component
- Zero leakage currents so that its input stage bias current does not induce an offset voltage or any current noise
- Zero offset voltage, drift and noise so that there is no error between input and desired output.

As with all designs, tradeoffs between amplifier properties have to be made depending on the performance required by the particular application.

Based on the tradeoffs possible between these amplifier properties, high performance amplifiers typically fall into one of three categories: parametric amplifiers (para-amps), electrometers, and instrumentation amplifiers. The main building block of these high performance amplifiers is the operational amplifier (op-amp), which typically has a differential input stage and a single-ended output stage. When a single-ended measurement is required, a single op-amp can be configured as an electrometer as shown in Figure 1.1a. Alternatively, an op-amp can be configured as a parametric amplifier by using a parametric device (typically a vibrating capacitor) with the op-amp, as shown in Figure 1.1b. When a differential measurement is required, an instrumentation amplifier, which is used to amplify a small differential signal in the presence of very high common-mode voltages, can be used.

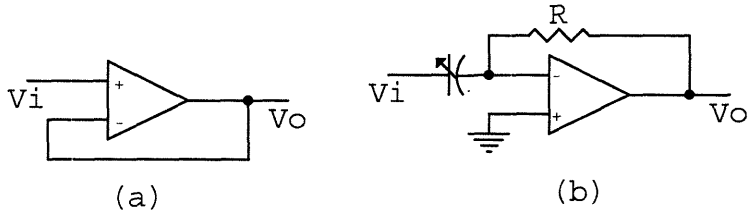


Figure 1.1: Non-inverting electrometer (a) and parametric amplifier (b)

The main tradeoff made in this design was bandwidth. Physical sensors used to make precision measurements, e.g. pH electrodes, often have capacitance as low as 100 fF and resistance greater than $10^{13}\Omega$. The resulting time constant is greater than 50 seconds, corresponding to a bandwidth less than 3.2 milliHertz [69]. In addition, many measurement variables such as temperature or pressure change slowly due to their

inherent physical bandwidths. Therefore, when designing an amplifier that will interface to one of these sensors, high bandwidth is not required. This thesis focuses on the design of a differential amplifier that uses a parametric device as its input stage to achieve a high input impedance, low drift, and high input common-mode voltage swing at the expense of unneeded bandwidth.

### 1.1.2 High Performance Amplifier Design Considerations

In contrast to electrometers, which are typically used to make single-ended measurements, the MEMS-enabled differential amplifier investigated in this thesis most closely resembles an instrumentation amplifier (in-amp). A good instrumentation amplifier has very high input impedance, high common-mode rejection ratio (CMRR > 80 dB), wide bandwidth (>100 kHz) and DC gain in the 1-1000 range [7]. Similar to in-amps, the MEMS-based differential amplifier in this design has high input impedance due to its vibrating capacitor input stage, and a precise DC gain due to its closed-loop operation. However, this design only has a moderate bandwidth (<1 kHz) and moderate untrimmed CMRR (60-70 dB), while adding galvanic isolation found in isolation amplifiers. Since this amplifier does not completely fall into any of the previously mentioned categories, the design implemented in this thesis shall simply be referred to as a differential amplifier.

At the core of any differential amplifier is an input stage that draws very little current, has very low input noise, and is robust enough to withstand overvoltage

conditions that occur during normal operation [1]. The specifications of a few high performance amplifiers along with the MEMS differential amplifier's predicted performance are shown in Table 1.1. Input currents of 100 pA or less have been reported in the literature [1,3,4,6]. The currents that high performance amplifiers are used to measure, are typically less than a few microamperes and can vary by more than 5 decades [2]. Since most designs of high performance amplifiers are based on op-amps, the limitations and imperfections of op-amps, will be briefly discussed in Section 1.2 of this chapter.

| | AD549L | AD629A | LTC2053 | MEMS diff. amp. (predicted) |
|---|---|---|---|---|
| Input Bias Current | 60 fA | N/A | 10 nA | 500 pA |
| Input Offset Voltage | 0.5 mV | 1 mV | 10 μV | 1 mV |
| Input Offset Voltage Drift $\frac{\mu V}{^{o}C}$ | 10 | 20 | 0.05 | |
| Input Voltage Noise @ 1 kHz | $35\frac{nV}{\sqrt{Hz}}$ | $550\frac{nV}{\sqrt{Hz}}$ | $52\frac{nV}{\sqrt{Hz}}$ | $55\frac{\mu V}{\sqrt{Hz}}$ |
| Input Impedance | $10^{13}\ \Omega$ | 800 kΩ | 4 MΩ (est) | |
| Input Common-mode swing | ±10 V | ±270 V | ±5.5 V | ±200 |
| Common-mode rejection ratio | 90 dB | 88 dB | 113 dB | 60-70 dB (untrimmed) |

Table 1.1: Specifications of selected high performance amplifiers. The AD549L is a fA electrometer, the AD629A is a high-voltage (250 V) in-amp, and the LTC2053 is a low-drift high CMRR in-amp.

In certain applications, where accessibility to the actual circuit is difficult, maintenance and recalibration are unacceptable and, for example, in the cases of satellites and downhole oil wells, sometimes impossible [12]. To achieve robustness, some designers have used dynamic feedback as described in [12], but most in-amp designers

use chopper stabilization (CHS) [11,13,14,15] or correlated double sampling (CDS) [16,24,30,31,32]. The latter of these two techniques is employed within the LTC2053 and the MEMS differential amplifier, but both techniques will be discussed in Section 1.3 of this chapter. This amplifier provides galvanic isolation due to its vibrating capacitor input stage. Therefore, isolation amplifier properties will also be discussed in Section 1.4 of this chapter.

## 1.2 AMPLIFIER IMPERFECTIONS

The implementation of solid state amplifiers, whether bipolar, MOS or JFET, will determine the limitations of the amplifier's performance. More specifically, the performance of measurement amplifiers is largely determined by the design of the input stage. However, regardless of the implementation of its input stage, the amplifier will exhibit the following properties in varying degrees: leakage currents, voltage offset, voltage offset drift, common-mode and differential-mode gain, common-mode rejection ratio, common-mode input range and input noise.

### 1.2.1 LEAKAGE CURRENT

An ideal voltage amplifier has infinite input impedance and therefore draws no current. In reality, very high impedances have been reached ($10^{15}\Omega$ as reported in [1]), but this and other finite values give rise to non-zero currents that *leak* into the amplifier's virtual ground node. These leakage currents are used to bias, or set the quiescent operating point, of the input transistors. Most of the early electrometer amplifier designs

employed either MOSFET or bipolar-compatible JFET input stages [1,3,4,6]. The gate of a MOSFET is low leakage by design but it requires diodes for protection against overvoltage conditions. These protection diodes have the adverse effects of lowering the common-mode impedance and increasing the input current. To circumvent the need for these diodes, the gate oxide of the FET would need to be thickened but this has the adverse side effect of worsening the device's noise performance [1].

The JFET, on the other hand, does not require the use of voltage clamps at their input. Since the input of a JFET is a reverse-biased p-n junction, the maximum input voltage is determined by the junction's reverse breakdown voltage. Current limiting can be achieved by using an external series resistor, with the cost of its thermal noise contributing to the input voltage noise of the amplifier [1].

Typical values of leakage currents at room temperature are in the 10-100 nA range for bipolar inputs; less than 10 pA for JFET input devices and less than one fA for MOSFET inputs [17]. These values worsen for a JFET because the leakage current increases with temperature. In the case of the AD549, a JFET input op-amp made by Analog Devices Inc., the input current goes up by a factor of 2.3 every 10 °C, as shown in Figure 1.2 [38].

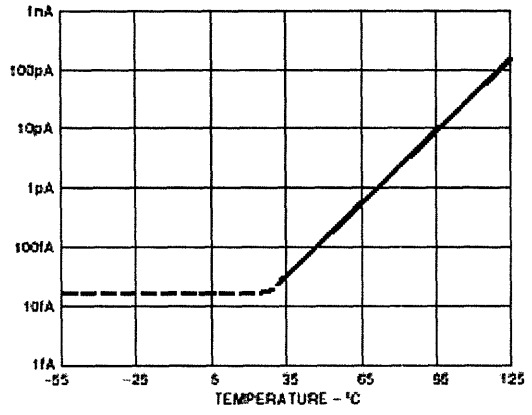


Figure 1.2: Leakage current versus temperature for AD549 op-amp [38]

### 1.2.2 VOLTAGE OFFSET

The voltage offset of an op-amp is made up of two components: a random offset and a systematic offset. The random offset is due to component mismatches within the amplifier and can be minimized with proper layout techniques and by using input transistors and active-load transistors with very large dimensions [21]. The systematic offset is due to the drift of the input stage being amplified by the voltage gain of the amplifier [18]. Typical values for input offset voltage are in the 1-10 mV range for MOSFET input amplifiers, 100-1000 μV for JFET input amplifiers and 10-100 μV for amplifiers having BJTs as the input devices.

An additional source of voltage offset includes leakage currents. As previously described, they will give rise to unwanted voltage drops in the resistors that form the feedback network. This will cause a non-zero voltage at the output of the amplifier when there is zero applied input voltage. Therefore, the input offset voltage is defined as the differential input voltage that must be applied to cancel the non-zero output voltage [17].

### 1.2.3 VOLTAGE OFFSET DRIFT

Most op-amps have terminals that are used to null the offset voltage with external circuitry, typically a potentiometer. However, after nulling the offset voltage, the amplifier may exhibit a non-zero offset as the amplifier's operating temperature changes. This variation of the offset with respect to temperature is called drift.

In field-effect transistors (MOSFETs & JFETs), the drain current varies with temperature due to two opposing effects. The mobility of carriers in the channel decreases with temperature causing a decrease in drain current, while the depletion layer width at the gate decreases with temperature thereby causing a widening of the channel and an increase in drain current. With the proper choice of biasing, these two effects can theoretically be made to cancel each other, as shown in [18-20]. Using this cancellation method typically results in voltage offset drift in the 10 μV/°C range, which is typical of amplifiers that don't employ the cancellation technique [1,17].

### 1.2.4 COMMON-MODE REJECTION RATIO (CMRR)

The input signal to an op-amp has two components: common-mode and differential-mode, and gives rise to corresponding output voltage components. The common-mode rejection ratio (CMRR) is defined as the magnitude of the ratio of differential gain to common-mode gain. It is a measure of the change in input offset

voltage that results from a unit change in common-mode input voltage [17]. Ideally, the CMRR would be infinite so that the offset would not change over the entire common-mode input voltage range. It is also interesting to note that the voltage offset of differential amplifiers and their CMRR result from the same mismatch effects [11].

Most simple analyses of CMRR of op-amps are satisfactory at low frequencies but are not valid above one kHz [9]. Below one kHz, the CMRR of the basic differential amplifier shown in Figure 1.3 is determined by the matching of the resistors [9]. At higher frequencies, the CMRR of the circuit is limited by the CMRR of the op-amp and any parasitic shunt capacitance seen by the feedback resistors. The CMRR is quoted in decibels and typical values are greater than 80 dB, although in some cases the CMRR may be difficult to measure [9].

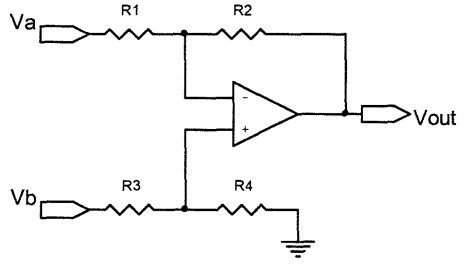


Figure 1.3: Simple differential amplifier

### 1.2.5 Input Common-mode Voltage Range (ICMVR)

The input common-mode voltage range (ICMVR) is defined as the range of input voltages in which all devices in the input stage remain in their active regions. A simplified example of a typical input stage is shown in Figure 1.4. In this MOSFET

example, the upper limit of the ICMVR is set by the saturation voltage of the input stage's bias current source, M5, and its value will be $V_{DD}$-$V_{DSsat,\ M5}$. The lower limit of the ICMVR will be set by the saturation voltage of the load device, M4, and its value will be $V_{SS}$+$V_{DSsat,\ M4}$. Recent designs have demonstrated rail-to-rail input swings using parallel input stages or switched capacitor techniques as shown in Linear Technologies' LTC2053 [65].

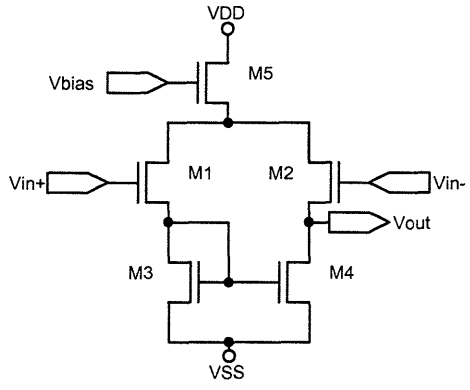


Figure 1.4: Typical MOSFET differential pair input stage

It is evident from these limits that one must maximize the supply voltages while minimizing $V_{DSsat}$ for the bias and load devices. However, the power supplies are limited by the fabrication process, and the $V_{DSsat}$ of the current source and load devices is fixed by other performance specifications, mainly the desired impedance at that node. One method of obtaining a wider ICMVR than the input stage will allow is to precede the input stage with a resistive divider. As is evident in Analog Devices' AD629, this achieves the desired goal, however it also attenuates the input signal by the same factor. Adjusting the gain of the amplifier corrects this attenuation, but the attenuator adds thermal noise to the input signal, amplifies the overall system's RTI noise level by the

inverse of the resistor attenuation factor, and lowers the common-mode and differential mode input impedance [39].

### 1.2.6 INPUT NOISE

Noise exists in circuits because (a) charge is not continuous but carried in discrete quantities and (b) carriers are generated thermally through random processes. Noise analysis is important because it will indicate the equivalent input noise or minimum detectable signal of the amplifier. Noise arises from the fluctuations in currents and voltages in electronic devices that are caused by various factors. The most common types of noise are shot noise, thermal noise, and low frequency or 1/f noise [17].

Shot noise occurs whenever there is a DC current flowing and arises from the fact that the passage of carriers across a pn-junction is a random event. Thermal noise, which mainly occurs in resistors, is due to the random thermal motion of electrons and as such, is directly proportional to temperature. Low frequency or flicker noise is so named from its first observance in vacuum tubes. It exists whenever a DC current flows in a semiconductor and is due to traps, crystal imperfections and contaminants [17, 23]. There is also a type of noise referred to as kT/C noise that occurs when resetting a voltage stored on a capacitor. This is of considerable importance in sampled-data systems and is due to the fact that the voltage on the capacitor is not the exact same value after every reset [22, 24], i.e. not exactly the reset voltage.

These noise sources are generally modeled as independent and uncorrelated and as such, can be computed separately. Since all noise voltage (or current) sources are based on random processes, noise is described by probability density functions (PDFs) having units of $\frac{V}{\sqrt{Hz}}$ or $\frac{A}{\sqrt{Hz}}$. Typical noise levels achieved with diode-protected MOSFET input amplifiers are 220 $\frac{nV}{\sqrt{Hz}}$ at 10 Hz and 80 $\frac{nV}{\sqrt{Hz}}$ at 100 Hz [1]. Bipolar-compatible JFET input amplifiers displayed similar noise levels namely, 300 $\frac{nV}{\sqrt{Hz}}$ at 10 Hz and 100 $\frac{nV}{\sqrt{Hz}}$ at 100 Hz [3]. For example, by using ion-implanted JFETs instead of bipolar-compatible JFETs, noise levels decrease to 60 $\frac{nV}{\sqrt{Hz}}$ at 10 Hz and 30 $\frac{nV}{\sqrt{Hz}}$ at 100 Hz in [5]. Burr-Brown's OPA27 has a bipolar input stage and it has achieved a noise level of 4.5 $\frac{nV}{\sqrt{Hz}}$ at one kHz. More recent designs such as shown in [11] have achieved noise levels as low as 8.5 $\frac{nV}{\sqrt{Hz}}$ using chopper stabilization, a signal processing technique that will be discussed in Section 1.3.2 of this chapter.

### 1.2.7 Input Stage Imperfections Summary

There are many amplifier imperfections that can give rise to measurement errors: leakage current, voltage offset, voltage-offset drift, CMRR, ICMVR, and input noise. Of these imperfections, leakage current, ICMVR and input noise are typically most crucial to instrumentation. To minimize the leakage currents, using an unprotected MOSFET differential-pair at the input will yield the best results. When optimizing noise performance, BJTs outperform MOSFETs for low source impedance applications, but JFETs are preferred over BJTs for moderate to high source impedance applications

because of their higher input impedance. However, excess leakage at high temperatures undermines JFET performance. Moreover, with these three semiconductor devices, the only way to expand the ICMVR is through attenuation of the common-mode of the input signal, which has the undesired effects of reducing the signal amplitude and worsening the overall amplifier's noise performance.

It is evident that the ideal solution is an input stage device that has the low leakage current of a MOSFET, the low noise performance of a BJT or JFET and the galvanic isolation of capacitive coupling. Currently, designers have to compromise performance when the input stage device is chosen. A capacitive input transducer, however, can simultaneously achieve low leakage, isolation and low noise for many measurement specifications. Depending on the breakdown voltage of the dielectric, an ultra-wide ICMVR can be achieved as well, thereby satisfying three of the requirements of a high performance amplifier. Another requirement, low-offset, can be minimized via offset reduction techniques described in the next section.

## 1.3 Input Offset And 1/f Noise Reduction Techniques

There are multiple signal processing approaches to reduce input noise in MOS amplifiers. The two most common techniques are correlated double sampling (CDS) and chopper stabilization (CHS). Most sampled data systems use CDS while continuous time systems use CHS. It is possible to employ both techniques in the same design, however no such designs have been reported at the time of this writing.

### 1.3.1 CHOPPER STABILIZATION

Chopper stabilization is a technique that modulates the input signal to a higher frequency, where low frequency, or 1/f noise, is negligible compared to the transistor's broadband noise. More specifically, the input is multiplied by a sine or a square wave, the latter creating replicas at the odd harmonic frequencies of the square wave. The resulting signal is fed through an amplifier that has a bandwidth of only twice the frequency of the square wave, or chopper frequency. The remaining signal is essentially the fundamental of the input signal, along with the fundamental component of the noise. There is a slight reduction in DC gain of the overall amplifier, but there is a significant reduction of the noise because the noise level at the chopper frequency is what gets demodulated [11,16].

A typical implementation of a chopper modulator is the configuration of four cross-coupled switches, as shown in Figure 1.5. Due to the non-idealities of this modulator, specifically the implementation of the switches, there is a residual offset voltage between the input and output. If the switches are MOSFETs, the contributions to the offset voltage will include clock feed-through and charge injection. Charge injection results from the release of channel charge through the drain and source terminals. The clock feed-through occurs due to the gate-to-drain and gate-to-source capacitors, and it results in a waveform similar to Figure 1.6 at the output of the modulator. The odd symmetry of the waveform indicates that all of its energy occurs at odd harmonics, which will be added to the modulated replicas of the input. If the in-amp is appropriately band-limited, then only the fundamental of the clock feed-through waveform will contribute to

the offset. Using this chopper stabilization technique, offset voltages as low as 100 nV have been achieved [15,16].

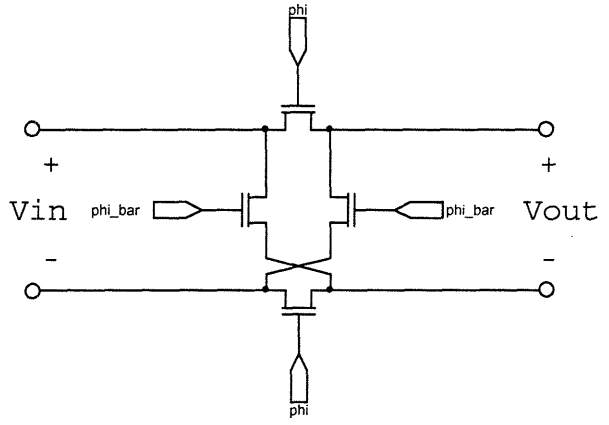


Figure 1.5: Chopper modulator

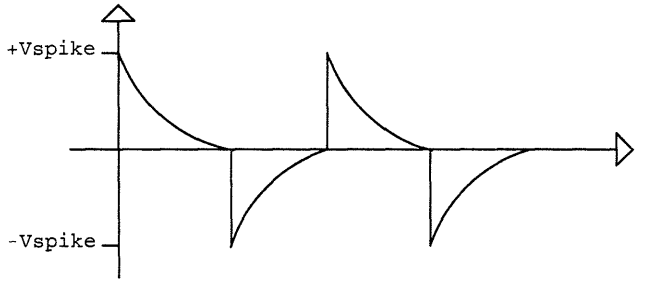


Figure 1.6: Typical clock feedthrough waveform

### 1.3.2 CORRELATED DOUBLE SAMPLING

The method of correlated double sampling (CDS) is based on autozeroing. Since its introduction over 50 years ago to reduce noise in charge-coupled devices, it has seen wide use in switched-capacitor circuits and other sampled data systems. As its name implies, there are two sampling operations: the first one to sample the amplifier offset plus noise, the second to sample the amplifier output plus any instantaneous noise [16].

In essence, CDS is autozeroing (AZ) followed by an additional sample-and-hold. Autozeroing is a method of sampling the noise and voltage offset of an amplifier and then subtracting the sampled quantity from the input or output of the amplifier. Ideally, the DC offset will be cancelled precisely since it will not change over time. However, a time varying quantity like 1/f noise will not be removed but its effects will be significantly suppressed due to the high-pass nature of the AZ process [16].

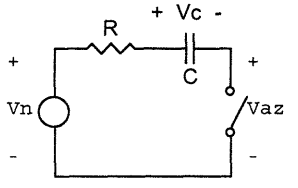


Figure 1.7: Basic autozeroing circuit

To better understand the effects of AZ on the noise performance of amplifiers, we will analyze the circuit in Figure 1.7. The noise source, $V_n$, is comprised of the DC offset of the amplifier, the 1/f noise and white noise components. During the sample phase, the switch is closed and $V_{az}$ is set to zero while $V_n$ is sampled onto the capacitor (if RC is much smaller than the sample interval). When the switch opens, the capacitor will block the DC component of $V_n$ but the other components will be propagated to $V_{az}$. It is shown in [16] that the power spectral density (PSD) of the autozeroed voltage, $S_{AZ}$, is made up of two components, the baseband noise, $S_N$, and the foldover components, $S_{fold}$, introduced by aliasing of the broadband noise. Those results are summarized below.

A PSD composed of both white and 1/f noise is expressed as $S_N$.

$$S_N = S_0\left(1 + \frac{f_c}{|f|}\right);\ f_c = \text{corner frequency}$$

As this noise passes through an amplifier with autozeroing, it is shaped by the $|H_0(f)|^2$ transfer function:

$$|H_0(f)|^2 = d^2\left\{\left[1-\frac{\sin(2\pi f T_h)}{2\pi f T_h}\right]^2+\left[\frac{1-\cos(2\pi f T_h)}{2\pi f T_h}\right]^2\right\}$$; d = duty cycle, $T_h$ is the hold time.

Upon inspection, one can see that this is a high-pass filter with a zero at the origin. This zero is what facilitates the cancellation of any DC offset. The high-pass filter reduces the white and 1/f noise in the baseband, however an additional noise quantity, $S_{fold}$, results from replicas of $S_N$ that occur at multiples of the sampling frequency. The resulting PSD is given by:

$$S_{AZ}(f) = |H_0(f)|^2 S_N + S_{fold}(f).$$

The second term in the above expression for $S_{AZ}(f)$, is caused by sampling the input noise below its Nyquist frequency and results in scaled replicas of $S_N$ aliasing or *folding* into the base band. This *foldover* term, $S_{fold}(f)$, can be written as:

$$S_{fold}(f) = S_0\left\{\left(\pi\frac{f_{3dB}}{f_S}-1\right)+2\frac{f_c}{f_S}\left[1+\ln\left(\tfrac{2}{3}\frac{f_{3dB}}{f_S}\right)\right]\right\}\sin c^2\left(\frac{f}{f_S}\right)$$; $f_{3dB}$ is the 3dB bandwidth of the amplifier, $f_s$ is the sampling frequency, *sinc(x) = sin(x)/x*

The Nyquist frequency, defined as the minimum frequency to sample a signal to avoid aliasing, is twice the noise bandwidth. In this case, the noise is broadband. Therefore, the noise bandwidth will be determined by $f_{3dB}$, which is typically higher than the sampling frequency [16]. Furthermore, if the undersampling factor, defined as the ratio of noise bandwidth to the sampling frequency, is much greater than one, then the foldover noise will dominate the baseband noise and in most cases the aliased noise is dominated by the broadband white noise [16].

To simplify the expression for $S_{AZ}(f)$, the following assumptions are made:

1. $|H_0(f)|^2 \leq 1.6$
2. The undersampling factor, $\frac{\frac{\pi}{2} f_{3dB}}{f_{sample}}$, is typically greater than $5\pi$, to allow for the full settling of a switched capacitor stage.

With these statements in mind, we can write $S_{AZ}(f)$ as:

$$S_{AZ}(f) \cong \pi \frac{f_{3dB}}{f_s} S_0,$$

This is very useful for performing quick, back-of-the-envelope calculations.

In summary, autozeroing is an effective method for canceling the voltage offset of an amplifier in addition to reducing its low frequency or 1/f noise. The tradeoff to this 1/f noise reduction is an increase in the amplifier's broadband noise due to the aliasing or foldover of the original broadband noise into the baseband. Similarly for CDS, there is a zero at the origin for the baseband transfer function that cancels any DC offset and significantly reduces the 1/f noise. However, the folded components will be scaled by different but comparable transfer functions to those described in the autozeroing process [16].

An additional problem with CDS is the need for switches at the input. These non-ideal switches have non-zero leakage currents that may be negligible at room temperature; however, multiple switches' leakage current will become significant as the ambient temperature rises, as was shown in Figure 1.2. In addition, the implementation of the switches may limit the ICMVR of the amplifier, as seen on the LTC2053.

### 1.3.3 Offset Reductions Techniques Summary

Chopper stabilization is most commonly used in continuous time systems. It does not provide a precise cancellation of the input offset voltage like CDS, but its high pass nature allows for significant attenuation of the offset, in addition to 1/f noise, without the penalty of broadband noise foldover. The caveat in using CHS lies in its implementation. The up-modulation required can be easily achieved by using parametric amplifiers, for they provide the modulation without a significant noise penalty or clock feedthrough from the switch implementation.

By using CDS, one can achieve a precise cancellation of input voltage offset and significant 1/f noise reduction. A possible drawback of using CDS is an increase in the amplifier's broadband noise due to aliasing. However, this noise can be minimized with an anti-aliasing filter. In addition, the need for switches at the inputs increases the input leakage current.

In this design, CDS is used. The MEMS structure is used to perform the up-modulation similar to a CHS modulator. Since this is a capacitive input, the drawbacks of using a switch modulator do not apply in this design. The demodulation is performed by using a CDS demodulating integrator. We reap the benefit of the precise DC offset cancellation that CDS provides without the potential for input leakage due to the switches. Since the switched capacitor techniques for CDS are typically easier to fully

integrate on an IC than continuous time CHS techniques, this topology was chosen to verify the CDS techniques that would be used on an integrated circuit.

## 1.4 ISOLATION AMPLIFIER OVERVIEW

In many measurement systems, there is a need to pass a signal from one component to another that doesn't necessarily share a common ground node or there is a very long distance between the sensor and the amplifier. As such, there is a possibility of there being a common-mode voltage between the two components due to either normal operation or a fault condition. To reject this common-mode voltage, the conductive path between the two systems should be broken. This goal is most often achieved by using an isolation amplifier [41].

Isolation amplifiers provide differential amplification while allowing negligible current to flow between its inputs and its outputs. They are typically used to prevent the formation of ground loops, reject common-mode voltages, or to guard against high voltages that may result during a fault condition. The three types of coupling methods that are most commonly used in isolation amplifiers are transformer coupling, optical coupling and capacitive coupling [40-43].

### 1.4.1 TRANSFORMER COUPLING

By including a transformer in the signal path, as shown in Figure 1.8a, one can achieve magnetic isolation. A major advantage of this technique is that it can be used to

transfer power, in addition to the desired signal, across the isolation barrier. This power is typically used to power the isolation amplifier's input stage circuitry but is also available for powering external circuitry [40].

A potential disadvantage to this technique is the relatively low bandwidth that is achievable. Most amplifiers of this type have bandwidths at or below 10 kHz [42]. Another potential disadvantage is leakage due to the interwinding capacitance. Care must be taken to limit this capacitance to a few picofarads so that AC noise on the primary does not couple into the secondary. Some companies, such as Intronics, have included a third winding between the primary and secondary as a method of reducing the interwinding capacitance [40]. Additional disadvantages to using this technique are the relatively high cost, size and weight of the magnetic core of the transformer.

Piezoelectric transformers are a possible alternative to magnetic core transformers. A piezoelectric transformer is made up of a piezoelectric transducer with two sets of terminals, as shown in Figure 1.8b. The input signal's electrical energy is converted to mechanical vibrations at the primary terminals and back to electrical energy at the secondary terminals. Piezoelectric transformers do not suffer from interwinding capacitance leakage like their magnetic counterparts and offer efficiencies as high as 92% [51]. However, their transfer characteristics vary based on load and temperature [43, 51, 52].

Another difficulty with using both magnetic and piezoelectric transformers is the transfer of DC signals across the barrier. The two most common methods of circumventing this difficulty involve either synchronous modulation of the signal, or digitizing the analog signal. The binary information is then sent across the barrier via the magnetic or piezoelectric transformer [42]. The use of these two methods to transfer DC signals across the barrier also results in an upper bandwidth limit on the order of 10 kHz [41, 42].


Figure 1.8: Transformer (a) & piezoelectric (b) isolation amplifiers

### 1.4.2 Optical Coupling

Opto-couplers, as shown in Figure 1.9, offer the capability of transferring signals across the barrier in analog form. The caveat here is that their transfer characteristics are highly nonlinear and require feedback techniques to achieve sufficient linearity. However, using feedback techniques limit the achievable bandwidth to roughly 100 kHz [41,50]. Therefore, to push the bandwidth out into the MHz region, feedback techniques are avoided and a differential approach is used. It is important to note that all opto-couplers exhibit degradation of the current transfer ratio; hence it is crucial that the isolation amplifiers' performance not be directly dependent on it [40]. In addition, they require floating power supplies on the input [50].

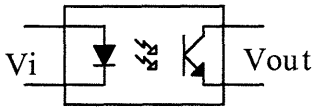


Figure 1.9: Optical isolation amplifier

### 1.4.3 CAPACITIVE COUPLING

Capacitive coupling is shown in Figure 1.10. It is a simple and inexpensive technique, as compared to using magneto- and opto-coupling. Another advantage of capacitive coupling is high reliability. For example, Burr Brown's ISO106 which has been reported to have an equivalent mean time-to-failure of 1660 years [40]. It is also less sensitive to ambient temperature than piezoelectric or electromagnetic coupling techniques [47].

Two typical disadvantages of capacitive coupling are the inability to transfer power across the barrier and the resulting coupling of unwanted AC common-mode voltages. Supplying power to the other side of the barrier typically requires an additional source galvanically isolated from the one used on the input side. The unwanted AC common-mode coupling has been reduced by making the coupling capacitors small in value [40].

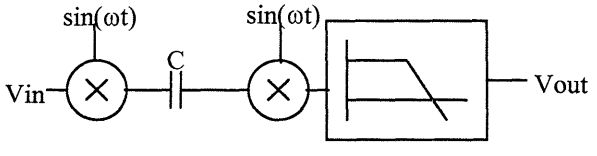


Figure 1.10: Capacitive isolation amplifier

### 1.4.4 ISOLATION AMPLIFIER SUMMARY

Transformer coupling is the most commonly used isolation technique, however it has several disadvantages. This technique does not easily lend itself to integration, thereby making it expensive. In addition, this technique requires a modulator on the input side, which requires power to transfer DC components of the signal across the barrier. Lastly, it has a relatively low achievable bandwidth: a few kHz, which is sufficient for most measurement applications.

Opto-coupling can directly transfer DC signals across the barrier and can achieve bandwidths on the order of MHz. However, they require power to be supplied to the input of the optical transformer, and the inherent nonlinearity of opto-couplers must be carefully taken into account in the design by either employing feedback and/or differential measurement techniques.

Capacitive coupling offers a high level of integration at a relatively low cost. A potential disadvantage is that unwanted AC common-mode voltages can flow across the barrier; however, this can be easily managed because capacitance values are picofarads or less on an IC, thereby reducing the amplitude of the unwanted common-mode signal. This can further be rejected by employing differential measurement techniques at the cost of a limited common-mode voltage range.

As with transformer-based isolators, capacitive-couplers require modulation to transfer signals across the barrier. This thesis builds on this concept and improves it by using vibrating capacitor techniques. The benefit of a MEMS transducer is that the required up-modulation to transfer DC signals across the barrier are achieved with the transducer itself. This results in the isolated measurement of DC signals, without the need for an additional power source.

## 1.5 THESIS OUTLINE

This thesis documents the design, analysis and results of a MEMS based differential amplifier that improves essential measurement parameters at the expense of bandwidth. This design consists of three major components:

- A **differential vibrating capacitor** fabricated using MEMS technology.
- A **self-resonating drive loop** that consists of half of the vibrating capacitor and circuits that start and keep the micro-machined capacitor vibrating at its mechanical resonance.
- A **sense loop** made up of the other half of the vibrating capacitor and circuits that detect and amplify the input signal.

Chapter 2 discusses the overall system design and presents a Simulink model that demonstrates the basic functionality of the amplifier. Chapter 3, the focus of this thesis, presents the mechanical structure, or beam, design. Chapters 4 and 5 discuss the design and results of the drive and sense loops, respectively. Chapter 6 presents the next logical steps in optimizing the performance of this amplifier, which lead to full integration. Transistor designs and some layouts will be presented therein, while Chapter 7 summarizes the overall amplifier's performance. Also, an ADICE® model of the

mechanical transducer was generated and was used to simulate operation of the entire design. This model is included in Appendix A.

# 2 SYSTEM DESIGN

This chapter presents a high level description of the MEMS-based parametric amplifier. The overall architecture along with its three major components will be introduced. To illustrate the principles of this system, a model of the amplifier was created in Simulink.

## 2.1 SYSTEM DESIGN INTRODUCTION

The block diagram of the difference amplifier is shown in Figure 2.1. Note that there are three major blocks: the mechanical sensor, the sense circuitry and the drive circuitry. One may view this system as a differential amplifier where the input stage is a micromachined electro-mechanical structure (MEMS) rather than a traditional transistor pair. The MEMS structure is connected to two separate but co-dependent feedback loops. The drive loop moves the MEMS structure, thereby causing the capacitor to vibrate. The sense loop detects and amplifies the input signal.

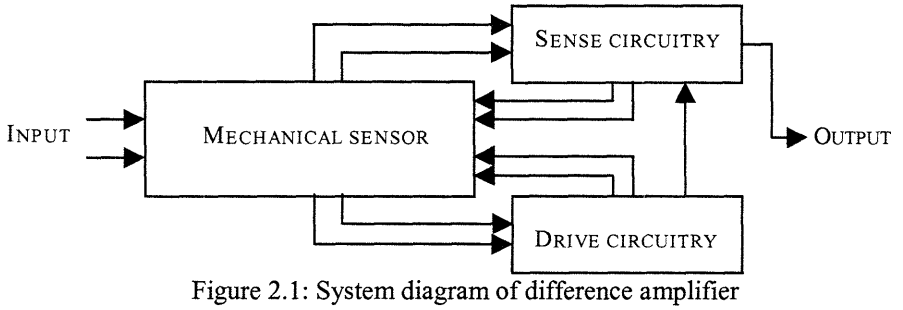


Figure 2.1: System diagram of difference amplifier

## 2.2 INPUT STAGE DESIGN

In this electro-mechanical design, a new approach to input stage design is used and will be presented in detail in Chapter 3. A micro-mechanical sense element is

configured as the input stage transconductor. A vibrating capacitor will couple the amplifier to the input and its operation will be an enhancement of well-known vibrating reed electrometers. The advantage to using a vibrating capacitor as the input transducer is that it does not suffer from Johnson and shot noise. In addition, its action does not depend on resistors or semiconductor junction effects or other dissipative processes that give rise to noise [28].

From Chapter 1, it is evident that the input stage mostly defines the performance of an amplifier. Since the input stages to the sense and drive blocks in this MEMS-based parametric amplifier are also transistor-based, they are subject to the previously mentioned amplifier imperfections. These imperfections cannot be avoided but their effects can be minimized by employing suitable system-level design techniques.

### 2.2.1 VIBRATING CAPACITOR OVERVIEW

The vibrating capacitor is the most commonly used parametric device. Its use dates back as early as 1947 as described in [29]. Its operation involves moving one capacitor plate relative to the other (fixed) one, which varies the separation between the capacitor plates or the area of overlap and hence, the overall capacitance. The capacitance of a parallel plate capacitor is given by: $C = \frac{\varepsilon A}{d}$, where $\varepsilon$ is the permittivity of the insulating material between the plates, $A$ is the area of overlap between the plates and $d$ is the separation between the plates. To modulate the value of a parallel plate capacitor,

there are three degrees of freedom: ε, $A$, and $d$. The limitations of our MEMS process restrict us to varying $A$ and $d$.

Varying the distance between the plates as mentioned above results in a nonlinear change in capacitance which could result in distortion of the input signal. Advantage can be taken of this distortion by using it to generate harmonics and as shown in [49], harmonic sensing can be used to minimize coupling of the drive voltage. In this thesis, a linear vibrating capacitor was implemented by varying the area of overlap between the plates. This approach has advantages and disadvantages over the traditional nonlinear vibrating capacitor and these tradeoffs will be discussed in the next two sections. These sections focus on the *linear* vibrating capacitor that results from changing the overlap area, and the *nonlinear* vibrating capacitor that results when the distance between the plates is varied.

Most vibrating capacitors reported at the time of this writing, whether or not they are micro-machined, operate in a single-ended fashion. Several applications, however, require measuring a small differential signal in the presence of a high common-mode signal, which motivates the need for a differential sense element. Let us start by analyzing the single-ended vibrating capacitor, as shown in Figure 2.2.

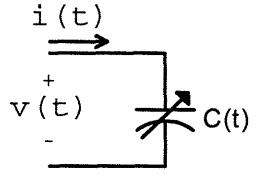


Figure 2.2: Single-ended vibrating capacitor symbol

The input signal *v(t)* and the time-varying capacitance *C(t)* can be expressed as

$$v(t) = V_S e^{j\omega_S t}$$

$$C(t) = C_O + \sum_{i=1}^{\infty} C_{M_i} e^{j\omega_{M_i} t}.$$

Variable $V_S$ is the amplitude of the input signal, $C_O$ is the static capacitance, $C_M$ is the i-th amplitude of the capacitance variation, $\omega_S$ is the signal bandwidth, and $\omega_{Mi}$ is the i-th harmonic of the capacitance modulation frequency. This frequency is sometimes referred to as the pump frequency as in [26, 27, 28]. We can now find the capacitor current *i(t)* by differentiating the capacitor's constituent relation, $Q = CV$.

$$i(t) = \frac{d}{dt}(C(t)v(t)) = v(t)\frac{d}{dt}C(t) + C(t)\frac{d}{dt}v(t)$$

$$= j\omega_S C_O V_S e^{j\omega_S t} + j(\omega_S + \omega_{M_1})C_{M_1} V_S e^{j(\omega_S + \omega_{M_1})t} + \sum_{i=2}^{\infty} j(\omega_S + \omega_{M_i})C_{M_i} V_S e^{j(\omega_S + \omega_{M_i})t}$$

From this expression for the capacitor current, it is evident that there are potentially three components. The first is a component due to the static capacitance that remains at the baseband. The signal of interest is the second term that has been up modulated by the modulation frequency. The third is harmonics that occur at multiples of the capacitor modulation frequency. All of these terms are depicted pictorially in Figure 2.3.

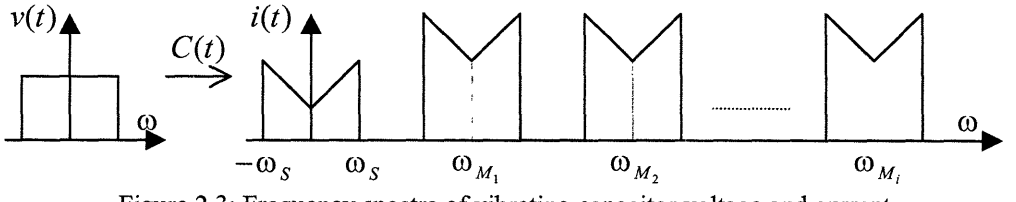


Figure 2.3: Frequency spectra of vibrating capacitor voltage and current

It is desired to suppress the baseband common-mode signal because it is difficult to band-limit or apply anti-aliasing filters to it (the band-limiting shown in Figure 2.3 is for clarity). A typical approach to bandlimiting the common-mode signal is shown in Figure 2.4. The differential mode signal is filtered by the $R$-$C_{DM}$ filter while the common-mode signal is filtered by the $R$-$C_{CM}$ filter. The differential mode capacitor $C_{DM}$ needs to be able to withstand the maximum differential input signal voltage which is generally well within normal process limits (<±24 V for ADI's BIMOS2E process). On the other hand, $C_{CM}$ needs to be able to stand-off voltages in the common-mode range of ±300 V. This tough requirement on $C_{CM}$ is what limits the use of this approach to perform high-voltage common-mode bandwidth limiting.

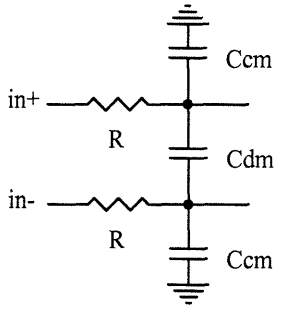


Figure 2.4: Differential- and common-mode bandlimiting

### 2.2.2 Motivation For Feedback

As will be shown in the next section, all possible methods of modulating capacitance yield up-modulated harmonic components of the vibrating capacitor current. These components have a frequency dependent pre-factor, $(\omega_S+\omega_M)$, that will cause distortion if the input is broadband. If a feedback term can be subject to the same

distortion, the overall system will be linear. To better understand this, consider the feedback system in Figure 2.5a. With the frequency dependent prefactor denoted as $\gamma$, it is presented to both the input and feedback signals. Simplifying the diagram in Figure 2.5b, it is evident that $\gamma$ is only present in the forward path of the loop and as such, it will be divided by the loop gain. Therefore, to obtain an overall linear amplifier, the loop gain needs to be very high to minimize the effects of $\gamma$.

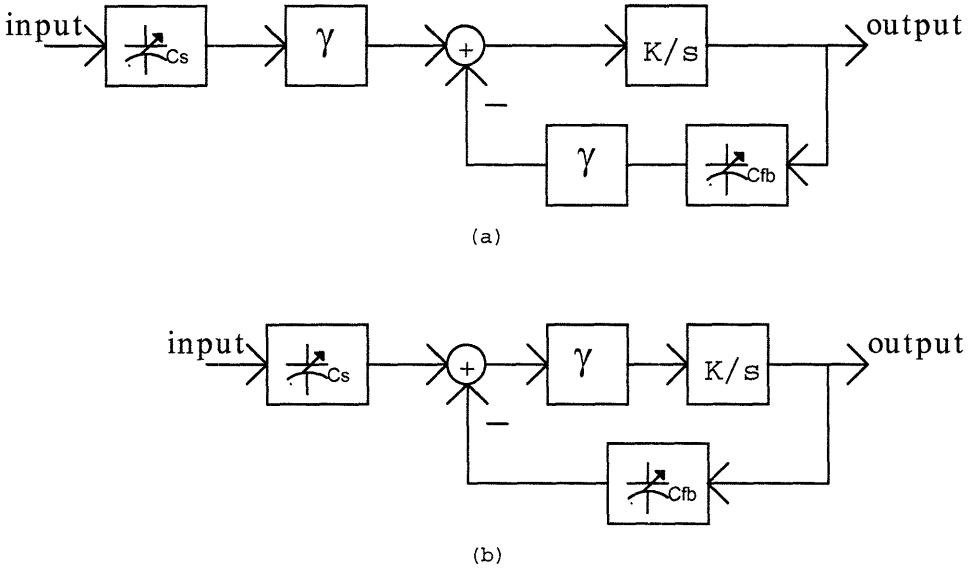


Figure 2.5: Signal chain showing frequency factor, $\gamma$, in the signal and feedback paths (a), simplified signal chain (b).

## 2.3 MEMS-BASED VIBRATING CAPACITOR DESIGN

In this section, we investigate the construction of differential vibrating capacitor based on changing the area of overlap, the gap between the plates, and the dielectric between the plates, all as a function of time.

### 2.3.1 LINEAR VIBRATING CAPACITORS

If the area of overlap between the capacitor plates is varied, then the result is two capacitors in parallel. In this case, the total capacitance is $C(t) = \frac{\varepsilon\left(A_O + A_M e^{j\omega_M t}\right)}{d}$, which easily separates into static and modulating capacitors, as shown in Figure 2.6.

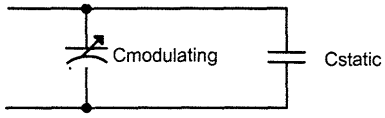


Figure 2.6: Modulating capacitor model for varying overlap area

To apply this principle to a differential amplifier operating on differential signals, consider the structure in Figure 2.7.

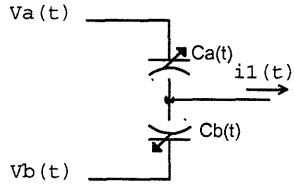


Figure 2.7: Differential variable capacitor

The variables are defined similar to the simple variable capacitor in Figure 1.9.

$$C_A(t) = C_O + C_M e^{j\omega_M t}$$
$$C_B(t) = C_O - C_M e^{j\omega_M t}$$
$$V_A(t) = V_O + \frac{V_S}{2} e^{j\omega_S t}$$
$$V_B(t) = V_O - \frac{V_S}{2} e^{j\omega_S t}$$

$C_A(t)$ and $C_B(t)$ are variable capacitors having $C_O$ and $C_M$ as the static and modulating capacitance amplitudes. $V_O$ and $V_S$ are the signal common-mode and differential-mode parts and $\omega_S$ and $\omega_M$ represent the signal and modulation frequencies, respectively.

Analysis of the differential variable capacitor yields:

$$\begin{aligned} i_1(t) &= V_A\frac{dC_A}{dt} + C_A\frac{dV_A}{dt} + V_B\frac{dC_B}{dt} + C_B\frac{dV_B}{dt} \\ &= (V_A - V_B)\frac{dC_A}{dt} + (C_O + C_M e^{j\omega_M t})\frac{dV_A}{dt} + (C_O - C_M e^{j\omega_M t})\frac{dV_B}{dt} \\ &= j(\omega_S + \omega_M)V_S C_M e^{j(\omega_S+\omega_M)t} + 2C_O\frac{dV_O}{dt} \end{aligned}$$

The first term in the above expression is the desired up-modulated signal term with an additional frequency weight and the second is due to the common-mode component of the input signal, as shown in Figure 2.8.

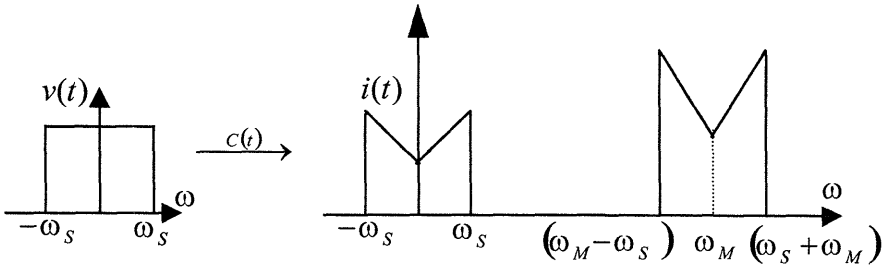


Figure 2.8: Frequency spectra of linear vibrating capacitor current

To reject the unwanted common-mode term in this design, the differential input can be inverted and applied to an identical differential variable capacitor. The output currents will then be subtracted, as shown in Figure 2.9.

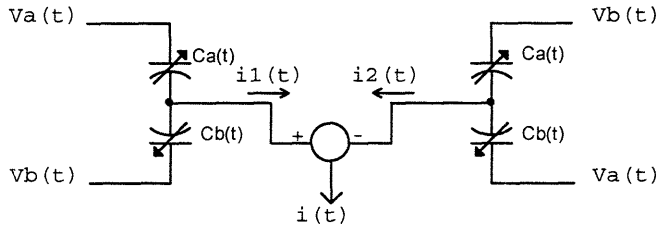

Figure 2.9: Fully differential variable capacitor

Analyzing the fully differential variable capacitor in Figure 2.9, we can write:

$$i_1(t) = V_A \frac{dC_A}{dt} + C_A \frac{dV_A}{dt} + V_B \frac{dC_B}{dt} + C_B \frac{dV_B}{dt}$$

$$i_2(t) = V_B \frac{dC_A}{dt} + C_A \frac{dV_B}{dt} + V_A \frac{dC_B}{dt} + C_B \frac{dV_A}{dt}$$

$$i(t) = i_1(t) - i_2(t) = (V_A - V_B)\frac{dC_A}{dt} + (C_A - C_B)\frac{dV_A}{dt} + (V_B - V_A)\frac{dC_B}{dt} + (C_B - C_A)\frac{dV_B}{dt}$$

$$= 2j(\omega_S + \omega_M)V_S C_M e^{j(\omega_S + \omega_M)t}$$

The significance of this result is that there are no terms due to the static capacitance of the variable capacitor or the common-mode voltage of the input signal. The only term that remains is the differential signal that is scaled and up-modulated by the sense capacitance, $C_M$, as shown in figure 2.10.

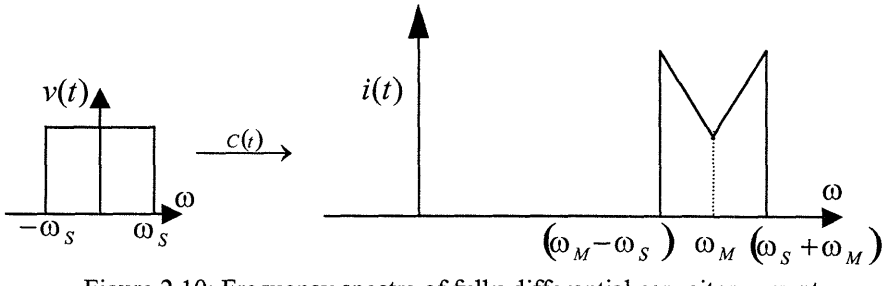

Figure 2.10: Frequency spectra of fully-differential capacitor current

## 2.3.1.1 Linear Vibrating Capacitor Common-Mode Performance

The equations for the force drive and electrical spring constant can be derived from the capacitance and are shown below. The force is constant and because it has no

spatial dependence, there is no electrical spring constant. This means that the common-mode voltage range will not be limited by the electrical spring constant, which is the main advantage of this vibration technique.

$$C = \frac{\varepsilon(A + A_o)e^{j\omega_M t}}{d_o} = C_o + C_M e^{j\omega_M t}$$

$$f = \nabla \tfrac{1}{2} C V^2 = \frac{\varepsilon b V^2}{2g}$$

$$k_e = \nabla f = 0$$

For a 1200μm x 1000μm structure with a resonant frequency of 30 kHz, the modulation capacitance will be on the order of 25 fF and it will have no common-mode restrictions imposed by the electrical spring constant. In practice, the common-mode voltage range is limited by the electrical breakdown of the isolation trenches and the breakdown of the air between the fingers. In the current process, the trenches will breakdown before the applied voltage reaches 200 V. The breakdown of the air in between the fingers occurs at 352 V, which is the minimum spark voltage for an air environment. Adjusting pressure and/or the gas environment can increase the spark voltage significantly [59].

### 2.3.1.2 Linear Vibrating Capacitor Dynamic Source Current

Another important design consideration in vibrating capacitors is the amount of dynamic current drawn from the source. Dynamic current is supplied by the source in order to maintain the voltage at a node while the capacitor vibrates. The fully differential structure will be connected to a pre-amplifier as shown in Figure 2.11. Each voltage source sees two capacitors in parallel, with one capacitor driven 180° out of phase with

the other. For the linear vibrating capacitor, the equivalent capacitance seen by the source is

$$C = \frac{\varepsilon(A_o + A_M e^{j\omega_M t})}{g} + \frac{\varepsilon(A_o - A_M e^{j\omega_M t})}{g} = \frac{2\varepsilon A_o}{g}.$$

From this expression, it is evident that the net input impedance to the MEMS amplifier is equivalent to one static capacitor. Ideally, as the capacitor vibrates, there is no additional current required by the source to maintain the desired voltage drops across the capacitors after this static capacitor is charged. In actuality, this current is nonzero and it depends on the degree of matching of the capacitors in the MEMS structure. For example, a 0.1 % mismatch in the MEMS structure will cause a dynamic current draw of 1.9 nA/V, which looks like an impedance of 530 MΩ. This current can be easily filtered at these frequencies by the capacitance of the bond wires in the IC.

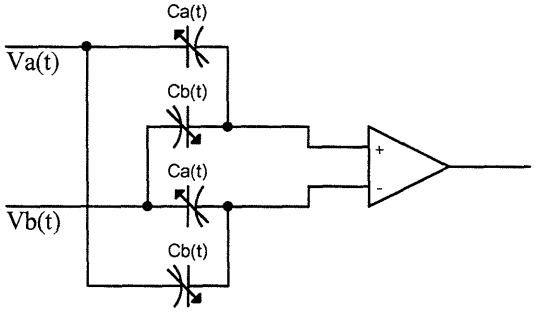


Figure 2.11: Fully differential capacitor and pre-amplifier.

### 2.3.2 NONLINEAR VIBRATING CAPACITORS

As an alternative approach to the linear vibrating capacitor, most vibrating capacitors vary the gap between the plates yielding a total capacitance that has the form

of: $C(t)=\frac{\varepsilon A}{d_O + d_M e^{j\omega_M t}}$. This can be re-written as $C(t)=\frac{\frac{\varepsilon A}{d_O}\frac{\varepsilon A}{d_M e^{j\omega_M t}}}{\frac{\varepsilon A}{d_O}+\frac{\varepsilon A}{d_M e^{j\omega_M t}}}$, which is the expression for the equivalent capacitance of two capacitors in series, as shown in Figure 2.12. It is evident from the above expression that one cannot easily separate the static and time-varying parts of the capacitance for simple cancellation of the unwanted common-mode and static capacitor terms of the output current. However, the following discussion will show how it is still possible to separate the common-mode and differential terms.

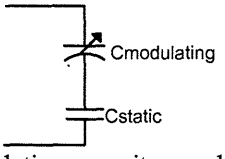

Figure 2.12: Modulating capacitor model for varying gaps

A Taylor series expansion of the above expression for *C(t)* yields:

$$C(t)=\frac{\varepsilon A}{d_o}\left[1-\frac{d_M}{d_o}e^{j\omega_M t}+\left(\frac{d_M}{d_o}e^{j\omega_M t}\right)^2-\left(\frac{d_M}{d_o}e^{j\omega_M t}\right)^3+.....\right]$$

The current from a differential vibrating capacitor structure similar to Figure 2.7 is:

$$i_1(t)=-\frac{\varepsilon A}{d_o}\frac{d_M}{d_o}j(\omega_M+2\omega_S)V_S e^{j(\omega_S+\omega_M)t}\left[1+\left(\frac{d_M}{d_o}\right)^2 e^{j(\omega_S+2\omega_M)t}+\left(\frac{d_M}{d_o}\right)^3 e^{j(\omega_S+3\omega_M)t}+\ldots\right]$$
$$+\frac{\varepsilon A}{d_o}\left(\frac{d_M}{d_o}\right)^2 2j\omega_M e^{j2\omega_M t}2V_o+2\frac{dV_o}{dt}\frac{\varepsilon A}{d_o}\left[\left(\frac{d_M}{d_o}\right)^2 e^{j(2\omega_M)t}+\left(\frac{d_M}{d_o}\right)^4 e^{j(4\omega_M)t}+\ldots\right]$$

From this expression, it is evident that the nonlinearities of the capacitor maps the differential-mode signal to odd harmonics of the modulation frequency while the common-mode term is mapped to even harmonics. As shown in [49], advantage can be

taken of this nonlinear mapping to perform harmonic sensing, which can be used to minimize sensitivity to the drive voltage.

If a fully differential vibrating capacitor similar to Figure 2.9 is built using this nonlinear vibrating capacitor, then the output current will be:

$$i(t) = -\frac{\varepsilon A}{d_o}\frac{d_M}{d_o}(\omega_M + 2\omega_S)V_S e^{j(\omega_S+\omega_M)t}\left[1+\left(\frac{d_M}{d_o}\right)^2 e^{j(\omega_S+2\omega_M)t} + \left(\frac{d_M}{d_o}\right)^3 e^{j(\omega_S+3\omega_M)t} + \ldots\right]$$

It is evident that the common-mode terms are canceled and that a square wave demodulator can demodulate these harmonics back to the baseband.

### 2.3.2.1 Nonlinear Capacitor Common-mode Performance

The equations for the force drive and electrical spring constant can be derived from the capacitance and are shown below. The significance of the electrical spring constant is the common-mode voltage range limit that it imposes on the system. For a nonlinear vibrating capacitor, we can write:

$$C = \frac{\varepsilon A}{d_o + d_M e^{j\omega_M t}}$$

$$f = \nabla \tfrac{1}{2} CV^2 = -\frac{\varepsilon A V^2}{2}\frac{1}{\left(d_o + d_M e^{j\omega_M t}\right)^2}$$

$$k_e = \nabla f = \frac{\varepsilon A V^2}{\left(d_o + d_M e^{j\omega_M t}\right)^3}$$

For a typical sensor of 1200μm by 1000μm and a resonant frequency of 30 kHz, the modulation capacitance is on the order of one pF. This is much larger than the 50 fF obtained from the linear vibrating capacitor, and the resulting improvements in sensitivity

and noise performance make this technique more desirable than its linear counterpart for low-noise applications. The mechanical spring constant that is typically required for this target oscillation frequency is 200 N-m. The structure will stop vibrating, or collapse, when the electrical spring constant equals the mechanical spring constant and for this structure, this occurs at a common-mode voltage of 9V. This upper bound to the common-mode voltage does not even approach the typical supply voltages of ±15 V. It is possible to improve the common-mode performance by widening the gaps, but at the cost of a larger die and decreased sensitivity.

### 2.3.2.2 Nonlinear Capacitor Dynamic Source Current

Another important design consideration in vibrating capacitors is the amount of dynamic current drawn from the source. Dynamic current is the current needed from the source when maintaining the voltage at a node while the capacitor vibrates. The fully differential structure will be connected to a pre-amplifier as shown in Figure 2.13. Each voltage source sees two capacitors in parallel, with one capacitor driven 180° out of phase with the other. For the nonlinear vibrating capacitor case, the equivalent capacitance is:

$$C = \frac{\varepsilon A}{d_o + d_M e^{j\omega_M t}} + \frac{\varepsilon A}{d_o - d_M e^{j\omega_M t}}$$
$$= \frac{2\varepsilon A d_o}{d_o^2 - d_M^2 e^{j2\omega_M t}}$$

The time dependence of this equivalent capacitance shows that dynamic current will be drawn from the sources as the capacitor vibrates. Since this is not a DC current, it is

possible to supply the dynamic charge with a shunt capacitor across the input terminals. However, one must note that the magnitude of this current is higher than that obtained by the area modulation case and as such, will require more filtering, i.e. a larger shunt capacitor.

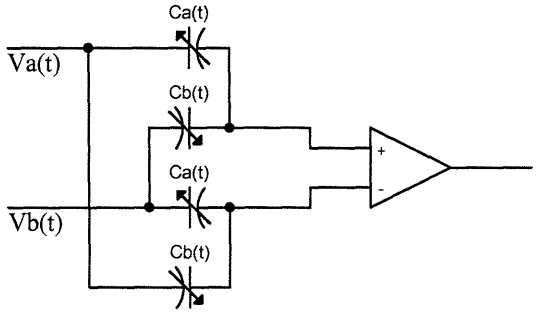


Figure 2.13: Fully differential capacitor and pre-amplifier.

### 2.3.3 DIELECTRIC MODULATION

The last form a capacitance modulation considered was changing the dielectric between the plates, as shown in Figure 2.14. The net change in capacitance with the inserted dielectric is:

$$\frac{\frac{\varepsilon_d A}{d}\frac{\varepsilon_o A}{2g}}{\frac{\varepsilon_d A}{d}+\frac{\varepsilon_o A}{2g}}.$$

Assuming that the minimum distance, $g$, is set by process limitations (and is identical to the previous analysis), we can take the limit of the above expression as the dielectric constant goes to infinity. The result is that the net capacitance between the plates is equivalent to two linear modulation capacitors in series:

$$\frac{\frac{\varepsilon_d A}{d}\frac{\varepsilon_o A}{2g}}{\frac{\varepsilon_d A}{d}+\frac{\varepsilon_o A}{2g}} \overset{\varepsilon_d \to \infty}{\approx} \frac{\varepsilon_o A}{2g}.$$

From the expression above, it is evident that this method will yield 50% of the maximum sensitivity capable of the process compared with previous capacitance modulation techniques. Due to the limited sensitivity achievable and the difficulty in its practical implementation, this technique was not seen as an effective vibrating capacitor.

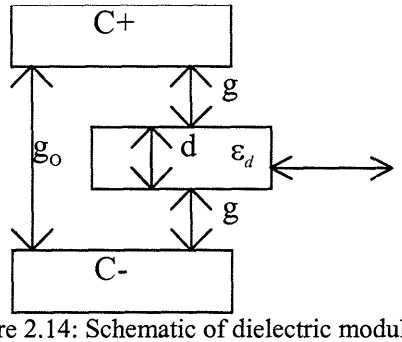

Figure 2.14: Schematic of dielectric modulation

### 2.3.4 VIBRATING CAPACITOR SUMMARY

In the two previous sections, two different types of vibrating capacitors were presented. A linear vibrating capacitor can be obtained by varying the overlap area between the plates. This type of vibrating capacitor is capable of a large common-mode range, typically on the order of 100 V. The downside of this approach is the relatively low modulation capacitance, which was predicted to be 25 fF in this design.

The alternate approach, using a nonlinear vibrating capacitor, has the advantage of yielding a much higher modulation capacitance, which for a comparable device to the one used in this design is on the order of one pF. The disadvantage to this technique is the

limitation on the common-mode range imposed by the negative electrical spring constant. The common-mode range in this case was limited to nine volts, which is well below the typical common-mode range of ±15 V or higher for instrumentation amplifiers. The choice of the modulation scheme depends on the needs of the particular application. For this thesis, a wide common-mode range was desired so a *linear* vibrating capacitor-based design was chosen for implementation.

## 2.4 DRIVE LOOP OVERVIEW

The goal of the drive loop is to keep the mechanical structure oscillating at its mechanical resonance. The drive circuitry, Figure 2.15, forms an oscillator feedback loop with the sensor and vibrates the capacitor. Using describing functions, this feedback loop is designed to keep the sensor oscillating at its mechanical resonance so as to maximize displacement, and thereby sensitivity to differential signals.

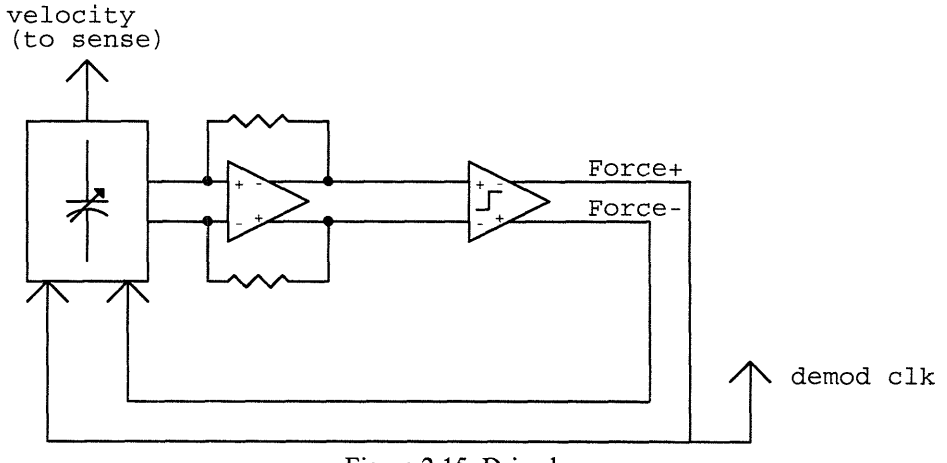


Figure 2.15: Drive loop

Figure 2.16 shows what the drive loop looks like at resonance. An amplifier senses the output current of the beam, which is analogous to the beam velocity. This is

converted to a voltage and fed into a comparator. The comparator drives the beam and provides the clock for the demodulator in the signal loop. The details of this design will be presented in Chapter 4, however a preliminary analysis shows that the sensed velocity is equal to

$$v_{sense} = \left(\frac{\varepsilon_o b}{g} V_{drive}^2\right)\left(\frac{1}{\beta}\right)\left(V_{bias}\frac{2\varepsilon_o b}{g}\right)(R).$$

Variable $\varepsilon_o$ is the permittivity of free space, $b$ is the thickness of the MEMS structure, $g$ is the gap between the plates, $V_{drive}$ is the electrostatic drive voltage, $\beta$ is the viscous damping in the system, $V_{bias}$ is the bias voltage of the input stage of the transresistance amplifier, and $R$ is the closed-loop gain of the transresistance amplifier.

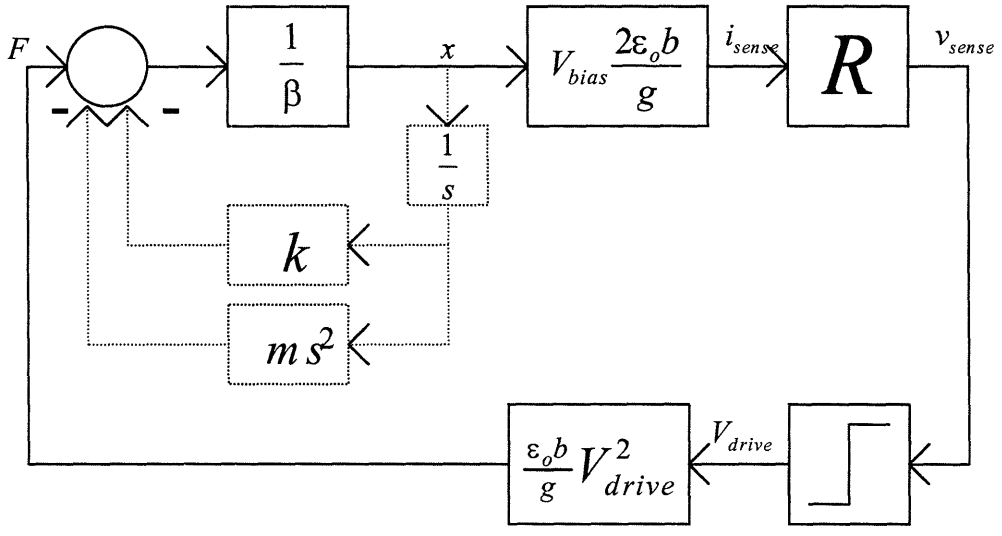


Figure 2.16: Drive loop at resonance

## 2.5 SENSE LOOP OVERVIEW

The sense loop's function is to read off the up-modulated differential signal, amplify it, and then demodulate it back into the baseband for readout. The sense circuitry is connected in a feedback loop with the mechanical sensor in order to form a self-

balanced bridge, as shown in Figure 2.17. This has the added benefit of making the circuit sensitivity immune to forward loop disturbances such as voltage offset and drift, along with nonuniformities in the MEMS structure due to etch mismatch. The velocity input to the mechanical sensor shown in Figure 2.17 is a mechanical input from the drive side of the beam. The drive and sense sides of the beam are mechanically coupled and are only separated here for simplicity.

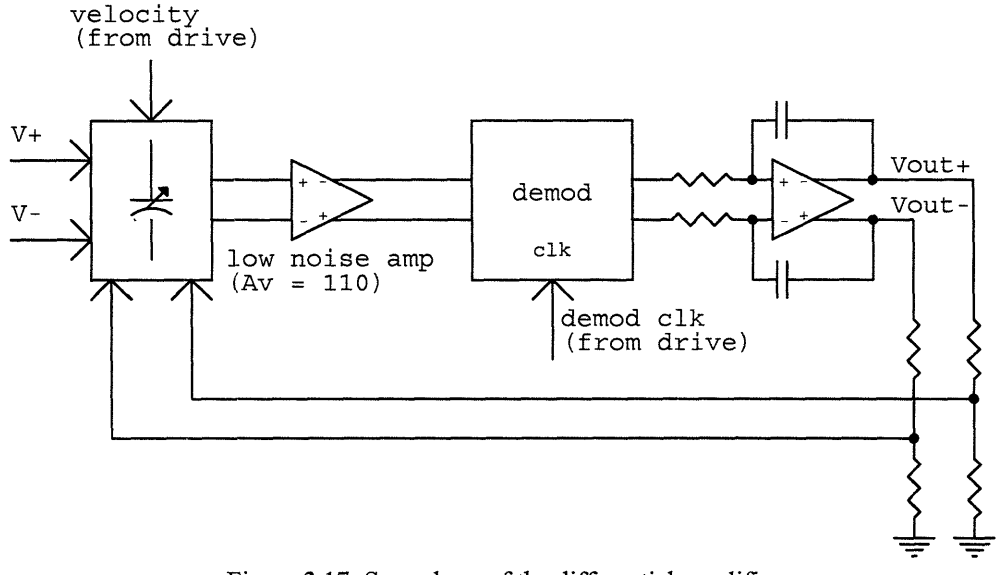


Figure 2.17: Sense loop of the differential amplifier

The differential input voltage signal is transduced into an AC current by the vibrating capacitor. This is a low-level signal, so a low-noise open-loop amplifier is used to detect it. It is important to note that care must be taken to bias the output node of the vibrating capacitor within the linear range of the pre-amplifier. The detected signal is then demodulated with the clock signal from the comparator of the drive loop and then fed into an integrator, which creates the output signal. The corresponding loop transmission is

$$L(s) = \left( \frac{2C_{sense}}{4C_{sense} + C_p} \right) \left( A_{v,preamp} \right) \left( A_{v,demod} \right) \left( \frac{1}{RCs} \right) f \,.$$

The closed-loop gain is set by $f$, the feedback ratio. The complete operation of the sense loop is described in Chapter 5.

## 2.6 SYSTEM MODELING OF THE MEMS AMPLIFIER

As described in the previous sections, the MEMS amplifier consists of two interdependent loops. To demonstrate system principles and the MEMS amplifier's principle of operation, the sensor, drive and sense loops were simulated using the Simulink modeling tool provided with MATLAB. The sense and drive loops were constructed using the built-in transfer function and gain blocks. A block diagram of the entire system is shown in Figure 2.18. The blocks used constants and values that were computed by a MATLAB script file that is in Appendix A.

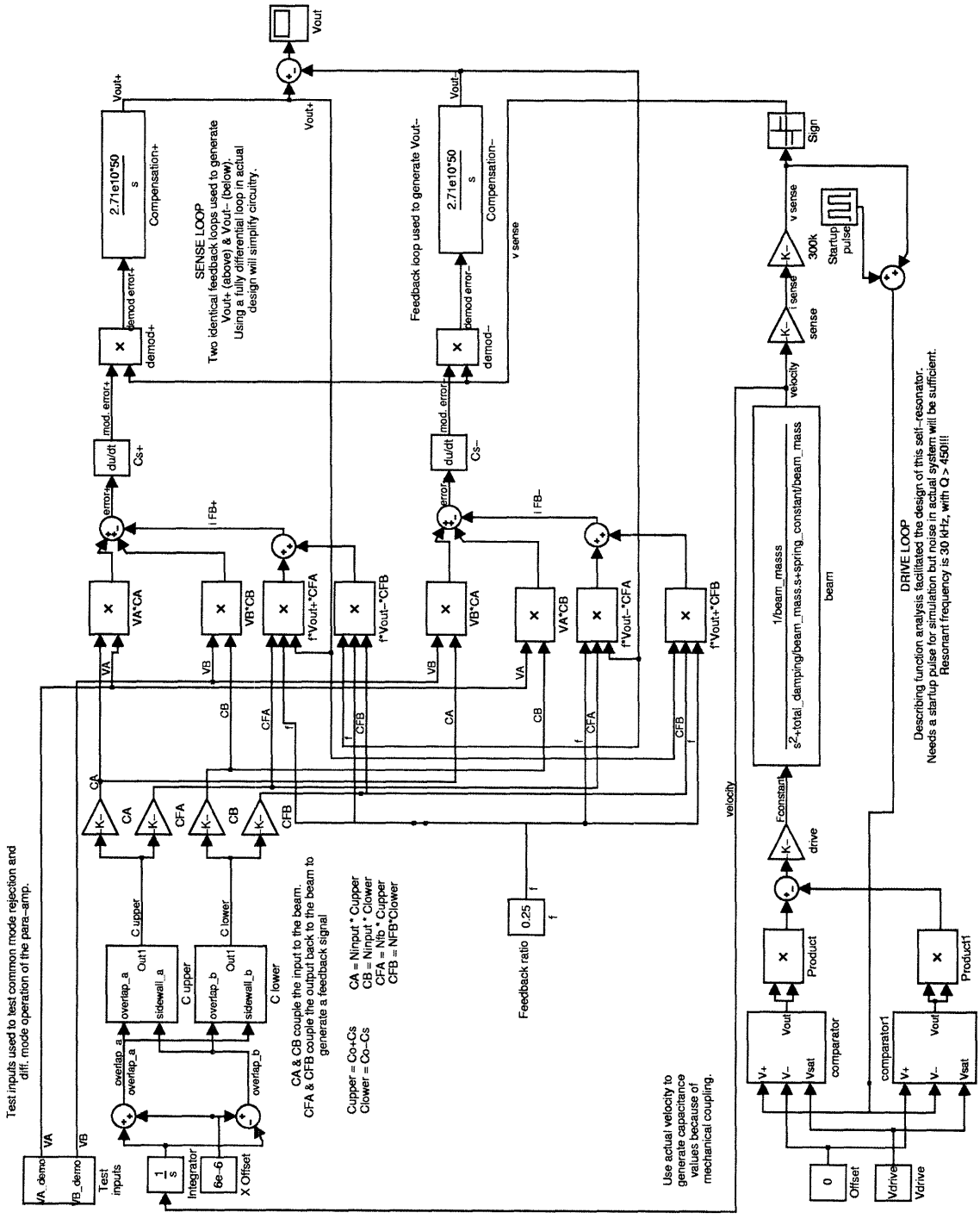


Figure 2.18: Complete Simulink model of the electrometer

### 2.6.1 DRIVE LOOP MODELING

Constructing a model of the drive loop involved translating the block diagram of Figure 2.1 into a block diagram involving Simulink blocks. Electrostatic force actuates the mechanical structure, and when driven at resonance, the velocity and force will be in phase. This was modeled using a transfer function block of the equation:

$$\frac{\dot{x}}{F} = \frac{s}{ms^2 + \beta sx + kx}.$$

The output of this block is velocity, which is converted into a current by the beam via a scale factor. This is modeled by using a gain block of value:

$$V_{bias}\frac{2\varepsilon_0 b}{g}.$$

This current is converted into a voltage by another gain block. This models the transresistance amplifier gain of 200kΩ. This voltage representation of velocity is squared off by comparator blocks, which were constructed using *sign* blocks and constants. The resulting square wave was squared and then converted into the force drive via a scale factor of:

$$N_f\frac{\varepsilon_0 b}{g}.$$

This therefore completes the drive loop. Figure 2.19 shows the velocity increasing gradually until it reaches its steady state value of $2\pi fX$ = 0.9 m/s. In Figure 2.19, $f$ is 30 kHz and $X$, the displacement amplitude, is 5 μm. The settling time of the second order system is approximately $8Q/2\pi f_{res}$, or 19 ms, as is confirmed in Figure 2.19. As expected, the velocity and force drive waveforms are in phase and are shown in Figure 2.20.

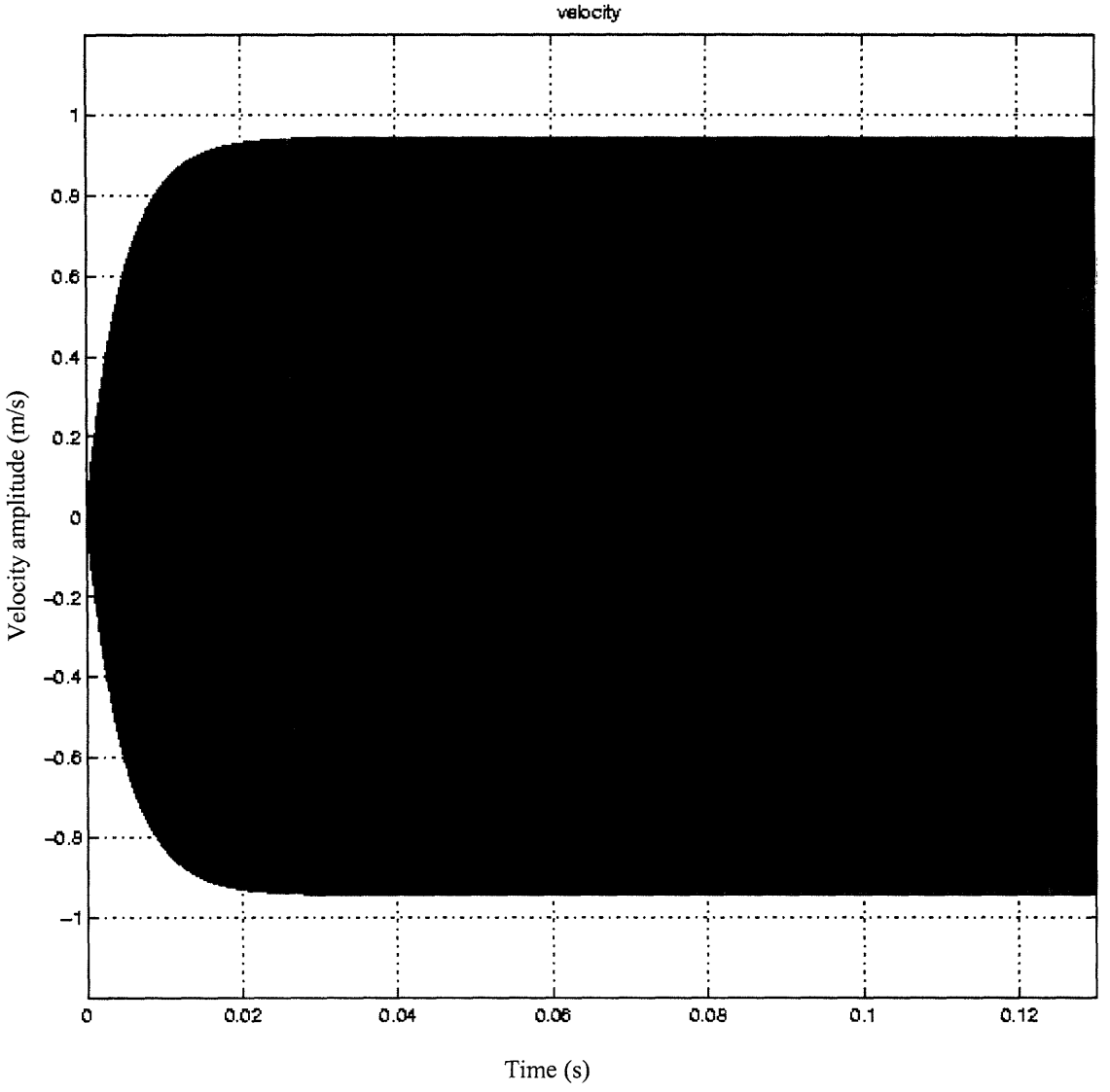


Figure 2.19: Velocity amplitude

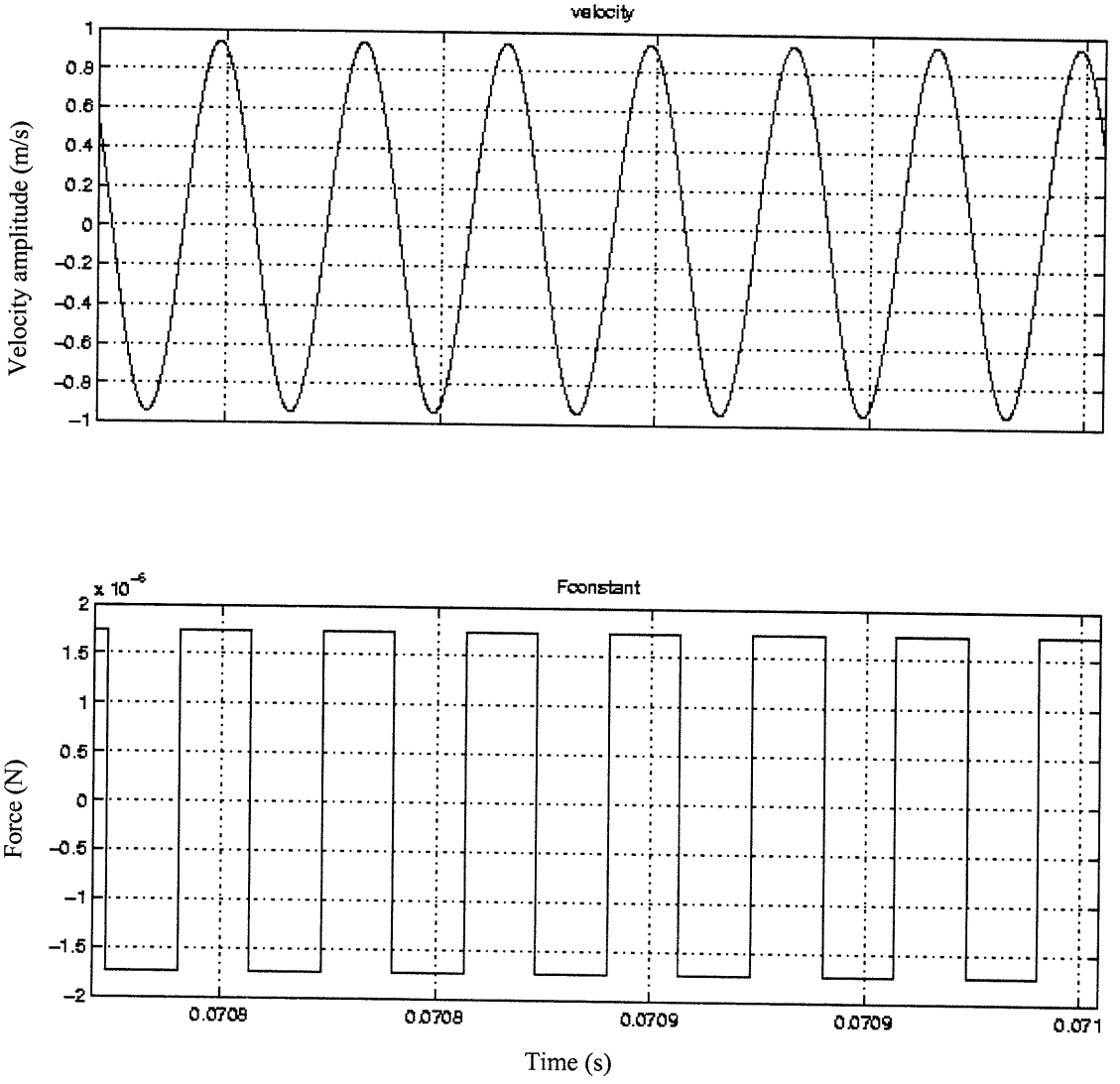


Figure 2.20: Velocity and force waveforms in steady state

## 2.6.2 SENSE LOOP MODELING

With the model of the drive loop operational, the sense loop model was designed. The velocity signal from the drive loop was integrated to generate beam position. Using position, the sense capacitors, $C_A$ and $C_B$, and the feedback capacitors, $C_{FA}$ and $C_{FB}$, could be generated. Then the charge induced on the beam at each terminal was computed, i.e. the *VA*CA* and *VB*CB* products. This error charge is added then differentiated to

generate the error current induced on the beam. The error current then fed blocks that represented the sense loop circuitry.

The error current is demodulated using the velocity sense, not the actual velocity for we will have no access to this directly in the actual circuit. The demodulator was implemented by a multiplier block, with its inputs being the error current and the velocity sense. The demodulated error is then fed into an integrator in order to drive the steady state error to zero, as shown in Figure 2.21. The output of the integrator was multiplied by a feedback ratio, *f*, to emulate a resistive divider, and the divided signal was fed back to the feedback ports to generate the *f*Vout+*CFA* and *f*Vout-*CFB* products. This then closed the single-ended sense loop.

To make the sense loop fully differential, an identical loop was created but the cross terms were computed instead, i.e. *VA*CB*, *VB*CA*, *f*Vout+*CFB*, and *f*Vout-*CFA*. The outputs of the two minor sense loops were then subtracted to yield an overall single-ended output. The response to a set of test inputs is shown in Figure 2.22.

With a closed-loop gain of four, the steady-state response to a differential input step of two should be eight, as is shown in Figure 2.22. The common-mode step of five is rejected. It is evident that the loop only responds to differential input signals and rejects common-mode signals, as desired.

The frequency response of the system is well behaved as well. The step response is first order as expected from a system with a loop transmission of:

$$L(s) = 2(\omega_S + \omega_M)C_M \frac{4}{\pi}\frac{1}{C_{\text{int}}s} f .$$

The factor of two comes from the differential to single-ended conversion, followed by the frequency weighting associated with the output current of the beam. Capacitor $C_M$ is the modulation capacitance amplitude while $C_{int}$ is the integrating capacitor size. The $4/\pi$ term comes from the amplitude of the first harmonic of the square wave demodulator, and lastly $f$ is the feedback ratio. The 10-90% risetime is 0.7 ms, which corresponds to a unity gain frequency of 649 rad/s. This result corresponds very well with the theoretical prediction of 650 rad/s given by the loop transmission.

In summary, a Simulink model of the instrumentation amplifier was constructed. The drive loop's operation was verified by generating a sinusoidal oscillation from a square wave drive at the predicted resonant frequency of the mechanical structure. The sense loop's operation was verified by having a system that responds only to differential signals that have a predictable and well-behaved frequency response.

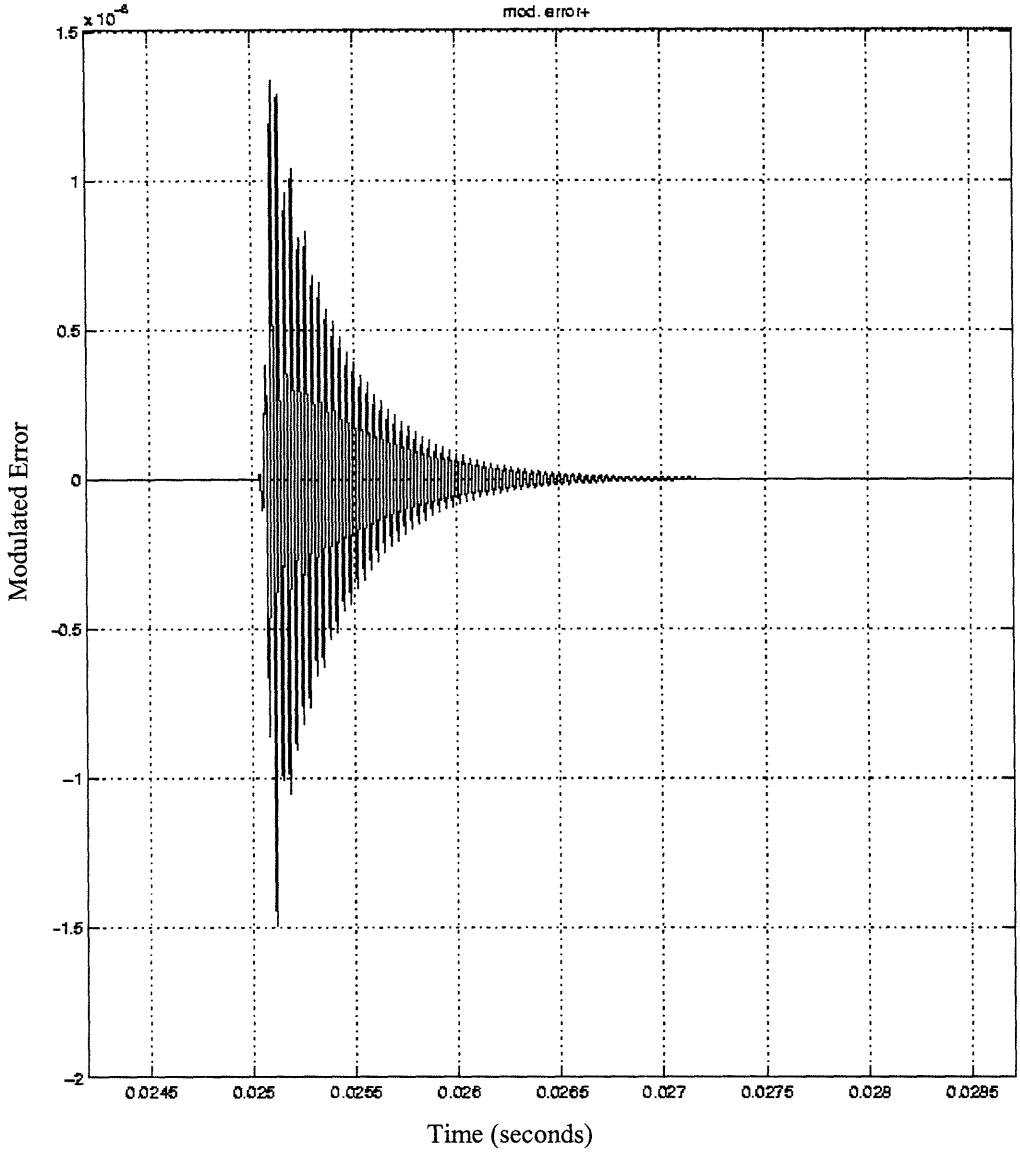


Figure 2.21: Error restored to zero after a differential voltage is applied

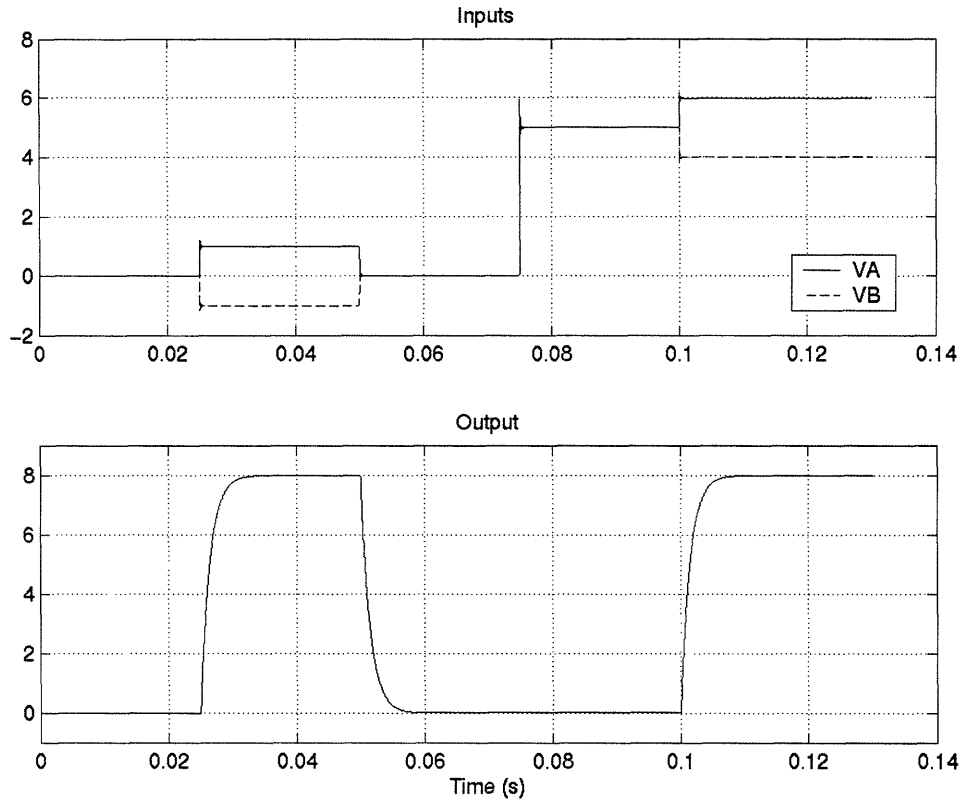


Figure 2.22: Step response of Simulink model of electrometer

## 2.7 SUMMARY OF THE MEMS AMPLIFIER PRINCIPLES AND PERFORMANCE TARGETS

In this chapter, the principles of capacitance modulation were presented. It was shown that there are three parameters available to modulate capacitance. The choice made in this design was area modulation because of the wider common-mode range it facilitated at the expense of sensitivity. Also, the drive and sense loops were defined and their functionality was verified with a model generated in MATLAB/Simulink.

The MEMS sensor provides galvanic isolation between the input and output, facilitating low-leakage currents over temperature and a wide common-mode range. In

addition, this galvanic isolation allows separation of the input and output ground traces, thereby preventing the formation of ground loops that might degrade circuit performance. State-of-the-art wide common-mode amplifiers are capable of withstanding common-mode voltages on the order of ± 200 V. This amplifier is targeting that range as well.

This architecture facilitates the up-modulation of the baseband signal of interest to the MEMS transducer's vibration frequency. This allows for the implementation of CDS and CHS offset compensation techniques. If the modulation frequency is set above the 1/f noise corner frequency of the sense loop's input amplifier, then relatively low-noise measurements are possible for low-frequency physical measurements. A summary of the performance goals is presented below in Table 2.1.

| | |
|---|---|
| Input Bias Current | < 1 pA |
| Input Offset Voltage | 1 mV |
| Input Voltage Noise @ 1 kHz | $50 \frac{\mu V}{\sqrt{Hz}}$ |
| Input Impedance | $10^{15}\ \Omega$ |
| Input Common mode swing | ±200 V |
| Common mode rejection ratio | 60 - 70 dB (untrimmed) |

Table 2.1: Predicted performance of differential amplifier

# 3 MEMS TRANSDUCER DESIGN

## 3.1 MOTIVATION

This design calls for a fully differential vibrating capacitor whose capacitance varies linearly with position. These qualities facilitate:

- Cancellation of the baseband common-mode component of the induced current that is due to the static capacitance.
- Closed-loop operation to minimize the effects of frequency weighting, provide a stable gain and allow for galvanic isolation
- Significant attenuation of dynamic current drawn from the source.

This chapter focuses on the design of a structure that meets these specifications along with the analysis of second order effects such as electrical spring constants, damping, and resonant modes of the arms.

## 3.2 SIMPLIFIED SKETCH AND DESIGN EQUATIONS

A simplified sketch of the mechanical transducer is shown in Figure 3.1. The transducer has eight I/O ports, four for the sense loop, and four for the drive loop. On each port, there is a set of moving fingers surrounded by two sets of fixed fingers. The moving fingers are attached to the central moving mass via moving arms. The fixed fingers are attached to fixed arms that are tied to the substrate.

To achieve the desired linear dependence of sense capacitance on position, the cross-sectional area has to change with position. It is evident that as the beam moves up for example, the area of overlap between the fixed and moving fingers increases in that

direction, thereby increasing the capacitance, and vice versa for the lower set of moving fingers.

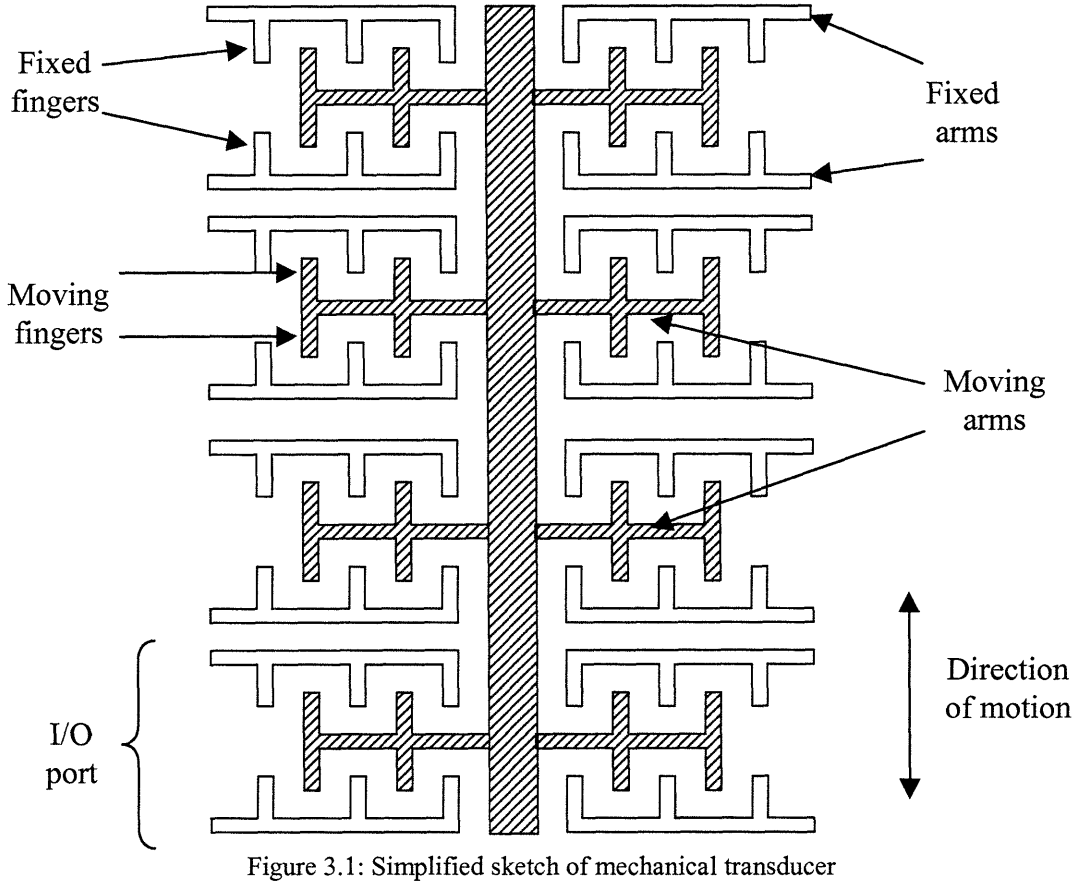


Figure 3.1: Simplified sketch of mechanical transducer

### 3.2.1 SOI-MEMS Fabrication Process

The transducer was fabricated using a modification of Analog Devices Inc.'s proprietary SOI-MEMS process. The outline for this process is shown in Figure 3.2. Starting with an SOI wafer, the first step is to define the electrically isolated but mechanically coupled sections by creating trenches. Then, the circuitry (CMOS, bipolar or BiMOS) is processed. After that, the MEMS structures are etched. The last step is to release the MEMS structure from the substrate, thereby allowing it to move.

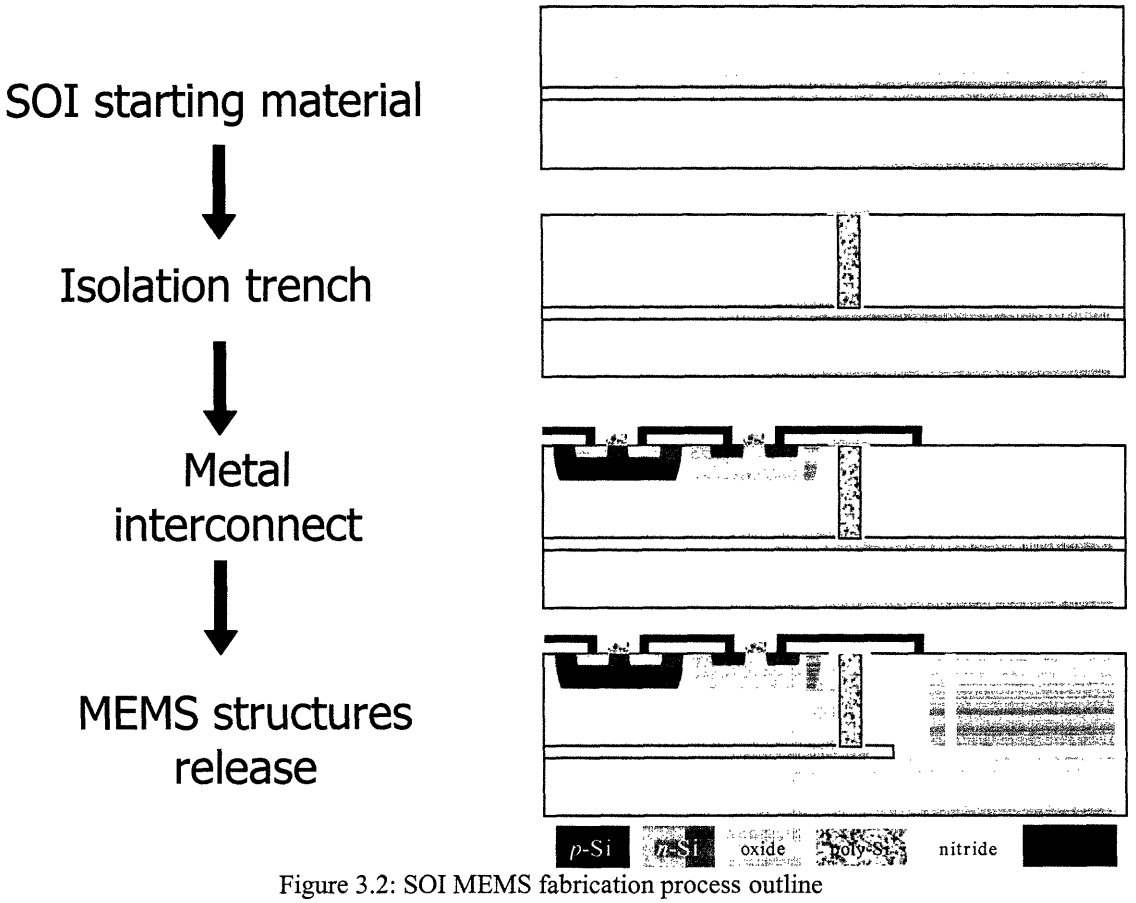

Figure 3.2: SOI MEMS fabrication process outline

### 3.2.2 Estimated Sensor Capacitors

To determine the size of the capacitance per moving finger achievable, we will examine an I/O port in detail, as shown in Figure 3.3. The capacitance between a moving finger and its two surrounding upper fixed fingers, $C_A$ and between a moving finger and its two surrounding lower fixed fingers, $C_B$, both have two components. The desired capacitance is due to the overlap area between the fingers, while the unwanted sidewall capacitance is due to the capacitor formed by the end of the moving finger with the fixed arm. These capacitors are shown pictorially in Figure 3.3a, and are given by:

$$C_A = C_{ova} + C_{swa}$$
$$C_B = C_{ovb} + C_{swb}$$

Using the dimensions given in Figure 3.3b, the above equations can be re-written as:

$$C_A = \underbrace{\varepsilon_o b\, ovla\left(\frac{1}{gapl} + \frac{1}{gapr}\right)}_{C_{ova}} + \underbrace{\frac{2\varepsilon_o b\, finger\_width}{gswa}}_{C_{swa}}$$
$$C_B = \underbrace{\varepsilon_o b\, ovlb\left(\frac{1}{gapl} + \frac{1}{gapr}\right)}_{C_{ovb}} + \underbrace{\frac{2\varepsilon_o b\, finger\_width}{gswb}}_{C_{swb}}.$$

In the above equations, $b$ is the height of the transducer.

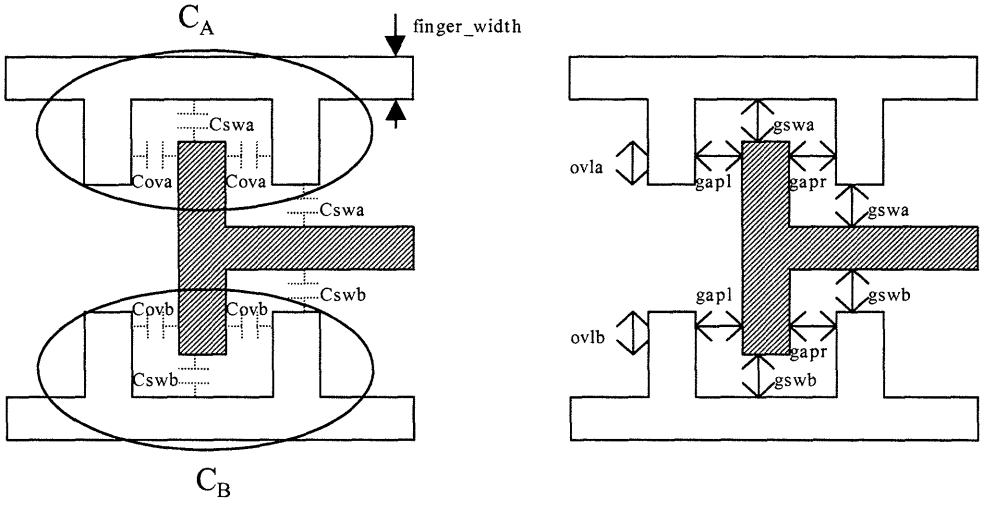


Figure 3.3: Detailed sketch of the transducer's I/O port showing capacitors (a) and dimensions (b)

To obtain the total capacitance at each I/O port of the transducer, simply multiply the previous expressions for $C_A$ and $C_B$ by the number of moving fingers for each port, N. The dimensions of each port are summarized in Table 3.1.

| $\varepsilon_o$ | b | ovla, ovlb | gapl, gapr | finger_width | gswa, gswb |
|---|---|---|---|---|---|
| 8.8e-12 F/m | 16.5 μm | 8±5 μm | 2 μm | 2 μm | 15±5 μm |

Table 3.1: Summary of I/O port dimensions

Plotted in Figure 3.4 are the unit overlap capacitance and the unit sidewall capacitance versus overlap. For the dimensions chosen, it is evident that the peak sidewall capacitance, $C_{gswa}$ and $C_{gswb}$, is an order of magnitude less than the desired minimum overlap capacitance. This is important because the overall capacitance needs to remain linear to maximize the sense loop's common-mode voltage range. What also helps maximize the common-mode voltage rejection in this design is the mapping of the common-mode components to the even harmonics of the clock frequency, as shown in Chapter 2.

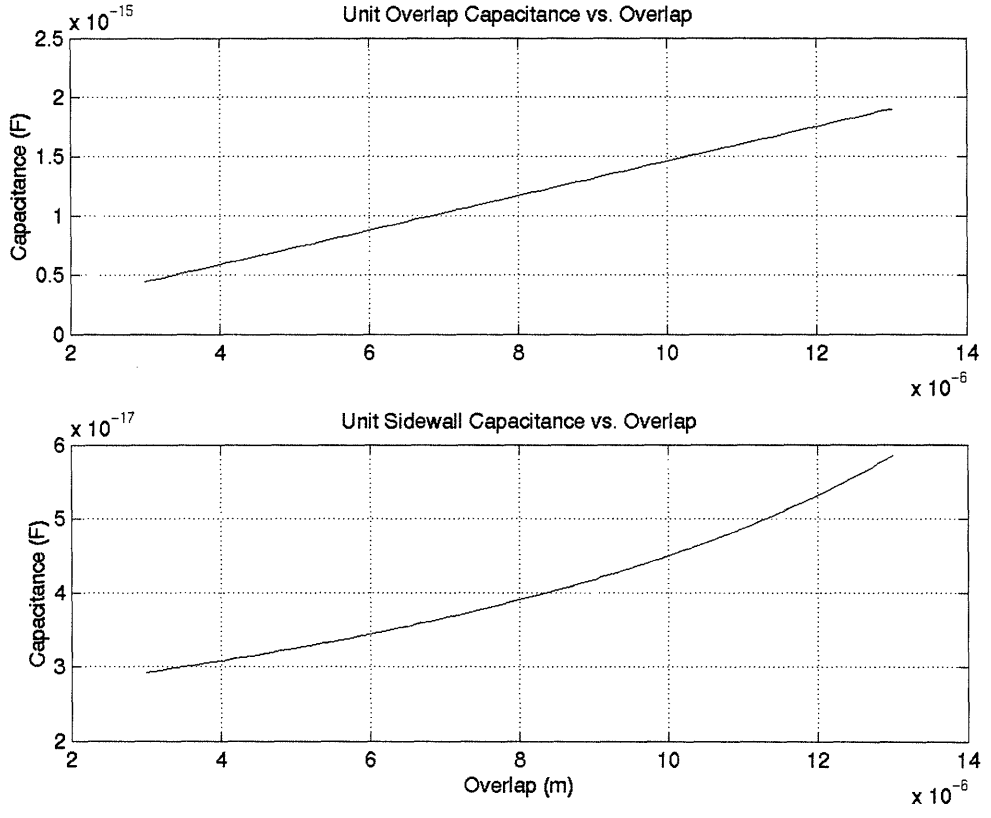


Figure 3.4: Unit overlap capacitance (a) and unit sidewall capacitance (b) vs. overlap

### 3.2.3 ELECTROSTATIC FORCES

As explained in the introduction, the beam will be actuated by electrostatic forces that are generated by applying voltages to fixed fingers while keeping the moving fingers at a known reference potential. To derive an expression for the unit attractive force between capacitor plates, we begin by taking the gradient of the energy stored in each capacitor.

$$\vec{f}_{net} = -\vec{\nabla}\left(\tfrac{1}{2}C_A V_A^2 + \tfrac{1}{2}C_B V_B^2\right)$$

Substituting the expressions for $C_A$ and $C_B$ derived in section 3.2.2, we have:

$$\vec{f}_{net} = \varepsilon_o b\left[\left(\frac{1}{gapl}+\frac{1}{gapr}\right)\left(\frac{V_A^2 - V_B^2}{2}\right) - \left(\frac{V_A^2}{gswa^2} - \frac{V_B^2}{gswb^2}\right) finger\_width\right]\hat{x}$$
$$+\left[\varepsilon_o b\left(\frac{1}{gapl^2}-\frac{1}{gapr^2}\right)\left(V_A^2 ovla + V_B^2 ovlb\right)\right]\hat{y}$$

The transducer will be driven one side at a time. In other words, if the moving structure is biased at zero volts, then $V_A$ will be non-zero only when the beam is to be pulled in that direction and vice versa for $V_B$.

In the above expression for the unit attractive force between the moving and fixed fingers, there are two components in the desired direction of motion (x), and one orthogonal to that direction (y). The first term is the desired force that we want to actuate the beam. It is constant in value, thereby facilitating a constant square-wave force drive. The second and third terms give rise to electrical spring constants, which will be discussed in the next section.

These forces are present on all fingers, depending on the voltages applied to the particular set of fixed fingers. It is desired to have the forces generated from the drive fingers dictate the beam motion regardless of the voltages applied to the sense fingers. However, on the sense side of the beam, this does not hold true. Voltages $V_A$ and $V_B$ on the sense side are of the form

$$V_A = V_{CM} + V_{DM}$$
$$V_B = V_{CM} - V_{DM}$$

Therefore, a torque is induced on the beam due to the following force:

$$\vec{f}_{net} = \frac{\varepsilon_o b}{2}\left(\frac{1}{gapl} + \frac{1}{gapr}\right)\left[(V_{CM} + V_{DM})^2 - (V_{CM} - V_{DM})^2\right]\hat{x}$$
$$= \frac{\varepsilon_o b}{2}\left(\frac{1}{gapl} + \frac{1}{gapr}\right)\left[4V_{CM}V_{DM}\right]\hat{x}$$

By using a cross-quad layout on the mechanical structure, the forces are distributed as shown in Figure 3.5. This demonstrates that in addition to better finger matching to enhance the CMRR, there is no net torque acting on the beam.

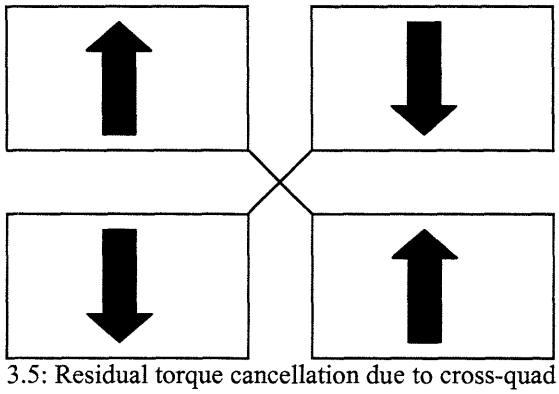

Figure 3.5: Residual torque cancellation due to cross-quad layout

### 3.2.4 ELECTRICAL SPRING CONSTANT

By computing the gradient of the force, or the electrical spring constant, it is evident that there is a finite voltage range in which the electrostatic force drive dictates the motion of the beam.

The electrical spring constant $k_e$, is given by:

$$\vec{k}_e = \vec{\nabla} f_{net}$$

$$\vec{k}_e = -\varepsilon_o bfinger\_width\left[\left(\frac{2V_A^2}{gswa^3} - \frac{2V_B^2}{gswb^3}\right)\right]\hat{x} - \left[\varepsilon_o b\left(\frac{2}{gapl^3} - \frac{2}{gapr^3}\right)\left(V_A^2 ovla + V_B^2 ovlb\right)\right]\hat{y}$$

In addition, from the above equation we can see that there is an electrical spring constant in both the x and y directions. The first term is what sets the common-mode voltage limit in the sense loop. When the common-mode component of $V_A$ (and $V_B$), is high enough to make the electrical spring constant comparable to the mechanical spring constant, there will be a significant shift in the resonant frequency and eventually the transducer will stop moving.

The second term describes a spring constant in the y-direction. This component will be shown very small in comparison to the mechanical spring constant in that direction. In other words, the sensor will be designed to be very stiff in the y-direction so that the effects of the electrical spring constant in this direction will be insignificant. A plot of both the x- and y-direction electrical spring constants versus common-mode voltage range will be plotted along with their mechanical counterparts in the next section.

### 3.2.5 MECHANICAL SPRING CONSTANT

As mentioned in the previous section, an electrical spring constant induces a force that tends to collapse the beam. This can also be viewed as increasing the overall compliance of the mechanical transducer, which is determined by silicon tethers that attach the moving mass to the substrate.

A simple tether is shown in Figure 3.6a. For displacements that are large relative to the length of the tether, the compliance exhibits nonlinear behavior [53]. To help minimize nonlinear flexure behavior, the folded tether design of Figure 3.6b was used. To derive the compliance of the folded tether, we begin by analyzing the simple tether of Figure 3.6a.

The vertical deflection at the unsupported end of the cantilever to a concentrated load is derived in [46] and is given by:

$$x = \frac{FL^3}{3EI},$$

where $F$ is the load, $E$ is the modulus of elasticity, and $I$ is the moment of inertia given by:

$$I = \tfrac{1}{12} W^3 t .$$

Using the folded tether structure of Figure 3.6b, the displacement will be shared equally between the two cantilevers. Since the compliance is defined as the ratio of load to displacement, the compliance of each of the beams is given by:

$$k = \frac{EtW^3}{L^3}.$$

This derivation is summarized in [48]. Four folded tethers were arranged as shown in Figure 3.7 and the net mechanical spring constant in the x-direction is:

$$k_{m,x} = 4\frac{EtW^3}{L_1^3 + L_2^3} = 2Et\left(\frac{W}{L}\right)^3.$$

In [53], the spring constants in the y- and z-directions are presented. They are given by:

$$k_{m,y} = \frac{EtW}{L};\ k_{m,z} = \frac{2EWt^3}{L^3}.$$

This tether design provides the required stiffness in the y- and z-directions along with the desired compliance in the x-direction.

Figure 3.6: Simple tether (a) and folded tether (b)

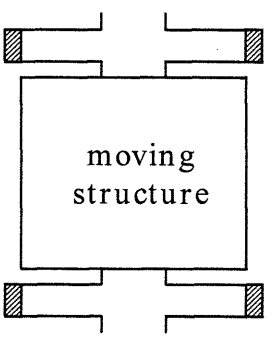

Figure 3.7: Arrangement of folded tethers

For this design, the x-, y-, and z-direction mechanical spring constants are 200 N/m, 3042 N/m and 130 GN/m. The mechanical spring constants were plotted against their electrical counterparts for the x- and y-directions in Figure 3.8. From this figure, it is evident that the electrical and mechanical spring constants in the x-direction will be equal at a common-mode voltage of roughly 3500 V. The spring constants in the y-direction will be equal at 1500 V. As previously mentioned, the spring is very stiff in the y-direction so the electrical spring constant in this direction will have a negligible effect on the common-mode performance of the sensor. One should not expect to fully utilize such a wide common mode range because the dielectric used in the trenches will breakdown well before this voltage is reached, as will be shown in Section 3.2.9.

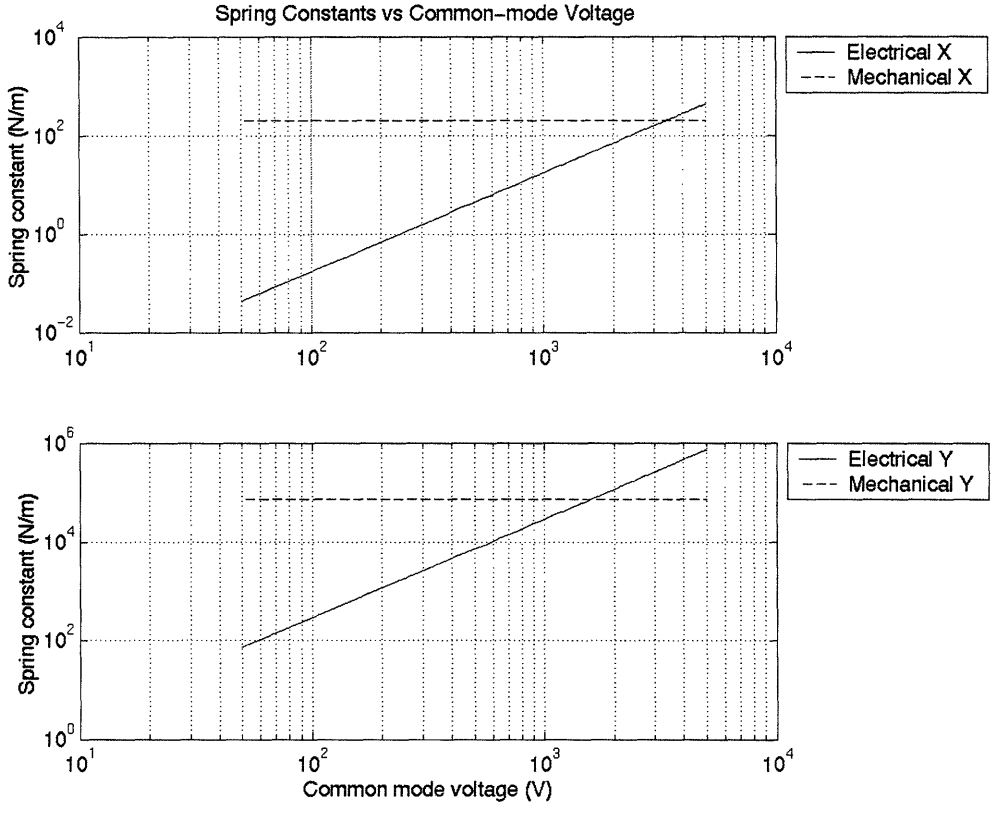


Figure 3.8: Electrical and mechanical spring constants versus common-mode voltage

### 3.2.6 DAMPING

The damping in the system must be well understood because it will limit the MEMS structure's range of motion when resonating. As the transducer moves, it will be subject to two types of damping, namely squeeze-film and shear. Squeeze-film damping is present when the air between two plates is forced out while the two plates move toward each other. This is shown pictorially in Figure 3.9b and is computed by using the following formula derived in [53]:

$$\beta_{sq} = \xi b \left( \frac{w}{g_{SW}} \right)^3 .$$

In the equation above, $\xi$ is the viscosity of air, $w$ is the width of the moving structure, $b$ is the height of the moving structure, and $g_{SW}$ is the gap between the moving structures. This formula assumes that $w >> b, g$ and is only valid under this condition [53,54]. In this design, $w$, $b$ and $g$ are all the comparable so the above equation is invalid as it assumes gas pressure falls to ambient levels at the edges of the fingers [68]. A more accurate estimate of this damping is derived in [68] as

$$\beta_{sq} = 7.2 b \xi \left( \frac{w}{g} \right)^3 .$$

Using the dimensions for this design, $w=2\mu m$, $b=16.5\mu m$, and $g=10\mu m$, the squeeze-film damping will be roughly $7 \times 10^{-9}$ kg/s.

Shear damping is present when one mass moves relative to another. In SOI MEMS designs, it is typically due to the moving structure's motion relative to the handle

wafer. In most designs, the dominant source of shear damping is between the moving structure and the handle wafer. In this design, there is no handle wafer, for it will be dissolved away during the backside release process. The moving fingers moving parallel to the fixed fingers are the next dominant source of damping in this design. This form of damping is shown in Figure 3.9a and can be computed using the following formula derived in [54]:

$$\beta_{sh} = \xi \frac{A}{d}.$$

In the equation above, $\xi$ is the viscosity of air, $A$ is the cross-sectional area of the moving mass and $d$ is the distance between the moving mass and the inertial mass. For this MEMS transducer, the shear damping is $2x10^{-6}$ kg/s, which dominates over the squeeze-film damping term.

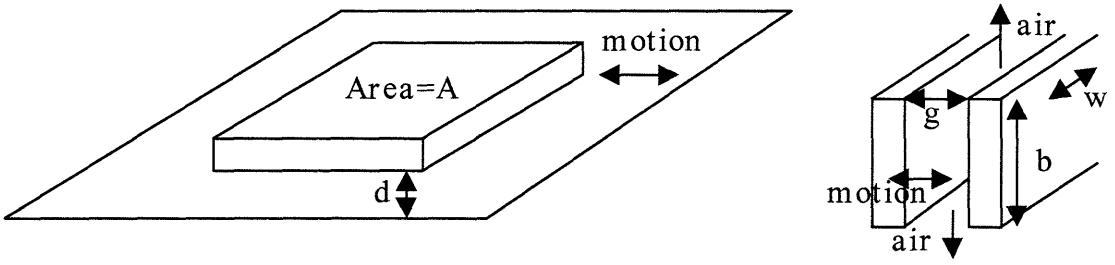


Figure 3.9: Shear damping (a) and squeeze-film damping (b)

### 3.2.7 Q AND RESONANT FREQUENCY

The $Q$, or quality factor of a second order system, is a measure of the ratio of stored energy to energy dissipated per cycle. The mechanical transducer in this design will behave as a mass-spring damper system governed by:

$$F_{electrostatic} = ms^2 x + (\beta_{sh} + \beta_{sq})sx + (k_m - k_e)x .$$

$F_{electrostatic}$ is the applied electrostatic force, $m$ is the total mass of the moving structure, $\beta_{sq}$ and $\beta_{sh}$ are the squeeze-film and shear damping terms as described in Section 3.2.4, $k_m$ is the mechanical spring constant and $k_e$ is the electrical spring constant. For a standard, second order characteristic equation:

$$s^2 + 2\alpha s + \omega_o^2 = 0 ,$$

the quality factor and resonant frequency are respectively defined as:

$$Q = \frac{\omega_o}{2\alpha}, \ \omega_o = \sqrt{\frac{k}{m}} .$$

In this system, the quality factor is:

$$Q = \frac{m\omega_o}{\beta_{sq} + \beta_{sh}} .$$

For $\omega_o = 2\pi 30$ kHz, $\beta_{sh} = 2\text{x}10^{-6}$ kg/s, m = $5.6\text{x}10^{-9}$ kg and $\beta_{sq} = 6.6\text{x}10^{-8}$ kg/s, the predicted quality factor is 451.

### 3.2.8 MECHANICAL MODES

All structures have frequencies at which they naturally resonate. These frequencies are integer multiples of some fundamental frequency, which depends on the dimensions of the structure and its composite material(s). In this design, the resonant frequencies of the fixed and mechanical arms are of importance. Care must be taken not to excite these modes, as they may cause damage to the device if the $Q$ of any mode is high enough and/or if the associated displacement causes the fixed and moving structures to collide.

They also limit performance by invalidating the rigid body assumption made in this design and creating parasitic harmonic signals in the sense loop.

The modes of greatest importance are in the x-direction (the desired direction of beam motion). The frequencies at which the x- and z- modes respectively will be excited are computed according to:

$$f_x = \frac{\lambda^2}{2\pi L^2}\sqrt{\frac{Ebw^3}{\frac{12M}{L}}}$$

$$f_z = \frac{\lambda^2}{2\pi L^2}\sqrt{\frac{Eb^3w}{\frac{12M}{L}}}.$$

In the above equations, $\lambda$ is a constant associated with the order of the mode, $E$ is the modulus of elasticity, $M$ is the mass of each arm, and $b$, $w$, and $L$ are measured as shown in Figure 3.10.

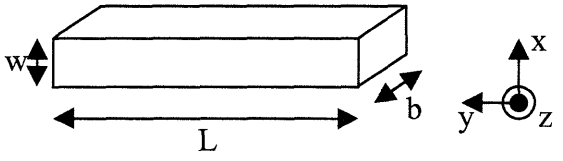


Figure 3.10: Dimensions and coordinates system used in modal analysis

The dimensions of the fingers were chosen so that the lowest mechanical mode will still be one order of magnitude greater than the mechanical structure's resonant frequency. The fixed finger modal frequencies are 326 kHz and 467 kHz in the x- and z-directions, respectively. The moving finger modal frequencies are 475 kHz and 435 kHz in the x- and z-directions, respectively.

### 3.2.9 ISOLATION

The sensor requires electrically isolated, mechanically coupled regions of silicon. This is facilitated by creating trenches. A trench is a nitride-polysilicon-nitride sandwich, which is shown in Figure 3.11.

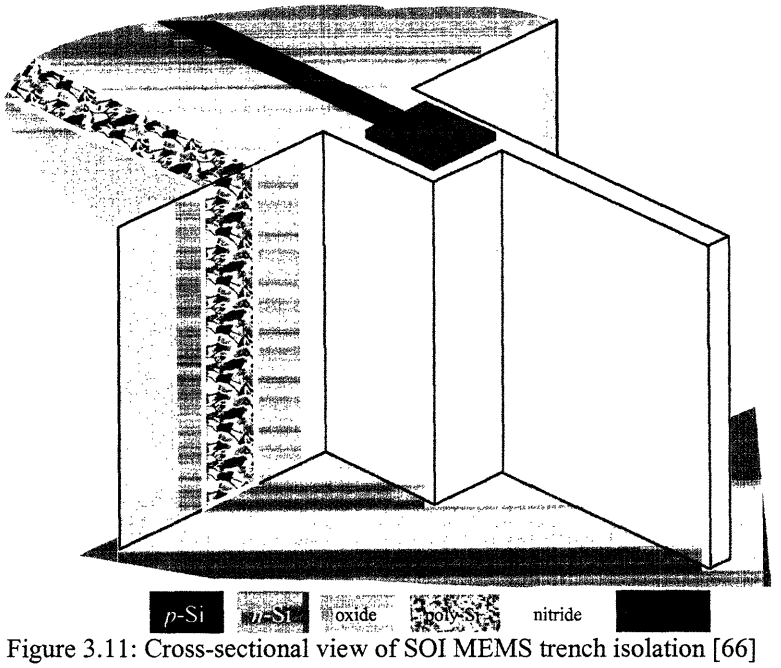


Figure 3.11: Cross-sectional view of SOI MEMS trench isolation [66]

The nitride layers are 120 nm thick and surround polysilicon, which has better mechanical properties. A significant parasitic shunt capacitance exists due to the thin layer of isolating nitride and is of concern. This contributes to the total parasitic capacitance at the beam's output terminal. The minimization of the trench capacitance and other contributors to the overall parasitic capacitance will be discussed in the next section.

As previously mentioned, the trench breakdown voltage will set the upper limit on the common-mode range of the parametric amplifier. The maximum electric field supportable in nitride films before breakdown occurs is roughly 12 MV/cm [57,58]. An estimate of the breakdown voltage based on the 240 nm of nitride used to line the trenches yields a breakdown voltage of 288 V. This is well below the upper limit of 3500 V set by the electrical spring constants. Note that using a thicker nitride layer can improve this by spreading the potential over a longer distance but the physics of the air gap between the fingers will limit this to about 500 V [59].

### 3.2.10 Parasitic Capacitance

The sense side of the MEMS structure can be modeled as a series-shunt capacitor network, as shown in Figure 3.12. From this model, it is evident that there is a shunt capacitance from the beam's output node to ground. The resultant capacitive divider reduces the overall MEMS parametric amplifier's sensitivity and is an effective gain term when referring the input noise of the pre-amplifier to the input terminals of the MEMS structure. Therefore, to increase sensitivity and minimize the noise, the parasitic shunt capacitance must be minimized. The previous sections have shown the origins of the $C_O$ and $C_M$ components. This section will show the components that contribute to the parasitic shunt capacitance and what efforts were made to reduce them.

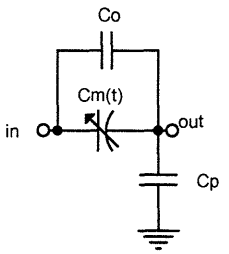


Figure 3.12: Model of the sense side of the MEMS structure

There are two main components that make up the beam's parasitic capacitance: a beam to handle wafer capacitance, and the trench capacitance. The capacitance between the beam and the handle wafer for our structure is roughly 0.6 pF. This capacitance is large due to the size of the sensor and the close proximity of the handle wafer (1 μm spacing). This capacitance can be reduced by either fabricating a smaller structure or using wafers with greater handle wafer separation. We could not reduce the size of the mechanical structure, because of the loss of sensitivity and the increase in RTI noise. In addition, the wafers available for fabrication were limited to 1 μm handle wafer separation. Therefore, a backside etch was used to release the MEMS structure from the substrate. In this process, the handle wafer is dissolved away, effectively eliminating the beam to handle capacitance.

The beam to anchor capacitance arises due to the trenches used for isolation, as discussed in the previous section. To minimize this parasitic shunt capacitance, multiple trenches can be used at the expense of occupying more area. A double trench is shown in Figure 3.13. As mentioned previously, this has the added benefit of boosting the standoff voltage as well.

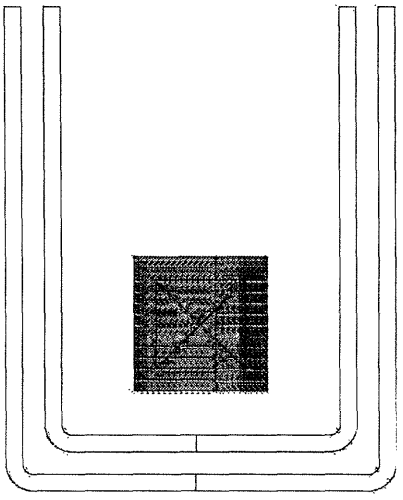

Figure 3.13: Layout of a double trench

To determine the optimum number of trenches to use, a plot of trench capacitance versus the number of trenches is shown in Figure 3.14. In this plot, it is evident that the greatest incremental reduction in capacitance occurs by using two trenches.

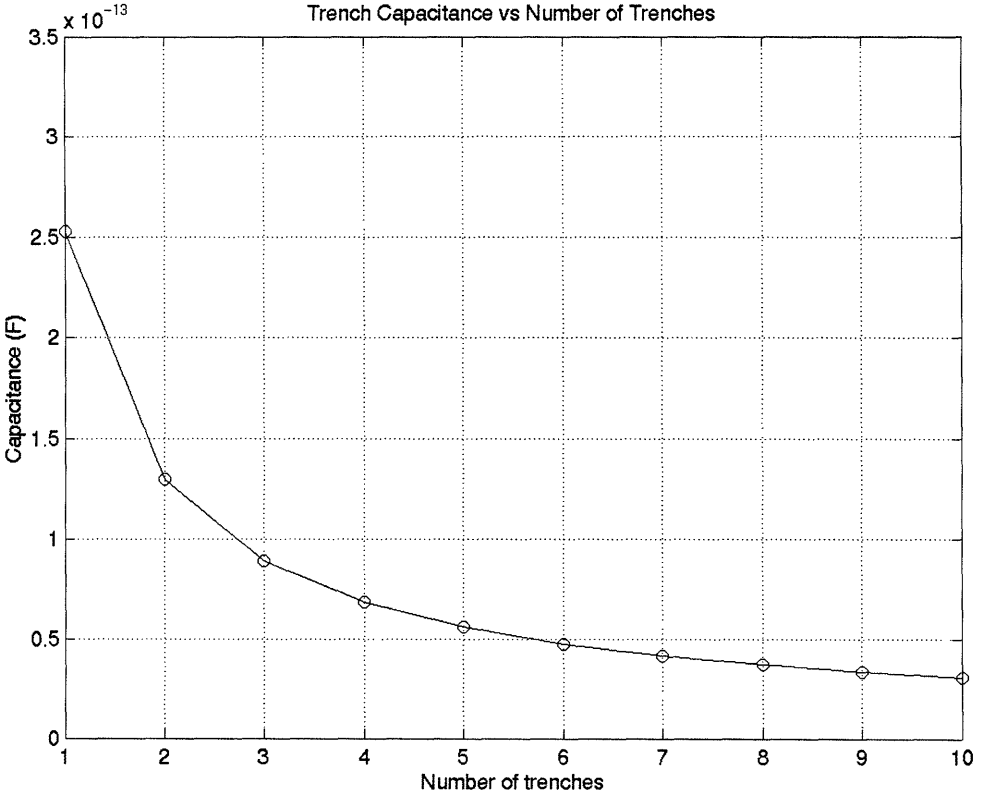


Figure 3.14: Trench capacitance vs. number of trenches

As an alternative to using two actual trenches as shown in Figure 3.13, the thickness of the nitride layers were doubled in this design, which has the same effect on the trench capacitance. This way, the trench capacitance was halved without increasing the size of the overall trench. These double trenches were not only used at the beam anchors but at every mechanically coupled, electrically isolated junction. Even with using twice as much nitride, the abundance of trenches makes the total shunt capacitance on the order of one pF. The reduction of the trench area is an area for future improvement.

### 3.2.11 LAYOUT

The dimensions of the transducer as compared to individual IC components will be quite large. Matched fingers are crucial to the high performance of this design so care must be taken in the layout to minimize the effects of etch variations, process gradients, and to suppress electrostatic forces. Similar to the common-centroid layout of a transistor differential pair, the transducer's layout used a cross-quad geometry.

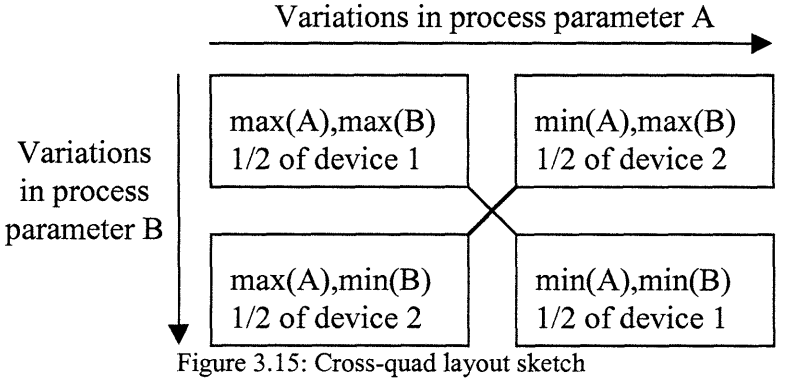

Figure 3.15: Cross-quad layout sketch

Figure 3.15 shows how a cross-quad layout minimizes effects of process parameter variations on devices that need to be matched. Both devices are split into two halves and are arranged in an 'X' pattern. From this arrangement, one-half of device 1 is subject to the maximum of parameters A and B while the other half sees the minimum of the parameters. For device 2, one-half of it sees the maximum of parameter A and the minimum of parameter B, while the other half sees the minimum of parameter A and the maximum of parameter B. To the extent to which the two process parameters are independent of one another, both devices will be made of the same amounts of parameters A and B and will be matched to a first order.

To achieve a cross-quad geometry layout in MEMS technology requires the ability to mechanically coupled electrically isolated structures. This is achieved using a modified version of Analog Devices Inc.'s proprietary SOI MEMS process and at the time of this writing is the first MEMS design to incorporate this. A microscope photo of a test structure that facilitated this is shown in Figure 3.16. The final layout of the transducer is shown in Figure 3.17.

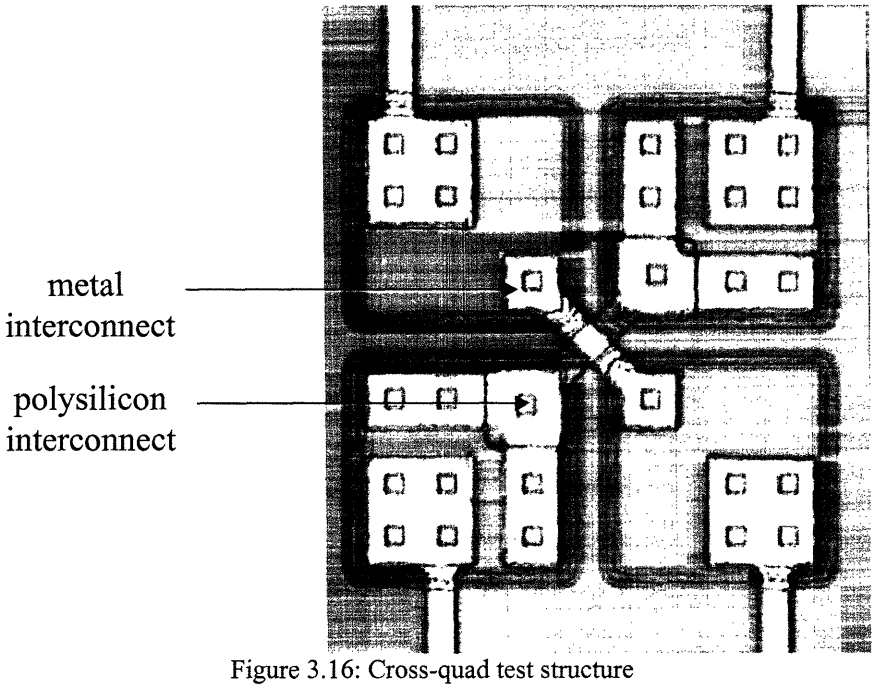


Figure 3.16: Cross-quad test structure

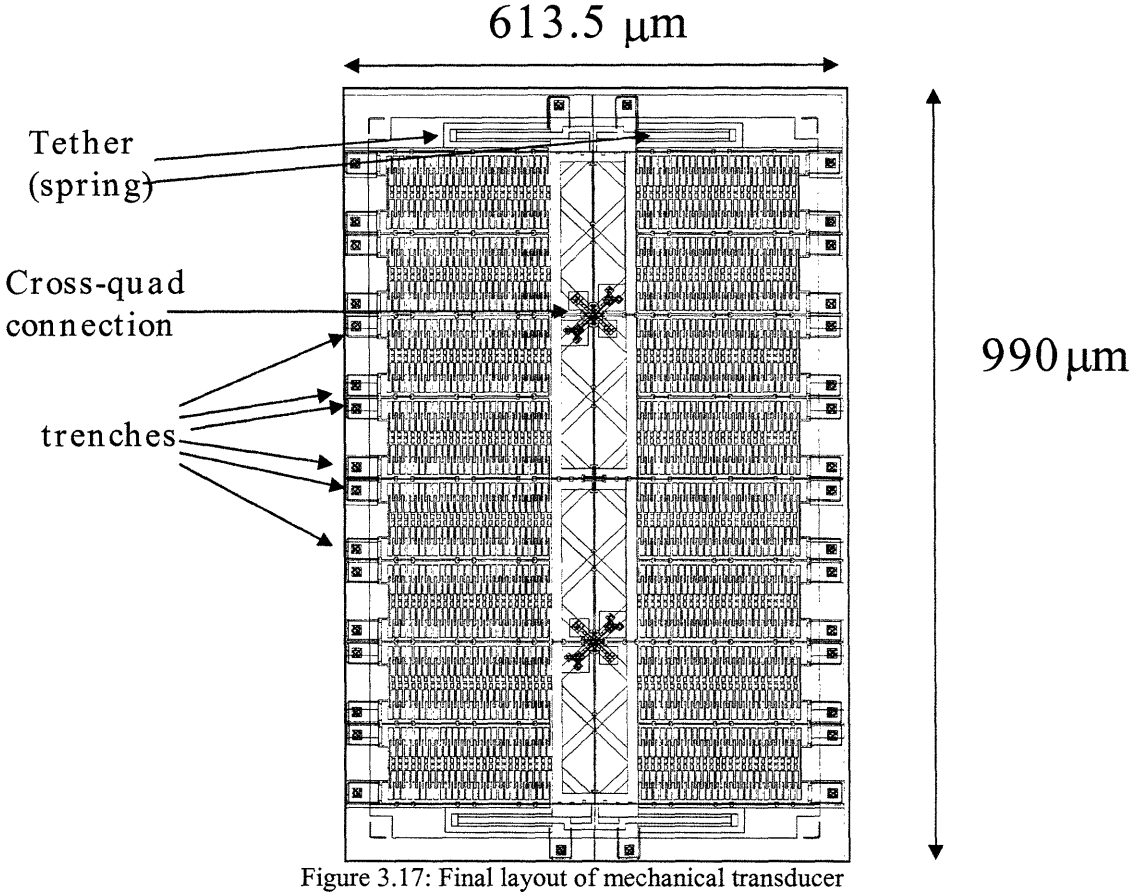


Figure 3.17: Final layout of mechanical transducer

### 3.2.12 Electrical Linearity of the Mechanical Sensor

The electrical linearity of silicon based capacitors is often a concern. For example, the gate capacitance of a MOSFET is nonlinear over a finite range of gate to bulk voltages. As described in [57], below the flatband voltage and above the threshold voltage, sheet charges are induced at the oxide interfaces that are directly proportional to voltage across the oxide. Therefore the capacitance in these regions is linear and is dictated by the dimensions of the transistor and the oxide thickness. The region where the capacitance is nonlinear is between the flatband and threshold voltages. In this region, the MOS capacitor is biased in depletion and the applied voltage will induce a depletion region in one of the fingers. Since the relationship between the depletion depth and the applied bias is nonlinear, the capacitance in this bias range is also nonlinear since the capacitance is inversely proportional to the depletion depth. A similar analysis can be performed on the finger capacitance structure used in this design.

As shown in Figure 3.18, the fixed and moving fingers have an air gap between them to form a silicon-air-silicon capacitor. For this capacitor, the flatband voltage will be zero volts, since both fingers are doped with the same concentration of acceptors. However, the thickness of the fingers (16.5 μm) gives rise to a dopant concentration gradient similar to the profile shown in Figure 3.19.

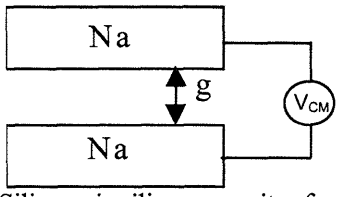

Figure 3.18: Silicon-air-silicon capacitor formed by fingers

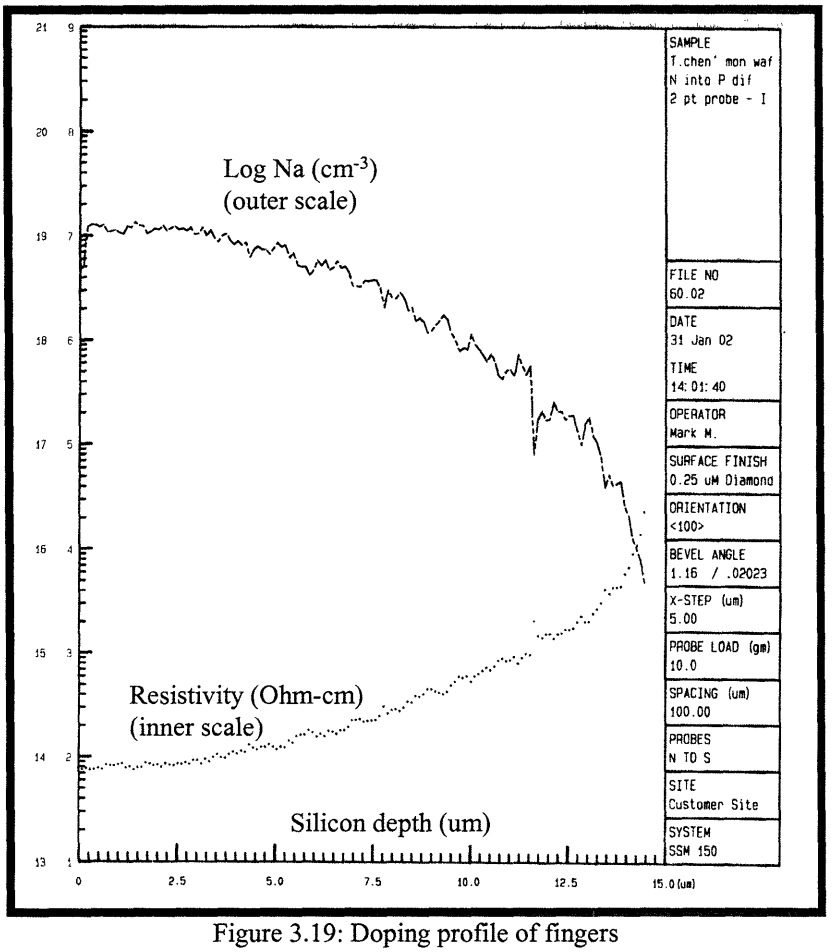

Figure 3.19: Doping profile of fingers

From Figure 3.19, it is evident that the dopant concentration varies between $10^{15}$ and $10^{19}$ $cm^{-3}$. The flatband voltage will not change over this range of dopant concentration but the threshold voltage will. The threshold voltage of this finger capacitor is given by:

$$V_T = V_{FB} - 2\phi_P + \frac{g\sqrt{2q\varepsilon_O Na(-2\phi_P)}}{\varepsilon_O}.$$

Figure 3.20 shows that the threshold voltage varies from 0.6 to 1.1 volts.

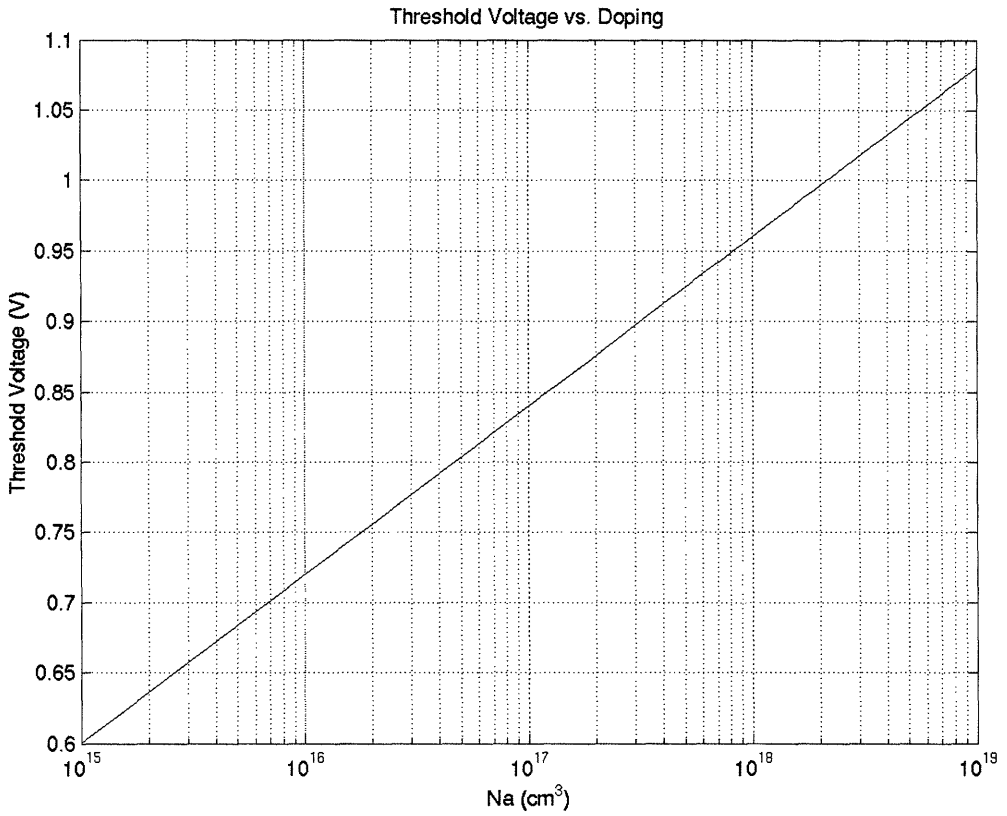


Figure 3.20: Threshold voltage versus dopant concentration

The depletion depth, $X_d$, is given by:

$$X_d = g\left(\frac{\varepsilon_s}{\varepsilon_O}\right)\left(\sqrt{1+\frac{2\left(\frac{\varepsilon_O}{g}\right)^2 V_{CM}}{q\varepsilon_S Na}}-1\right).$$

It is evident from the above equation that the depletion depth will be maximum in the regions where the dopant concentration is $10^{15}$ $cm^{-3}$. In Figure 3.21, the depletion depth is plotted from flatband to the maximum inversion voltage and it shows that the maximum depletion depth is less than 200 nm. This maximum depletion depth is much smaller than

the finger width of 2 μm. Symmetry about the flatband voltage of zero is due to the symmetry of the silicon-air-silicon capacitor.

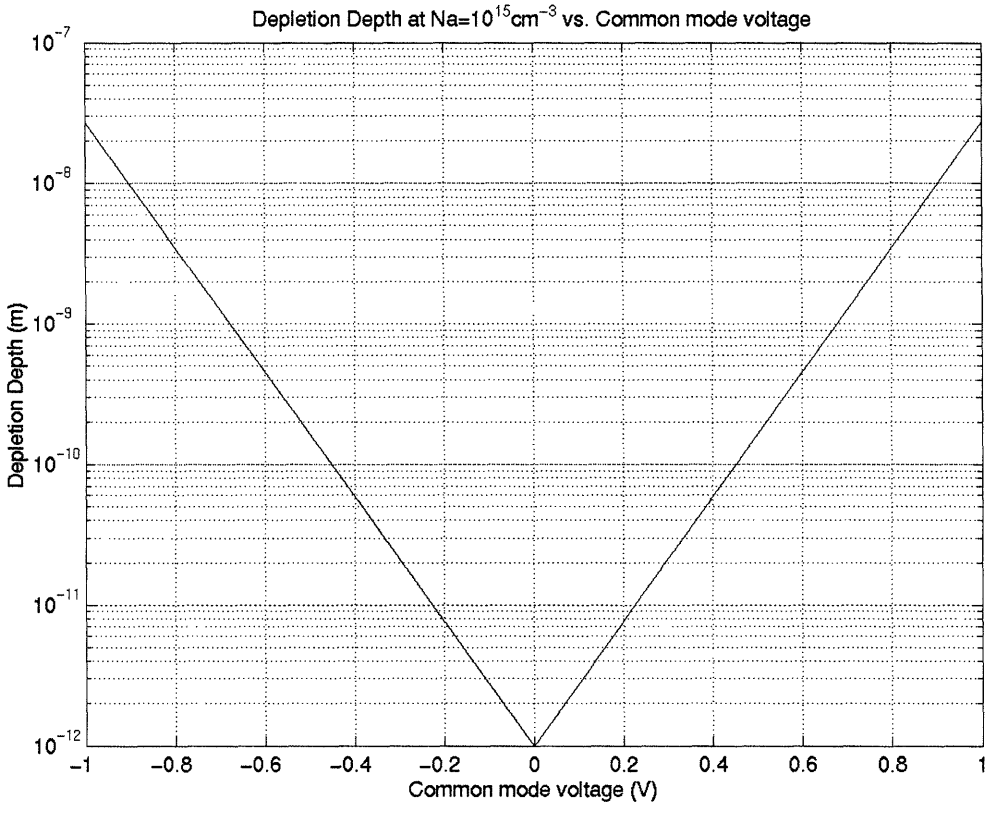


Figure 3.21: Depletion depth versus common mode voltage

In the common-mode voltage range of ±1 times the threshold voltage, the depletion capacitance is in series with the nominal finger capacitance. Since the depletion depth is so small, the depletion capacitance will be very large compared to the nominal finger capacitance. Since the smaller capacitance dominates when capacitors are connected in series, the change in capacitance will be negligible as shown in Figure 3.22.

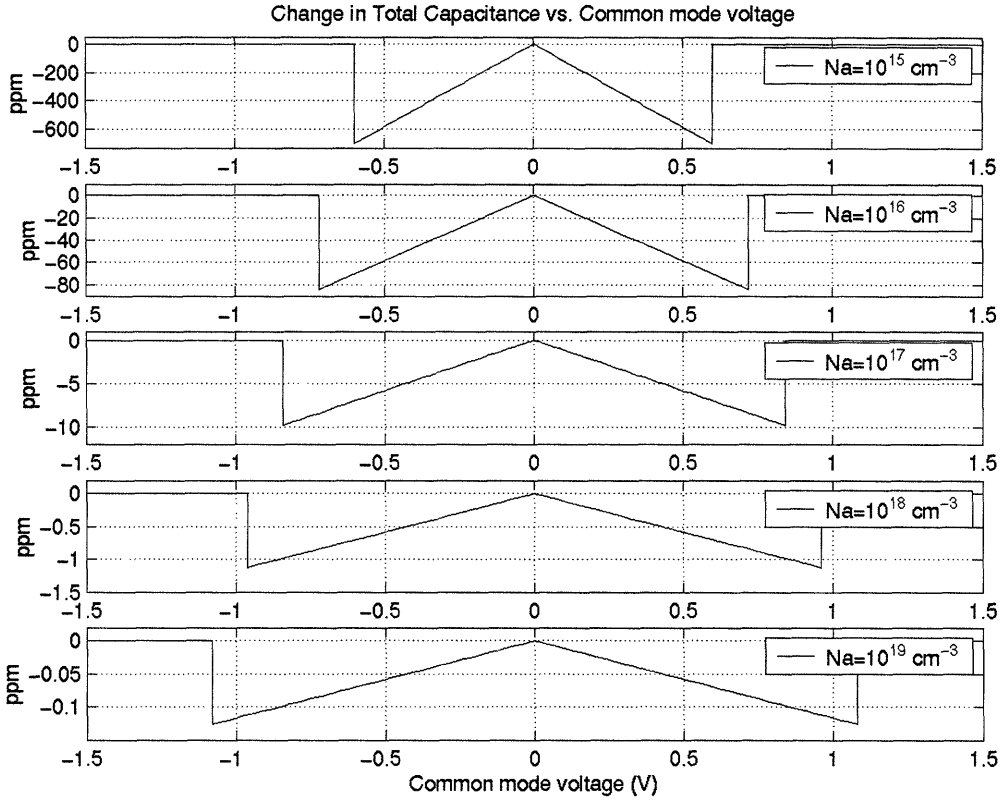


Figure 3.22: Change in capacitance versus common mode voltage

Figure 3.22 shows that when the absolute value of the common mode voltage is less than roughly one volt, the capacitance will change as a function of the common mode voltage. However, the maximum change in capacitance is less than 800 ppm from its nominal value. In addition, the threshold voltage is small, so it does not take a high voltage to invert the surface of the finger. When the surface of the fingers is inverted, then the capacitance between the fingers is dictated by the sheet charge that is induced on their surfaces. Since these sheet charges are at a fixed distance from one another and their value is directly proportional to the applied voltage, the overall capacitance is constant.

### 3.2.13 MECHANICAL TRANSDUCER DESIGN SUMMARY

As discussed in the previous chapter, a linear vibrating capacitor was desired because of its wider common mode range over a comparably sized nonlinear vibrating capacitor and suppression of dynamic input terminal currents. The main trade-off is the smaller modulation capacitance achievable with a linear vibrating capacitor. To increase the modulation capacitance, it is possible to increase the length of the moving arms and the number of fingers. However, the modal frequency of the moving arms varies as the inverse square of the arm length, while the modulation capacitance varies linearly with the arm length (number of fingers). It was desired that the first moving arm modal frequency be roughly one order of magnitude higher than the desired resonant frequency of 30 kHz to ensure rigid body motion. Using a target modal frequency of 300 kHz in the equations derived in Section 3.2.8, resulted in a moving arm length of 200 μm and an upper limit of 25 fingers per arm.

Since the sense side of the beam had to be fully differential, the upper half of the structure was divided into two electrically isolated, mechanically coupled vibrating capacitors. This resulted in a 2:1 finger ratio between the drive and sense sides of the beam: 50 fingers per input on the sense side and 100 fingers per input on the drive side.

Such a large structure will inevitably be subject to process variations. By using a cross-quad layout, these effects can be minimized. In addition, this facilitates cancellation

of the torque induced by the residual force due to the common mode components of the input signal.

This layout scheme uses trenches to create electrically isolated, mechanically coupled regions of silicon. The disadvantage of using trenches is the parasitic capacitance that is caused by their nitride lining. Doubling this lining cuts this capacitance in half, without significantly compromising the mechanical strength of the trench.

In addition to the trench capacitance, there is another parasitic capacitance between the sensor and the handle wafer. This capacitance is fixed and can only be reduced by either reducing the overall sensor size or by grinding away the handle wafer. Reducing the sensor size would compromise performance, so the handle wafer was dissolved away using a backside release process. Eliminating the handle wafer had the added benefit of a significant reduction in the shear damping present in the system, which also reduced the required drive voltage to achieve the desired displacement and increased the $Q$-factor of the sensor.

A summary of the transducer's specifications is in Table 3.2. The model used to analyze the electrical characteristics of the mechanical structure is shown in Figure 3.23 and a SEM photo of the transducer is shown in Figure 3.24. Its layout is also shown in Figure 3.25.

| | |
|---|---|
| Maximum displacement | +/- 5 μm |
| Number of sense fingers,<br>Number of feedback fingers | 50 |
| Number of drive fingers,<br>Number of sense fingers | 100 |
| $C_O$ | 60 fF |
| $C_M$ | 25 fF |
| $C_P$ | 1 pF |
| Total mass | 5.6e-9 kg |
| $Q$ | 451 |
| Resonant frequency | 30 kHz |
| Fixed arm modal frequencies | 326 kHz, 2 MHz |
| Moving arm modal frequencies | 475 kHz, 3 MHz |
| Footprint | 990 μm x 613.5 μm |

Table 3.2: Mechanical transducer specifications summary

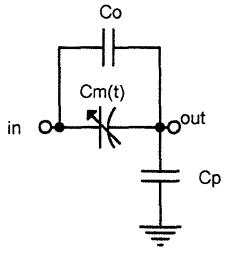


Figure 3.23: Model of the sense side of the MEMS structure

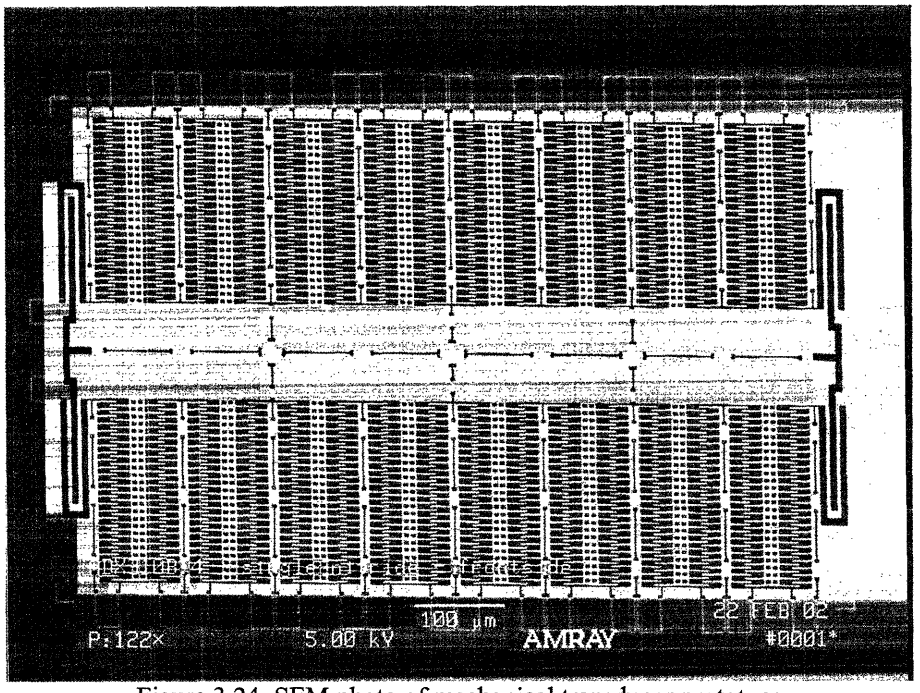


Figure 3.24: SEM photo of mechanical transducer prototype

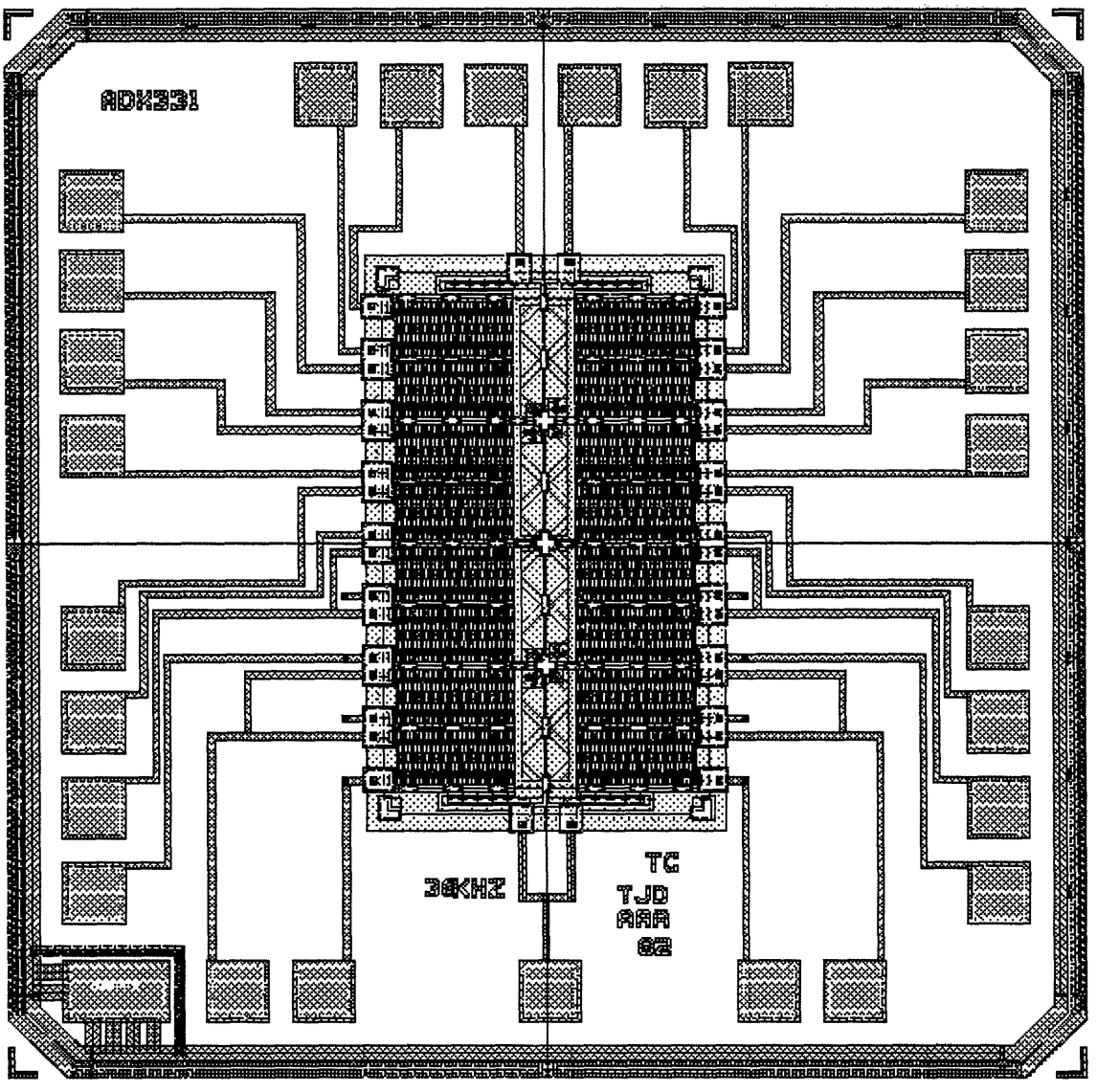


Figure 3.25: Final chip layout of MEMS transducer

## 3.3 MECHANICAL SENSOR MODELING

To facilitate simulation, a model of the mechanical sensor was created in ADICE using behavioral models. As shown in Figure 3.26, the model consists of summation, multiplication, and '1/x' blocks that were designed using Verilog-a[1]. The code used to

[1] The Verilog-a blocks were developed by Bill Crocker, Analog Devices Inc.

implement these blocks is included in Appendix A. Voltage-controlled voltage sources and voltage-controlled current sources were needed to model the physical parameters as well. These idealized sources are included with the ADICE package. Figure 3.27 shows the symbol used to represent the model of the mechanical structure which was named ADX331.

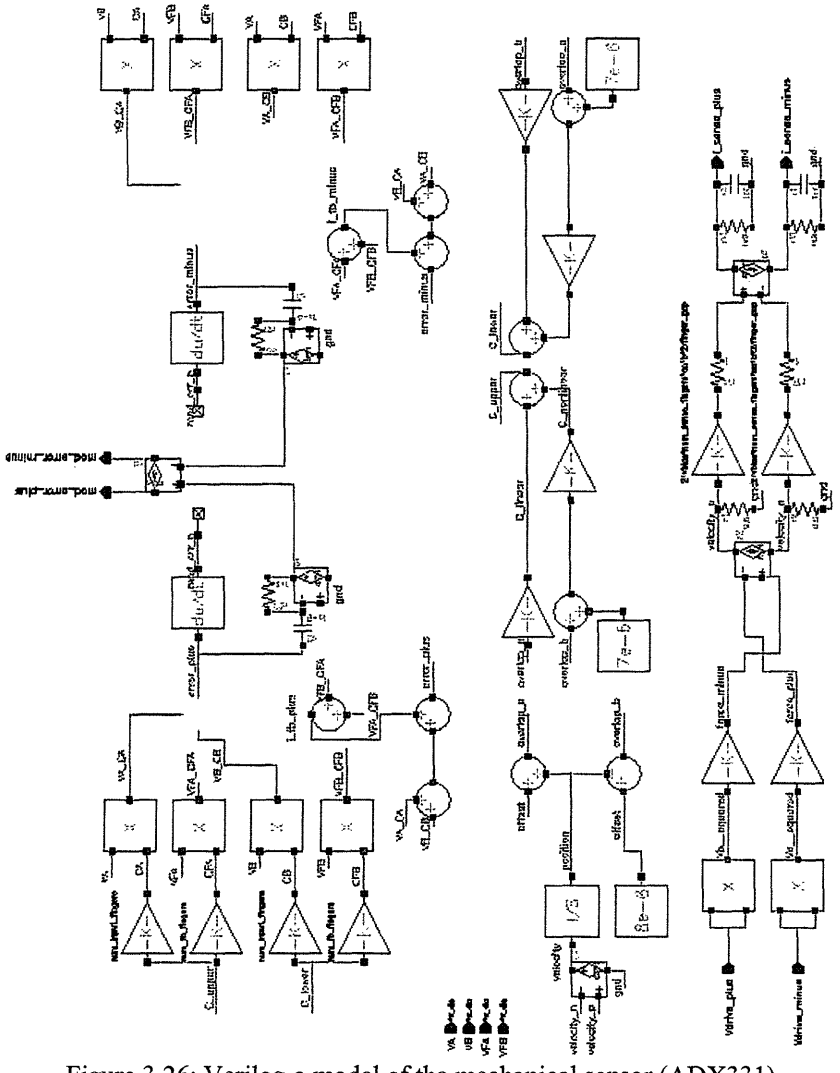

Figure 3.26: Verilog-a model of the mechanical sensor (ADX331)

This model will be used to validate transistor-level designs presented in Chapter 6.

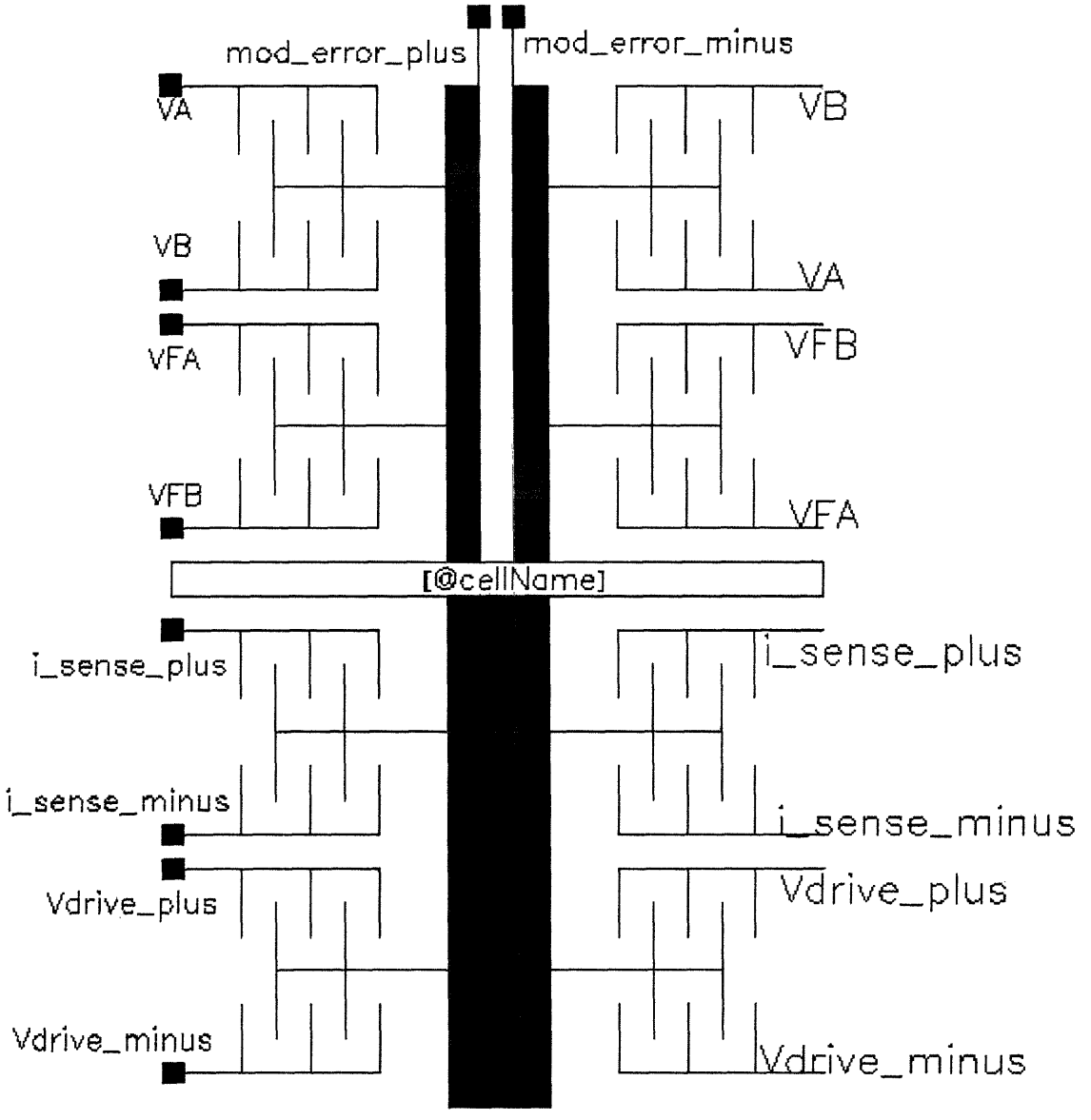


Figure 3.27: Symbol used to represent the mechanical sensor (ADX331)

# 4 DRIVE LOOP

## 4.1 MOTIVATION

The purpose of this loop is to vibrate the capacitive transducer at the resonant frequency of the MEMS structure. By operating at resonance, the displacement of the beam is maximized yielding the maximum capacitance modulation and the highest attainable signal-to-noise ratio for the system.

The transfer function of electrostatic force to displacement for the MEMS transducer in Chapter 3, as illustrated in Figure 4.1, is:

$$X = \frac{F_{electrostatic}}{ms^2 + \beta s + k}.$$

From this plot is evident that a factor of two shift in frequency from resonance will cause more than a factor of 100 (40 dB) decrease in displacement. It is therefore crucial that the transducer be driven at its resonant frequency in order to maximize displacement for a given drive voltage. By maximizing displacement, the signal current from the beam is maximized as well.

The resonance peak shown in Figure 4.1 can shift with process variations and temperature. Therefore, a robust approach is needed to insure that the structure will vibrate at its mechanical resonance. This goal is achieved by using a closed-loop design.

The bandpass nature of the force-to-displacement transfer function is coupled with a square-wave electrostatic force drive and a velocity-detection amplifier to form a

self-resonant oscillator. Therefore, the loop does the job of keeping the beam oscillating at its resonant frequency. The relatively high Q (451) of the transducer will attenuate the harmonics of the square wave drive and will yield a sinusoidal displacement, as desired. In addition, the force square wave drive can be used as the phase reference for the sense loop's demodulator.

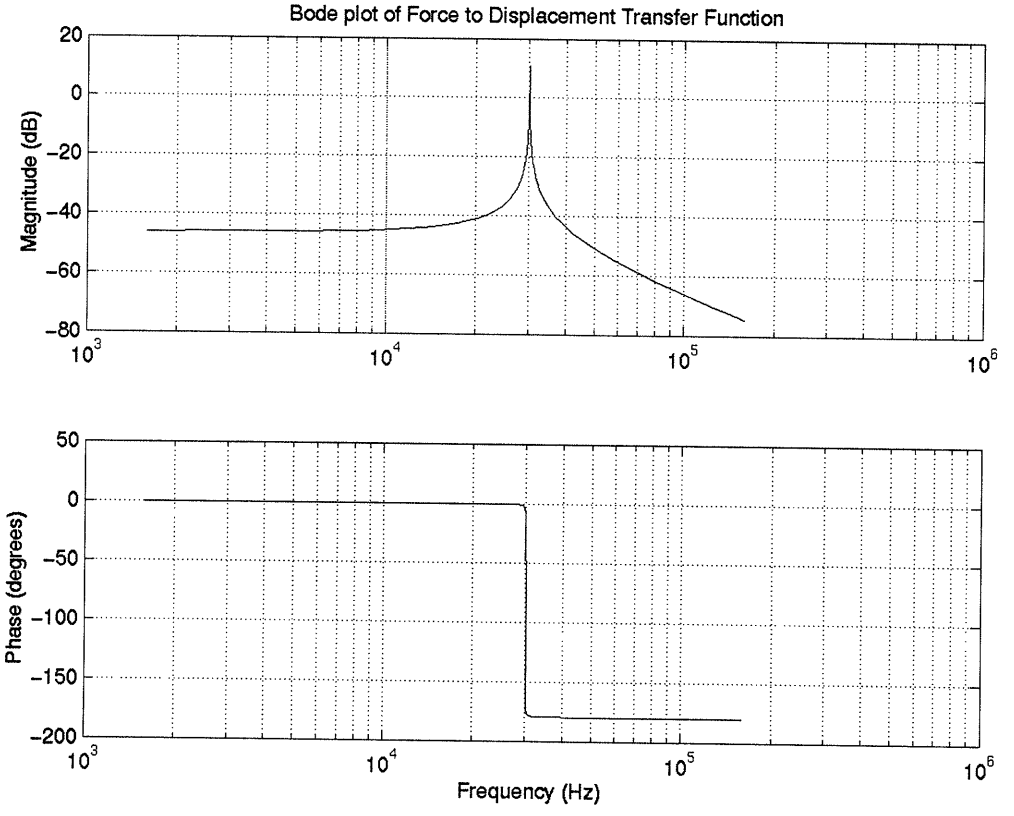


Figure 4.1: Bode plot of force to displacement transfer function

To design such a constant amplitude, fixed-frequency oscillator, feedback and stability analyses are required. To generate a square wave typically involves using a comparator, which is a nonlinear element. This makes direct application of linear analysis techniques difficult. Describing functions provides a method to effectively analyze this nonlinear system [45].

## 4.2 DRIVE LOOP DESIGN OVERVIEW

The drive loop uses the lower half of the mechanical sensor as shown in Figure 4.2. The goal of this loop is to vibrate the sensor at its mechanical resonance to ensure maximum displacement and sensitivity.

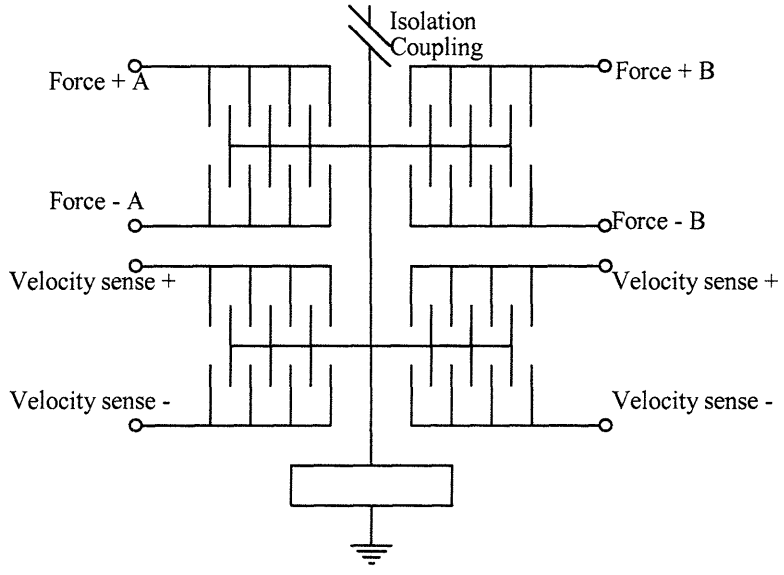


Figure 4.2: Lower half of mechanical structure used in the drive loop

The drive loop block diagram is shown in Figure 4.3. The minor loop represents the second order transfer function from electrostatic force to velocity. At resonance, the force is linearly related to velocity, with the resonant frequency determined by the spring constant $k$, and the mass of the transducer, $m$. The velocity of the beam is converted to a current by the modulating capacitance. The velocity sense current is converted to a voltage by a transresistance amplifier and is converted to a square wave by a comparator. The comparator output drives a few switches, which are used to apply the electrostatic force to the transducer.

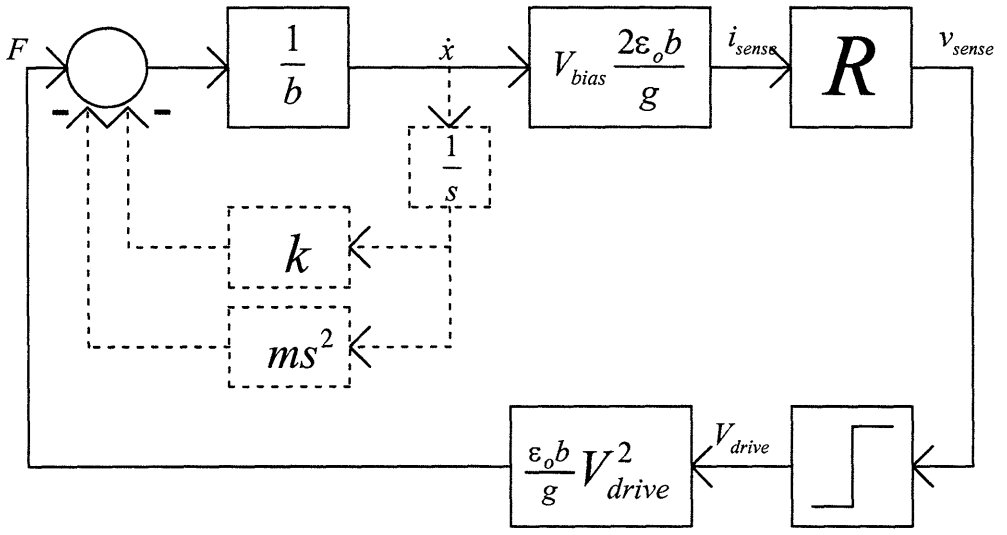


Figure 4.3: Block diagram of drive loop

## 4.3 DESCRIBING FUNCTION ANALYSIS

As long as a nonlinear element does not rectify or produce sub-harmonics of its input signal, then the output of the can be represented by a Fourier series. With an input of

$$v_I = E\sin\omega t,$$

the first two terms in the Fourier series of the output of the nonlinear element will be of the form:

$$v_O \approx A_1(E,\omega)\cos\omega t + B_1(E,\omega)\sin\omega t.$$

The describing function is defined as

$$G_D(E,\omega) = \frac{\sqrt{A_1^2(E,\omega)+B_1^2(E,\omega)}}{E}\angle\tan^{-1}\frac{A_1(E,\omega)}{B_1(E,\omega)}.$$

For a comparator without hysteresis, its describing function is simply

$$G_D(E,\omega) = \frac{4}{\pi}\frac{E_N}{E}.$$

In the above equation, $E_N$ is the output level of the comparator [45].

To maintain a constant amplitude oscillation, the loop transmission, when using ideal representations for all elements of Figure 4.3, should be:

$$|L(s)| = \left(\frac{\varepsilon_o b}{g} V_{drive}^2\right)\left(\frac{1}{\beta}\right)\left(V_{bias}\frac{2\varepsilon_o b}{g}\right)(R)\left(\frac{4F}{\pi E}\right) = 1.$$

As mentioned previously, each component of the drive loop will contribute phase as they propagate signals. To determine the sensitivity of the drive loop to phase, Figure 4.4 was generated. From this plot, it is evident that the drive loop is not overly sensitive to phase. Even with a phase error of 20 degrees, the sensitivity is still greater than 95% of its maximum value. The next sections will present the phase and offset contributions of the drive loop components.

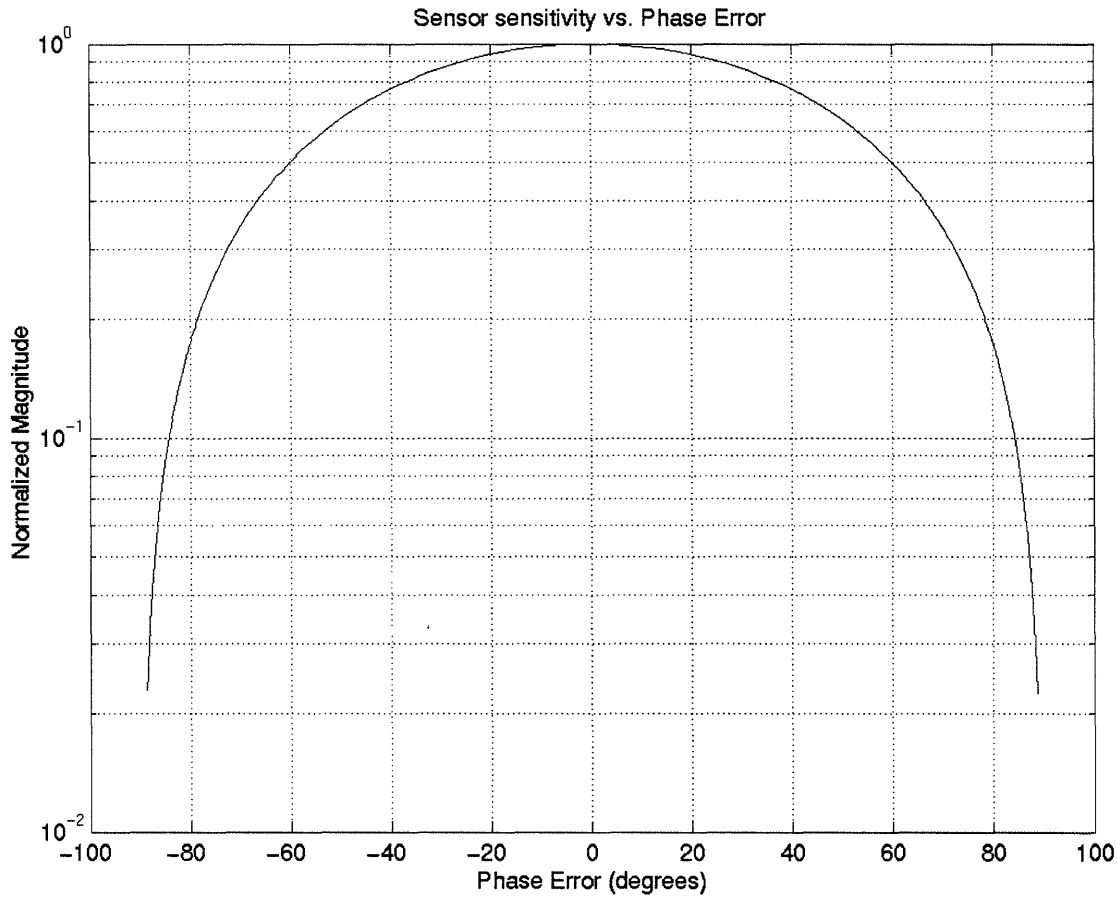

Figure 4.4: Sensor sensitivity versus phase error

## 4.4 DRIVE LOOP CONSIDERATIONS

The drive loop uses the lower four I/O ports of the mechanical transducer, with the moving structure biased at ground potential, as shown in Figure 4.2. The drive loop circuitry is shown in Figure 4.5. The sense amplifier is a transresistance amplifier that detects and amplifies the current coming from the transducer, which is proportional to velocity. The differential amplifier provides more gain and performs a differential to single-ended conversion. The AC coupling strips the offset of the sense and differential amplifiers from the signal and feeds into the comparator which then squares off the signal to generate a force drive.

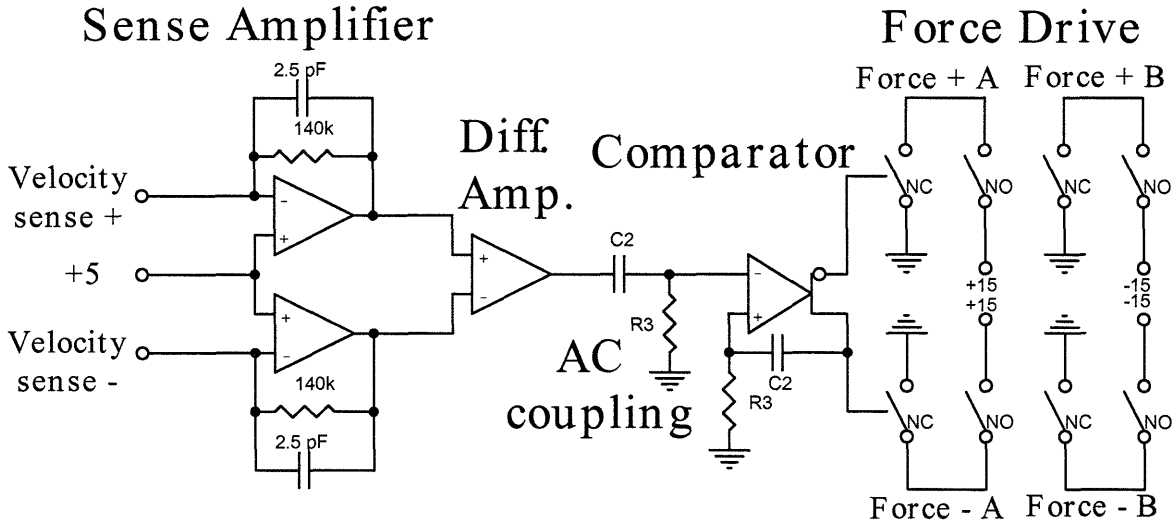


Figure 4.5: Drive loop circuitry

In addition to the phase delay through each of the elements in Figure 4.5, there are four main design issues: thermal noise from the sense and differential amplifiers, comparator hysteresis, comparator offset, and clock feedthrough. The thermal noise level must be kept to a minimum because the signal coming from the transducer is very weak. As the signal is amplified, so is the noise from the previous stage. This amplified noise will trigger the comparator more than once as the signal nears the trip point. Multiple transitions cause variations in the locations of the rising and falling edges of the output square wave as shown in Figure 4.6. The variations in the location of the edge of the comparator output cause variations in the integration time of the demodulator of the sense loop, which appears at the output as noise.

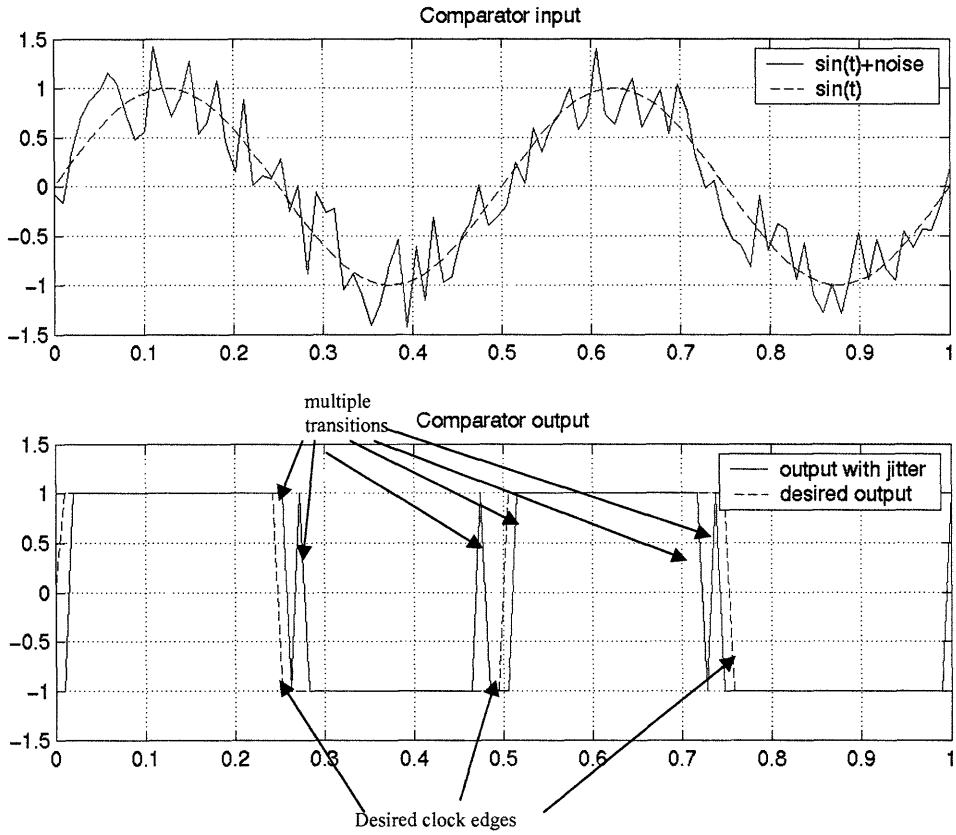

Figure 4.6: Effect of noise on comparator output

To minimize the effects of multiple transitions, hysteresis is commonly used. This works very well, however, the associated phase lag can be significant. For example, a 10% DC hysteresis band contributes six degrees of negative phase. However, the negative phase can be canceled with positive phase that can be obtained from an AC coupling network.

The DC offset of the signal needs to be minimized so that the residual charge spikes from the square-wave force drive are balanced and therefore won't cause an offset at the output of the integrator in the sense loop. Most of this offset is minimized by AC coupling the signal to the comparator with a high-pass filter. High-pass filtering has the

added advantage of providing the AC network with the ability to provide positive phase, and if the values are chosen properly the AC network can reset the overall phase lag to zero. If phase becomes an issue in the drive loop, it is theoretically possible to design a feedback loop to servo the phase between the force and velocity to exactly zero degrees as shown in Figure 4.7.

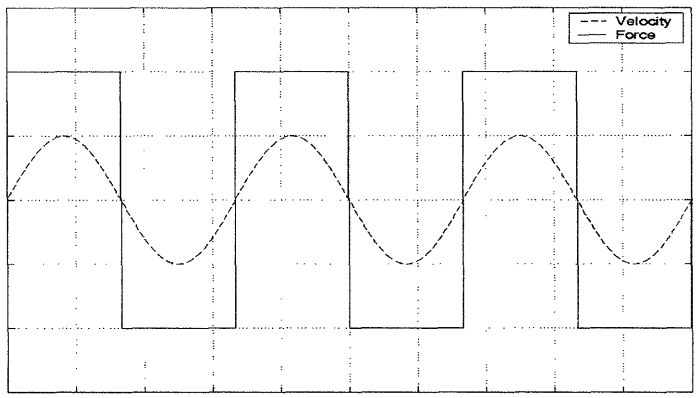

Figure 4.7: Electrostatic force and velocity at resonance

It is also important to note that the force +A and force +B terminals of Figure 4.2 are driven with voltages of opposite polarity. They are still driven with the same force because the electrostatic force is proportional to the square of the drive voltage. The dual polarity drive provides a means of minimizing the effect of feedthrough to the velocity sense terminals by providing zero net charge into the velocity sense amplifier's summing node.

## 4.5 Overview of Drive Loop Circuit Design

This section describes the circuitry used in the drive loop and the corresponding phase lag analysis.

### 4.5.1 VELOCITY DETECTION

When the mechanical sensor is vibrating at its resonant frequency, the electrostatic force is in phase with velocity and they are related by:

$$F_{electrostatic} = \frac{\dot{X}}{\beta}.$$

The electrostatic force causes the mechanical sensor to move in the direction of the applied voltage. As the sensor moves, its capacitance changes and this change in capacitance induces a current. The velocity of the sensor is inferred by measuring this current according to the following formula:

$$i_{sense} = V_{bias}\frac{dC_{drive}}{dt} = V_{bias}N_{drive}\frac{\varepsilon_O b}{g}\dot{X}.$$

For the parameters in this design, this current is 24 nA at resonance.

### 4.5.2 SENSE AMPLIFIER

The sense amplifier is a differential transresistance amplifier made using Burr-Brown OP627 op-amps, as shown in Figure 4.8. The maximum offset of each amplifier is 500 μV, for an upper bound of one mV. The parasitic shunt capacitance at the negative terminal makes the OP627 unstable, although it is stable at unity-gain. The loop transmission around the crossover frequency when accounting for this shunt capacitance is:

$$L(s) = \frac{10^7}{s(140k\Omega * 8pF * s + 1)}.$$

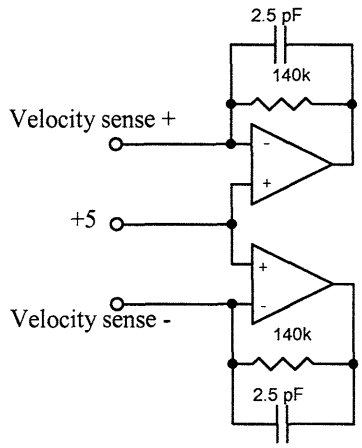


Figure 4.8: OP627-based sense amplifier

The phase margin of 4.8° is shown in the bode plot of Figure 4.9.

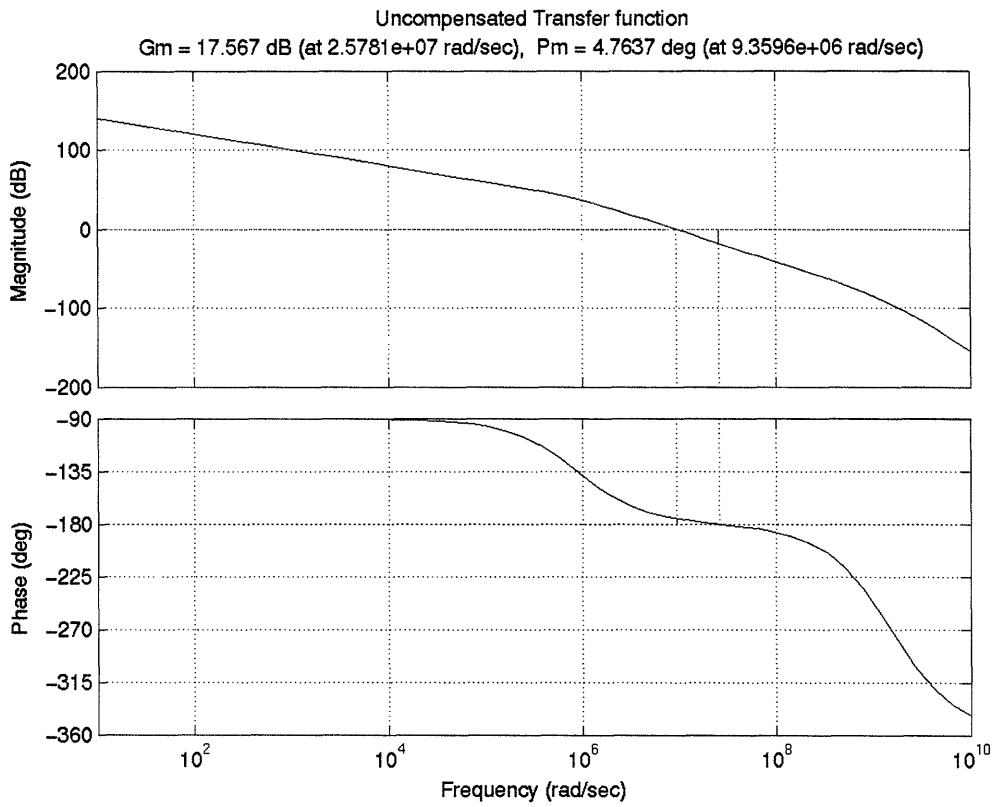


Figure 4.9: Uncompensated loop transmission of sense amplifier

A 2.5 pF capacitor was placed in parallel with the 142 kΩ feedback resistor to compensate for the parasitic capacitance at the inverting terminals of the op-amps. The compensated loop transmission around the crossover frequency is:

$$L(s) = \frac{10^7(140k\Omega * 2.5pF * s + 1)}{s(140k\Omega * (2.5pF + 8pF)s + 1)}.$$

This system has a phase margin of 60° at a unity gain frequency of 498 kHz as shown in Figure 4.10.

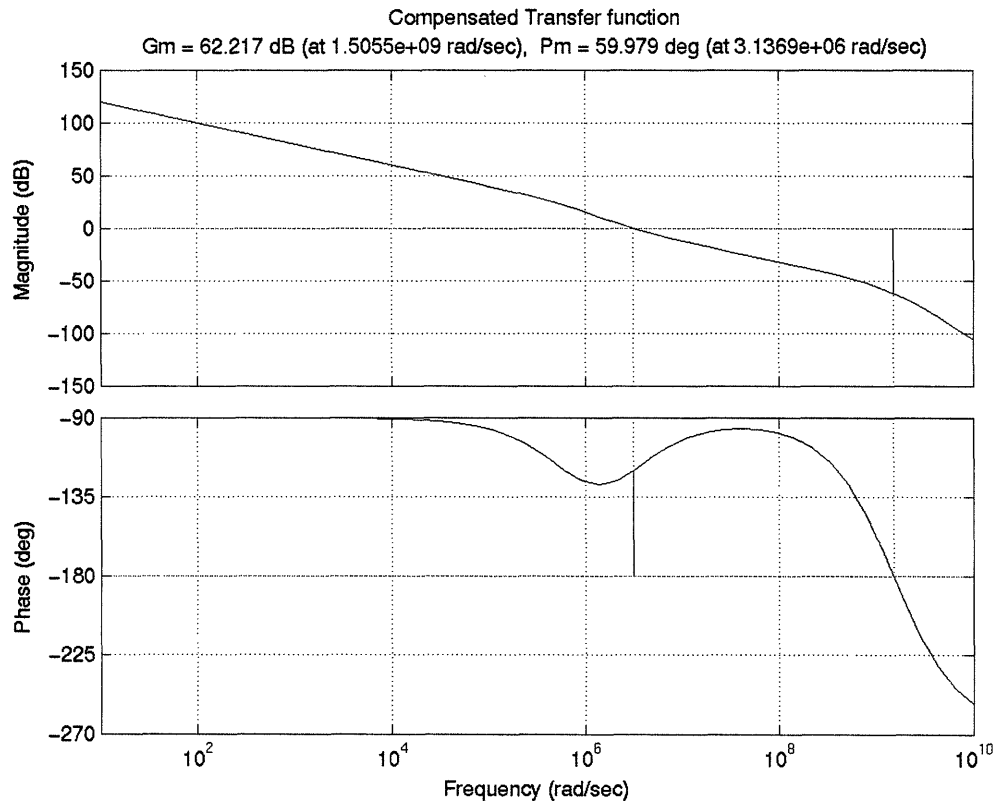


Figure 4.10: Compensated loop transmission of sense amplifier

A 30 kHz signal propagating through this amplifier will experience

$$-\tan^{-1}\frac{30kHz}{498kHz},$$

or -3.4° of phase. The signal amplitude at the output of this amplifier is approximately:

$$i_{sense}*(142k\Omega),$$

or 3.3 mV, with a random offset bounded by twice the offset of each op-amp, or one mV.

### 4.5.3 Differential Amplifier

The sense voltage is converted from a differential to a single-ended signal by using Linear Technologies LT1102 as shown in Figure 4.11. At a gain of 50, it has a bandwidth of roughly 1.7 MHz, and input referred offset voltage of one mV. The phase contribution of this stage is:

$$-\tan^{-1}\frac{30kHz}{1.7MHz}$$

or -1°. The signal amplitude is now 2*50(3.3 mV) or 335 mV. The cumulative offset has increased to 50(1mV+1mV) or 100 mV.

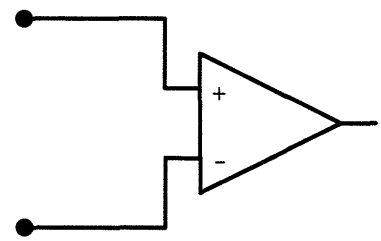


Figure 4.11: LT1102 differential amplifier

### 4.5.4 AC Coupling

The cumulative offset at this stage is roughly one-third of signal amplitude. If this were fed into the comparator, the duty cycle would drop down to 0.2. This drop in duty cycle will cause a drop in the effective loop gain of the drive loop and a 20% loss in sensitivity

of the sense loop, as shown in Figure 4.12. To minimize these errors, the sense velocity signal is filtered with the high pass network shown in Figure 4.13. The transfer function of this stage is:

$$\frac{RCs}{RCs+1}.$$

This can be designed to have either zero phase or positive phase that cancels the negative phase from the previous stages. For simplicity, zero phase was achieved by using a 1 μF capacitor and a 100 Ω resistor. The magnitude of the filter is unity at the resonant frequency, so the signal amplitude remains at 335 mV. The cumulative offset has been reset to zero, so the feedthrough spikes from the force drive will be centered on zero, which minimizes the spikes' offset contribution to the integrator in the sense loop. The zero-crossing detection of the comparator is also optimized.

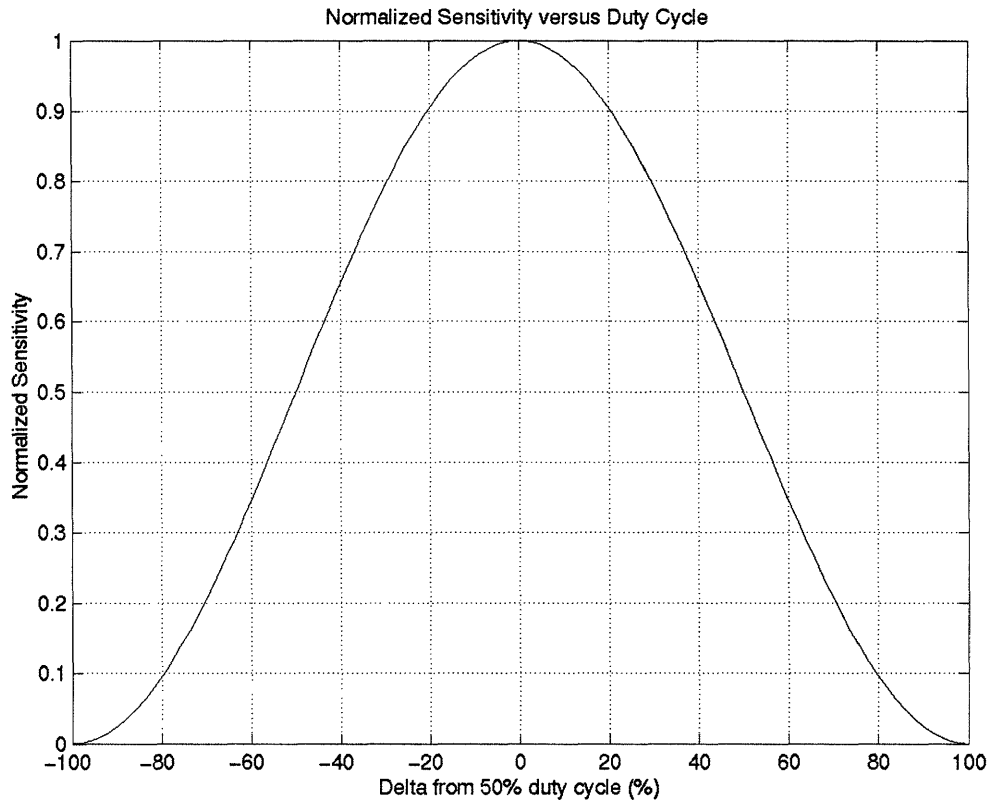


Figure 4.12: Normalized sensitivity versus duty cycle

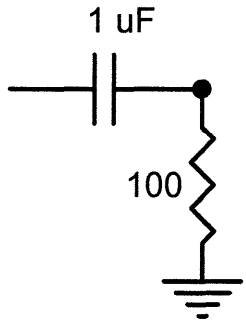


Figure 4.13: AC coupling network

### 4.5.5 COMPARATOR

The comparator is a Linear Technologies LT1016 series component. With complimentary TTL outputs and a gain of 3000, the comparator resolution is roughly one mV which

results in a phase lag estimated to be 1°. The signal, which is centered on 30 kHz, is very slow when compared to the 10 ns resolution time of the comparator. Therefore, any noise that exists at its input will cause multiple transitions. The typical solution to this problem is to use DC hysteresis. The tradeoff with this is the phase contribution ($\alpha$) is proportional to the ratio of the amount of hysteresis ($E_H$) to the signal level ($E_S$) and can be expressed as:

$$\alpha = \sin^{-1}\left(\frac{E_H}{E_S}\right).$$

The noise level at the input to the comparator is 4 $\mu V/\sqrt{Hz}$. Multiplying by the square root of the noise bandwidth of $\pi/2*500$ kHz yields 3.5 $mV_{rms}$ of noise. According to [54], the peak-to-peak noise will be six times this or 21 $mV_{pp}$. Since the predicted signal level is 335 millivolts, DC hysteresis would contribute two degrees of negative phase.

Although DC hysteresis is not overly problematic, what is desired is that when the comparator makes a decision, that it not be allowed to make another one for roughly one-half of a cycle. This is achieved by using AC hysteresis, as shown in Figure 4.14. By placing a capacitor in the positive feedback path around the capacitor, it achieves this function with minimal phase contribution.

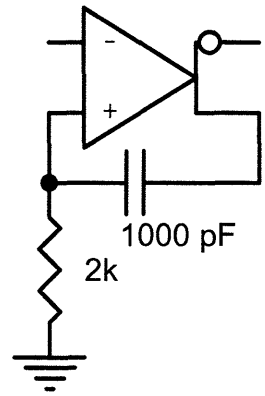


Figure 4.14: LT1016 comparator with AC hysteresis

### 4.5.6 SWITCHES

The switches used are in the Maxim MAX303 family of analog switches. With a 100ns turn-on time, the switches will contribute:

$$100ns*30kHz*360°,$$

or 1.1° of negative phase.

### 4.5.7 ELECTROSTATIC FORCES

In this design, the switches that were used limited the drive voltages used on the mechanical sensor to ±15 V. The electrostatic force generated is:

$$F_{electrostatic} = N_{drive}\frac{1}{2}\frac{\varepsilon_o b}{g}V_{drive}^2 = 816nN.$$

Without the $Q$-enhancement obtained from the self-resonant drive loop, this would yield a displacement of:

$$X = \frac{F_{electrostatic}}{k_{mechanical}} = 4nm .$$

This would correspond to sense capacitance of only 13.2 aF ($10^{-18}$ F). However, by always operating at the resonant frequency of the mechanical sensor the predicted displacement is:

$$X = \frac{F_{electrostatic}}{\beta(2\pi f)} = 2.27\mu m .$$

The corresponding sense capacitance of 7.5 fF, is more than 500 times greater than what is achievable when operating off-resonance, thanks to the $Q$ enhancement.

## 4.6 RESULTS

The design of this loop resulted in a cumulative phase error of -7°. This phase error results in a displacement (sensitivity) of more than 95% of the possible maximum value and a 50-50 duty cycle. The measured velocity sense and force drive (comparator output) waveforms are shown in Figure 4.15. The velocity and force are in phase as expected. The resonant frequency of 26.1 kHz is within 15% of its predicted value and is sensitive to etch variations in the tethers. In addition, the velocity amplitude is 300mV, as compared to its predicted value of 335mV. This confirms that the drive loop is functioning as expected.

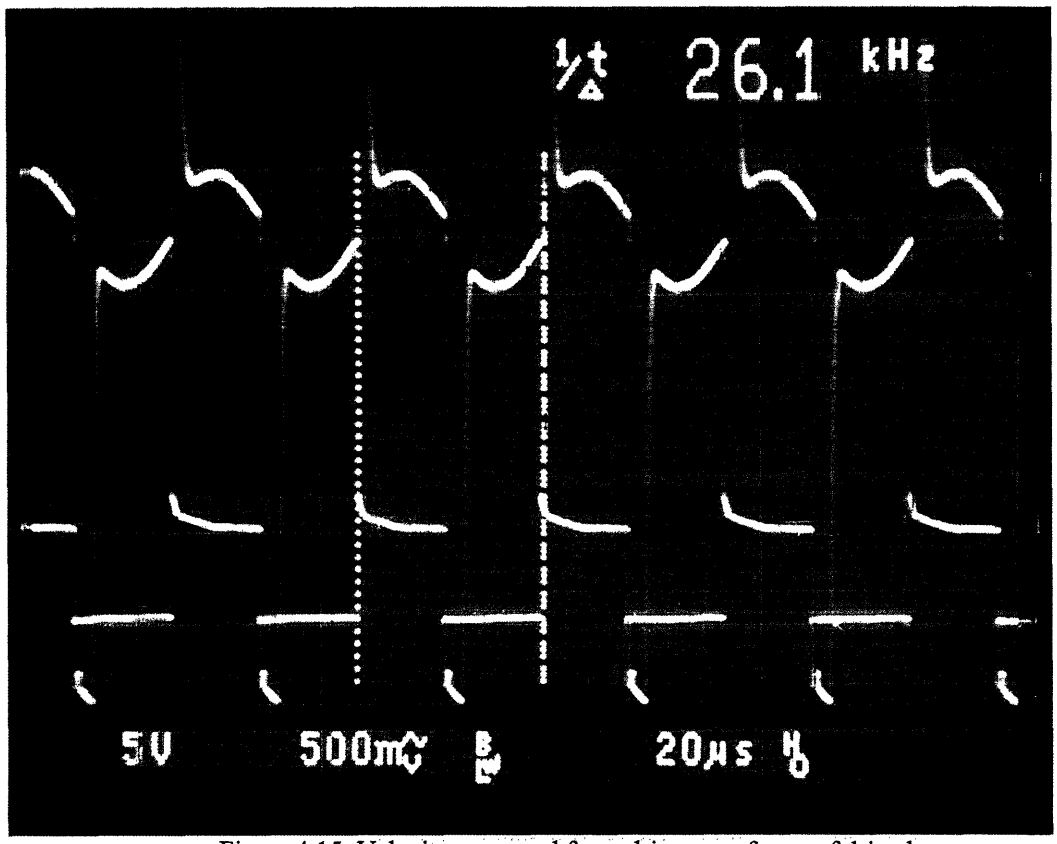

Figure 4.15: Velocity sense and force drive waveforms of drive loop

## 4.7 ADDITIONAL MEASUREMENTS

Additional measurements were made to further qualify the drive loop's operation. The circuit was placed in a bell jar and the sensed velocity was plotted as a function of atmospheric pressure. To insure that the loop behaves as expected, the velocity's dependence on the square of the drive voltage was confirmed. In addition, the resonant frequency was plotted as a function of the common mode voltage applied to the sense fingers.

### 4.7.1 VACUUM MEASUREMENTS

As the air surrounding the mechanical sensor was pumped down, the velocity was measured and plotted in Figure 4.16. Since damping varies directly with atmospheric pressure, then for a constant force, the velocity should increase as the pressure is decreased due to the decrease in squeezed-film damping [54]. This is shown by the force to velocity relationship of the beam oscillating at its mechanical resonance: $F = \beta v$. The plot confirms the inverse relationship between damping and beam velocity with a constant force drive.

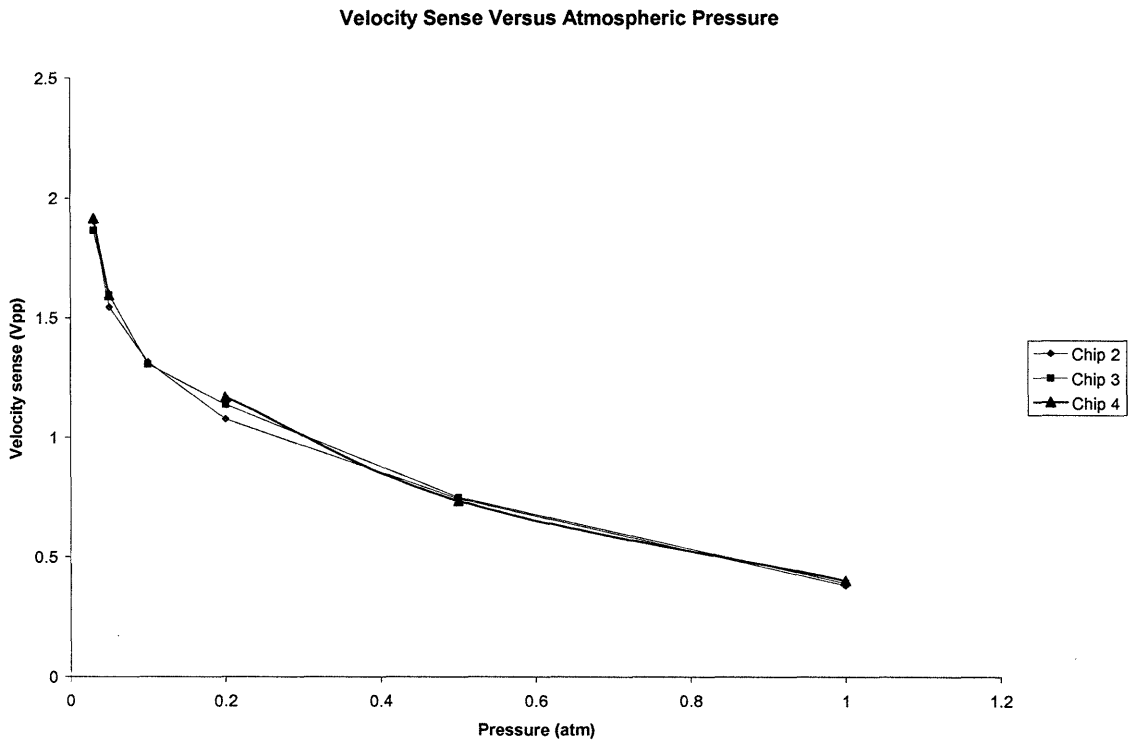


Figure 4.16: Velocity sense as a function of atmospheric pressure

Since the velocity is directly proportional to the displacement of the beam, then as the beam displacement increases with low pressure, the velocity increases according to

the formula: $v=2\pi fX$. If the atmospheric pressure is sufficiently reduced with a fixed force drive, then the moving fingers will eventually collide with the fixed fingers and mechanical modes of the moving arms will be excited. This is confirmed in Figure 4.17, where one can see an oscillation superimposed on the velocity sense waveform. The frequency of this secondary oscillation is 472 kHz, which is less than one percent different from the first predicted modal frequency of 475 kHz.

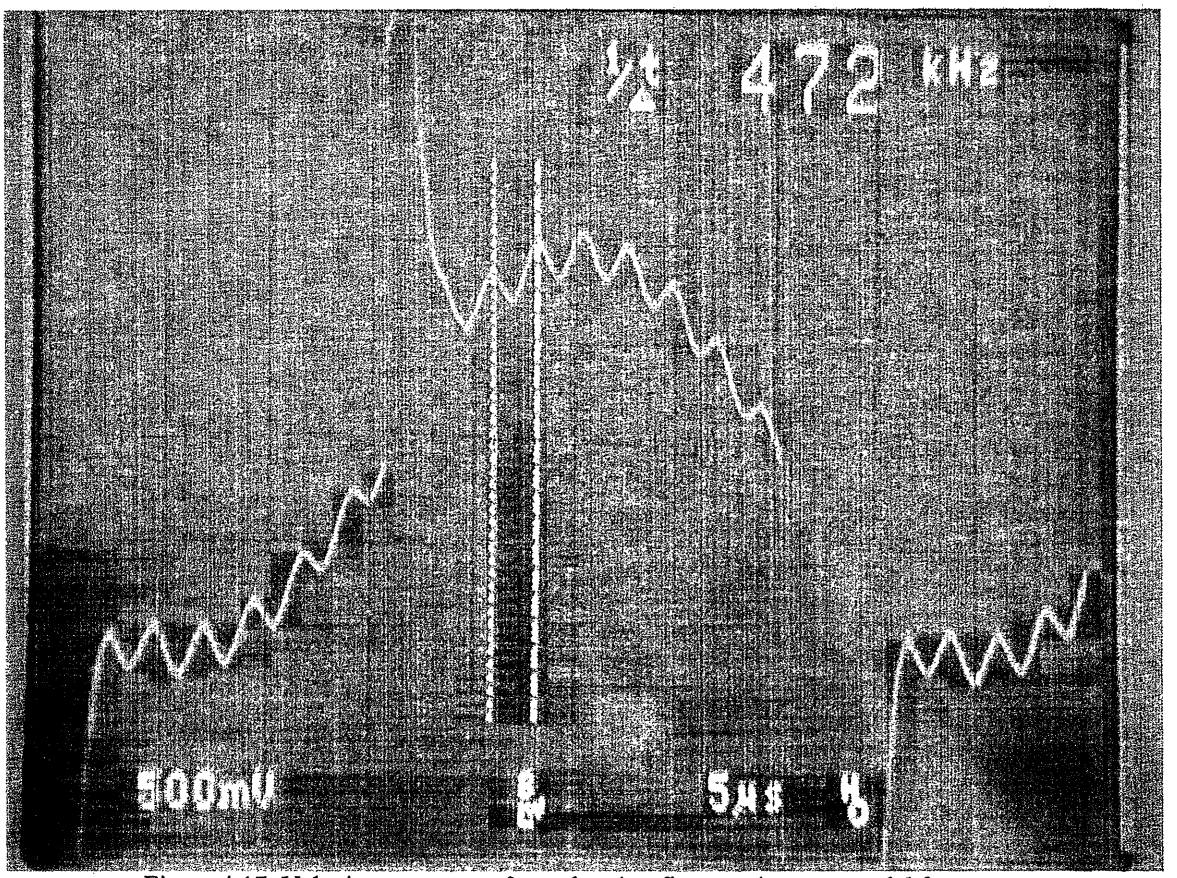

Figure 4.17: Velocity sense waveform showing first moving arm modal frequency

### 4.7.2 Resonant Frequency Shift vs Common Mode Voltage

The resonant frequency was measured on a spectrum analyzer as a function of the common mode voltage to investigate the effects of the electrical spring constant

described in Section 3.2.4. Since the electrical spring constant is so small, its effect on the resonant frequency is negligible as shown in Figure 4.18. Note that it does follow the expected V-squared dependence.

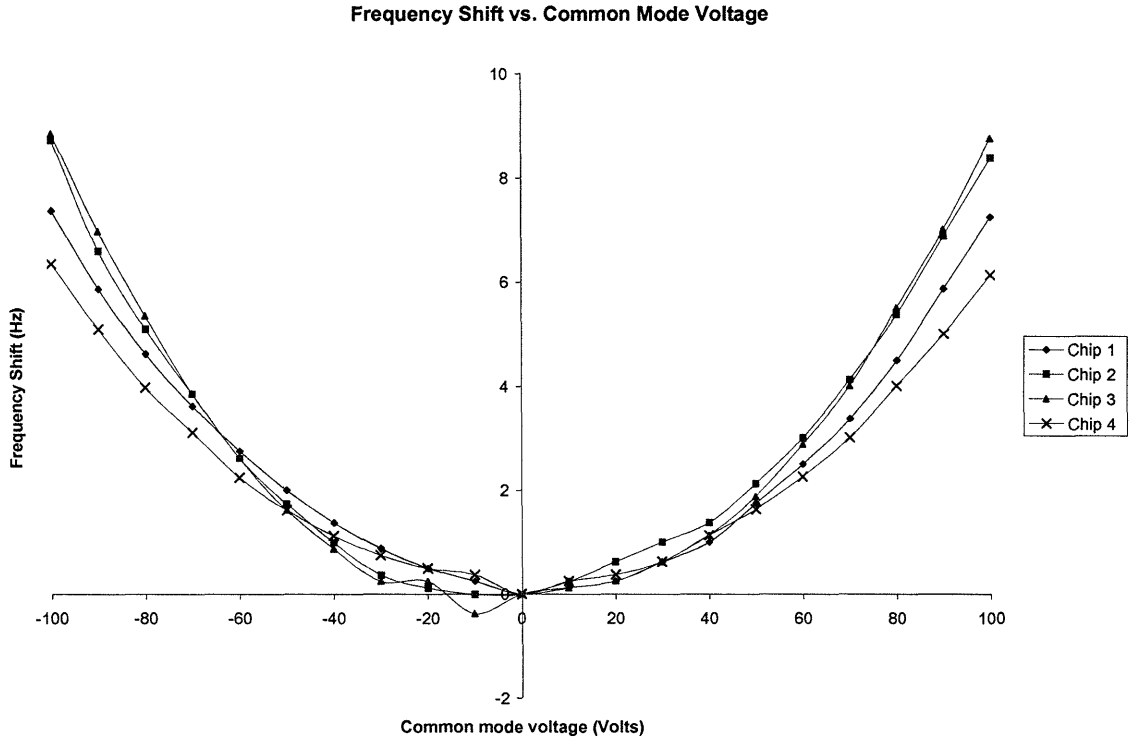


Figure 4.18: Resonant frequency shift vs. common mode voltage

## 4.7.3 SQUARE LAW ERROR

As derived in Chapter 3, the electrostatic force applied to the beam is proportional to the square of the voltage applied to the fingers. So, for two separate drive voltages (12 V and 15 V), we can write $\frac{V_{drive1}^2}{V_{drive2}^2} = \frac{\dot{x}_1}{\dot{x}_2} = 1.56$. The velocity sense was measured at these two drive voltages and their ratio was compared to the square law's prediction. For most

chips, the deviation from its ideal value is less than 10 % and these results are plotted in Figure 4.19.

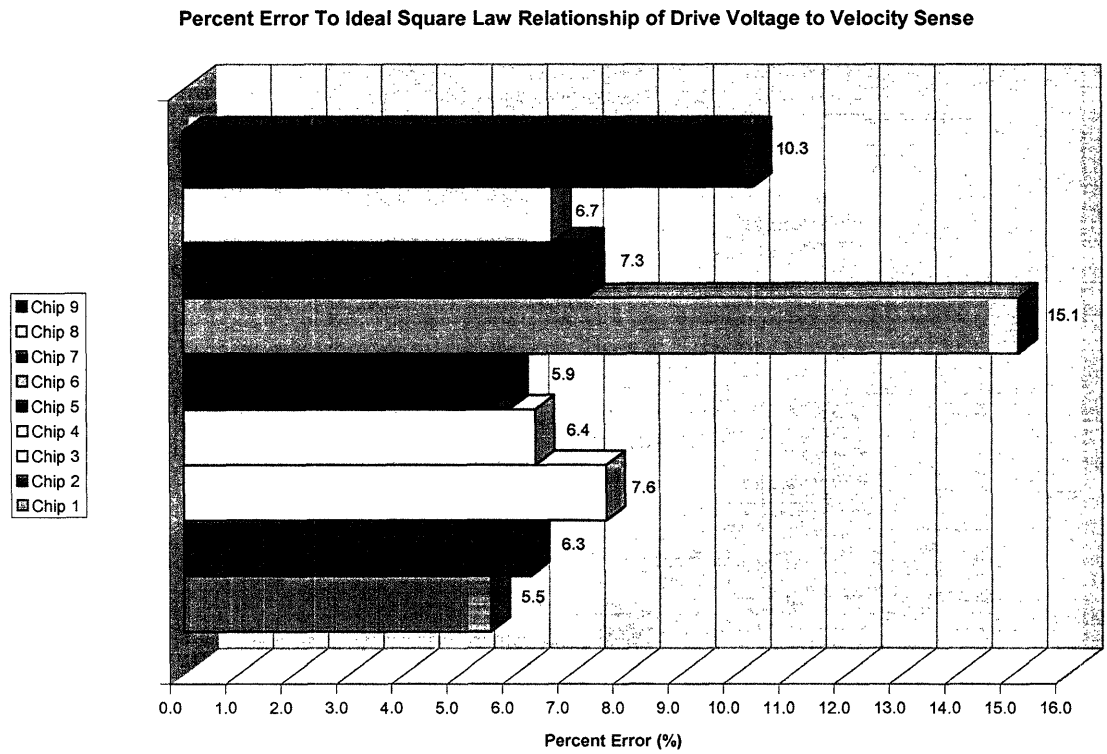


Figure 4.19: Drive voltage square law error measurements

## 4.8 SUMMARY

The purpose of the drive loop is to vibrate the MEMS transducer at its mechanical resonant frequency, which ensures maximum sensitivity. The MEMS structure was actuated with an electrostatic square wave force drive. This resulted in a sinusoidal displacement due to the high $Q$ of the beam's second order transfer function. To ensure a constant amplitude displacement, the beam was placed in a feedback loop and this loop was analyzed by describing functions. In addition, the tradeoffs between phase lag and

sensitivity were discussed and the phase contribution of each of the elements in the drive loop was computed.

# 5 SENSE LOOP

## 5.1 MOTIVATION

This design involves the implementation of a MEMS-based galvanically isolated differential amplifier that uses linear capacitance modulation to obtain measurement accuracy down to DC. As mentioned in Chapter 1, all semiconductor amplifiers present low frequency, 1/f noise. The presence of this noise makes low-level DC measurements difficult or sometimes, impossible. A technique that circumvents this is correlated double sampling, which involves sampling the noise and offset one clock cycle and then subtracting it from the actual signal on the other clock cycle.

The sense loop uses the upper-half of the mechanical structure that is driven at resonance by the drive loop as a vibrating capacitor. The up-modulated signal is then amplified and demodulated with a synchronous clock derived from the drive loop's force signal. A feedback loop is closed with a set of shunt MEMS capacitors to provide stable gain and includes an integrator to drive steady state errors to zero.

## 5.2 DESIGN OVERVIEW

As shown in Figure 5.1, the upper half of the resonant structure is used as the summing junction of the sense loop. Figure 5.2 shows the circuitry involved in detecting and demodulating the input signal. When a differential signal is applied to the inputs of the beam, a low-level up-modulated signal is generated at the Vsense± terminals. This AC signal is amplified by a differential sense amplifier and is filtered by an anti-alias filter.

The resulting signal is demodulated and integrated to generate the output voltage and a differential signal to cancel the induced charge on the beam. The sense amplifier, anti-aliasing filter and integrating demodulator used in this design will be presented in Section 5.3. To enhance linearity and add robustness to temperature and process variations, feedback is applied through a set of shunt fingers, which provides for accurate sensing while maintaining galvanic isolation.

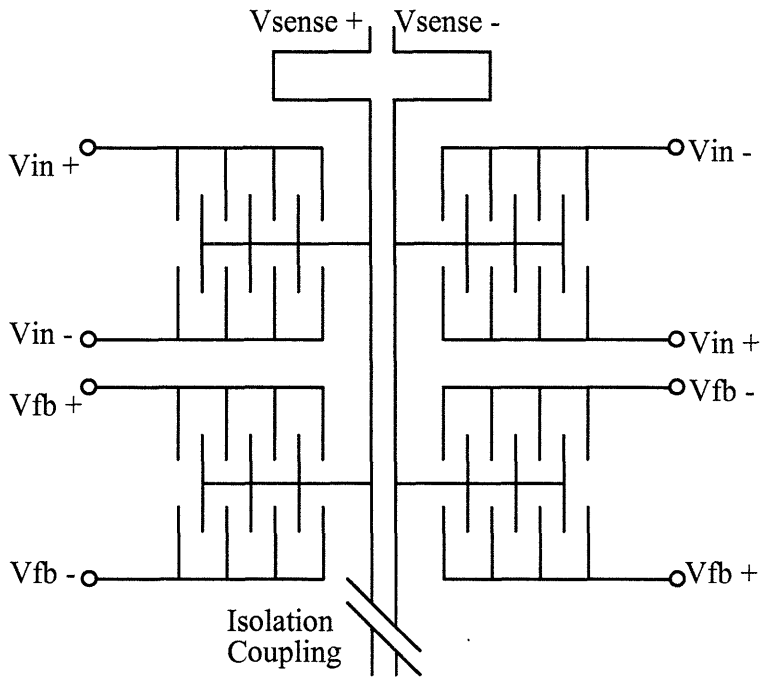


Figure 5.1: Upper-half of the mechanical transducer used in the sense loop

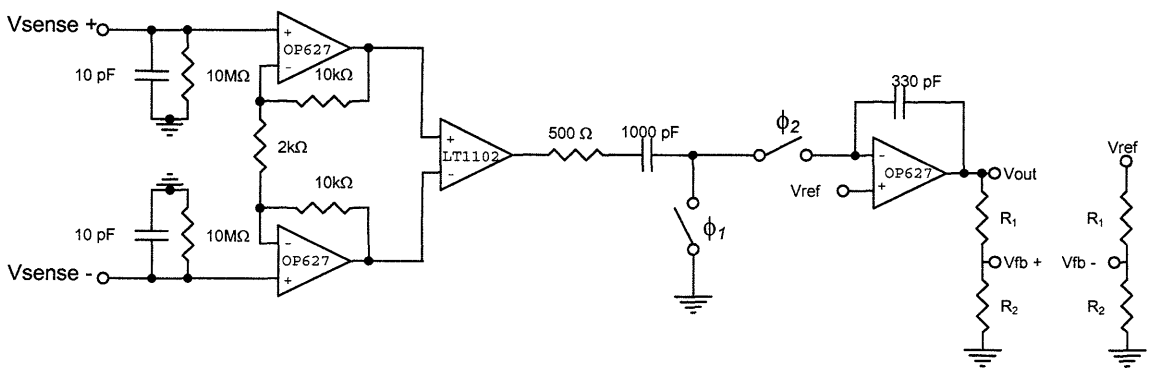


Figure 5.2: Sense loop circuitry

## 5.3 DESIGN CONSIDERATIONS

There are many ways to implement the sense loop, each with potential advantages and disadvantages. Correlated double sampling (CDS), as described in section 1.3.1, was used as the demodulation scheme with large resistors setting the DC bias of the beam nodes. As with the drive loop, proper clock phasing is required to maximize sensitivity, which depends on the bandwidth of the elements of the sense loop. Care must also be taken to minimize the amount of noise aliasing that occurs, while maintaining a reasonable amount of closed loop bandwidth and degree of stability.

### 5.3.1 DEMODULATION SCHEME

As mentioned in Section 1.3.1, correlated double-sampling (CDS) and chopper stabilization (CHS) are two common methods of reducing 1/f noise in amplifiers. As summarized in Section 1.3.3, both methods provide input noise reduction, but CDS has the added benefit of placing a zero at the origin, which offers a higher degree of input offset voltage attenuation. However, the draw back is that since CDS is a sampling process, there will be a potentially significant increase in broadband noise due to foldover. In this design, CDS was chosen as the demodulation scheme. A detailed noise analysis is presented in Section 5.3.5.

### 5.3.2 BIASING SCHEME

The output terminal of the MEMS transducer is a capacitive node whose DC bias must be controlled. There were three devices considered in setting the DC bias of the beam: back-to-back diodes, a large resistor, and a reset switch.

The diode-based biasing scheme is shown in Figure 5.3. The diodes will keep the voltage at the beam node within a forward diode drop of the desired beam bias voltage. However, diodes present three unwanted effects to the system: parasitic capacitance, nonlinear recovery and leakage current. When the common mode voltage changes at the inputs of the mechanical structure, the voltage on the beam will also change. This is due to the capacitive divider formed between the static capacitance and the total shunt parasitic capacitance at the beam node. When the common mode voltage changes, then the parasitic capacitance at the beam node will change. This causes the differential signal to be a function of the common mode voltage, which is undesired.

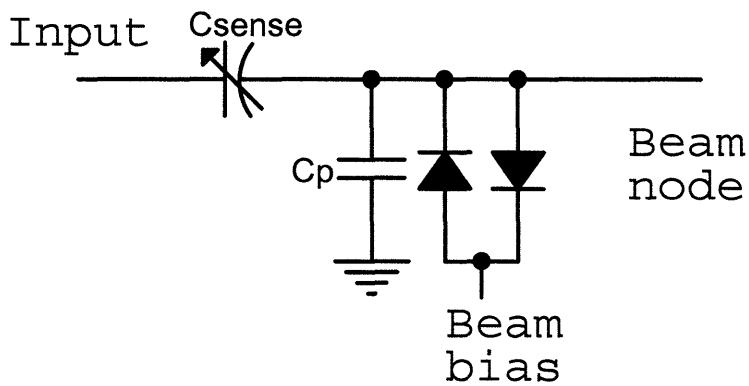


Figure 5.3: Diode biasing scheme

In addition, when a transient overvoltage condition occurs, the recovery time of the system will be nonlinear because the diode's parasitics are a function of its bias. During the time in which the diodes are conducting, the differential signal to the pre-amplifier will be zero.

On the other hand, using a large resistor to set the DC bias of the beam node yields a linear response to overvoltage transients. This configuration is shown in Figure 5.4. The large resistance value required, typically tens of meg-ohms to gig-ohms, will also require a long recovery time. If the pre-amplifier were to be integrated onto the same IC as the mechanical transducer, then there would be a major issue to address. To achieve acceptable performance, matched resistors with at least 10 MΩ resistance must be fabricated. In addition to the difficulty of fabricating such large valued resistors on an IC, fabricating a matched pair of large valued resistors is also difficult.

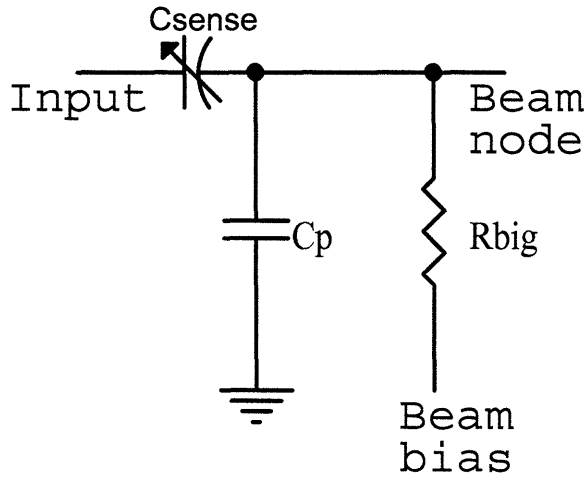


Figure 5.4: Large resistor biasing scheme

The reset switch, as shown in Figure 5.5, has two advantages over the large resistor and the cross-coupled diodes. It is very easy to fabricate matched switches on an IC. Switched reset recovery time to common-mode transients is lower by many orders of magnitude if the reset occurs during each clock cycle and if the subsequent settling is allowed to proceed. The disadvantages to using a reset switch are that the loop is no longer in the continuous time domain, and as with any sampled-data system, there will be aliased kT/C noise. This noise can be rejected with a proper CDS clocking scheme.

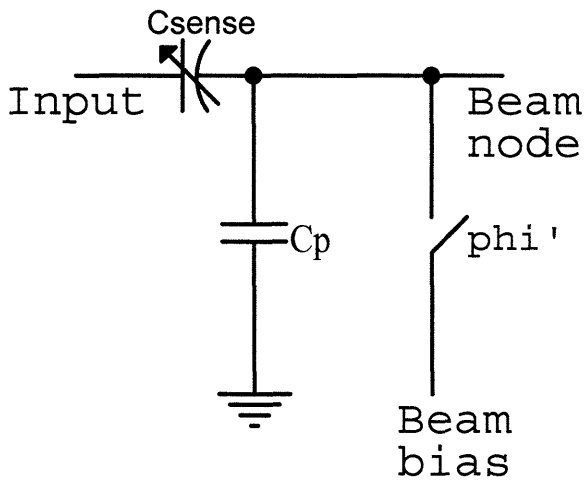


Figure 5.5: Reset switch biasing scheme

In this prototype, the main goal was a proof-of-principle so the sense loop circuitry was not integrated with the sensor. Therefore, a ten meg-ohm resistor was used to set the DC bias of the beam node. To address the matching and noise issues, many resistors were measured in order to find a matched pair, and their noise contribution will be discussed in Section 5.3.5. Although discrete resistive biasing was used, the associated noise does not dominate noise performance.

### 5.3.3 CLOCKING

The signal coming from the beam node is up modulated by the vibrating mechanical transducer. In order to properly demodulate the signal, proper phasing must be maintained. As shown in Figure 5.6, the force and velocity are in phase when the transducer is excited at its mechanical resonance. The error signal, however, is in phase with the modulating capacitance, which is in phase with position. To maximize the detection of the signal, the phase contributions from the sense loop circuitry must be minimized and the demodulator clock should be in phase with the force drive.

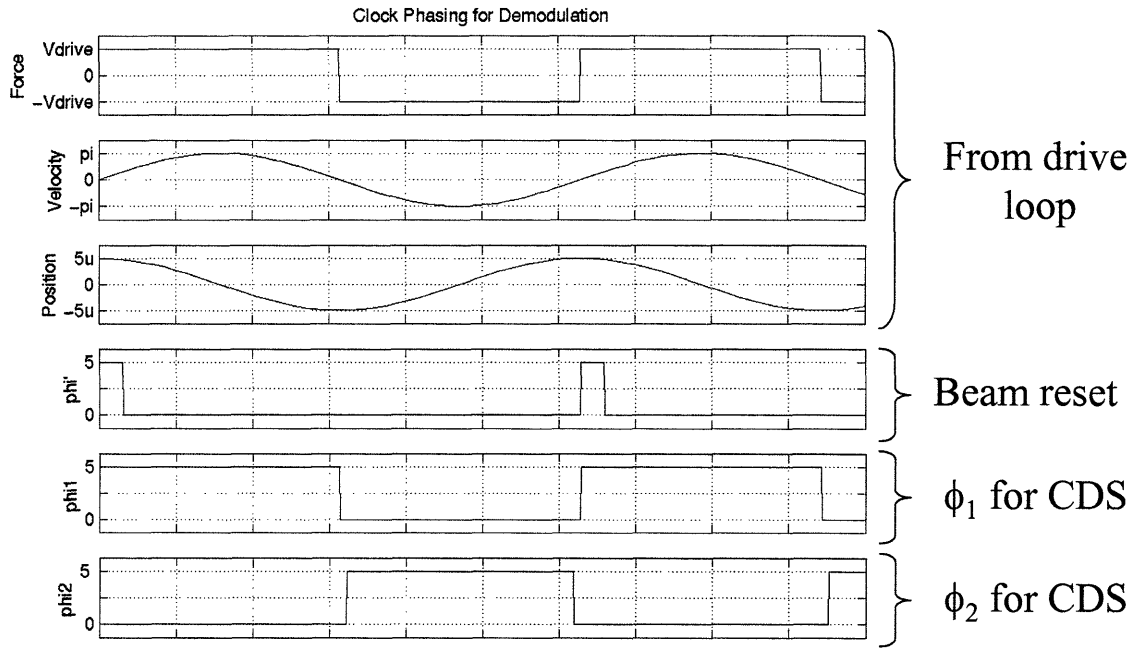


Figure 5.6: Clock phasing for demodulation

### 5.3.4 STABILITY ANALYSIS

Before the loop can be closed, the transfer function of each element in the sense loop must be determined. The elements in the loop are shown in Figure 5.2. The amplitude of the signal as it passes through the transducer is attenuated by a factor of:

$$\frac{2C_s}{C_p + 4C_s}.$$

The pre-amplifier gain is:

$$\frac{2R_2}{R_1}G$$

This appears as a scale factor because the pre-amplifier's bandwidth will be much higher that the loop crossover to minimize its phase delay.

The wide bandwidths of the amplifiers in the sense loop help maximize the overall sensitivity of the loop. However, this is a sampled data system, so the high bandwidth of the sense loop components will cause a significant amount of noise to fold into the Nyquist band. Therefore, the signal must be band-limited before it is sampled to reduce the effects of this aliasing. Therefore, a $RC$ network consisting of $R_s$ and $C_s$ is used as a passive anti-aliasing filter for the CDS integrator.

The CDS integrator transfer function is derived using discrete time analysis methods. For the two-phase non-overlapping clocks and circuitry shown in Figure 5.7, the difference equation is:

$$V_o[n+1]-V_o[n]=-\frac{C_s}{C_f}\frac{1}{R_sC_ss+1}\left(V_i\left[n+\tfrac{1}{2}\right]-V_o[n]\right).$$

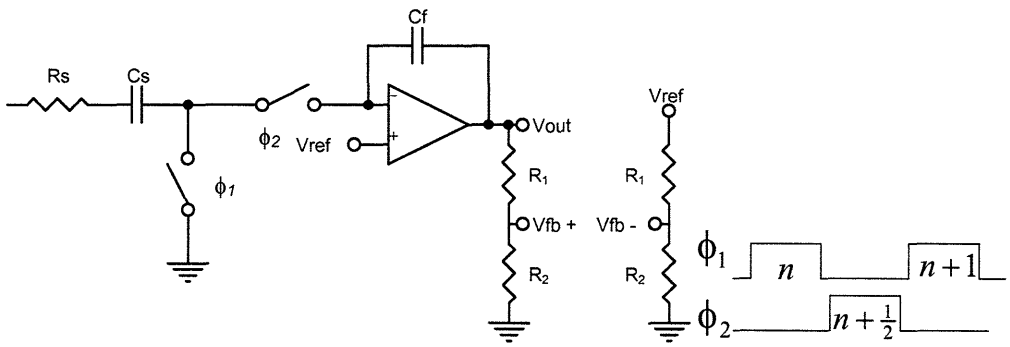


Figure 5.7: Demodulating integrator circuitry and two-phase clocking scheme

Taking the discrete time Fourier transform of the above difference equation yields the input output relation for this circuit:

$$\frac{V_o}{V_i}=-\frac{C_s}{C_f}\frac{1}{R_sC_ss+1}e^{\frac{-j\omega T}{4}}\frac{\sin\left(\frac{\omega T}{4}\right)}{\sin\left(\frac{\omega T}{2}\right)}$$

To simplify this expression, we can take advantage of the fact that the input to this block is up-modulated: $\omega=\omega_{res}+\omega_{sig}$. Expanding the above equation and noting that $\omega_{res}T = 2\pi$, we have;

$$\frac{V_o}{V_i}=-\frac{C_s}{C_f}\frac{1}{R_sC_ss+1}e^{\frac{-j(\omega_{res}+\omega_{sig})T}{4}}\frac{\overbrace{\sin\left(\frac{\omega_{res}T}{4}\right)}^{1}\cos\left(\frac{\omega_{sig}T}{4}\right)+\sin\left(\frac{\omega_{sig}T}{4}\right)\overbrace{\cos\left(\frac{\omega_{res}T}{4}\right)}^{0}}{\underbrace{\sin\left(\frac{\omega_{res}T}{2}\right)}_{0}\cos\left(\frac{\omega_{sig}T}{2}\right)+\sin\left(\frac{\omega_{sig}T}{2}\right)\underbrace{\cos\left(\frac{\omega_{res}T}{2}\right)}_{-1}}$$

$$\frac{V_o}{V_i}=-\frac{C_s}{C_f}\frac{1}{R_sC_ss+1}\overbrace{e^{\frac{-j\omega_{res}T}{4}}}^{-j}\frac{\overbrace{\cos\left(\frac{\omega_{sig}T}{4}\right)}^{1}}{-\sin\left(\frac{\omega_{sig}T}{2}\right)}\approx\frac{C_s}{C_f}\frac{1}{j}\frac{1}{\frac{\omega_{sig}T}{2}}$$

Noting that $\omega_{sig}$ is the baseband signal, it is evident that this block is a non-inverting, demodulating integrator with a transfer function of:

$$\frac{V_o}{V_i} = \frac{2C_s}{C_f}\frac{1}{R_sC_ss+1}\frac{f_{CLK}}{j\omega}.$$

With the feedback ratio of $f = \frac{R_2}{R_1 + R_2}$, set by the resistive divider at the output, the block diagram of the sense loop is:

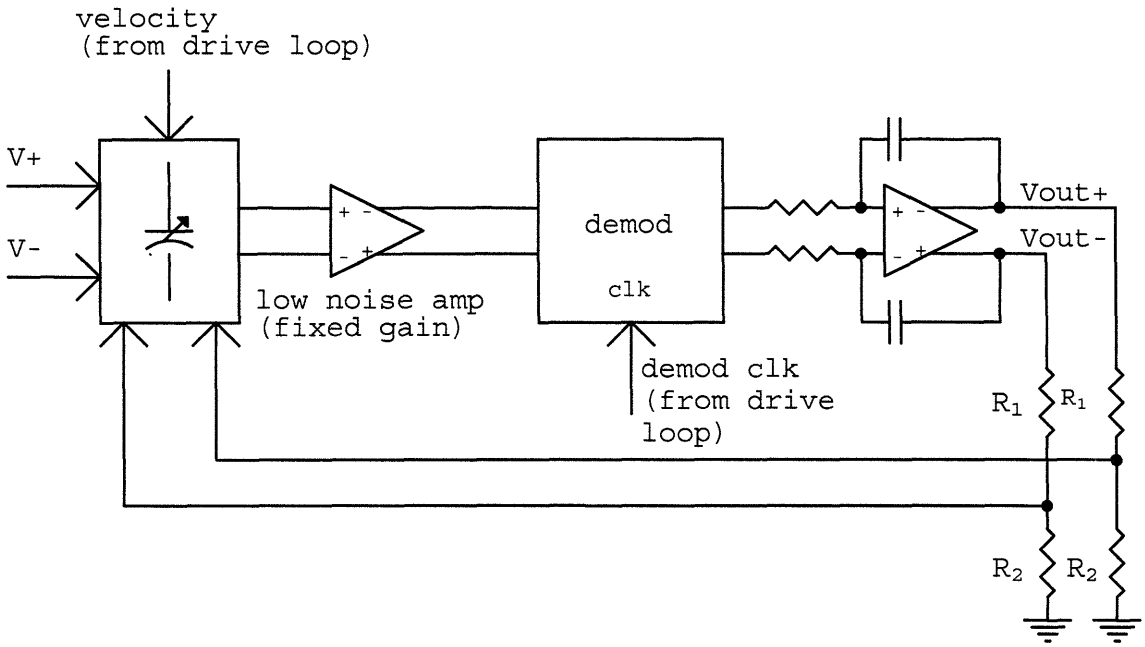


Figure 5.8: Block diagram of sense loop

The first order loop transmission, L(s), is:

$$L(s) = \left(\frac{2C_{sense}}{C_p + 4C_{sense}}\right)\left(A_{v,preamp}\right)\left(\frac{2C_sf_{CLK}}{sC_f}\frac{1}{R_sC_ss+1}\right)f$$

The sense loop was simulated using a model created in ADICE®. The resulting risetime is 2.7 ms, which corresponds to a bandwidth of 128 Hz and is within 10% of the hand calculation prediction of 141 Hz. The step response is shown below in Figure 5.9.

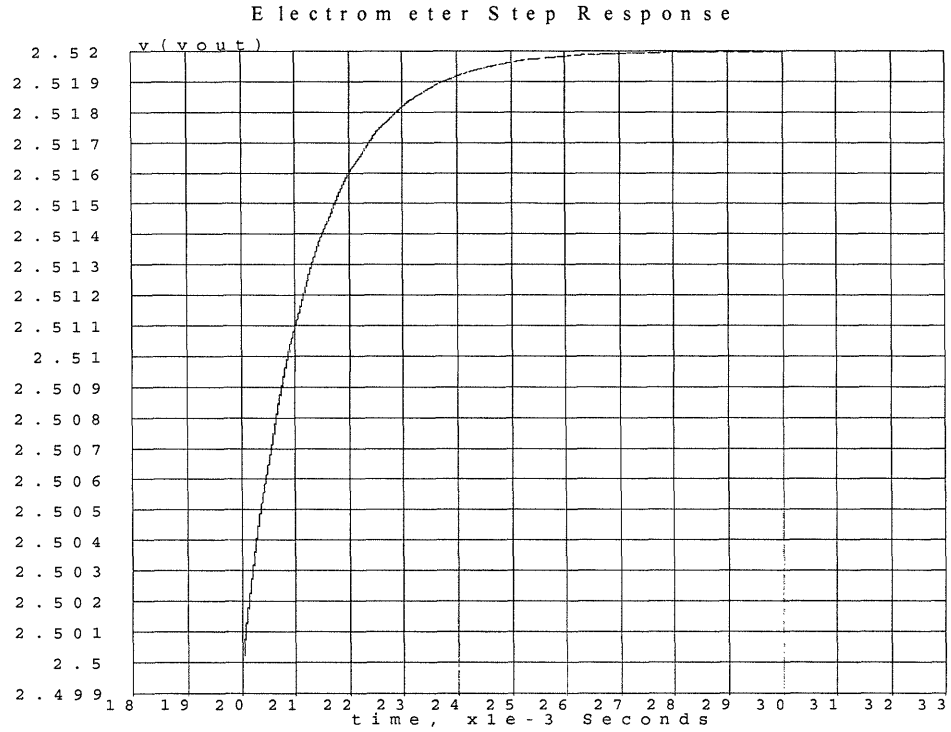

Figure 5.9: Simulated electrometer step response

### 5.3.5 NOISE ANALYSIS

The noise model of the sense loop's circuitry is shown in Figure 5.9. This section describes the major sources of broadband noise in the sense loop.

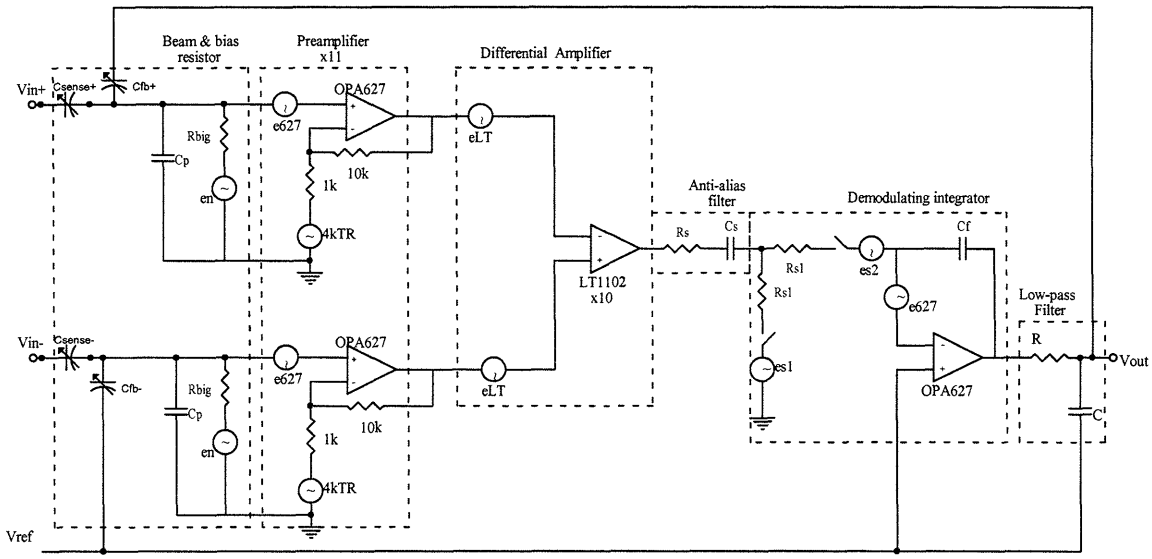


Figure 5.10: Noise model of sense loop circuitry

Since broadband noise is non-deterministic, it is described in terms of probability density functions or PDFs with units of $V^2_{rms}/Hz$. The noise at the input of the pre-amplifier can be expressed as:

$$2\left[4kTR_{BIG}\left|\frac{1}{R_{BIG}C_P s+1}\right|^2+e_{627}^2+4kT\left(1k\Omega \parallel 10k\Omega\right)+e_{LT}^2\left(\frac{1}{11}\right)^2\right]=\left(\frac{8nV}{\sqrt{Hz}}\right)^2.$$

The first term represents the filtering by the low pass filter formed by the beam biasing resistor and the parasitic capacitance at the input of the pre-amplifier. The second term is the input voltage noise of the OPA627. The third term represents the noise contribution due to the feedback resistors of the OPA627. The last term is the noise of the following differential amplifier, the LT1102, reflected back to the pre-amplifier's input. The factor of two accounts for the fact that there are two identical but statistically independent paths that contribute to the overall noise of the system. The noise at this node is dominated by the OPA627 and its feedback resistors.

The anti-alias filter of *Rs* and *Cs* limit the bandwidth of the noise at the input of the sampling demodulating integrator. For *Rs* = 500 Ω and *Cs* = 1000 pF, the noise bandwidth is 499 kHz. This is much higher than the Nyquist frequency of 26 kHz/2 or 13 kHz. Therefore, aliasing will occur and noise will fold into the Nyquist bandwidth. The total noise at the output will consist of direct and sampled-and-held noise densities [56], however, in this design, the sampled-and-held noise dominates.

Since this is a closed loop system, the noise at the output can be computed by traversing the feedback path from the output to the summing node. The noise at the summing node will be scaled by the inverse of the feedback attenuation of $\frac{Cfb}{C_P}$. The next scale factor is due to aliasing: $\sqrt{\frac{\frac{1}{4}}{\frac{1}{2}f_c R_s C_S}}$ Finally, to convert the PDF to rms, we multiply by the square root of the noise bandwidth: $\sqrt{\frac{1}{4RC}}$.

The component noise values are summarized in the Table 5.1.

| $R_S$ | $C_S$ | $f_c$ | $C_p$ | $e_{627}^2$ | $e_{LT}^2$ | $e_{S_1}^2, e_{S_2}^2$ | C | R |
|---|---|---|---|---|---|---|---|---|
| 500 | 1000 pF | 26 kHz | 10 pF | 4 $\frac{nV}{\sqrt{Hz}}$ | 20 $\frac{nV}{\sqrt{Hz}}$ | 1 $\frac{nV}{\sqrt{Hz}}$ | 0.1 μF | 32.4 kΩ |

Table 5.1: Summary of noise parameters

With these values, the predicted noise at the output is 55 $\mu V/\sqrt{Hz}$ or 486 $\mu V_{rms}$. Note that since this was computed for a unity gain system, this output noise is the same as the referred to input (RTI) noise.

## 5.4 EXPERIMENTAL RESULTS

To verify the functionality of sense loop circuitry, the loop was not closed and the input into the demodulating integrator was plotted with zero input and a 10 V differential input signal. These are shown in Figure 5.11 and Figure 5.12, respectively. The output of the pre-amplifier is:

$$V_{error} = \left(\frac{C_S}{C_P}\right)\left(A_{v,preamp}\right)V_{diff}.$$

For a displacement of 2.1μm, the sense capacitance is:

$$C_{sense} = \frac{N_{sense}\varepsilon_o bX}{g} = 9fF.$$

With an estimated parasitic capacitance, $C_P$, of 10 pF and a pre-amplifier gain, $A_{v,\ preamp}$, of 110, the peak-to-peak amplitude of the error signal should be 0.825 $V_{pp}$. This is confirmed in Figure 5.12.

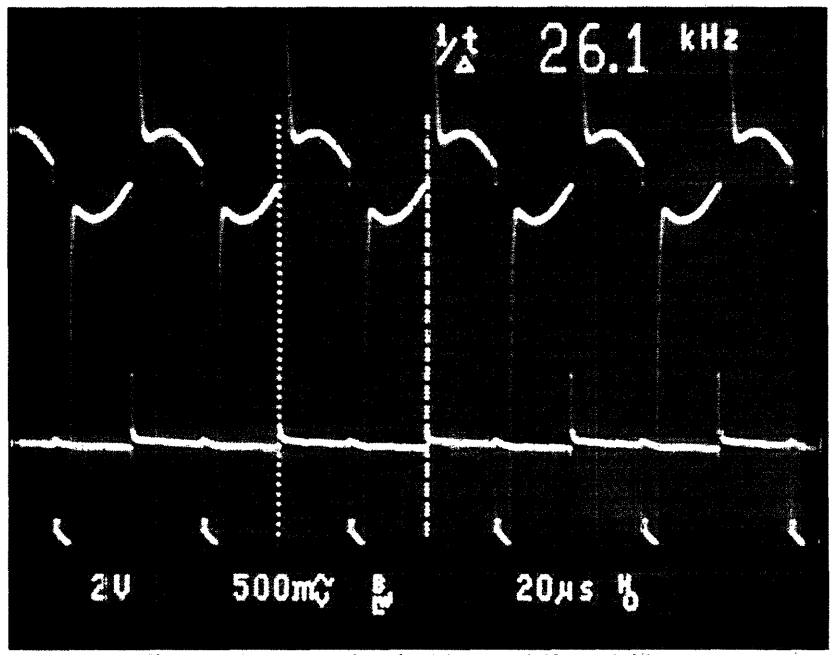

Figure 5.11: Error signal with zero differential input

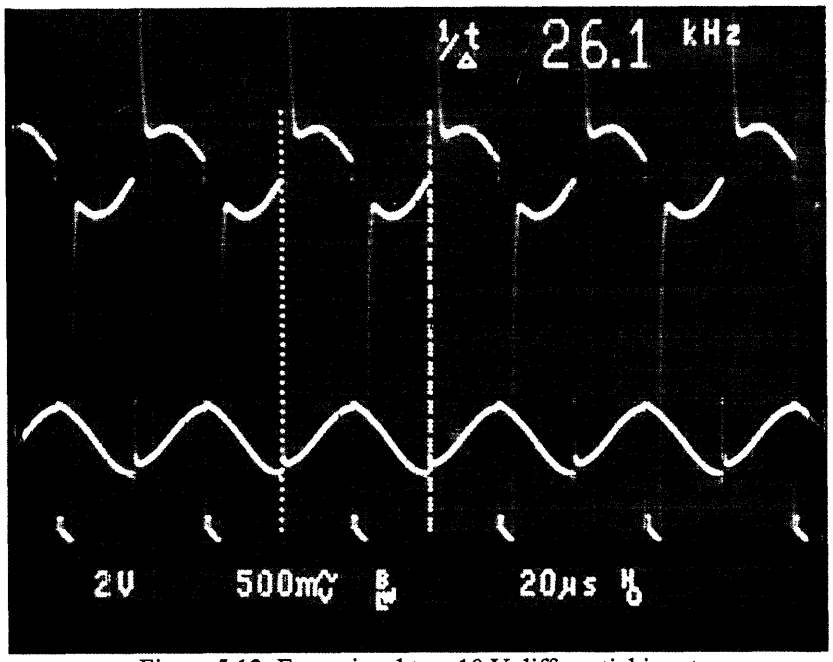

Figure 5.12: Error signal to a 10 V differential input

With the modulation capacitance accurately predicted, the first order sense loop was closed with a feedback ratio, $f$, of one. The corresponding loop transmission is:

$$L(s) = \left( \frac{2C_{sense}}{C_p + 4C_{sense}} \right) \left( A_{v,preamp} \right) \left( \frac{2C_s f_{CLK}}{sC_f} \right) f .$$

The measured risetime of this configuration is 3ms, corrsponding to a bandwidth of 120 Hz. This closely agrees with simulated prediction of 127Hz.

There was significant residual clock noise at the output of the first order system so an additional pole added to make the loop second order yielding a loop transmission of:

$$L(s) = \left( \frac{2C_{sense}}{C_p + 4C_{sense}} \right) \left( A_{v,preamp} \right) \left( \frac{2C_s f_{CLK}}{sC_f} \right) f \frac{1}{RCs + 1} .$$

The extra pole was placed at the desired crossover frequency to give the second order response shown in Figure 5.13. The closed loop gain is one, and the target bandwidth was 50 Hz. The measured risetime of 4 ms confirms this prediction. The overshoot of 25 %

corresponds to a phase margin of 45°, which is consistent with a second order system with its highest pole placed at the crossover frequency.

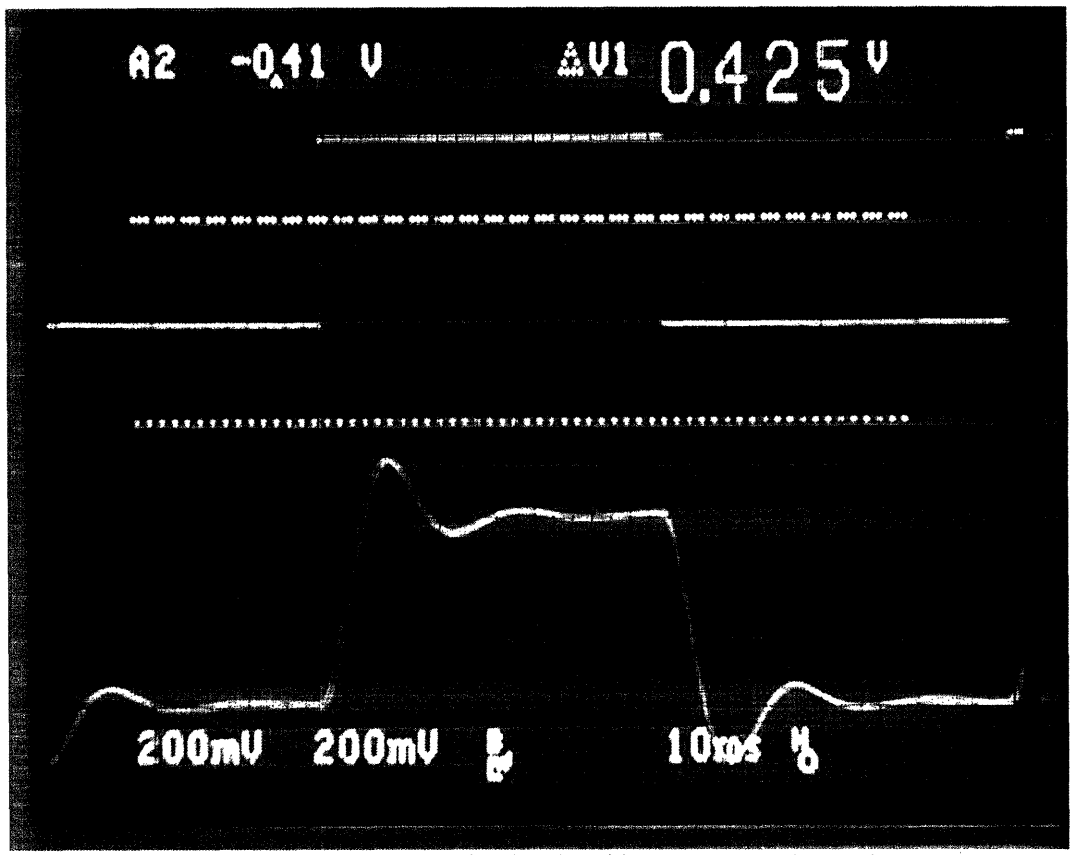

Figure 5.13: Second order closed loop response of sense loop

With the differential mode operation confirmed, the common-mode performance was measured. The common-mode performance of this design will be dictated by the etch variations in the mechanical structure. Since the MEMS transducer was fabricated using a new process, etch variation data was not readily available. The response to a 4 V common-mode step input is shown in Figure 5.14. The amplitude is less than 20 mV, which corresponds to a common-mode rejection ratio of roughly 50 dB. To improve the

CMRR of the amplifier, trimming techniques will have to be investigated, including a built-in offset.

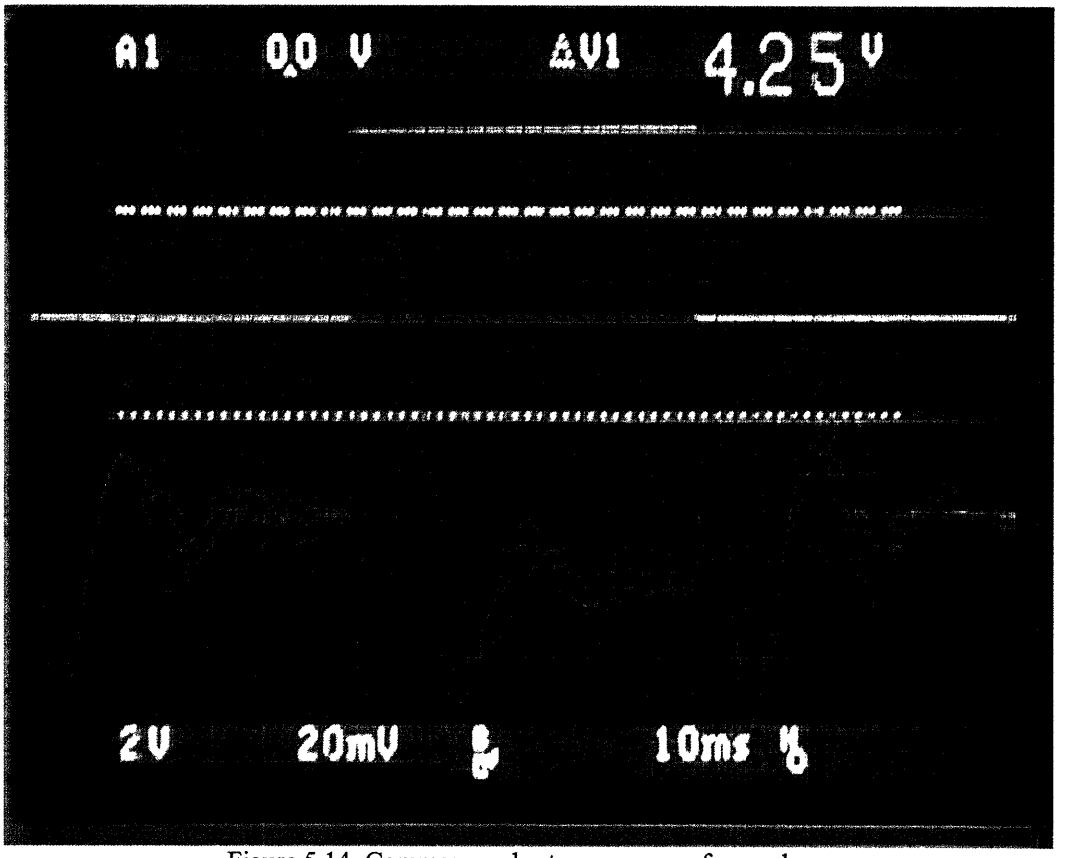


Figure 5.14: Common mode step response of sense loop

The noise was measured at the output with a RF millivoltmeter. The measured value of 575 $\mu V_{rms}$ (65 $\mu V/\sqrt{Hz}$) is comparable to the prediction of 486 $\mu V_{rms}$ (55 $\mu V/\sqrt{Hz}$) and within the tolerance of the noise calculations.

## 5.5 ADDITIONAL MEASUREMENTS

Additional measurements were taken to further characterize the amplifier's performance. Leakage currents were measured on the beam's isolation trenches and on a few test

structures. These measurements were made over multiple wafers to obtain a distribution of the leakage. The amplifier's differential operation was confirmed at a moderately high voltage (50 V). The last measurement taken was the CMRR as a function of common-mode voltage.

### 5.5.1 Leakage Currents

The first measurements were made on the cross-quad test structure shown in Figure 5.15. This structure used trenches to create four electrically isolated, but mechanically coupled regions. This structure has air gaps that are representative of the cross-quad interconnect that was used on the actual mechanical sensor. The results shown in Figure 5.16 show that there is roughly 200 pA of leakage current between the cross-quad isolated regions of silicon.

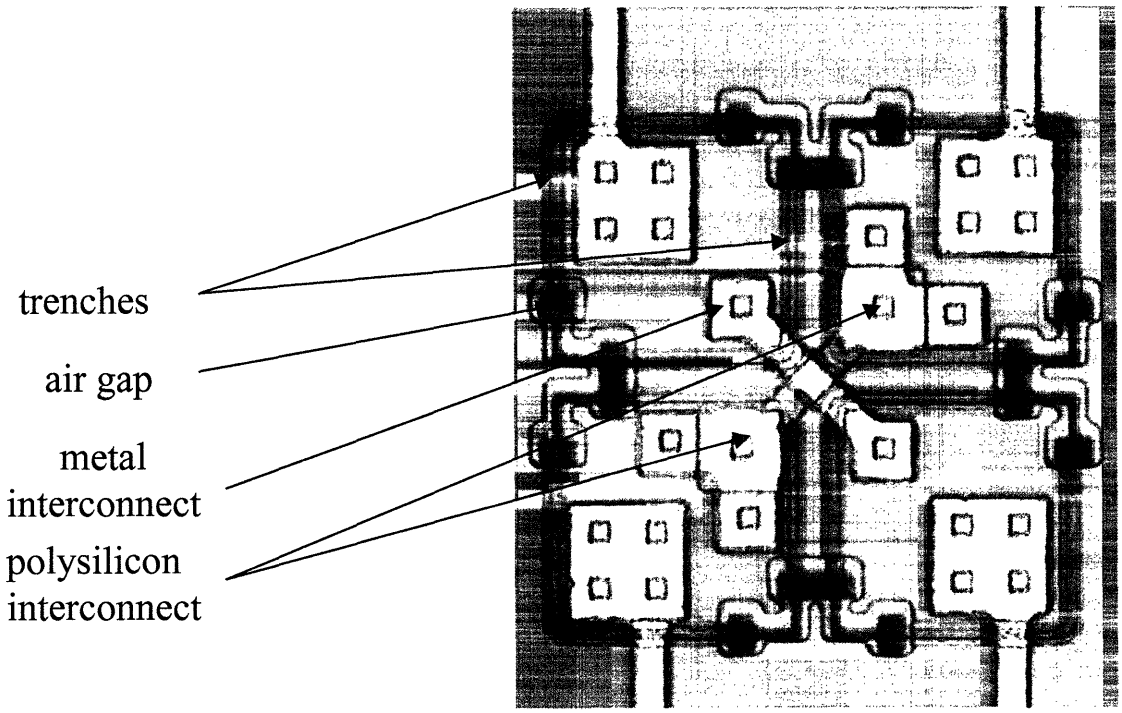


Figure 5.15: Cross-quad test structure

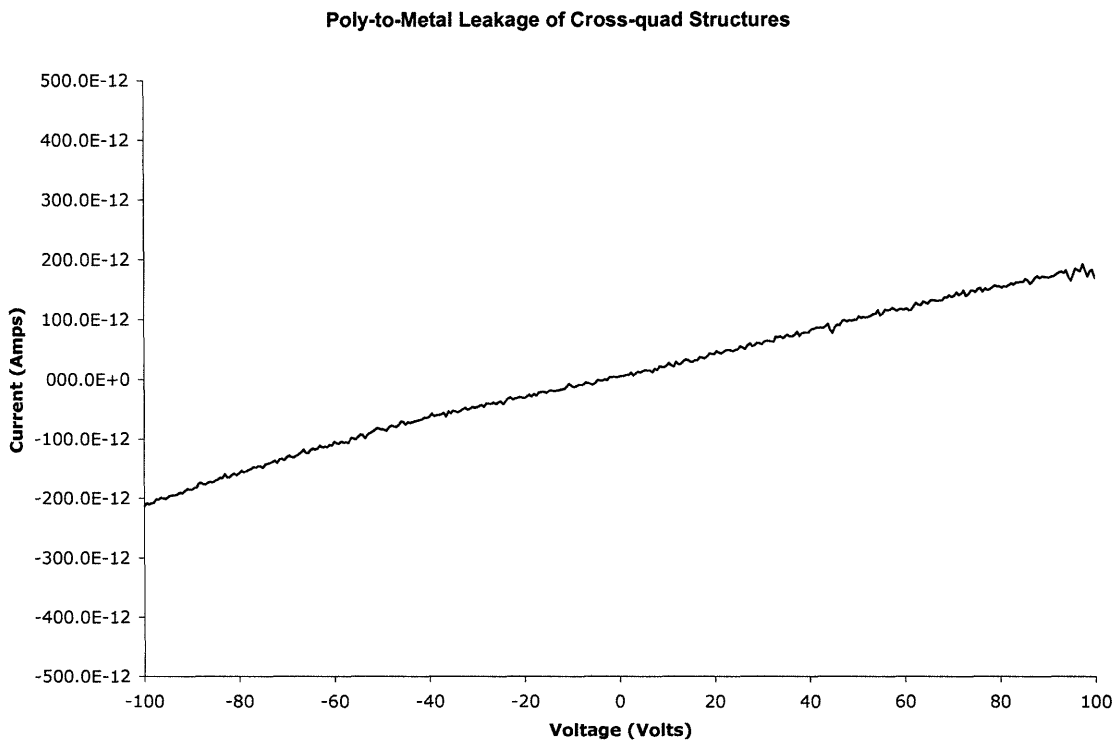


Figure 5.16: Leakage current of cross-quad test structure

The leakage of the trenches was measured next. Significant research being done on the isolation properties of silicon nitride films used as insulators [60-64]. The isolation properties of nitride films depend on temperature, the applied electric field and the stress applied to the film [61,63]. In this experiment, the leakage performance of the trenches was measured before and after the release process to determine if some of the processing steps damage the nitride lining of the isolation trenches. As seen in Figures 5.17 and 5.18, the leakage current does increase after releasing the MEMS structure from the substrate. Although not explored in this design, alternative release steps should be investigated so that the trenches' leakage performance is not compromised.

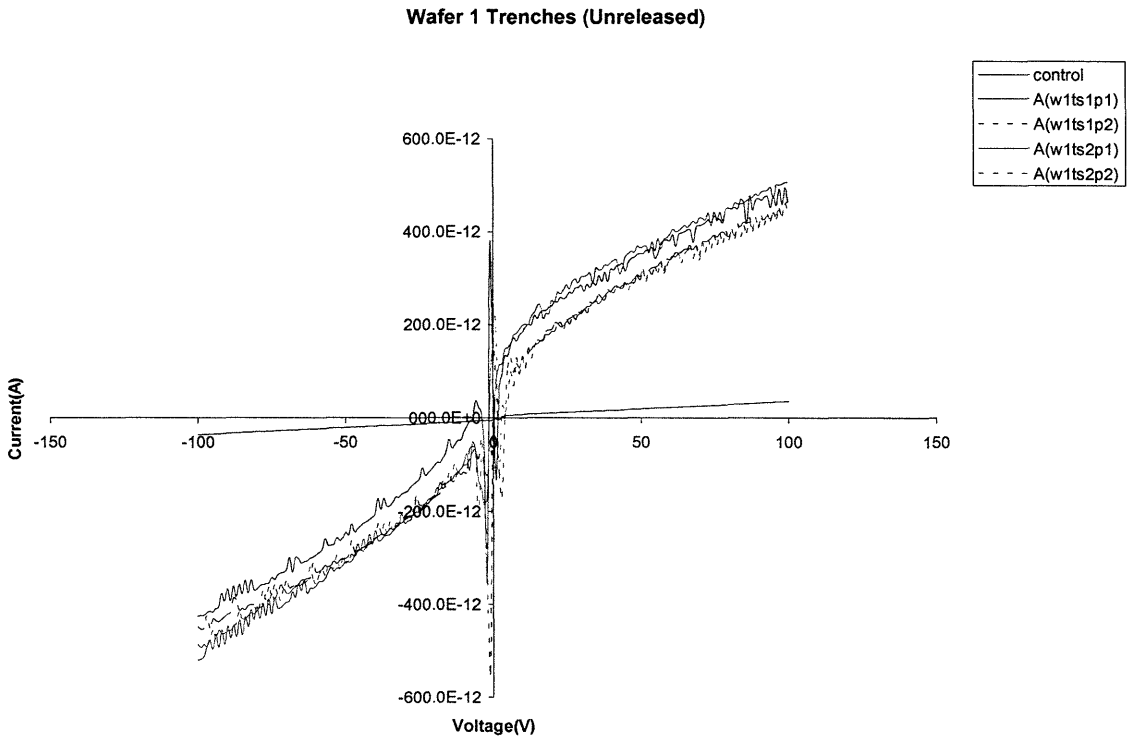


Figure 5.17: Leakage of unreleased trench test structures

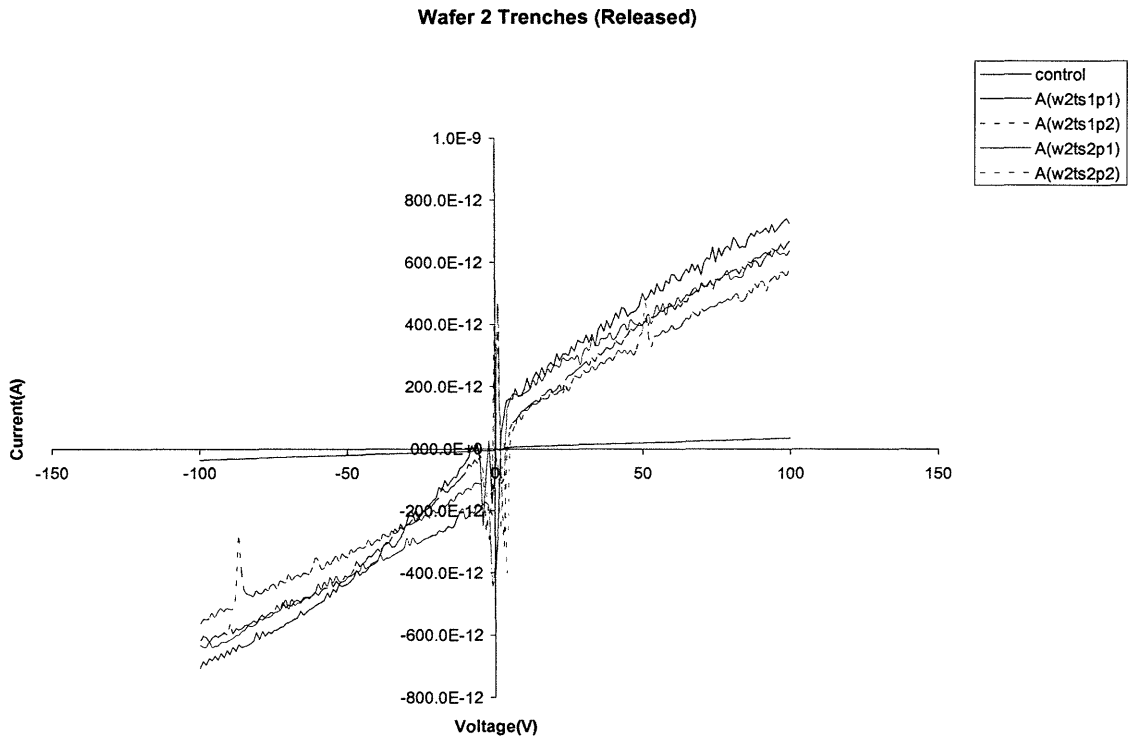


Figure 5.18: Released test structure leakage currents

## 5.5.2 DIFFERENTIAL OPERATION AT 50 $V_{CM}$

The linearity of the difference amplifier was confirmed with a common mode voltage of a 50 V applied to the inputs. The results from three samples indicate that the common mode component was rejected and the differential input voltage was amplified with a uniform gain as shown in Figure 5.19. This is not a surprise since the resonant frequency did not shift significantly when it was plotted against the common mode voltage in Figure 4.17.

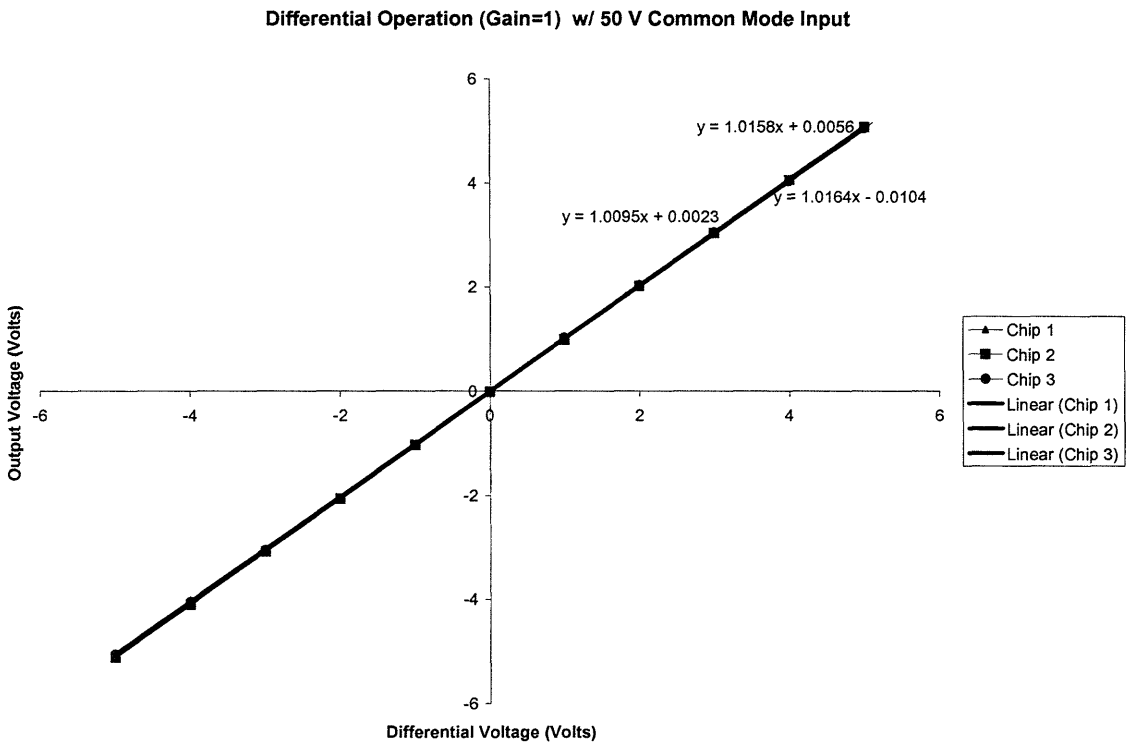


Figure 5.19: Differential mode operation with 50 $V_{CM}$ input

## 5.5.3 CMRR VS COMMON MODE VOLTAGE

The common-mode rejection ratio (CMRR) was measured over a common-mode voltage range of +/- 100 Volts. Each data point of this measurement was taken on a spectrum analyzer by applying the common mode voltage, noting the velocity sense signal's frequency, and computing the change in its frequency when the common mode voltage was returned to zero. As shown in Figure 5.20, most chips had CMRR's bounded between 50-60 dB, and they did not vary by more than 10 dB over the entire common-mode voltage range. Some of the measured CMRRs were greater than the expected 50 dB but this simply indicates that there are a few sensors with a greater degree of etch matching.

Also indicated by this plot is the need for developing a trim for the amplifier so that is CMRR can be raised to the 80-100 dB range.

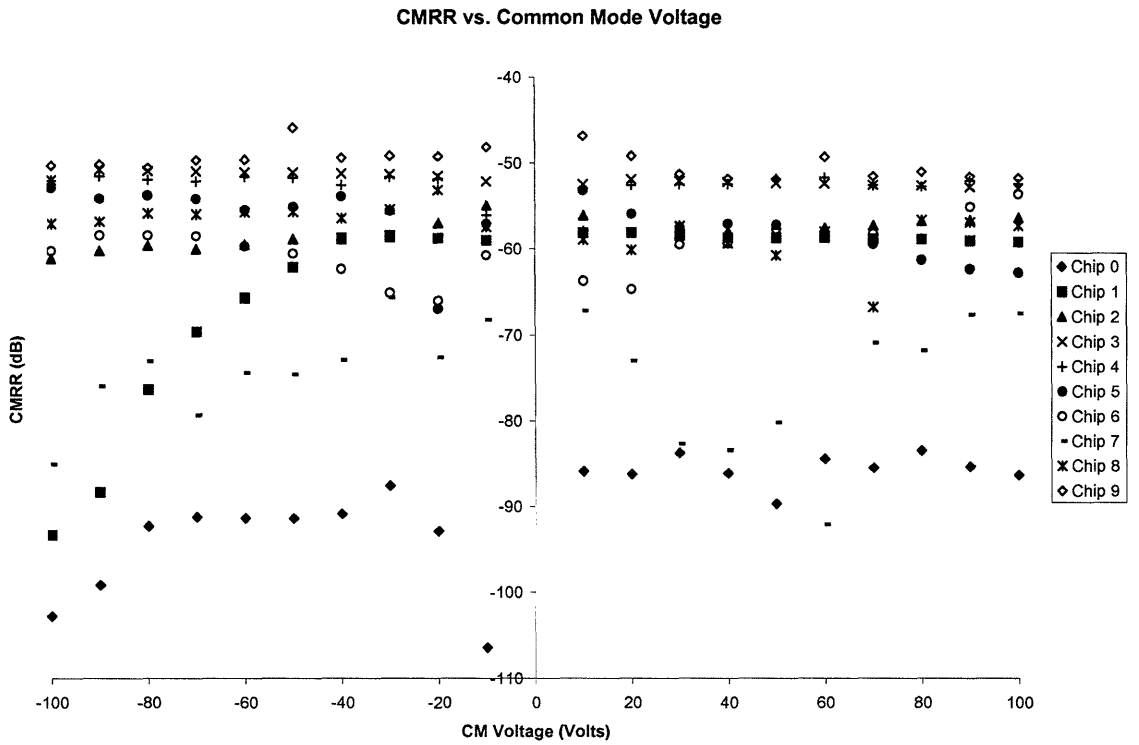


Figure 5.20: CMRR vs. Common mode voltage

## 5.6 SUMMARY

In this chapter, the operation and design tradeoffs associated with the sense loop were discussed. Its closed-loop operation was predicted and confirmed with laboratory measurements of the frequency response and noise performance. Proper operation of the loop was further confirmed while high common-mode voltages were applied and the robustness of the galvanic isolation was demonstrated via measurements of leakage currents, which arise predominantly from the trenches.

# 6 FUTURE WORK

As presented in the previous chapters, the performance of this electrometer was limited because all of the required circuitry was external to the IC. More specifically, the noise performance and the input referred offset can be drastically reduced by integrating most or all of the sense electronics. In this chapter, the next design steps will be presented. The first step is to redesign the beam so that it uses a less expensive manufacturing process. The second step will integrate as few transistors as necessary, namely the reset switches and the transistors that make up the differential input stage of the pre-amplifier. The rest of the circuitry will be external. The next step is full integration, in which *all* required circuitry will be on the same chip as the mechanical transducer. In the last section, theoretical limits of the noise and offset performance of this topology will be discussed.

## 6.1 NEW BEAM DESIGN

The previous transducer used electrical contacts on the mechanical structure itself to implement a cross-quad layout. This layout technique was chosen to minimize the effects of linear process gradients. It is commonly used when precise matching of transistors is required. Although cross-quading improves the matching of two structures, it complicates the SOI-MEMS release process. In its current implementation, one is forced to perform a backside release rather than the traditional frontside release to free the mechanical structure from the substrate.

### 6.1.1 FRONT-SIDE RELEASE PROCESS

The front-side release process involves exposing the patterned SOI-MEMS structure to hydrofluoric acid (HF), from the top (or front). The HF reacts with the buried oxide that holds the MEMS structure to the handle wafer to form $H_2O$. This water is then evaporated and the MEMS structure is released from the substrate, with the handle wafer intact.

### 6.1.2 BACKSIDE RELEASE PROCESS

If the current transducer design used the above mentioned frontside release process, the HF would attack the polysilicon and metal used to form the cross-quad connection. To avoid this, the backside release grinds away the handle wafer from the bottom (or backside). Then, from the backside, the buried oxide is exposed to HF and the resulting water is evaporated. The extra processing steps here make this unsuitable for manufacturing because of their expense.

### 6.1.3 NEW TRANSDUCER DESIGN

The feature that makes the current transducer difficult to manufacture is the cross-quad connection in the center of the moving mass. Therefore, the new design shown in Figure 6.1 has no cross-quad connections. It has roughly the same footprint as its predecessor but the pin-out will be slightly different.

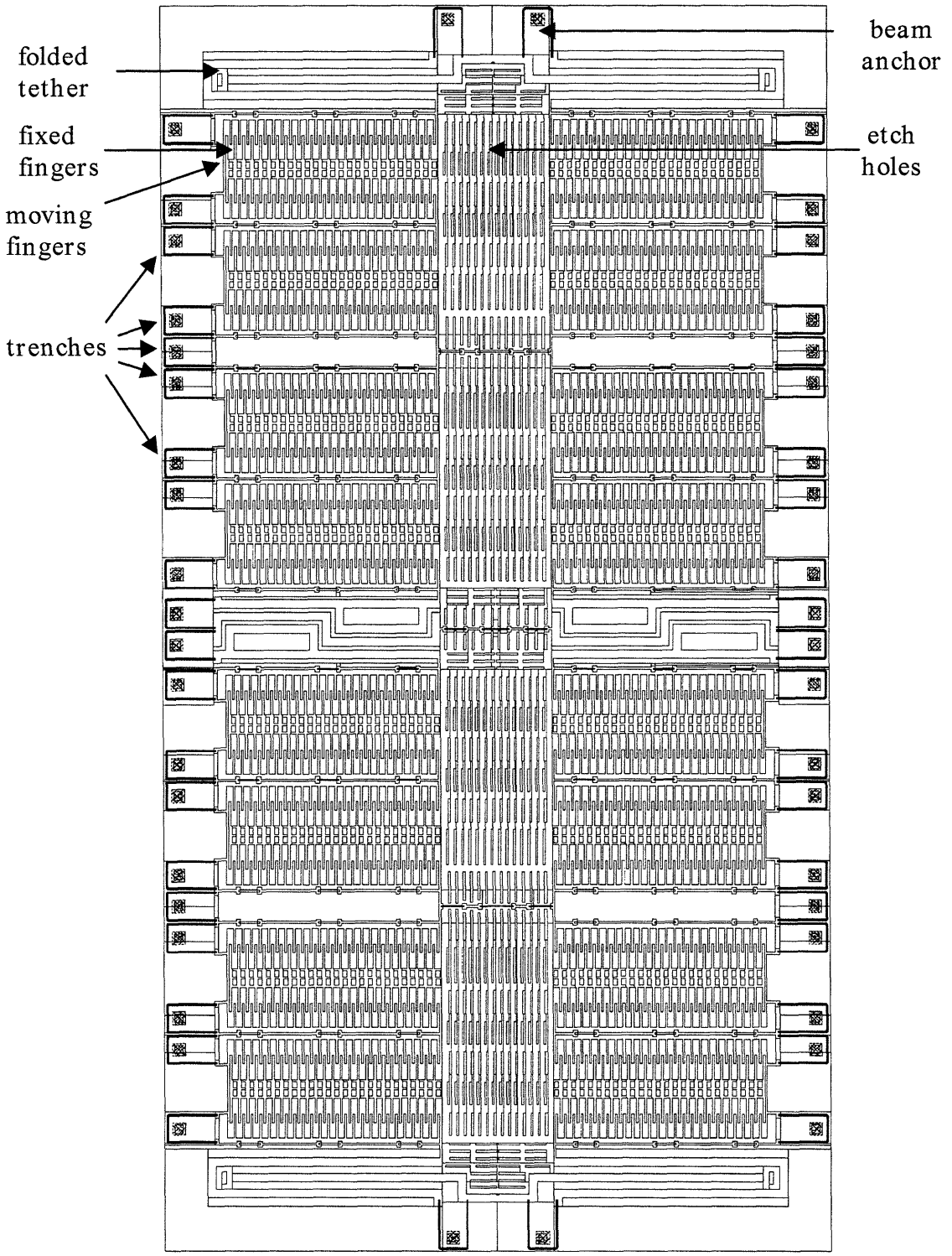


Figure 6.1: New mechanical transducer layout

### 6.1.4 NEW TRENCH DESIGN

The trenches determine the leakage currents, common-mode voltage range and the parasitic capacitance at the beam's output node. When a dielectric that outperforms silicon nitride is found, then a better sensor can be designed with a minimal change in sense loop and drive loop circuitry.

## 6.2 DIFFERENTIAL PAIR INTEGRATION

### 6.2.1 BEAM WITH DIFF PAIR

The previous design had poor offset and noise performance mostly because the critical sense nodes of the transducer were connected to bond pads. The bond pads in addition to the input capacitance of the following pre-amplifier greatly increase the parasitic capacitance at the beam's critical node. By integrating the input transistors of the pre-amplifier with the transducer, the beam's critical nodes are subject to the gate capacitance of the transistors, which is an order of magnitude less than before.

In addition, the beam-biasing scheme will change from a large resistor to a switched reset. The switch drive will be derived from the clock signal of the demodulating integrator. The proposed chip layout using Analog Devices' BIMOS2E (2μm) process is shown in Figure 6.2. From this plot, it is evident that not all of the circuitry will fit on the same chip.

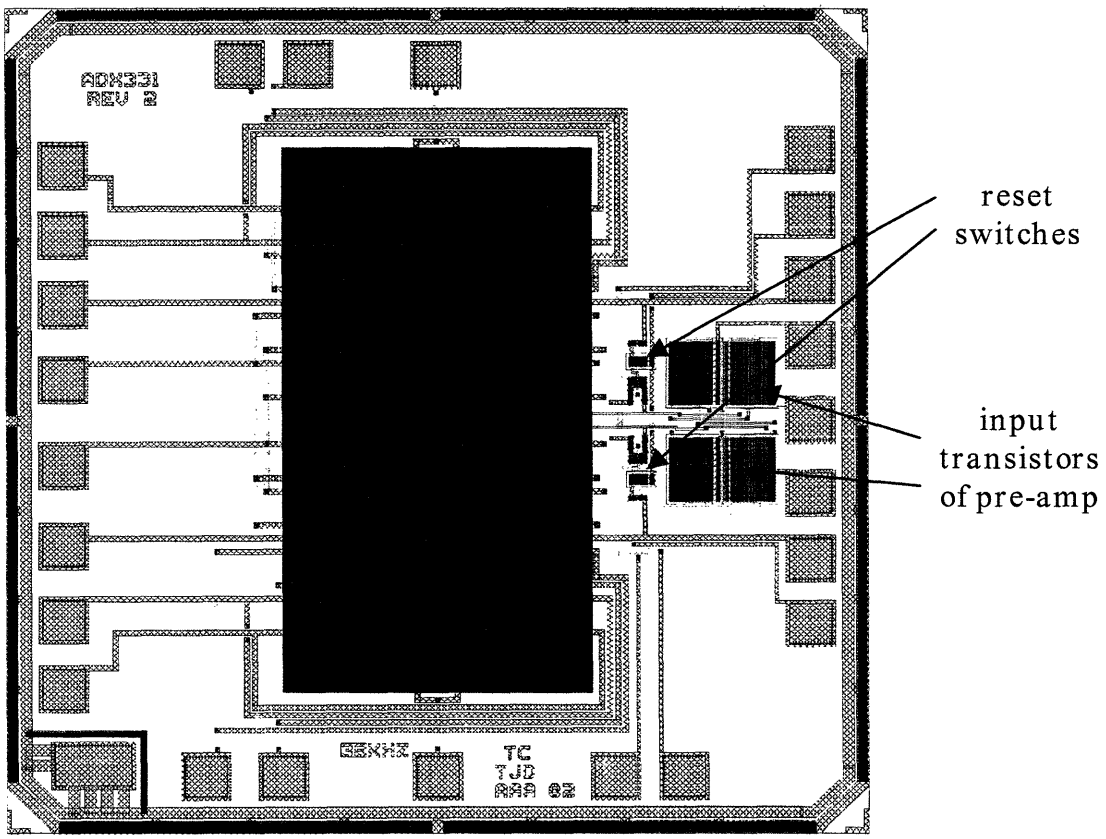

Figure 6.2: Chip layout showing integrated switches and transistors

### 6.2.2 External Circuitry (BIMOS2E)

The required external circuitry is similar to the previous design. In the sense loop, the pre-amplifier needs to be completed with discrete components. A possible design is shown in Figure 6.3. The rest of the loop can be closed with similar components from the previous design, similar to Figure 5.2. The drive loop circuitry can be made up of the same components as the current design.

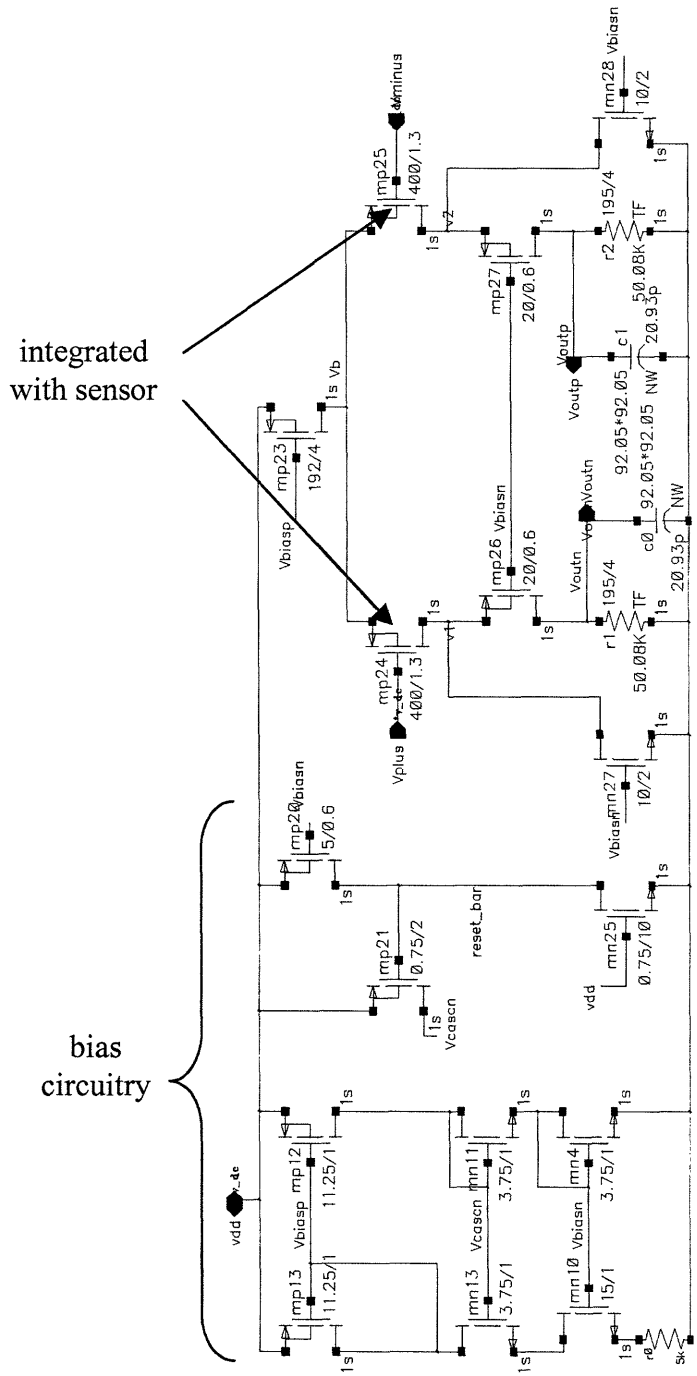


Figure 6.3: Proposed pre-amplifier design

### 6.2.3 PREDICTED PERFORMANCE

Careful inspection of the chip layout in Figure 6.2 shows that the input and output terminals of the beam are guarded by ground traces. This minimizes coupling of force

spikes into the inputs thereby reducing the offset of the amplifier as compared to the design used in this thesis. The optimal design is a fully integrated structure, which is presented in the next section.

By not exposing the transducer's critical nodes, the beam attenuation factor decreases. This attenuation becomes gain when referring the kT/C noise of the reset switch and pre-amplifier's input noise to the input terminals of the transducer. Noise analysis shows that the kT/C noise of the reset switch is actually rejected by the CDS integrator therefore the main noise contribution will be from the input differential pair of transistors, whose noise performance can be carefully optimized.

The proposed pre-amplifier's AC performance is shown in Figure 6.4. The noise corner frequency is approximately 3 kHz and the broadband noise at the resonant frequency of 26 kHz is 7.4 nV/√Hz. With the input differential pair integrated with the sensor, the shunt capacitance at the beam's sense nodes drops from 10 pF to 2 pF. The noise density of this system will be determined by the equivalent noise at the beam's sense node, the attenuation factor when referring the noise to the input and the aliasing factor due to using CDS for offset reduction.

The noise at the input is √2*7.4 nV/√Hz or 10 nV/√Hz, which is a little higher than the 8 nV/√Hz that was present in the prototype. The factor of √2 accounts for the fact that the noise at each of the pre-amplifier's inputs is uncorrelated. Since the parasitic capacitance drops by a factor of 5, the amplification due to the capacitance divider

formed between the sense capacitor and the beam's parasitic capacitance will drop from 1100 in this prototype to 220. The aliasing factor will not change from 6 as it was in this thesis. The predicted RTI noise density will be

$$\sqrt{2}\left(7.4\frac{nV}{\sqrt{Hz}}\right)*\left(\frac{2pF}{9fF}\right)*6,$$

or 14 μV/√Hz, which is almost a factor of four below the 55 μV/√Hz achieved in the prototype.

The offset performance will be limited by the offset of the integrator, the pre-amplifier gain and the inverse of the attenuation at the beam's sense node. If we have negligible clock feedthrough and an integrator with 100 μV of offset voltage, the RTI offset is:

$$100\mu V\left(\frac{1}{65}\right)\left(\frac{2pF}{9fF}\right)\approx 340\mu V.$$

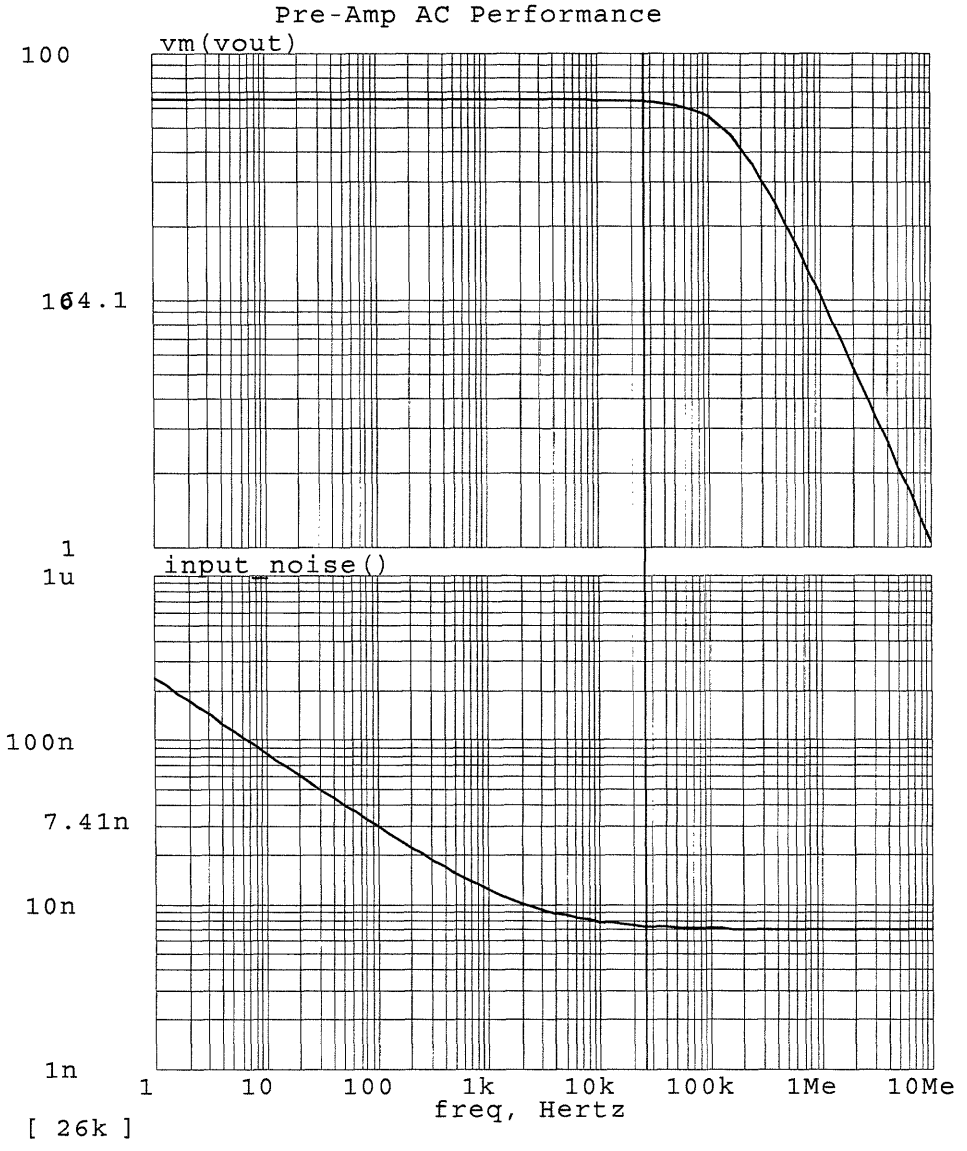


Figure 6.4: Noise performance of pre-amplifier

## 6.3 FULL INTEGRATION

### 6.3.1 NEW PROCESS

As was evident with the previous chip layout, a better CMOS process must be sought in order to integrate all of the electronics with the mechanical transducer. Using Analog Devices' EP118 (0.6μm) process, the drive and sense loops' circuitry was designed.

### 6.3.2 DRIVE LOOP CIRCUITRY(EP118)

The transresistance amplifier is used to detect the beam velocity in the form of a current and it requires a fully differential operation amplifier. This schematic is shown in Figure 6.5. The topology chosen was a folded cascode with high swing current mirrors. A fully differential op-amp requires common-mode feedback so this circuitry was included in this design as well.

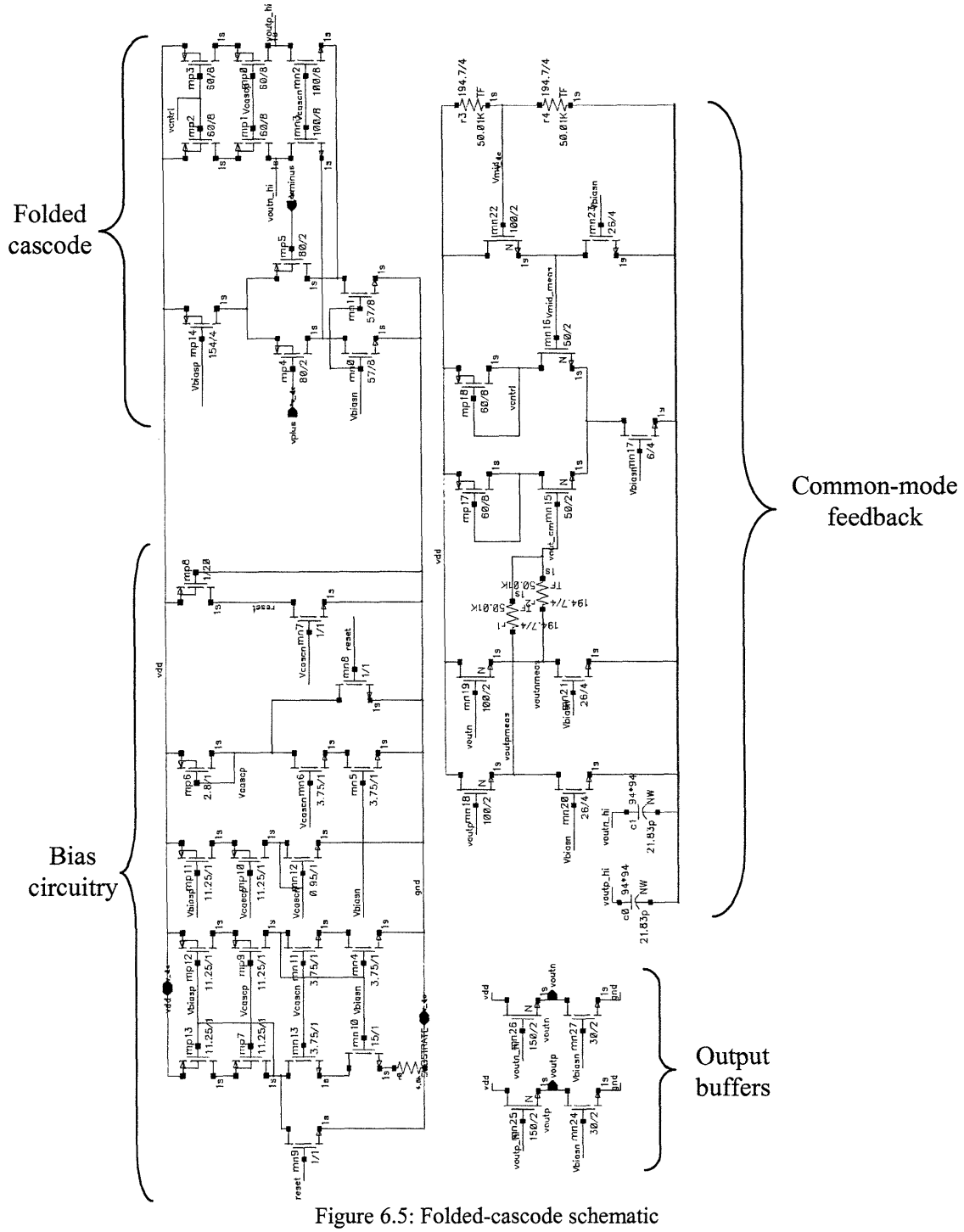


Figure 6.5: Folded-cascode schematic

The comparator was made up of a wide-swing high bandwidth op-amp followed with inverters to square up the output as shown in Figure 6.6. This output is then fed to

inverter drivers that have high-voltage transistors. This is required because the drive voltage required is much higher than the maximum drain-to-source voltage that simple transistors can withstand.

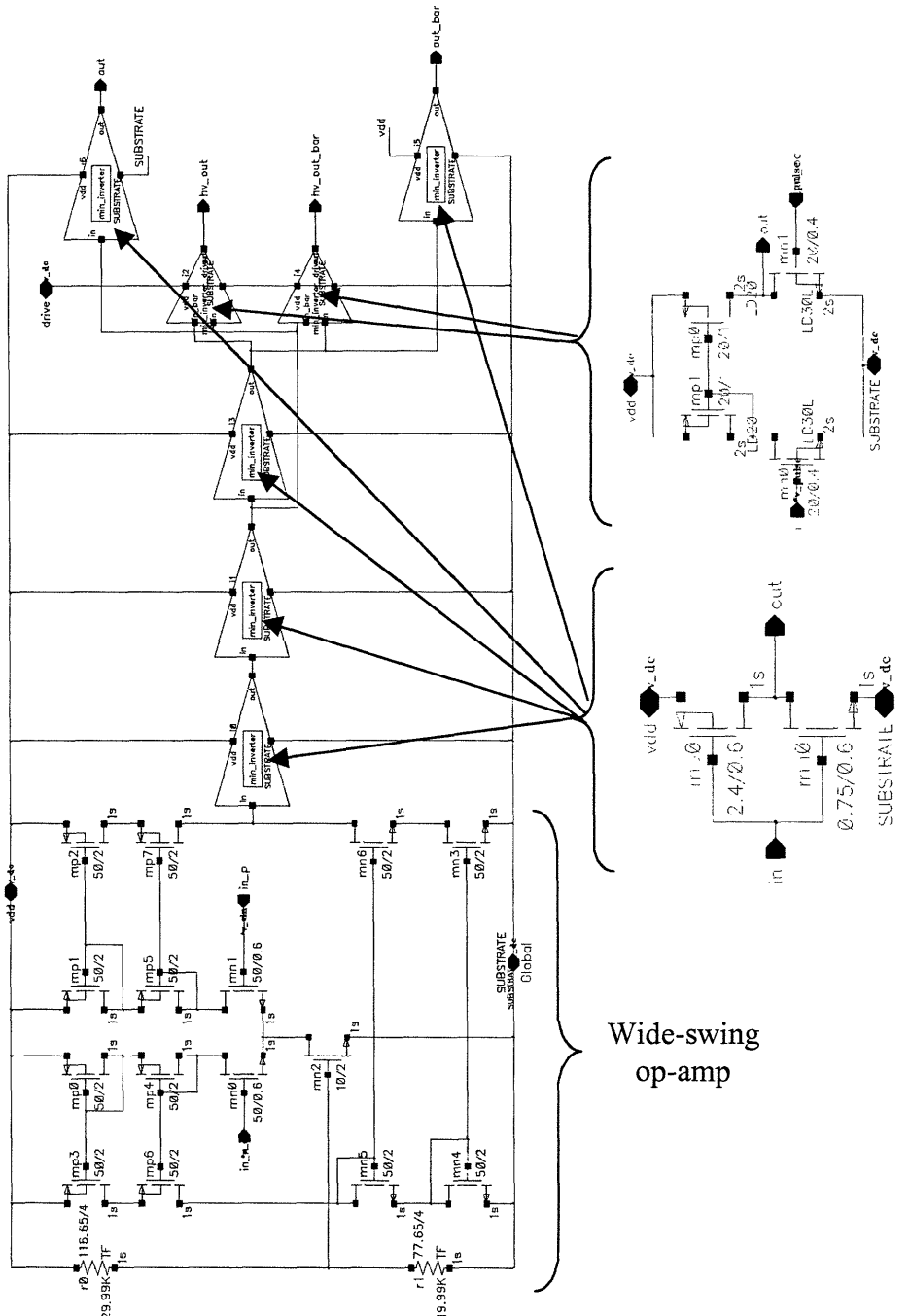


Figure 6.6: Comparator schematic and its subcircuits

The output of the comparator is then fed to a non-overlapping clock generator, shown in Figure 6.7. This two-phase clocking scheme is required by the demodulating integrator in the sense loop. This circuitry also generates the reset pulse for the beam's reset switches.

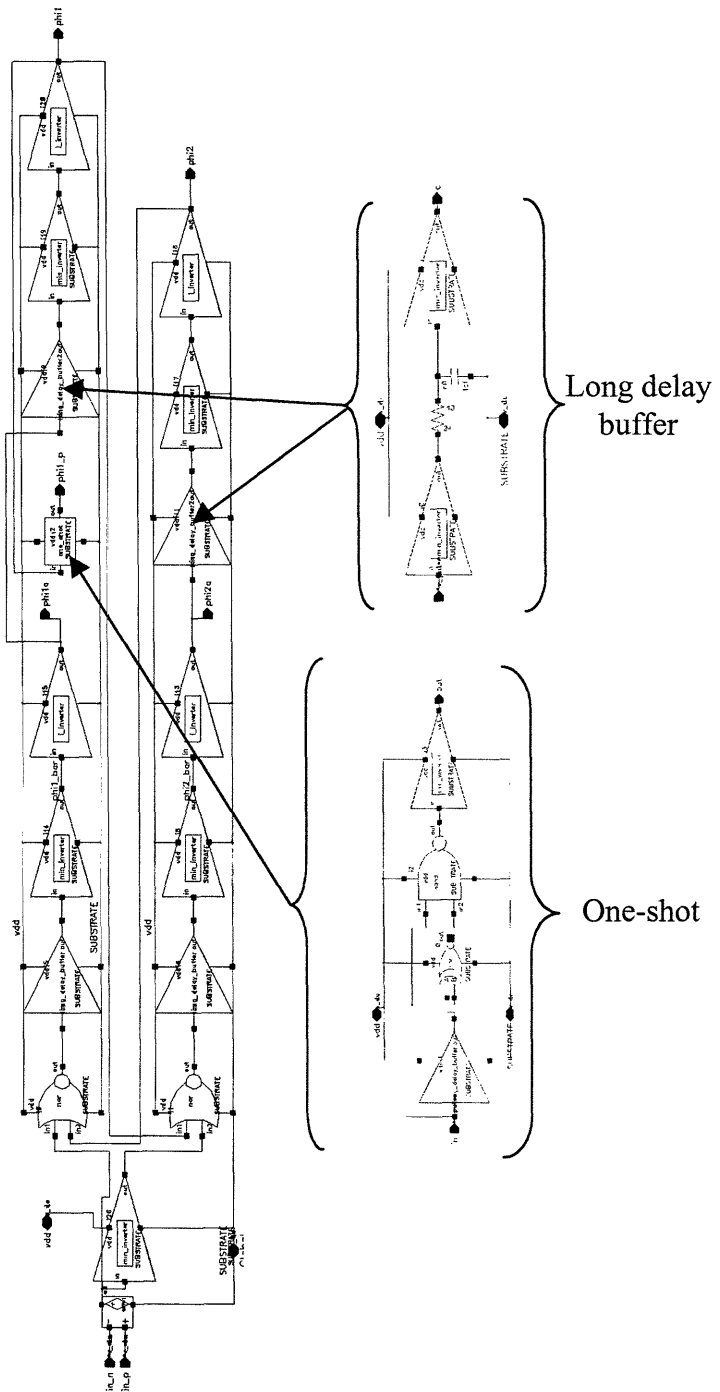


Figure 6.7: Non-overlapping clock generator and its sub-circuits.

### 6.3.3 SENSE LOOP CIRCUITRY(EP118)

The proposed reset switches are CMOS transmission gates with dummy transistors used to minimize charge injection. They were configured as shown in Figure 6.8, with a minimum sized inverter used to generate the inverted reset clock pulse. To minimize the size of the switch, the dummy switches were made to be minimum size, so that the actual switch transistor can be only twice minimum geometry.

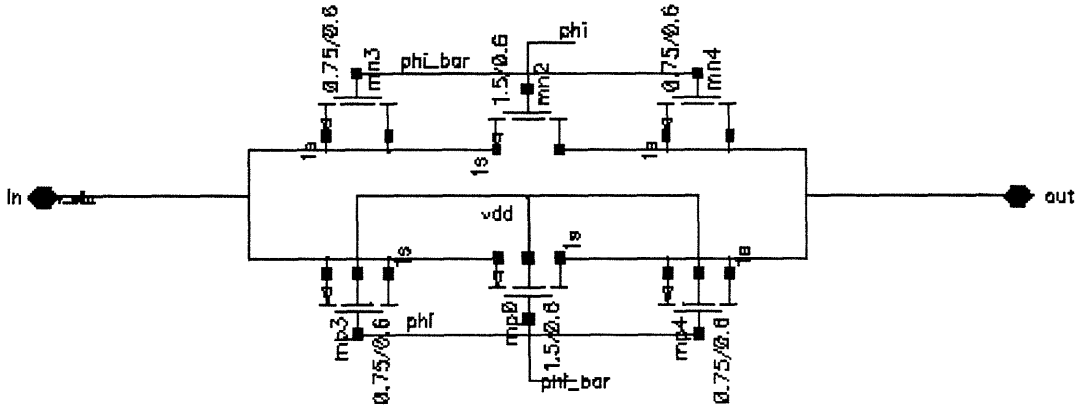


Figure 6.8: CMOS analog switch

The pre-amplifier is a fully differential, open loop, resistively loaded fixed gain amplifier, as shown in Figure 6.9. The input differential pair is cascoded to minimize the effects of Miller multiplication of the gate to drain capacitance, Cgd. The input transistors are sized to minimize their 1/f noise corner and thermal noise floor. To lower the thermal noise for a fixed size transistor, its transconductance must be increased by increasing its bias current. To maintain a modest gain while achieving reasonable output swing, some of the current flowing through the input transistor must be shunted away from the load via two long transistors.

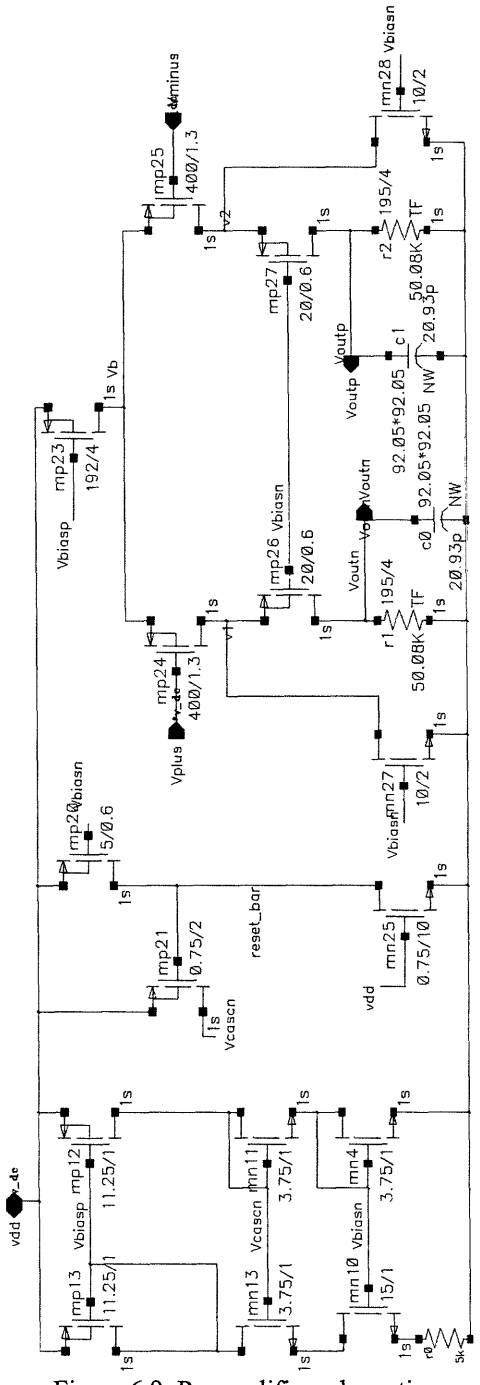


Figure 6.9: Preamplifier schematic

The demodulating integrator is the next stage. This stage required a fully differential operational amplifier, so the folded cascode of the drive loop was used, as

shown in Figure 6.5. Since this is a switched capacitor amplifier, it required switches. The switches are identical to the reset switches show in Figure 6.8.

The last circuit element needed was a differential to single-ended converter. This too had to be a switched capacitor circuit requiring switches and a single-ended operational amplifier. The fully differential op-amp of Figure 6.5 was converted into a single-ended op-amp shown in Figure 6.10.

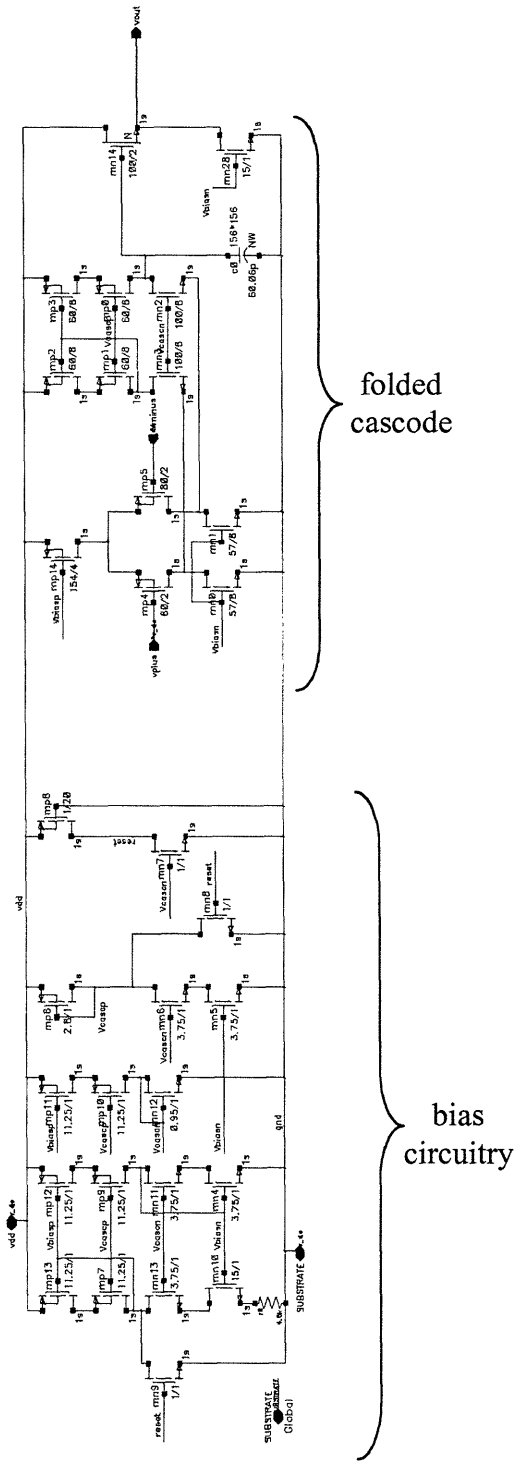


Figure 6.10: Single-ended folded cascode schematic

### 6.3.4 PREDICTED NOISE AND VOLTAGE OFFSET PERFORMANCE

Since the drive circuitry is integrated and includes special high-voltage transistors, the displacement amplitude will increase from 2 μm to 5 μm, corresponding to an increase in modulation capacitance from 9 fF to 23 fF. This design will have similar parasitic shunt capacitance and pre-amplifier noise performance as the design that only integrated the input differential pair of the pre-amplifier. In addition, aliasing factor will remain the same. Since the only change is the factor of 2.5 increase in sense capacitance, the noise will decrease by the same factor. The predicted RTI noise density for this design is 5.6 μV/√Hz.

The RTI voltage offset will decrease as well. Assuming that the integrator's offset voltage is 100 μV, then when referring this back to the overall input, we must multiply by 1/65*2pF/23fF to yield an offset of 135 μV. One must note that this result assumes negligible clock feedthrough.

## 6.4 DISPLACEMENT AMPLITUDE CONTROL

If the application requires precise displacement amplitude control, this can be achieved by adding a minor loop to the drive loop shown in Figure 4.3. This loop could be used to account for changes in the damping and process variations. The loop achieves its function by varying the drive voltage of the beam, which modifies the electrostatic force applied

to the beam and hence, the beam displacement. The resulting block diagram is shown below in Figure 6.11.

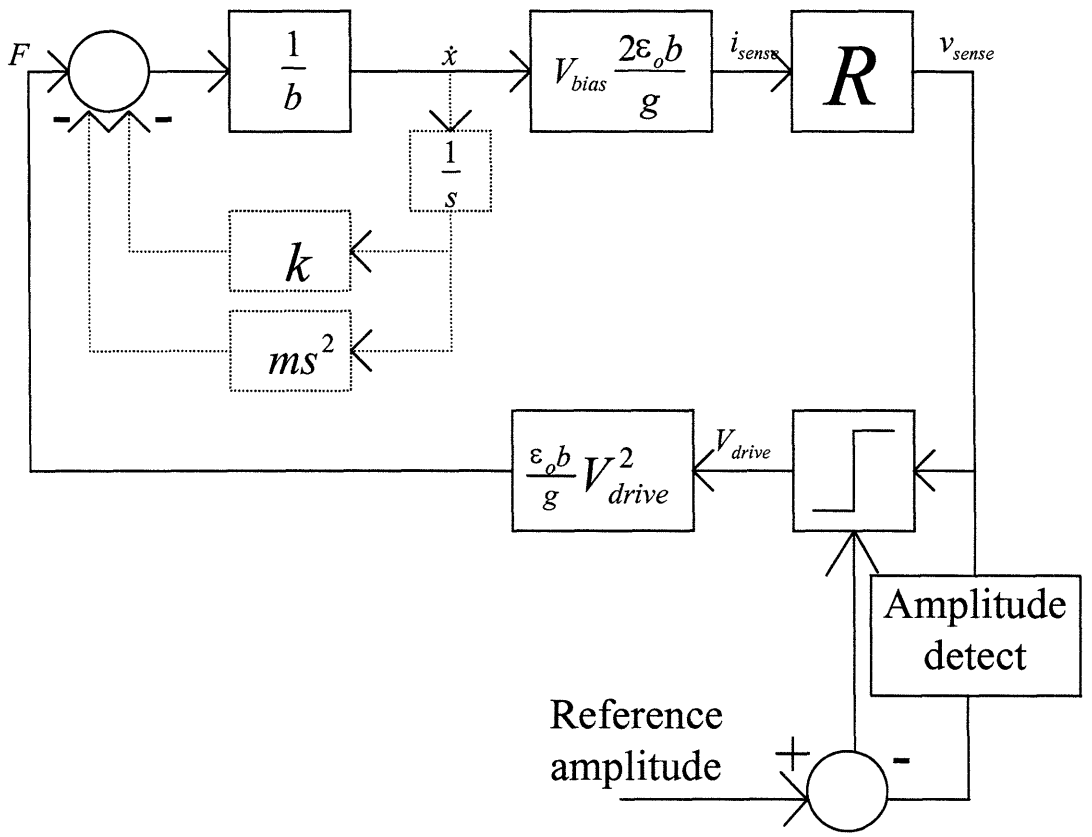


Figure 6.11: Drive loop with displacement amplitude control

## 6.5 NOISE AND OFFSET PERFORMANCE LIMITATIONS

In the previous sections, the noise and offset performance of new designs were discussed. The underlying assumptions were that the trenches were the same as was used in this thesis and that the offset reduction technique was CDS. It was shown that the noise performance depends on the ratio of sense capacitance to parasitic shunt capacitance at the beam node and the amount of aliasing due to sampling. In this section, we will predict the noise and offset performance of the MEMS differential amplifier assuming optimal sense and parasitic shunt capacitance and compare using CDS against CHS.

### 6.5.1 Optimal Sensor/Preamplifier Interface

The modulation capacitance of the current sensor is roughly 25 fF, assuming a 5 μm displacement amplitude. Since the modulation capacitance is directly proportional to number of fingers on the sense arms, we will assume an upper limit of 100 fF for the sense capacitance. This increase in sense capacitance will require increasing the area of the sense half of the mechanical structure. The dimensions of this new structure will be on the verge of violating the rigid body assumptions made when analyzing the beam motion.

Optimizing this interface implies making the sense, feedback and parasitic shunt capacitance equal. Making all of these capacitors equal to the optimal sense capacitance of 100 fF implies that the optimal attenuation at the sense node will be 1/4.

### 6.5.2 Optimal CDS Noise and Offset Performance

The sense loop of the MEMS differential amplifier that employs CDS is shown in Figure 6.12. The noise performance will be determined by the equivalent noise at the beam's sense nodes. This noise is determined by the pre-amplifier's input noise and the noise associated with the device used to bias the beam.

The bias device could be either a reset switch or large resistor implemented by a long FET. Diode biasing was rejected because of its nonlinear performance as described in section 5.3.2. In the prototype, a resistor of 10 MΩ was used. The thermal noise associated with it was heavily filtered by the large shunt parasitic capacitance at the beam's sense node. This resistance value is difficult to achieve on an IC, therefore, the beam will be biased with a reset switch. The kT/C noise associated with the reset switch will be rejected to first order by using the clocking scheme described in section 5.3.3.

If the noise at the beam's sense nodes is dominated by the pre-amplifier's input noise, we can represent this noise density as $e_n$. When referring the noise to the overall input, the noise at each of the beam's sense nodes are uncorrelated so the effective RTI noise from them will be multiplied by a factor of √2. The capacitance divider ratio is 1:4, again if all capacitors at the beam node are the same. The aliasing factor will be computed based on a noise bandwidth that is π/2*10 times greater than the modulation frequency. This factor is chosen based on minimizing the phase shift and maximizing sensitivity. The total noise is:

$$\left(\sqrt{2}e_n\right)(4)\left(\sqrt{\frac{\frac{\pi}{2}(10f_c)}{\frac{1}{2}f_c}}\right) \approx 32e_n\left(\frac{V}{\sqrt{Hz}}\right).$$

If the pre-amplifier has an $e_n$ of 10 nV/√Hz as shown in Figure 6.13, the RTI noise density will be 452 nV/√Hz. It is important to note that the noise corner frequency of the input transistors will go up as they are made smaller. Consequently, it may be necessary to increase the beam's resonant frequency so that it is past the 1/f noise corner frequency of the input transistors.

The offset of the overall amplifier will be determined by referring the integrator's offset back to the input terminals assuming negligible clock feedthrough. Assuming we have an integrator with 100 μV of offset and a pre-amplifier with a gain of 100, the RTI offset of the amplifier will be 100 μV/100*4 or 4 μV.

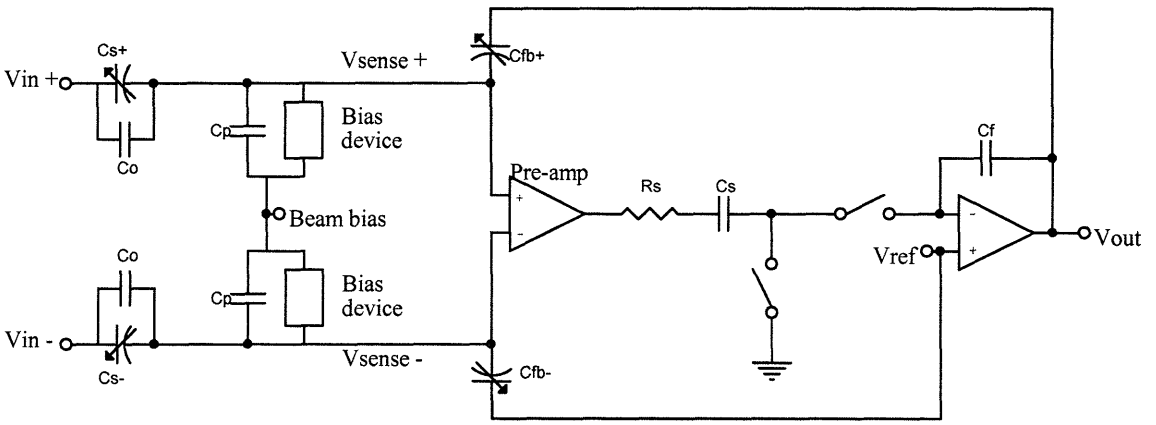


Figure 6.12: Sense loop of MEMS amplifier that uses CDS

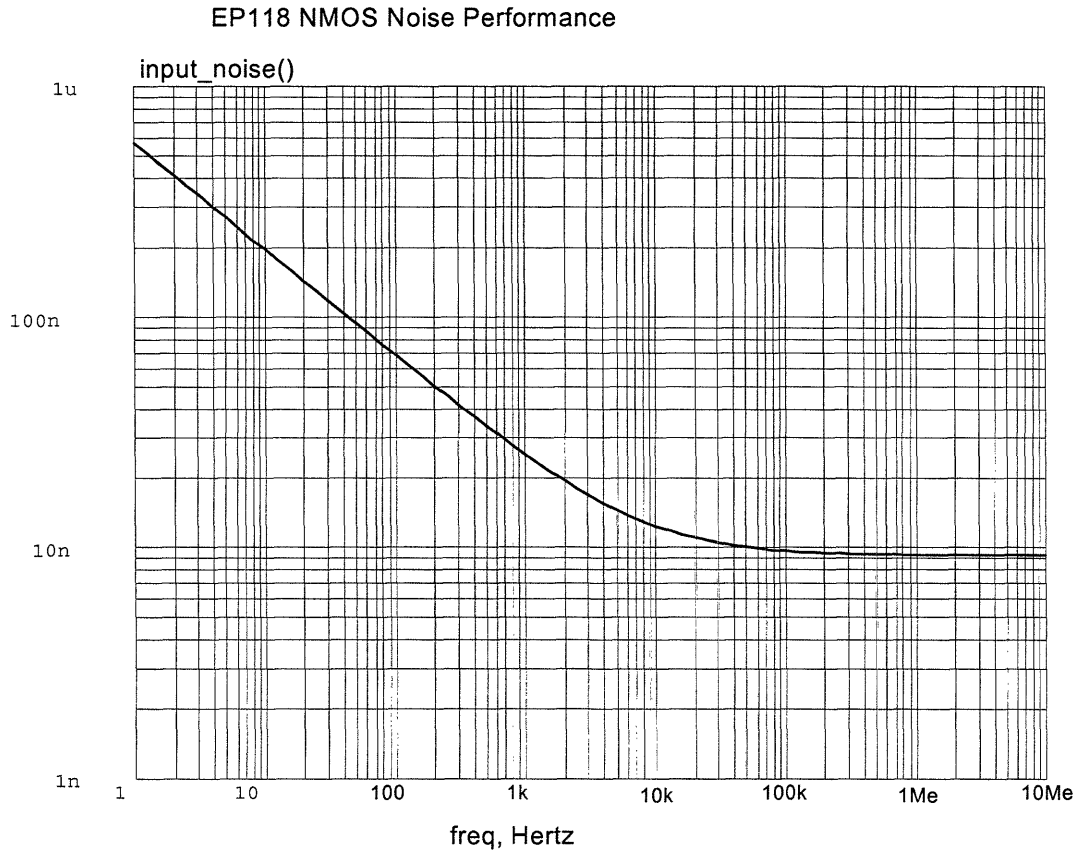

Figure 6.13: Input noise of optimized pre-amplifier

### 6.5.3 Optimal CHS Performance

The sense loop of the MEMS differential amplifier that employs CHS is shown in Figure 6.14. AC coupling is used to enhance the offset performance, as CHS does not provide a zero at the origin like CDS. As with the CDS case, the noise performance will be determined by the pre-amplifier's input noise and the noise associated with the device used to bias the beam.

The choice of bias device is between a large resistor and a switch. Using a switch to bias the beam will result in a kT/C noise density of 32 $\mu V/\sqrt{Hz}$ in a bandwidth of

$\pi/2$*100 Hz. Referring this noise density to the input yields a noise density of 128 $\mu V/\sqrt{Hz}$, which is worse than the current system.

Therefore, we must use a resistor to bias the beam. The minimum size for the bias resistor will be determined by the resonant frequency of the beam and the shunt parasitic capacitance at the beam's sense node. If the parasitic capacitance is 100 fF and we have the same resonant frequency of 26 kHz, the bias resistor must be larger than $\frac{1}{2\pi(26kHz)(100fF)} = 61M\Omega$. The noise density associated with this resistor is 1 $\mu V/\sqrt{Hz}$, which will be much larger than pre-amplifier's input noise. Referring this noise density back to the overall input, the RTI noise density will be 4 $\mu V/\sqrt{Hz}$, which is an order of magnitude worse than using CDS.

The offset performance will be dictated by clock feedthrough as described in [11,16]. The inherent offset is modulated out of band by the demodulator but the spikes from the clock feedthrough will demodulate to the origin to cause a *residual* offset [11, 14-16]. The residual offset performance can be optimized by using a bandpass filter whose center frequency is tuned to the modulation frequency. In this design, the bandpass filter is implemented by the *Rs-Cc* high pass filter and the 3-dB frequency of the amplifier. The actual amplitude of the residual offset is difficult to predict because it depends on parasitic paths. However, submicrovolt offset voltages have been achieved using a bandpass filter [11].

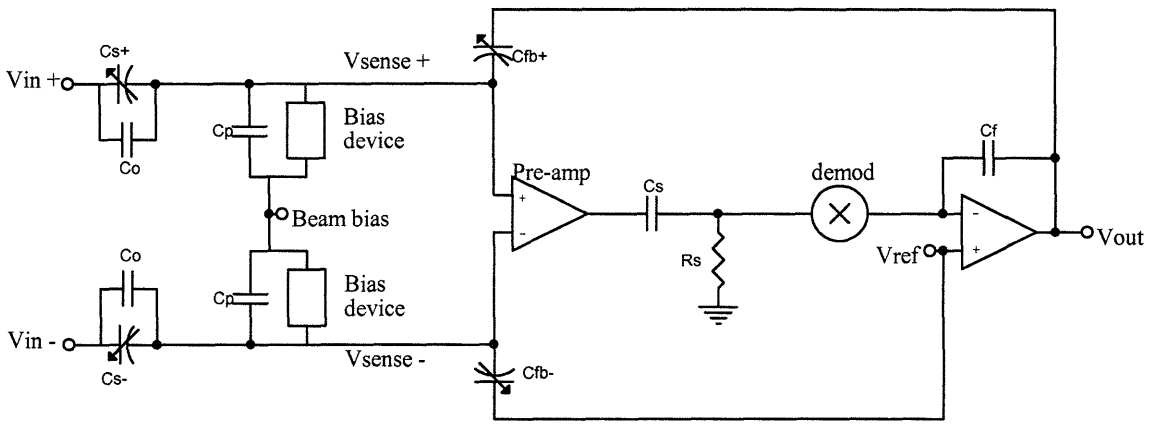


Figure 6.14: Sense loop of MEMS amplifier that uses CHS

### 6.5.4 Optimal Performance Summary

At the beam's sense node, there is a capacitive attenuator formed between the sense capacitance and the static, shunt and feedback capacitors. This attenuation becomes gain when referring noise performance to the amplifier input. This gain is minimized when all capacitors are the same size.

The MEMS differential amplifier can be implemented using CDS or CHS. When integrating all of the circuitry with the sensor, the noise and offset reduction technique that is implemented is determined by how the beam is biased. The two possible biasing methods are using a large resistor or a reset switch.

Regardless of what is used to bias the beam, that device's noise will tend to dominate the noise at the beam's sense node. In a discrete design, the thermal noise associated with a large resistor will be heavily filtered due to the large shunt capacitor seen by the resistor. However, in an integrated design where the shunt capacitance is on

the order of 100 fF, the large resistor's thermal noise will dominate the noise at the beam's sense node unless the resistor can be made significantly larger 10 MΩ.

The same trend is observed when using a reset switch. The kT/C noise will dominate the noise present on the beam node. This noise can be rejected to first order when using CDS with the appropriate clocking scheme. For this reason, CDS offers better noise performance over CHS when considering the optimum integrated solution. CHS does not offer a practical way to reject the thermal noise associated with the beam biasing resistor, or the kT/C noise of the reset switch, therefore the preferred offset reduction technique is CDS in this MEMS differential amplifier design. A comparison of the optimal MEMS amplifier's performance to another high common-mode differential amplifier, the AD629, is shown below in Table 6.1.

| | OFFSET VOLTAGE | CMRR | ICMVR | BW | NOISE |
|---|---|---|---|---|---|
| AD629 | 1 mV | 88 dB | ± 270 | 500 kHz | 550 nV/√Hz |
| MEMS diff-amp | 1 μV[2] | 60-70 dB[3] | ±288[4] | 4 kHz[5] | 452 nV/√Hz |

Table 6.1: Comparison of optimal MEMS amplifier performance to Analog Devices' AD629

[2] Actual value depends clock feedthrough, which is determined by chip layout

[3] Untrimmed value.

[4] Theoretical breakdown of trenches derived in section 3.2.9.

[5] Bandwidth is limited to roughly 1/6-th of the modulation (sampling) frequency [56].

# 7 THESIS SUMMARY AND CONCLUSIONS

This chapter summarizes the work done in this thesis and presents conclusions based on the measurements presented in the previous chapters. This chapter has four sections: a MEMS sensor summary, a drive loop summary, a sense loop summary and a future work summary.

## 7.1 MEMS SENSOR SUMMARY

As described in Chapter 3, this design called for a fully differential vibrating capacitor whose capacitance varies linearly with position. This design is in contrast to typical vibrating capacitors, which are single-ended and whose capacitance have a nonlinear dependence on position. The properties of this novel design facilitate wide common-mode voltages and the elimination of dynamic currents drawn from the source.

This design has demonstrated that a fully differential vibrating capacitor can be fabricated using SOI MEMS technology. A key feature of this design is its cross-quad layout which minimized the effects of etch variations, process gradients and helped to suppress residual electrostatic forces while maximizing the overall amplifier's CMRR.

The design of the MEMS structure required the ability to create electrically isolated, but mechanically coupled regions. The creation of the regions was achieved using isolation trenches. A trench is a nitride-polysilicon-nitride sandwich as shown in

Figure 3.11. Two thin (120nm) layers of nitride surround a polysilicon layer that provides mechanical support.

The trenches used in the mechanical sensor limit the performance of the sensor in two ways. They provide a parasitic shunt capacitance to the inputs and facilitate leakage currents. This shunt capacitance is 2 pF and is much larger than the modulation capacitance of 9 fF. These two capacitors form an attenuator at the mechanical sensor input terminals. Not only does this attenuation reduce the input signal; it amplifies the input referred noise by the same factor. In addition, the thin nitride layers of the trenches limit the maximum voltage that can be dropped across them. The current trenches will breakdown at ±125V.

Therefore, in future designs, a significant amount of effort needs to be spent reducing the physical layout of the trench, while increasing the thickness of the nitride lining. The reduction in area of the trench will decrease its shunt capacitance and the amplifier's effective input referred noise. The increase in thickness of the nitride lining will increase the voltage that can applied at the terminals before the electric field across the nitride reaches its breakdown value. Furthermore, the thicker nitride lining will increase the common-mode voltage range of the amplifier while reducing the net shunt capacitance.

Another factor that limits the common-mode voltage range of the amplifier is the electrical spring constant. This increases the overall compliance of the beam and is

computed by taking the gradient of the electrostatic force. In this design, the electrical spring constant in both the x- and y-directions are not comparable to their mechanical counterparts until the common-mode voltage applied is several thousands of volts. Since the isolations trenches will break down before 300 V is reached, the electrical spring constants were not a concern in this design.

The compliance of the beam was set by four folded tethers that attached to the substrate. It was shown in section 3.2.5 how to design these tethers to be a known compliance in the desired direction of motion, while being very stiff in the other two directions thereby rejecting of out of plane motion. This mechanical compliance along with the mechanical structure's mass set its resonant frequency when placed in the drive loop.

## 7.2 DRIVE LOOP SUMMARY

The drive loop is responsible for vibrating the sensor at its resonant frequency, as was described in the previous section. The beam is actuated by a square wave electrostatic force drive. Due to the high-$Q$ second order transfer function from force to displacement, the square wave will yield a sinusoidal displacement at the MEMS structure's mechanical resonance, as desired.

To maintain a constant amplitude and fixed frequency oscillation, feedback and stability analysis was performed using describing functions. As described in chapter 4,

the phase delay through each of the components of the drive loop needs to be minimized to maximize the sensitivity of the overall amplifier.

The square wave force drive was implemented using a comparator to excite the beam. Comparators are very sensitive to noise at their input, for this noise is the cause of multiple transitions. A common technique for reducing multiple transitions is to apply DC hysteresis to the comparator, which essentially separates the low-to-high and high-to-low transition voltages. The tradeoff for the reduction in multiple transitions is additional phase delay through the comparator directly proportional to the amount of hysteresis applied.

In this design, AC hysteresis was implemented instead of DC hysteresis. This involves using a RC network in the feedback path of the comparator instead of two resistors. The way AC hysteresis works is that after the comparator trips, the trip point of the comparator is moved to one of the voltage supply rails for a few time constants. As long as the time constant of the RC network is roughly 10 % of the clock period, this has the benefit of only allowing the comparator to trigger once per cycle without increasing its phase delay.

With the phase of the drive loop components minimized, the displacement of the mechanical structure is maximized. In Chapter 4, it is shown how to design for specific displacement amplitudes. Our results indicate that there is only a 10% discrepancy

between the calculated and achieved displacement amplitude while there is a 15% discrepancy between the predicted and measured resonant frequencies.

## 7.3 SENSE LOOP SUMMARY

The sense loop performed the processing of the input signal. With the beam vibrating at a fixed frequency and amplitude, the differential input signal was modulated up to the resonant frequency of the beam. At this frequency, the pre-amplifier's input noise is dominated by broadband components, which facilitates a higher SNR for the overall amplifier. After amplification at this frequency, the signal is synchronously demodulated and is converted into a single-ended measurement of the differential input.

The demodulation scheme could have been CDS or CHS. Correlated double sampling was chosen over chopper stabilization because CDS is less sensitive to duty cycle variations in the demodulation clock, and it offers better offset performance due to its zero at the origin. An additional reason for implementing CDS in this design is that switched capacitor CDS techniques are easier to implement on an IC than CHS in the fabrication process that was available.

To maximize the amplitude of the demodulated signal, the components in the sense loop needed to have bandwidths much higher than the modulation frequency. Since the demodulator was implemented using correlated double sampling, significant aliasing of the pre-amplifier noise was observed. This observation was made after an anti-aliasing

filter was placed in the loop. The noise performance of the sense loop was modeled and the performance predictions closely matched the observed noise measurement.

The bandwidth of the sense loop can be set within 10% of a desired frequency using bode analysis. A sense loop model was created in both MATLAB and ADICE and the results obtained from these models agreed with laboratory measurements. The upper limit of the bandwidth achieved was set by the force drive signal of the drive loop coupling into the CDS integrator's summing node. This upper limit will be removed with a change in layout and integrating some of the pre-amplifier circuitry on the same substrate as the sensor. This will be discussed in Chapter 7.

## 7.4 FUTURE WORK SUMMARY

As was mentioned in the previous chapter, improvements in performance can only be achieved by integration of the drive and sense loops' circuitry with the beam. At the very least, the differential pair of the pre-amplifier of the sense loop must be integrated. With this topology, the noise and offset performance improved from 55 $\mu V/\sqrt{Hz}$ and one mV to 14 $\mu V/\sqrt{Hz}$ and 340 $\mu V$, respectively. Full integration facilitated noise and offset performance of 452 $nV/\sqrt{Hz}$ and 1 $\mu V$, respectively.

This performance depends on the implementation of the demodulator. Chopper stabilization will offer worse noise performance than chopper stabilization if large valued resistors (> 100 $M\Omega$) cannot be easily fabricated. In addition, CDS offers better offset performance because of its zero at the origin.

# APPENDIX A: MATLAB/SIMULINK MODEL

A model of the electrometer was constructed using the MATLAB and Simulink modeling software. The sense and drive loops were constructed using the built-in transfer function and gain blocks. A block diagram of the entire system is shown in Figure A.1. The blocks used constants and values that were computed by a MATLAB script file that is in Appendix A.3.

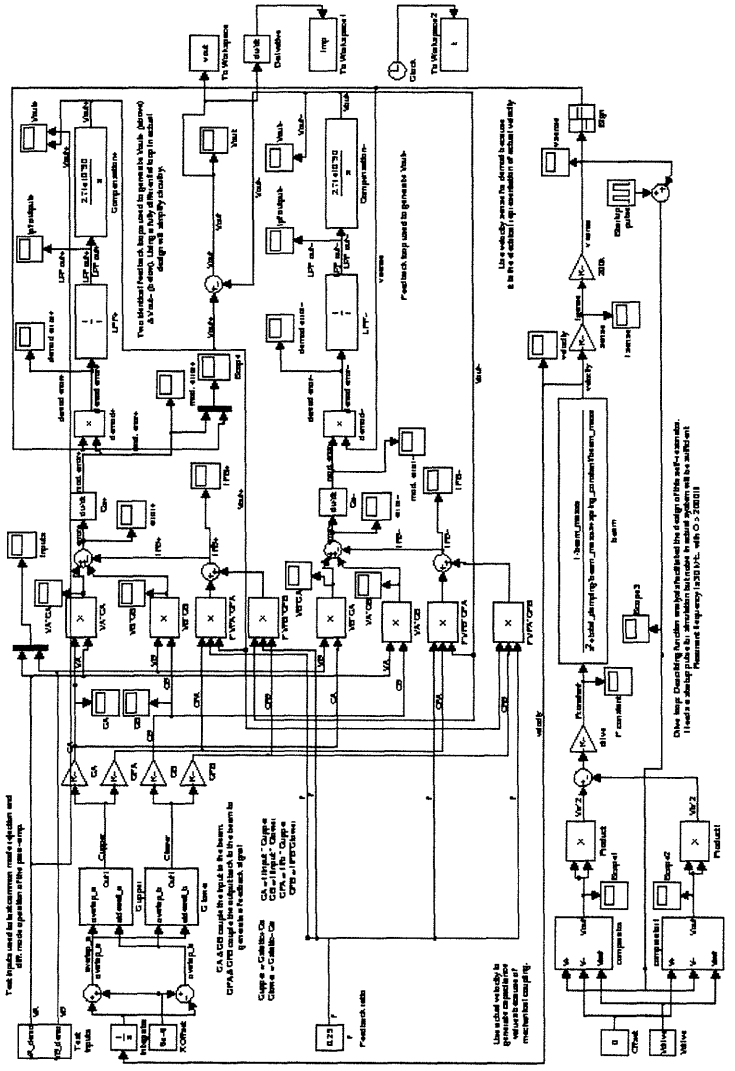

Figure A.1: Complete Simulink model of electrometer

## A.1 DRIVE LOOP

Constructing a model of the drive loop involved translating the block diagram of Figure 4.3 into a block diagram involving Simulink blocks. The electrostatic force actuates the mechanical structure, and when driven at resonance, the velocity and force will be in phase. This was modeled using a transfer function block of the equation:

$$\frac{\dot{x}}{F} = \frac{s}{ms^2 + \beta sx + kx}.$$

The output of this block is velocity, which is converted into a current by the beam via a scale factor. This is modeled by using a gain block of value:

$$V_{bias}\frac{2\varepsilon_0 b}{g}.$$

This current is converted into a voltage by another gain block. This models the transresistance amplifier gain of 200kΩ. This voltage representation of velocity is squared off by comparator blocks, which were constructed using *sign* blocks and constants. The resulting square wave was squared and then converted into the force drive via a scale factor of:

$$N_f\frac{\varepsilon_0 b}{g}.$$

This therefore completes the drive loop. The resulting velocity and force drive waveforms are shown in Figure A.2.

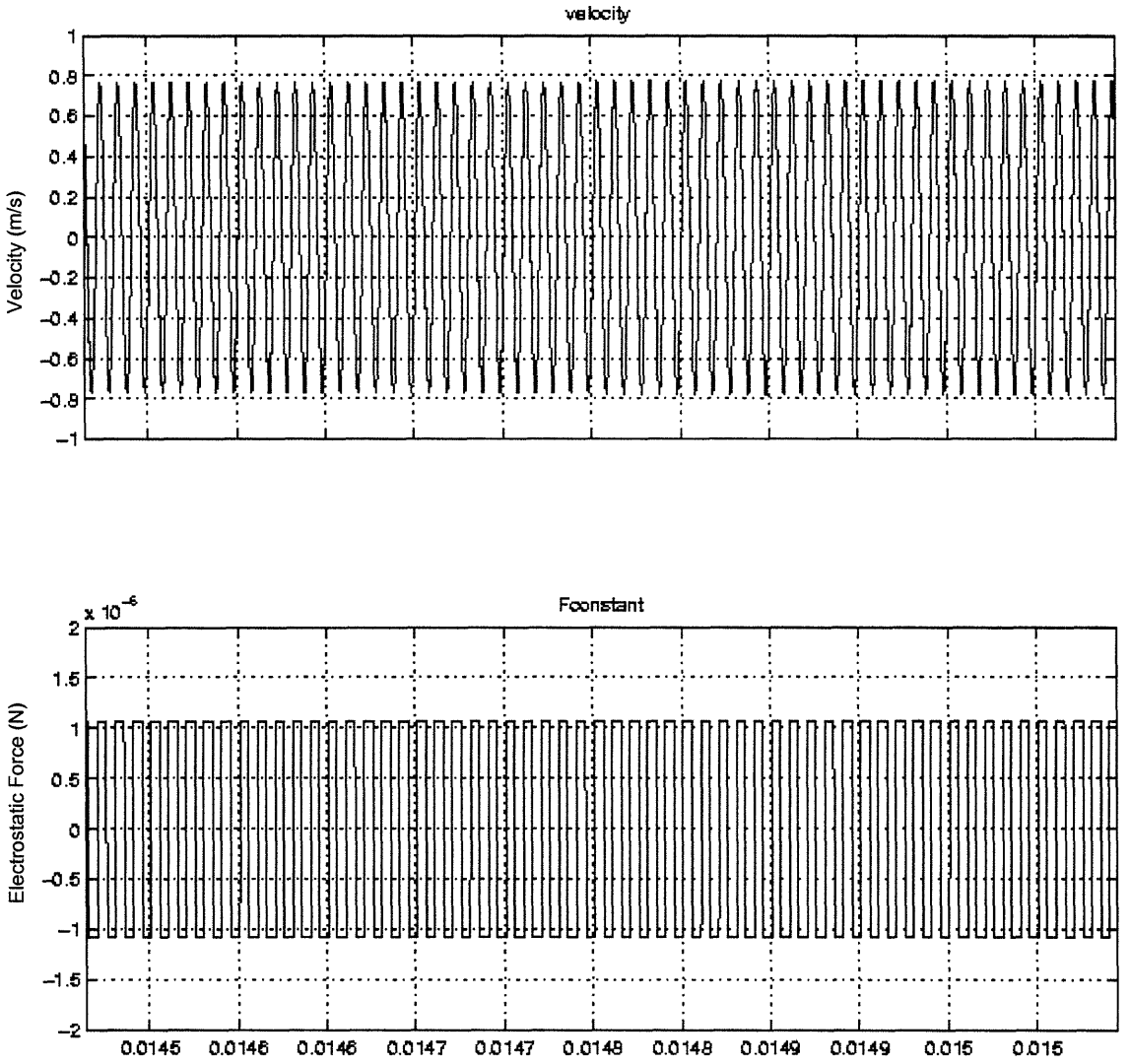

Figure A.2: Force and velocity waveforms.

## A.2 SENSE LOOP

With the model of the drive loop operational, the sense loop was designed. The velocity signal from the drive loop was integrated to generate beam position. Using position, the sense capacitances, $C_A$ & $C_B$, and the feedback capacitances, $C_{FA}$ & $C_{FB}$, could be generated. Then the charge induced on the beam at each terminal was computed, ie the

*VA*CA & VB*CB* products. This error charge is added then differentiated to generate the error current induced on the beam. The error current then fed blocks that represented the sense loop circuitry.

The error current was first demodulated using the velocity sense, not the actual velocity for we will have no access to this directly in the actual circuit. The demodulator was implemented by a multiplier block, with its input being the error current and the velocity sense. The demodulated error is then fed into an integrator in order to drive the steady state error to zero. The output of the integrator was multiplied by a feedback ratio, *f*, to emulate a resistive divider, and the divided signal was fed back to the feedback ports to generate the *VFA*CFA & VFB*CFB* products. This then closed the single-ended sense loop.

To make the sense loop fully-differential, an identical loop was created but the cross terms were computed instead, ie *VA*CB*, *VB*CA*, *VFA*CFB*, & *VFB*CFA*. The outputs of the two minor sense loops were then subtracted to yield an overall single-ended output. The response to set of test inputs is shown in Figure A.3.

With a closed-loop gain of four, the steady-state response to a differential input step of two should be eight, as is shown in the figure. The common-mode step of five is rejected. It is evident that the loop only responds to differential input signals and rejects common-mode signals, as desired.

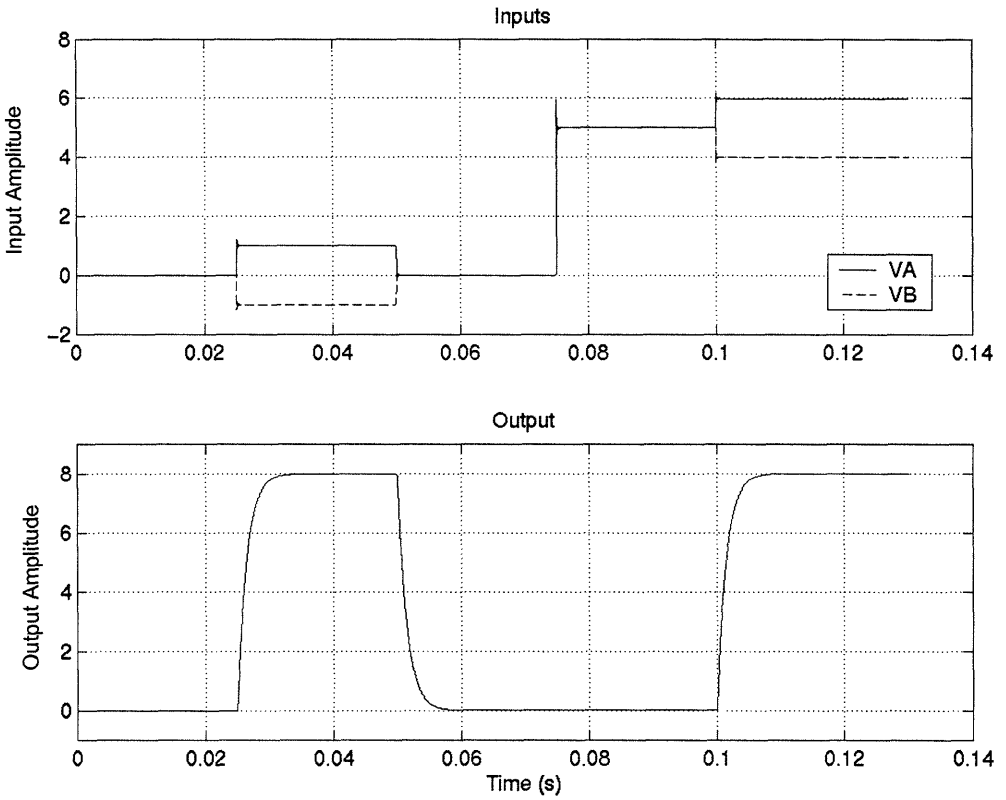


Figure A.3: Step response of Simulink model of electrometer

## A.3 MATLAB SCRIPT FILE

This MATLAB script was used to calculate parameters for the Simulink model and to generate various plots.

```
% Constants
E = 130e9; % Young's modulus (Pa)
rho = 2333; % Density of Si (kg/m3)
eo = 8.86e-12; % permittivity of free space (F/m)
esi = 11.7; % relative permittivity of Si
eni = 7.5; % relative permittivity of Nitride
eox = 3.9; % relative permittivity of oxide
visc = 18.5e-6; % viscosity of air at 25 degC (kg/m/sec)
k = 1.380658e-23; % Boltzmann's constant in (J/K)
T = 300; % temp. (K)
numplots=0;
modulating_frequency=30e3; %chopper frequency (Hz)
parasitic_capacitance=1e-12;

% Dimensions
h = 2e-6; % gap between beam and substrate (m)
b_nom = 16.5e-6; % structural silicon thickness (m)
etch_variation = 0.125e-6; % absolute value of maximum etch variation (m)
b_variation = 1e-6; % absolute value of thicknes variation (m)
delta = linspace(-1*etch_variation,etch_variation,101); % etch variation used in calculations (m)
beta = linspace(-1*b_variation,b_variation,101); % thickness variation
b = b_nom-2*beta; % structure thickness with variations
```

```
MIN=1;
nominal=51;
MAX = 101;
displacement_amplitude = 5e-6; % peak amplitude of oscillation (m)
x=linspace(-1,1,101); % unit range of motion in x
y=linspace(-1,1,101); % unit range of morion in y
beam_width = 105e-6; %Beam width (m)
%xbeam_thickness = 4e-6; %Cross beam thickness (m)

%Input Voltages
common_mode_voltage = 1; % Common-mode voltage (V)
differential_mode_voltage= 1; %Differential-mode voltage (V)
Va = common_mode_voltage + differential_mode_voltage/2;
Vb = common_mode_voltage - differential_mode_voltage/2;
noise_voltage = 10e-9; %Sense amp noise (v/rt. Hz)

% Input fingers
num_input_fingers = 50; % number of input fingers

% Feedback fingers
num_fb_fingers = 50; % number of feedback fingers

% Force fingers
num_force_fingers = 100; % number of force fingers

% Sense fingers
num_sense_fingers = 100; % number of sense fingers


% Self-test fingers
num_self_test_fingers = 0; % number of self test fingers

% All fingers
finger_gap_nom = 2e-6; % nominal finger gap (m)
finger_gap_variation = 0.99*finger_gap_nom; % absolute value of the gap variation (m)
finger_gap_left= finger_gap_nom.*(1 + 1/finger_gap_nom.*y*finger_gap_variation); % finger gap on left of finger (m)
finger_gap_right=finger_gap_nom.*(1 - 1/finger_gap_nom.*y*finger_gap_variation); % finger gap on right of finger (m)
finger_overlap_min = 3e-6; % overlap of fingers (m)
finger_overlap_max = finger_overlap_min + 2*displacement_amplitude ; % maximum finger overlap (m)
finger_sidewall_gap_min = 10e-6; % minimum fixed finger edge to moving finger beam (m)
finger_sidewall_gap_max = finger_sidewall_gap_min + 2*displacement_amplitude % maximum sidewall gap (m)
sidewall_center = (finger_sidewall_gap_min + finger_sidewall_gap_max)/2; % center of sidewall range (m)
overlap_center = (finger_overlap_max + finger_overlap_min)/2; % center of displacement range (m)
overlap_a = overlap_center.*(1+1/overlap_center.*x*(finger_overlap_max - finger_overlap_min)/2); % range of overlap values for top cap (m)
overlap_b = overlap_center.*(1-1/overlap_center.*x*(finger_overlap_max - finger_overlap_min)/2); % range of overlap values for bot cap (m)
finger_sidewall_gap_a = sidewall_center.*(1-1/sidewall_center.*x*(finger_sidewall_gap_max -finger_sidewall_gap_min)/2); % range of sidewall gap values for top cap (m)
finger_sidewall_gap_b = sidewall_center.*(1+1/sidewall_center.*x*(finger_sidewall_gap_max-
finger_sidewall_gap_min)/2); % range of sidewall gap values for bott cap (m)
finger_width = 2e-6 +2*delta; % finger width (m)
finger_length = 2*displacement_amplitude + finger_overlap_min + finger_sidewall_gap_min % finger length (m)
num_finger_rows = 4;
fixed_arm_thickness = 11.5e-6 + 2*delta; % thickness of each fixed arm (m)
moving_arm_thickness = 18e-6 + 2*delta; % thickness of each moving arm (m)
fixed_finger_spacing = 2e-6; % Distance between fixed fingers (m)
beam_height = 2*(moving_arm_thickness(nominal)+2*finger_length+2*(finger_length-overlap_center)+2*fixed_arm_thickness)+7*fixed_finger_spacing; %Height of beam (m)

% Finger capacitances vs overlap
```

```
unit_overlap_capacitance_a =
eo*b(nominal)*(1/finger_gap_left(nominal)+1/fi
nger_gap_right(nominal)).*overlap_a; %
Overlap Capacitance values for top cap (F)
unit_overlap_capacitance_b =
eo*b(nominal).*overlap_b*(1/finger_gap_left(no
minal)+1/finger_gap_right(nominal)); % Overlap
Capacitance values for bot cap (F)
unit_sidewall_capacitance_a=
2*eo*finger_width(nominal)*b(nominal)./finger
_sidewall_gap_a; % Sidewall capacitance values
for top cap (F)
unit_sidewall_capacitance_b=
2*eo*finger_width(nominal)*b(nominal)./finger
_sidewall_gap_b; % Sidewall capacitance values
for bot cap (F)
total_sense_capacitance_a =
num_input_fingers.*(unit_overlap_capacitance_
a+unit_sidewall_capacitance_a); % total sense
cap a (F)
total_sense_capacitance_b =
num_input_fingers.*(unit_overlap_capacitance_
b+unit_sidewall_capacitance_b); % total sense
cap b (F)
figure
numplots=numplots+1;
subplot(2,1,1)
plot(overlap_a,unit_overlap_capacitance_a,'b--
',overlap_a,unit_sidewall_capacitance_a,'r:',overl
ap_a,total_sense_capacitance_a,'k-')
legend('Unit Overlap','Unit Sidewall','Total',-1)
xlabel('Overlap (m)')
ylabel('Capacitance (F)')
title('Sense Capacitance A vs. Overlap A')
grid
subplot(2,1,2)
plot(overlap_a,unit_overlap_capacitance_b,'b--
',overlap_a,unit_sidewall_capacitance_b,'r:',overl
ap_a,total_sense_capacitance_b,'k-')
legend('Overlap','Sidewall','Total',-1)
xlabel('Overlap (m)')
ylabel('Capacitance (F)')
title('Sense Capacitance B vs. Overlap A')
grid

% Finger capacitances vs etch variations
unit_overlap_capacitance_a =
eo.*b*overlap_a(nominal)*(1/finger_gap_left(no
minal)+1/finger_gap_right(nominal)); % Overlap
Capacitance values for top cap (F)
unit_overlap_capacitance_b =
eo.*b*overlap_b(nominal)*(1/finger_gap_left(no
minal)+1/finger_gap_right(nominal)); % Overlap
Capacitance values for bot cap (F)
unit_sidewall_capacitance_a=
2*eo.*finger_width.*b./finger_sidewall_gap_a(n
ominal); % Sidewall capacitance values for top
cap (F)
unit_sidewall_capacitance_b=
2*eo.*finger_width.*b./finger_sidewall_gap_b(n
ominal); % Sidewall capacitance values for bot
cap (F)
total_sense_capacitance_a =
num_input_fingers.*(unit_overlap_capacitance_
a+unit_sidewall_capacitance_a); % total sense
cap a (F)
total_sense_capacitance_b =
num_input_fingers.*(unit_overlap_capacitance_
b+unit_sidewall_capacitance_b); % total sense
cap b (F)
% figure
% numplots=numplots+1;
% subplot(2,1,1)
% plot(delta,unit_overlap_capacitance_a,'b--')
% legend('Overlap',-1)
% xlabel('Etch variations (m)')
% ylabel('Capacitance (F)')
% title('Unit Overlap Capacitance vs. Etch
Variations')
% grid
% subplot(2,1,2)
% plot(delta,unit_sidewall_capacitance_a,'k-')
% legend('Sidewall',-1)
% xlabel('Etch variations (m)')
% ylabel('Capacitance (F)')
% title('Unit Sidewall Capacitance vs. Etch
Variations')
% grid

%Input Cap Sensitivities to etch variations
sensitivity_a_x =
num_input_fingers*eo.*b*(1/finger_gap_left(no
minal)+1/finger_gap_right(nominal))+2*eo.*fin
ger_width.*b/finger_sidewall_gap_a(nominal)^2
; % Sensitivity of cap A w.r.t. x (F/m)
sensitivity_b_x = num_input_fingers*-
1*eo.*b*(1/finger_gap_left(nominal)+1/finger_g
ap_right(nominal))-
2*eo.*finger_width.*b/finger_sidewall_gap_b(n
ominal)^2; % Sensitivity of cap B w.r.t. x (F/m)
sensitivity_a_y =
num_input_fingers*eo*overlap_a(nominal).*b*(
-
1/finger_gap_left(nominal)^2+1/finger_gap_righ
t(nominal)^2); % Sensitivity of cap A w.r.t y
(F/m)
sensitivity_b_y =
num_input_fingers*eo*overlap_b(nominal).*b*(
-
1/finger_gap_left(nominal)^2+1/finger_gap_righ
t(nominal)^2); % Sensitivity of cap B w.r.t y
(F/m)
```

```
% figure
% numplots=numplots+1;
% subplot(2,1,1)
%                 plot(delta,sensitivity_a_x,'b-
',delta,abs(sensitivity_b_x),'r--')
% legend('Cap A','abs(Cap B)',-1)
% xlabel('Etch Variations (m)')
% ylabel('Sensitivity (F/m)')
% title('X Capacitance Sensitivities to Etch
Variations')
% grid
% subplot(2,1,2)
%                 plot(delta,sensitivity_a_y,'b-
',delta,sensitivity_b_y,'r--')
% legend('Cap A','Cap B',-1)
% xlabel('Etch Variations (m)')
% ylabel('Sensitivity (F/m)')
% title('Y Capacitance Sensitivities to Etch
Variations')
% grid

%Input Cap Sensitivities to y disturbances
sensitivity_a_x                 =
num_input_fingers*eo*b(nominal).*(1./finger_g
ap_left+1./finger_gap_right)+num_input_fingers
*2*eo*finger_width(nominal)*b(nominal)/finger
_sidewall_gap_a(nominal)^2; % Sensitivity of
cap A w.r.t. x (F/m)
sensitivity_b_x     =     num_input_fingers*-
1*eo*b(nominal).*(1./finger_gap_left+1./finger_
gap_right)-
num_input_fingers*2*eo*finger_width(nominal)
*b(nominal)/finger_sidewall_gap_b(nominal)^2;
% Sensitivity of cap B w.r.t. x (F/m)
sensitivity_a_y                 =
num_input_fingers*eo*overlap_a(nominal)*b(no
minal).*(-
1./finger_gap_left.^2+1./finger_gap_right.^2); %
Sensitivity of cap A w.r.t y (F/m)
sensitivity_b_y                 =
num_input_fingers*eo*overlap_b(nominal)*b(n
ominal).*(-
1./finger_gap_left.^2+1./finger_gap_right.^2); %
Sensitivity of cap B w.r.t y (F/m)
% figure
% numplots=numplots+1;
% subplot(2,1,1)
%                 plot(y,sensitivity_a_x,'b-
',y,abs(sensitivity_b_x),'r--')
% legend('Cap A','abs(Cap B)',-1)
%     xlabel('Normalized     Y     disturbances
(2*delta/g0)')
% ylabel('Sensitivity (F/m)')
% title('X Capacitance Sensitivities to Y
Disturbances')
% grid
% subplot(2,1,2)
% plot(y,sensitivity_a_y,'b-',y,sensitivity_b_y,'r--
')
% legend('Cap A','Cap B',-1)
%     xlabel('Normalized     Y     disturbances
(2*delta/g0)')
% ylabel('Sensitivity (F/m)')
% title('Y Capacitance Sensitivities to Y
Disturbances')
% grid

% Electrical Force & Spring constants
electrical_force_x                 =
num_input_fingers*eo*b(nominal)*((1/finger_ga
p_right(nominal)+1/finger_gap_left(nominal))*(
Vb^2-Va^2)/2-
finger_width(nominal)*(Va^2./finger_sidewall_
gap_a.^2-Vb^2./finger_sidewall_gap_b.^2)); %
Electrical force in xdir (N)
electrical_force_y                 =
num_input_fingers*eo*b(nominal).*(1/finger_ga
p_left(nominal)^2-
1/finger_gap_right(nominal)^2).*(Va^2.*overlap
_a+Vb^2.*overlap_b); % Electrical force in y
(N)
electrical_spring_constant_x                 =
num_input_fingers*eo*finger_width(nominal)*b
(nominal).*(2*Va^2./finger_sidewall_gap_a.^3+
2*Vb^2./finger_sidewall_gap_b.^3);          %
ELectrical Spring constant in X (N/m)
electrical_spring_constant_y                 =
num_input_fingers*eo*b(nominal)*(1/finger_ga
p_left(nominal)^3+1/finger_gap_right(nominal)^
3).*(Va^2.*overlap_a+Vb^2.*overlap_b);      %
Electrical spring constant in y (N/m)

% figure
% numplots=numplots+1;
% subplot(2,1,1)
%             plot(overlap_a,electrical_force_x,'b-
',overlap_a,electrical_force_y,'r--')
% legend('X force','Y Force',-1)
% xlabel('Overlap (m)')
% ylabel('Force (N)')
% title('Electrical Forces vs Overlap')
% grid

electrical_force_x2                 =
num_input_fingers*eo.*b*(1/finger_gap_right(n
ominal)+1/finger_gap_left(nominal))*(Vb^2-
Va^2)/2-
eo.*finger_width.*b*(Va^2/finger_sidewall_gap
_a(nominal)^2+Vb^2/finger_sidewall_gap_b(no
minal)^2); % Electrical force in xdir (N)
electrical_force_y2                 =
num_input_fingers*eo.*b*(1./finger_gap_left(no
```

```
minal)^2-
1/finger_gap_right(nominal)^2).*(Va^2*overlap
_a(nominal)+Vb^2*overlap_b(nominal));      %
Electrical force in y (N)
electrical_spring_constant_x2                =
num_input_fingers*eo.*finger_width.*b*(2*Va^
2/finger_sidewall_gap_a(nominal)^3+2*Vb^2/fi
nger_sidewall_gap_b(nominal)^3); % ELectrical
Spring constant in X (N/m)
electrical_spring_constant_y2                =
num_input_fingers*eo.*b*(1/finger_gap_left(no
minal)^3+1/finger_gap_right(nominal)^3)*(Va^
2*overlap_a(nominal)+Vb^2*overlap_b(nominal
)); % Electrical spring constant in y (N/m)
% subplot(2,1,2)
%                %plot(delta,electrical_force_x2,'b-
',delta,electrical_force_y2,'r--')
% plot(delta,electrical_force_x2,'b-')
% %legend('X force','Y force',-1)
% legend('X force',-1)
% xlabel('Etch Variations (m)')
% ylabel('Force (N)')
% title('Electrical Forces vs Etch Variations')
% grid
% figure
% numplots=numplots+1;
% subplot(2,1,1)
%
plot(overlap_a,electrical_spring_constant_x,'b-
',overlap_a,electrical_spring_constant_y,'r--')
% legend('X spring','Y spring',-1)
% xlabel('Overlap (m)')
% ylabel('Spring constant (N/m)')
% title('Electrical spring constants vs Overlap')
% grid
% subplot(2,1,2)
%     plot(delta,electrical_spring_constant_x2,'b-
',delta,electrical_spring_constant_y2,'r--')
% legend('X spring','Y spring',-1)
% xlabel('Etch Variations (m)')
% ylabel('Spring constant (N/m)')
% title('Electrical spring constants vs Etch
variations')
% grid

electrical_force_x3                          =
num_input_fingers*eo*b(nominal).*(1./finger_g
ap_right+1./finger_gap_left)*(Vb^2-Va^2)/2-
eo*finger_width(nominal)*b(nominal)*(Va^2/fi
nger_sidewall_gap_a(nominal)^2+Vb^2/finger_s
idewall_gap_b(nominal)^2); % Electrical force
in xdir (N)
electrical_force_y3                          =
num_input_fingers*eo*b(nominal).*(1./finger_g
ap_left.^2-
1./finger_gap_right.^2)*(Va^2*overlap_a(nomin
al)+Vb^2*overlap_b(nominal));      %  Electrical
force in y (N)
electrical_spring_constant_x3                =
num_input_fingers*eo*finger_width(nominal)*b
(nominal)*(2*Va^2/finger_sidewall_gap_a(nomi
nal)^3+2*Vb^2/finger_sidewall_gap_b(nominal)
^3); % ELectrical Spring constant in X (N/m)
electrical_spring_constant_y3                =
num_input_fingers*eo*b(nominal).*(1./finger_g
ap_left.^3+1./finger_gap_right.^3)*(Va^2*overl
ap_a(nominal)+Vb^2*overlap_b(nominal));      %
Electrical spring constant in y (N/m)
% figure
% numplots=numplots+1;
% subplot(2,1,1)
%                plot(y,electrical_force_x3,'b-
',y,electrical_force_y3,'r--')
% %plot(delta,electrical_force_x3,'b-')
% legend('X force','Y force',-1)
% %legend('X force',-1)
% xlabel('Normalized Y disturbances')
% ylabel('Force (N)')
% title('Electrical Forces vs Y Disturbances')
% grid
% subplot(2,1,2)
% plot(y,electrical_spring_constant_y3,'r--')
% %plot(delta,electrical_force_x3,'b-')
% legend('Y spring',-1)
% %legend('X force',-1)
% xlabel('Normalized Y disturbances')
% ylabel('Spring Constant (N/m)')
% title('Electrical Spring Constants vs Y
Disturbances')
% grid

%Static & Modulating Capacitances
time=linspace(0,1/modulating_frequency,101);
ovla=(finger_overlap_max+finger_overlap_min)
/2-(finger_overlap_max-
finger_overlap_min)/2.*cos(2*pi*modulating_fr
equency.*time);
ovlb=(finger_overlap_max+finger_overlap_min)
/2+(finger_overlap_max-
finger_overlap_min)/2.*cos(2*pi*modulating_fr
equency.*time);
total_capacitance_a=num_input_fingers*eo*b(n
ominal)*(1/finger_gap_left(nominal)+1/finger_g
ap_right(nominal)).*ovla+2*eo*finger_width(no
minal)*b(nominal)./ovlb;
static_capacitance=num_input_fingers*eo*b(no
minal)*(1/finger_gap_left(nominal)+1/finger_ga
p_right(nominal))*(finger_overlap_max+finger_
overlap_min)/2+2*eo*finger_width(nominal)*b(
nominal)/((finger_overlap_max+finger_overlap_
min)/2)
```

```
modulating_capacitance=num_input_fingers*eo
*b(nominal)*((finger_overlap_max-
finger_overlap_min)/2*(1/finger_gap_left(nomin
al)+1/finger_gap_right(nominal))+2*finger_widt
h(nominal)/((finger_overlap_max+finger_overla
p_min)/2)*(finger_overlap_max-
finger_overlap_min)/(finger_overlap_max+finge
r_overlap_min))
estimated_capacitance_a=static_capacitance-
modulating_capacitance.*cos(2*pi*modulating_f
requency.*time);
estimated_capacitance_b=static_capacitance+mo
dulating_capacitance.*cos(2*pi*modulating_freq
uency.*time);
error=(total_capacitance_a-
estimated_capacitance_a)./total_capacitance_a*1
00;
% figure
% numplots=numplots+1;
% subplot(2,1,1)
%                plot(ovla,total_capacitance_a,'b-
',ovla,estimated_capacitance_a,'k--')
% legend('Total','Estimated',-1)
% xlabel('Overlap (m)')
% ylabel('Capacitance (F)')
% title('Total Capacitance & Estimated
Capacitance vs Overlap')
% grid
% subplot(2,1,2)
% plot(ovla,error,'b-')
% legend('Error',-1)
% xlabel('Overlap (m)')
% ylabel('Error (%)')
% title('Normalized Error vs Overlap')
% grid

%Signal & Noise currents
frequency=linspace(0,modulating_frequency,101
);
signal_current=2*pi.*frequency*2*modulating_
capacitance*(Va-Vb);
common_mode_current                =
2*pi.*frequency*static_capacitance*(Va+Vb);
noise_current                      =
2*pi.*frequency*(2*static_capacitance+parasitic
_capacitance)*noise_voltage.*sqrt(frequency);
estimated_rti_noise                =
(2*static_capacitance+parasitic_capacitance)/(2*
modulating_capacitance)*noise_voltage;
figure
numplots=numplots+1;
subplot(2,1,1)
plot(frequency,signal_current,'b-
',frequency,common_mode_current,'k--')
legend('Signal','Common Mode',-1)
xlabel('Frequency (Hz)')
ylabel('Current (A)')
title('Current vs Modulating Frequency')
grid
subplot(2,1,2)
plot(frequency,noise_current,'r:')
legend('Noise',-1)
xlabel('Frequency (Hz)')
ylabel('Current (A)')
title('Current vs Modulating Frequency')
grid

% Etch slots/holes
etch_slot_w                =                beam_width-
2*(moving_arm_thickness(nominal)+sqrt(2)*mo
ving_arm_thickness(nominal)/2)  +  2*delta;%
etch slot width (m)
% etch_slot_l = 20e-6 + 2*delta; % etch slot
length (m)
% etch_slot_sp = 4e-6 - 2*delta;  % etch slot
spacing (m)
etch_slot_d                                =
7.5*etch_slot_w(nominal)^2./(beam_width.*bea
m_height/2); % etch slot density correction
factor
rho_c = rho *  etch_slot_d; % corrected silicon
density (kg/m^3)
rho_c_nom = rho_c(nominal)

pack

%Parasitic Capacitances
trench_width = 1.5e-6; %Trench width (m)
nitride_thickness    =    2400e-10;    %Nitride
thickness (m)
poly_thickness             =             trench_width-
2*nitride_thickness;  %Polysilicon  backfill
thickness (m)
fixed_finger_anchor_sidewall = 40e-6; %fixed
finger anchor sidewall length (m)
fixed_finger_anchor_endwall = 25e-6; %fixed
finger endwall length (m)
beam_anchor_sidewall = 40e-6; %beam anchor
sidewall length (m)
beam_anchor_endwall = 25e-6; %beam anchor
endwall length (m)
trench_inner_corner_radius = 1e-6; %trench
inner corner radius (m)
trench_outer_corner_radius                 =
trench_inner_corner_radius+trench_width;
%trench outer corner radius (m)
rho_polysilicon = 2.4e-5; %resistivity of
polysilicon (ohm-m)
beam_mass = 5.6e-9; %mass of beam (kg)
CALCULATED
inner_nitride_capacitance                  =
eo*eni.*(2*beam_anchor_sidewall.*b/nitride_thi
```

```
ckness+beam_anchor_endwall.*b/nitride_thickn
ess+pi.*b/log((trench_inner_corner_radius+nitri
de_thickness)/trench_inner_corner_radius)); %
Inner nitride capacitance (F)
outer_nitride_capacitance =
eo*eni.*(2*beam_anchor_sidewall.*b/nitride_thi
ckness+beam_anchor_endwall.*b/nitride_thickn
ess+pi.*b/log((trench_outer_corner_radius+nitri
de_thickness)/trench_outer_corner_radius)); %
Outer nitride capacitance (F)
poly_resistance =
rho_polysilicon*poly_thickness./(b*(2*beam_an
chor_sidewall+beam_anchor_endwall));
%Polysilicon resistance (ohms)
poly_resistance(nominal) % Nominal Polysilicon
resistance (ohms)
beam_anchor_capacitance =
inner_nitride_capacitance.*outer_nitride_capacit
ance./(outer_nitride_capacitance+inner_nitride_c
apacitance); %Parasitic capacitance of one
anchor (F)
beam_anchor_to_handle_capacitance =
eo*eox*((beam_anchor_sidewall*beam_anchor_
endwall+(beam_anchor_endwall-
2*trench_inner_corner_radius)*trench_inner_cor
ner_radius)/h+pi*trench_inner_corner_radius^2/
(2*h)) % Beam anchor to handle wafer
capacitance (F)
beam_to_handle_capacitance =
eo*beam_mass./(h.*b.*rho_c); %Beam to handle
wafer capacitance (F)
parasitic_capacitance2 =
2*(beam_anchor_to_handle_capacitance+beam_
anchor_capacitance(nominal));
num_input_fingers2=1:101;
static_capacitance2=num_input_fingers2*eo*b(n
ominal)*(1/finger_gap_left(nominal)+1/finger_g
ap_right(nominal))*(finger_overlap_max+finger
_overlap_min)/2+2*eo*finger_width(nominal)*b
(nominal)/((finger_overlap_max+finger_overlap
_min)/2);
modulating_capacitance2=num_input_fingers2*
eo*b(nominal)*((finger_overlap_max-
finger_overlap_min)/2*(1/finger_gap_left(nomin
al)+1/finger_gap_right(nominal))+2*finger_widt
h(nominal)/((finger_overlap_max+finger_overla
p_min)/2)*(finger_overlap_max-
finger_overlap_min)/(finger_overlap_max+finge
r_overlap_min));
signal_current2=2*pi*frequency(101)*2.*modul
ating_capacitance2*(Va-Vb);
common_mode_current2 =
2*pi*frequency(101).*static_capacitance2*(Va+
Vb);
noise_current2 =
2*pi*frequency(101)*(2*static_capacitance2+pa
rasitic_capacitance2)*noise_voltage*sqrt(freque
ncy(101));
estimated_rti_noise2 =
(2.*static_capacitance2+parasitic_capacitance2).
/(2.*modulating_capacitance2)*noise_voltage;
figure
numplots=numplots+1;
subplot(2,1,1)
plot(num_input_fingers2,signal_current2,'b-
',num_input_fingers2,common_mode_current2,'k
--')
legend('Signal','Common Mode',-1)
xlabel('Number of fingers')
ylabel('Current (A)')
title('Current vs Number of Fingers')
grid
subplot(2,1,2)
plot(num_input_fingers2,noise_current2,'r:')
legend('Noise',-1)
xlabel('Number of fingers')
ylabel('Current (A)')
title('Current vs Number of Fingers')
grid
% figure
% numplots=numplots+1;
% subplot(2,1,1)
%
plot(num_input_fingers2,estimated_rti_noise2,'b
-')
% legend('RTI Noise',-1)
% xlabel('Number of fingers')
% ylabel('Noise (V/rt Hz)')
% title('Estimated RTI Noise vs Number of
Fingers')
% grid
% subplot(2,1,2)
%
plot(num_input_fingers2,static_capacitance2,'k--
',num_input_fingers2,modulating_capacitance2,'
b-
',num_input_fingers2,ones(1,101)*beam_to_han
dle_capacitance(nominal),'r:',num_input_fingers
2,ones(1,101)*parasitic_capacitance2,'m-
.',num_input_fingers2,ones(1,101)*beam_anchor
_capacitance(nominal),'m--
',num_input_fingers2,ones(1,101)*beam_anchor
_to_handle_capacitance,'r-')
%          legend('Static','Modulating','Beam-
handle','Total parasitic','Beam Anchor','Beam
Anchor to handle',-1)
% xlabel('Number of fingers')
% ylabel('Capacitance (F)')
% title('Capacitance vs Number of Fingers')
% grid

% keyboard
```

```
%Muliple trenches
trench_separation=2e-6; % Separation between trenches (m)
trench_sidewall=40e-6;
trench_endwall=25e-6;
num_trenches = 1:10;
num_trenches=1:1;
inner_nitride_capacitance2 = eo*eni.*(2*(beam_anchor_sidewall+trench_separation.*(num_trenches-1))*b(nominal)/nitride_thickness+(beam_anchor_endwall+trench_separation.*(num_trenches-1))*b(nominal)/nitride_thickness+pi*b(nominal)/log((trench_inner_corner_radius+nitride_thickness)/trench_inner_corner_radius)); % Inner nitride capacitance (F)
outer_nitride_capacitance2 = eo*eni.*(2*(beam_anchor_sidewall+trench_separation.*(num_trenches-1))*b(nominal)/nitride_thickness+(beam_anchor_endwall+trench_separation.*(num_trenches-1))*b(nominal)/nitride_thickness+pi*b(nominal)/log((trench_outer_corner_radius+nitride_thickness)/trench_outer_corner_radius)); % Outer nitride capacitance (F)
beam_anchor_to_handle_capacitance2 = eo*eox.*(((beam_anchor_sidewall+trench_separation.*(max(num_trenches)-1)).*(beam_anchor_endwall+trench_separation.*(max(num_trenches)-1))+((beam_anchor_endwall+trench_separation.*(min(num_trenches)-1))-2*trench_inner_corner_radius)*trench_inner_corner_radius/h)+pi*trench_inner_corner_radius^2/(2*h)) % Beam anchor to handle wafer capacitance (F)
%for i=1:10,
%
total_trench_capacitance(i)=1/(sum(1./inner_nitride_capacitance2(1:i))+sum(1./outer_nitride_capacitance2(1:i)));
  %end
num_input_fingers = 50;
num_arms =2; % Number of arms per input
fixed_finger_spacing = 2e-6; % Distance between fixed fingers (m)
%beam_height = 2*(moving_arm_thickness(nominal)+2*finger_length+2*(finger_length-overlap_center)+2*fixed_arm_thickness)+7*fixed_finger_spacing; %Height of beam (m)
beam_height = 1007e-6; %from layout
%beam_area = beam_height * beam_width; %Beam area (m^2)
beam_area = 155996.6e-12; %Beam area from layout (m^2)
moving_arm_area = num_input_fingers/num_arms*(2*finger_gap_left(nominal)+finger_width(nominal))*moving_arm_thickness(nominal)+num_input_fingers/num_arms*(2*finger_length+finger_width(nominal))*finger_width(nominal); %Area of each arm (m^2)
%beam_mass = rho_c(nominal)*b(nominal)*beam_area(nominal)+2*num_finger_rows*num_arms*moving_arm_area*rho*b(nominal) % More accurate beam mass (kg)
total_trench_capacitance=1/(sum(1./inner_nitride_capacitance2(1:1))+sum(1./outer_nitride_capacitance2(1:1)));
parasitic_capacitance3 = (beam_anchor_to_handle_capacitance2+total_trench_capacitance*4+0*beam_to_handle_capacitance(nominal));
estimated_rti_noise3 = (2.*static_capacitance2+parasitic_capacitance3)./(2.*modulating_capacitance2)*noise_voltage;

figure
numplots=numplots+1;
subplot(2,1,1)
plot(num_trenches,inner_nitride_capacitance2,'bo',num_trenches,outer_nitride_capacitance2,'kx',num_trenches,beam_anchor_to_handle_capacitance2,'rd',num_trenches,inner_nitride_capacitance2,'b-',num_trenches,outer_nitride_capacitance2,'k-',num_trenches,beam_anchor_to_handle_capacitance2,'r-')
legend('Inner','Outer','Anchor',-1)
xlabel('Number of trenches')
ylabel('Capacitance (F)')
title('Nitride Capacitances vs Number of Trenches')
grid
subplot(2,1,2)
plot(num_trenches,total_trench_capacitance,'ko',num_trenches,total_trench_capacitance,'k-')
legend('Total',-1)
xlabel('Number of trenches')
ylabel('Capacitance (F)')
title('Trench Capacitance vs Number of Trenches')
grid
figure
numplots=numplots+1;
subplot(2,1,1)
semilogy(num_input_fingers2,estimated_rti_noise3,'b-')
legend('RTI Noise',-1)
xlabel('Number of fingers')
```

```
ylabel('Noise (V/rt Hz)')
title('Estimated RTI Noise vs Number of Fingers')
grid
subplot(2,1,2)
plot(num_input_fingers2,static_capacitance2,'k--',num_input_fingers2,modulating_capacitance2,'b-',num_input_fingers2,ones(1,101)*beam_to_handle_capacitance(nominal),'r:',num_input_fingers2,ones(1,101)*parasitic_capacitance3,'m-.',num_input_fingers2,ones(1,101)*total_trench_capacitance,'m--',num_input_fingers2,ones(1,101)*beam_anchor_to_handle_capacitance2,'r-')
legend('Static','Modulating','Beam-handle','Total parasitic','Beam Anchor','Beam Anchor to handle',-1)
xlabel('Number of fingers')
ylabel('Capacitance (F)')
title('Capacitance vs Number of Fingers')
grid

% Finger modes
lambda1 = 1.8751;
lambda2 = 4.6941;
% moving_finger_mass = moving_arm_area/num_arms*b(nominal)*rho % mass of one arm of moving fingers (kg)
moving_finger_mass = 1.81e-10 % from layout (kg)
% fixed_arm_length = (num_input_fingers/num_arms)*(2*finger_gap_left(nominal)+2*finger_width(nominal))+finger_width(nominal)+finger_gap_left(nominal); % length of fixed arm (m)
fixed_arm_length = 208e-6 % from layout (m)
% moving_arm_length = num_input_fingers/num_arms*(2*finger_gap_left(nominal)+2*finger_width(nominal)); %length of moving arm (m)
moving_arm_length = 200e-6 % from layout (m)
% fixed_finger_area = (num_input_fingers/num_arms+1)*((2*finger_gap_left(nominal)+finger_width(nominal))*finger_width(nominal)+(finger_length-finger_width(nominal))*finger_width(nominal)); % Area of fixed finger arm (m^2)
fixed_finger_area = 2314e-12 % from layout (m)
% fixed_finger_mass = fixed_finger_area*b(nominal)*rho % mass of one arm of fixed fingers (kg)
fixed_finger_mass = 8.9e-11 % from layout
fixed_finger_x_mode_1 = lambda1^2/(2*pi*fixed_arm_length^2)*sqrt(E*b(nominal)*fixed_arm_thickness(nominal)^3*fixed_arm_length/(12*fixed_finger_mass)) % first x mode frequency of fixed finger (Hz)
fixed_finger_x_mode_2 = lambda2^2/(2*pi*fixed_arm_length^2)*sqrt(E*b(nominal)*fixed_arm_thickness(nominal)^3*fixed_arm_length/(12*fixed_finger_mass)) % second x mode frequency of fixed finger (Hz)
fixed_finger_z_mode_1 = lambda1^2/(2*pi*fixed_arm_length^2)*sqrt(E*b(nominal)^3*fixed_arm_thickness(nominal)*fixed_arm_length/(12*fixed_finger_mass)) % first z mode frequency of fixed finger (Hz)
fixed_finger_z_mode_2 = lambda2^2/(2*pi*fixed_arm_length^2)*sqrt(E*b(nominal)^3*fixed_arm_thickness(nominal)*fixed_arm_length/(12*fixed_finger_mass)) % second z mode frequency of fixed finger(Hz)
moving_finger_x_mode_1 = lambda1^2/(2*pi*moving_arm_length^2)*sqrt(E*b(nominal)*moving_arm_thickness(nominal)^3*moving_arm_length/(12*moving_finger_mass)) % first x mode frequency of moving finger (Hz)
moving_finger_x_mode_2 = lambda2^2/(2*pi*moving_arm_length^2)*sqrt(E*b(nominal)*moving_arm_thickness(nominal)^3*moving_arm_length/(12*moving_finger_mass)) % second x mode frequency of moving finger(Hz)
moving_finger_z_mode_1 = lambda1^2/(2*pi*moving_arm_length^2)*sqrt(E*b(nominal)^3*moving_arm_thickness(nominal)*moving_arm_length/(12*moving_finger_mass)) % first z mode frequency of moving finger (Hz)
moving_finger_z_mode_2 = lambda2^2/(2*pi*moving_arm_length^2)*sqrt(E*b(nominal)^3*moving_arm_thickness(nominal)*moving_arm_length/(12*moving_finger_mass)) % second z mode frequency of moving finger (Hz)

%Spring constants
common_mode_voltage = linspace(0,2000,101); % Common-mode voltage (V)
differential_mode_voltage= 1; %Differential-mode voltage (V)
Va = common_mode_voltage + differential_mode_voltage/2;
Vb = common_mode_voltage - differential_mode_voltage/2;
mechanical_spring_constant = beam_mass*(2*pi*100e3)^2; % Mechanical spring constant required (N/m)
electrical_spring_constant_x2 = num_input_fingers*eo*finger_width(nominal)*b(nominal).*(2.*Va.^2/finger_sidewall_gap_a(no
```

```
minal)^3+2.*Vb.^2/finger_sidewall_gap_b(nomi
nal)^3); % ELectrical Spring constant in X
(N/m)
electrical_spring_constant_y2 =
num_input_fingers*eo*b(nominal)*(1/finger_ga
p_left(nominal)^3+1/finger_gap_right(nominal)^
3).*(Va.^2*overlap_a(nominal)+Vb.^2.*overlap
_b(nominal)); % Electrical spring constant in y
(N/m)
figure
subplot(3,1,1)
loglog(common_mode_voltage,electrical_spring
_constant_x2,'k-
',common_mode_voltage,electrical_spring_const
ant_y2,'b-
',common_mode_voltage,ones(101)*mechanical
_spring_constant,'r-')
legend('Electrical X','Electrical Y','Mechanical
X',-1)
xlabel('Common mode voltage (V)')
ylabel('Spring constant (N/m)')
title('Spring Constants vs Common-mode
Voltage')
grid


%% Damping
%shear_damping_x =
visc*beam_mass/(rho*b(nominal)*h)+(2*num_i
nput_fingers+2*num_fb_fingers+num_force_fin
gers+num_sense_fingers)*2*visc*b(nominal)*fi
nger_overlap_max/finger_gap_left(nominal);
%Shear damping (kg/s)
%shear_damping_x =
(2*num_input_fingers+2*num_fb_fingers+num_
force_fingers+num_sense_fingers)*2*visc*b(no
minal)*finger_overlap_max/finger_gap_left(nom
inal); %Shear damping (kg/s)
shear_damping_x = visc*beam_area/h;
squeeze_film_damping_x =
finger_width(nominal)*(num_input_fingers*2+2
*num_fb_fingers+num_force_fingers+num_sens
e_fingers)*visc*(b(nominal)/min(finger_sidewal
l_gap_a))^3; %Squeeze film damping (kg/s)
geen_factor_x = 4-
(3*b(nominal)/((finger_gap_left(nominal)/h)^3*(
finger_gap_left(nominal)+finger_width(nominal)
)/3+b(nominal))); %Geen squeeze film factor
resonant_frequency_x =
sqrt(abs(mechanical_spring_constant-
electrical_spring_constant_x2)/beam_mass)/(2*p
i); % Resonant frequency in x vs common mode
voltage (Hz)
q_mechanical_x =
beam_mass*2*pi.*resonant_frequency_x./(shear
_damping_x+(squeeze_film_damping_x*geen_f
actor_x)); %Q in x direction
total_damping =
shear_damping_x+(squeeze_film_damping_x*ge
en_factor_x);
damping_force =
2*pi*frequency(101)*displacement_amplitude*(
shear_damping_x+(squeeze_film_damping_x*ge
en_factor_x)); %External force required to
displace the beam (N)
max_common_mode_voltage = 100; %
Maximum common mode voltage (Volts)
max_electrical_spring_constant_x =
num_input_fingers*eo*finger_width(nominal)*b
(nominal)*(2*max_common_mode_voltage^2/m
in(finger_sidewall_gap_a)^3); % ELectrical
Spring constant in X (N/m)
spring_constant = mechanical_spring_constant-
max_electrical_spring_constant_x;
spring_force =
displacement_amplitude*(mechanical_spring_co
nstant-max_electrical_spring_constant_x);
drive_voltage =
sqrt(damping_force*finger_gap_left(nominal)/(e
o*b(nominal)*num_force_fingers)); %Voltage
required to generate force
subplot(3,1,2)
semilogx(common_mode_voltage,resonant_freq
uency_x,'k-')
xlabel('Common-mode voltage (V)')
ylabel('Resonant frequency (Hz)')
title('Resonant frequency vs. common-mode
voltage')
legend('X',-1)
grid
subplot(3,1,3)
semilogx(common_mode_voltage,q_mechanical
_x,'k-')
xlabel('Common mode voltage (V)')
ylabel('Q')
title('Mechanical Q vs common mode voltage')
legend('Qx',-1)
grid
gmin=linspace(2e-6,10e-6,101); %Range of
possible sidewall gaps (m)
squeeze_film_damping_x2 =
0*finger_width(nominal)*(2*num_input_fingers
+2*num_fb_fingers+num_sense_fingers+num_f
orce_fingers)*visc.*(b(nominal)./gmin).^3;
%Squeeze film damping (kg/s)
external_force2 =
pi/4*2*pi*frequency(101)*displacement_amplit
ude.*(shear_damping_x+(squeeze_film_dampin
g_x2*geen_factor_x)); %External force required
to displace the beam (N)
```

```
drive_voltage = sqrt(external_force2*finger_gap_left(nominal)/(eo*b(nominal)*num_force_fingers)); %Voltage required to generate force


figure
subplot(2,1,1)
plot(gmin,ones(101)*shear_damping_x,'k-',gmin,squeeze_film_damping_x2,'b-')
xlabel('Minimum sidewall gap (m)')
ylabel('Damping (kg/s)')
title('Damping vs. Minimum sidewall gap')
legend('Shear','Squeeze',-1)
grid
subplot(2,1,2)
plot(gmin,drive_voltage,'k-')
xlabel('Minimum sidewall gap (m)')
ylabel('Drive voltage (V)')
title('Drive voltage vs sidewall gap')
legend('Drive',-1)
grid

%% Resonator/Drive
Vdrive=drive_voltage(101); %drive voltage (V)
Vbias=15; %Bias voltage of beam (V)
feedback_resistor = 200e3; %max feedback resistor on sense amp
static_capacitance3=num_sense_fingers*eo*b(nominal)*(1/finger_gap_left(nominal)+1/finger_gap_right(nominal))*(finger_overlap_max+finger_overlap_min)/2+2*eo*finger_width(nominal)*b(nominal)/((finger_overlap_max+finger_overlap_min)/2);
modulating_capacitance3=num_sense_fingers*eo*b(nominal)*((finger_overlap_max-finger_overlap_min)/2*(1/finger_gap_left(nominal)+1/finger_gap_right(nominal))+2*finger_width(nominal)/((finger_overlap_max+finger_overlap_min)/2)*(finger_overlap_max-finger_overlap_min)/(finger_overlap_max+finger_overlap_min));
signal_current3=2*pi*frequency(101)*2.*modulating_capacitance3*(2*Vbias);
common_mode_current3 = 2*pi*frequency(101).*static_capacitance3*(Va+Vb);
noise_current3 = 2*pi*frequency(101)*(2*static_capacitance3+parasitic_capacitance3)*noise_voltage*sqrt(frequency(101));
estimated_rti_noise4 = (2.*static_capacitance3+parasitic_capacitance3)./(2.*modulating_capacitance3)*noise_voltage;
noise_bandwidth = 1e6; % Noise bandwidth (Hz)
op_amp_noise_current = sqrt((2*pi*noise_bandwidth)^2*(static_capacitance3+parasitic_capacitance3)^2*noise_voltage^2);
resistor_noise_current = sqrt(4*k*T*noise_bandwidth/feedback_resistor);


sense_static_capacitance=num_sense_fingers*eo*b(nominal)*(1/finger_gap_left(nominal)+1/finger_gap_right(nominal))*(finger_overlap_max+finger_overlap_min)/2+2*eo*finger_width(nominal)*b(nominal)/((finger_overlap_max+finger_overlap_min)/2); %Drive sense capacitance (F)
sense_modulating_capacitance=num_sense_fingers*eo*b(nominal)*((finger_overlap_max-finger_overlap_min)/2*(1/finger_gap_left(nominal)+1/finger_gap_right(nominal))+2*finger_width(nominal)/((finger_overlap_max+finger_overlap_min)/2)*(finger_overlap_max-finger_overlap_min)/(finger_overlap_max+finger_overlap_min)); %Drive modulating capacitance (F)
constant_drive_force = num_force_fingers*eo*b(nominal)*(1/finger_gap_left(nominal)+1/finger_gap_right(nominal))*Vdrive^2/2; %Constant drive force (N)
nonlinear_drive_force = num_force_fingers*eo*b(nominal)*Vdrive^2./finger_sidewall_gap_a; %Nonlinear drive force (N)
figure
plot(finger_sidewall_gap_a,ones(101)*constant_drive_force,'k--',finger_sidewall_gap_a,nonlinear_drive_force,'b-')
title('Constant vs Nonlinear force drive')
xlabel('Overlap (m)')
ylabel('Force (N)')
drive_force = num_force_fingers*eo*b(nominal)*((1/finger_gap_left(nominal)+1/finger_gap_right(nominal))*Vdrive^2/2-Vdrive^2/min(finger_sidewall_gap_a)*finger_width(nominal)); %total_drive_force (N)
beam_velocity=drive_force*4/pi/total_damping; %Beam Velocity (m/s)
sense_signal_current = 2*Vbias*eo*b(nominal)*num_sense_fingers*((1/finger_gap_left(nominal)+1/finger_gap_right(nominal))+8*finger_width(nominal)/(finger_overlap_max+finger_overlap_min)^2)*beam_velocity; %Sense current

%recompute drive voltage to ensure desired displacement
```

```
actual_displacement_amplitude                    =
beam_velocity/(2*pi*frequency(101));
desired_velocity                                 =
2*pi*frequency(101)*displacement_amplitude;
desired_force                                    =
total_damping*desired_velocity*pi/4;
actual_drive_voltage                             =
sqrt(desired_force*finger_gap_left(nominal)/(eo
*b(nominal)*num_force_fingers));      %Voltage
required to generate force

% yesno = input('Print all graphs? (1=yes)');
% if yesno == 1
%     bwc = input('Color? (1=yes)');
%    if bwc == 1
%       options = '-dpsc2';
%       printer = '-Pcolor-3c';
%    else
%       options = '-dps2';
%       printer = '-Plp32';
%    end
%    for i=1:numplots
%          print(i,options,printer)
%       end
%    end
%% Input anti-aliasing filter
[aafnum,aafden]=cheby1(8,0.01,2*pi*12.5e3,'s');
[lpfnum,lpfden]=cheby1(8,0.01,2*pi*25e3,'s');
```

# REFERENCES


1. J. P. Close and L. W. Counts, "A 50 fA Junction-Isolated Operational Amplifier," IEEE Journal of Solid-State Circuits, vol. 23, no. 3, pp. 843-851, June 1988.

2. S. A. Rajput and S. C. Garg, "High Current Injection Effects of the Switching JFET's in the Current Electrometers," IEEE Transactions on Instrumentation and Measurement, vol. 45, no. 1, pp. 314-316, February 1996.

3. O. H. Shade, Jr., "A New Generation of MOS/Bipolar Operational Amplifiers," RCA Rev., vol. 37, pp. 404-424, September 1976.

4. D. Fullagar, "Better Understanding of FET Operation Yields Viable Monolithic JFET Op-Amp," Electron., pp. 98-101, November 1972.

5. R. W. Russell and D. D. Culmer, "Ion Implanted JFET-bipolar Monolithic Analog Circuits," ISSCC Dig. Tech. Papers, pp. 140-141, no. 243, February 1974.

6. R. Kaller, "With Input Bias Current of 40 fA, Op Amp IC Makes Low Level Measurements," Electron. Des., pp. 142-145, May, 1986.

7. H. Huang, S. Karthikeyan, and E. K. F. Lee, "A 1 V Instrumentation Amplifier," The 42$^{nd}$ Midwest Symposium on Circuits and Systems, Volume 1, pp. 170-173, 1999.

8. A. A. Khan and A. Kumar, "A Novel Instrumentation Amplifier With Reduced Magnitude and Phase Errors," IEEE Transactions on Instrumentation and Measurement, vol. 40, no. 6, pp. 1035-1038, December 1991.

9. R. Pallás-Areny and J. G. Webster, "Common Mode Rejection Ratio in Differential Amplifiers," IEEE Transactions on Instrumentation and Measurement, vol. 40, no. 4, pp. 669-676, August 1991.

10. C. Toumazou, F. J. Lidgey, and C. A. Makris, "Current-Mode Instrumentation Amplifier," IEE Colloquium on Current Mode Analogue Circuits, pp. 8/1-8/5, June 18, 1990.

11. C. Menolfi, and Q. Huang, "A Fully Integrated, Untrimmed, CMOS Instrumentation Amplifier with Submicrovolt Offset," IEEE Journal of Solid-State Circuits, vol. 34, no. 3, pp. 415-420, March 1999.

12. P. de Jong, G. Meijer, A. van Roermund, "A 300 °C Dynamic-Feedback Instrumentation Amplifier," IEEE International Solid State Circuits Conference, pp 322-323, February 1998.

13. A. Harb, Y. Hu, and M. Sawan, "New CMOS Instrumentation Amplifier Dedicated to Very Low Amplitude Signal Applications," Proceedings of the 6th IEEE International Conference on Electronics, Circuits and Systems, vol. 1, pp. 517-520, 1999.

14. S. Wei, and H. C. Lin, "CMOS Chopper Amplifier for Chemical Sensor," IEEE Transactions on Instrumentation and Measurement, pp. 77-80, February 1992.

15. A. Bakker, K. Thiele, and J. Huijsing, "A CMOS Nested Chopper Amplifier with 100 nV Offset," IEEE International Solid-State Circuits Conference, pp. 156-157, February 2000.

16. C. C. Enz, and G. C. Temes, "Circuit Techniques for Reducing the Effects of Op-Amp Imperfections: Autozeroing, Correlated Double Sampling, and Chopper Stabilization," Proceeding of the IEEE, vol. 84, pp. 1584-1614, November 1996.

17. P. Gray and R. Meyer, "Analysis and Design of Analog Integrated Circuits", John Wiley & Sons, Inc, 1992.

18. G. A. Girgis, M. E. Rizkalla, and M. M. Holdmann, "Temperature Stability of a CMOS Operational Amplifier," Proceedings of the 33rd Midwest Symposium on Circuits and Systems, vol. 2, pp. 689-691, 1990.

19. M. E Rizkalla, M. M. Holdmann, and R. A. Barton, "Design of a Minimum Drift JFET Differential Amplifier," Proceedings of the 32nd Midwest Symposium on Circuits and Systems, vol. 1, pp. 439-441, 1990.

20. M. E Rizkalla, and M. M. Holdmann, "Design of a minimum drift characteristic for differential MOSFET amplifier," IEEE International Symposium on Circuits and Systems, vol. 4, pp. 3234-3237, 1990.

21. P. K. Chan, L. Siek, H. C. Tay, and J. H. Su, "A Low-Offset Class-AB CMOS Operational Amplifier," IEEE International Symposium on Circuits and Systems, vol. 3, pp. 455-458, May 2000.

22. J. Hynecek, "Spectral Analysis of Reset Noise Observed in CCD Charge-Detection Circuits," IEEE Transactions on Electron Devices, vol. 37,no. 3, pp. 640-647, March 1990.

23. A. A. Aina, "Enhanced performance of a low noise discrete pre-amplifier stage," M.Eng Thesis, Massachusetts Institute of Technology, 1997.

24. H. M. Wey, and W. Guggenbühl, "An Improved Correlated Double Sampling Circuit for Low Noise Charge-Coupled Devices," IEEE Transactions on Circuits and Systems, vol. 37, no. 12, pp. 1559-1565, December 1990.

25. E. A. M. Klumperink, S. L. J. Gierkink, A. P. van der Wel, and B. Nauta, "Reducing MOSFET 1/f Noise and Power Consumption by Switched Biasing," IEEE Journal of Solid-State Circuits, vol. 35, no. 7, pp. 994-1001, July 2000.

26. A. Olkhovets, D. W. Carr, J. M. Parpia, and H. G. Craighead, "Non-degenerate Nanomechanical Parametric Amplifier," IEEE International Micro Electro Mechanical Systems Conference, pp. 298-300, 2001.

27. D. Rugar, and P. Grütter, "Mechanical Parametric Amplification and Thermomechanical Noise Squeezing," Physical Review Letters, vol. 67, no. 6, August 1991.

28. J. P. Raskin, A. R. Brown, B. T. Khuri-Yakub, and G. M. Rebeiz, "A Novel Parametric-Effect MEMs Amplifier," IEEE Journal of Microelectromechanical Systems, vol. 9, no. 4, December 2000.

29. H. Palevsky, R. K. Swank, and R. Grenchik, "Design of Dynamic Condenser Electrometers," The Review of Scientific Instruments, vol. 28, no. 5, pp. 298-314, May 1947.

30. J. M. Pimbley and G. J. Michon, "The Output Power Spectrum Produced by Correlated Double Sampling," IEEE Transactions on Circuits and Systems, vol. 38, no. 9, pp. 1086-1090, September 1991.

31. S. Ranganathan, N. Inerfield, S. Roy, and S. L. Garverick, "Sub-Femtofarad Capacitive Sensing for Microfabricated Transducers Using Correlated Double Sampling and Delta Modulation," IEEE Transactions on Circuits and Systems II: Analog and Digital Signal Processing, vol. 47, no. 11, pp. 1170-1176, November 2000.

32. J. Hynecek, "Theoretical Analysis and Optimization of CDS Signal Processing Method for CCD Image Sensors," IEEE Transactions on Electron Devices, vol. 39, no. 11, pp. 2497-2507, November 1992.

33. B. K. Marlow, D. C. Greager, R. Kemp, and M. B. Moore, "Highly Sensitive Capacitance Measurement for Sensors," Electronics Letters, vol. 29, no. 21, pp. 1844-1845, October 1993.

34. F. W. Sears, and P. A. Stokstad, "Electrostatics Demonstrations With A Vibrating Reed Electrometer," American Journal of Physics, vol. 36, no. 8, pp. 752-756, August 1968.

35. B. E. Boser, "Electronics For Micromachined Inertial Sensors," IEEE International Conference on Solid-State Sensors and Actuators, pp. 1169-1172, June 1997.

36. B. Stefanelli, J.P. Bardyn, A. Kaiser, and D. Billet, "A Very Low Noise CMOS Preamplifier For Capacitive Sensors," IEEE Journal of Solid-State Circuits, vol. 28, no. 9, pp. 971-978, September 1993.

37. C. L. Stong, "An Electrometer, A Temperature-Control Apparatus And A Simple Electric Motor," The Amateur Scientist, pp. 106-110.

38. Analog Devices, Inc., "Ultralow Input Bias Current Operational Amplifier," Analog Devices AD549 Specifications Sheet.

39. Analog Devices, Inc., "Ultralow Input Bias Current Operational Amplifier," Analog Devices AD629 Specifications Sheet.

40. T. Fleming, "Isolation Amplifiers Break Ground Loops and Achieve High CMRR," EDN, vol. 24, pp. 97-102, December 1987

41. S. Nihtianov, "Magnetogalvanic Approach to Isolation of Analog Circuits," IEEE Transactions on Instrumentation and Measurement, vol. 43, no. 4, August 1994.

42. P. Waugh, "Techniques Used For Isolation Amplifiers," IEE Colloquium on Measurement Techniques For Power Electronics, pp. 3/1-3/4, 1991.

43. P. J. M. Smidt and J. L. Duarte, "Powering Neon Lamps Through Piezoelectric Transformers," The 27th Annual IEEE Power Electronics Specialists Conference, vol.1, pp. 310-315.

44. A. Olkhovets, D. W. Carr, J. M. Parpia, and H. G. Craighead, "Non-Degenerate Nanomechanical Parametric Amplifier," The 14th IEEE International Conference on Micro Electro Mechanical Systems, pp. 298-300, 2001.

45. J. K. Roberge, "Operational Amplifiers: Theory and Practice," John Wiley and Sons, Inc, 1975.

46. J. M. Gere, and S. P. Timoshenko, "Mechanics of Materials, " third edition, 1990.

47. S. Sung, J. G. Lee, T. Kang, and J. W. Song, "Development of a Tunable Resonant Accelerometer With Self-Sustained Oscillation Loop," Proceedings of the IEEE National Aerospace and Electronics Conference, pp. 354-361, 2000.

48. X. Zhang, and W. C. Tang, "Viscous Air Damping In Laterally Driven Microresonators," Proceedings of the IEEE Workshop on Micro Electro Mechanical Systems, pp. 199-204, 1994.

49. P. S. Riehl, "Micromachined Resonant Electrometer," MS thesis, UC Berkeley, 2000.

50. S. C. Tang, S. Y. R. Hui, H. S. Chung," A Low-Profile Wide-Band Three-Port Isolation Amplifier With Coreless Printed-Circuit-Board (PCB) Transformers," IEEE Transactions on Industrial Electronics, vol. 48, no. 6, pp. 1180-1187, December 2001.

51. A. M. Flynn, and S. R. Sanders, "Fundamental Limits on Energy Transfer and Circuit Considerations for Piezoelectric Transformers," IEEE Transactions on Power Electronics, vol. 17, no. 1, pp. 8-14, January 2002.

52. Piezo Systems Technical Literature [Online]. Available: http://www.piezo.com.

53. G. K. Fedder, "Simulation of Microelectromechanical Systems," PhD thesis, Dept. of Electrical Engineering and Computer Sciences, University of California at Berkeley, Berkeley, California, September 1994.

54. S. W. Senturia, "Micorsystem Design," Kluwer Academic Publishers, Boston, MA, 2001.

55. C. D. Motchenbacher, and F. C. Fitchen, "Low-Noise Electronic Design," John Wiley & Sons, 1973.

56. R. Gregorian, G. C. Temes, "Analog MOS Integrated Circuits For Signal Processing," John Wiley & Sons, 1986.

57. R. T. Howe, and C. G. Sodini, "Microelectronics -- An Integrated Approach," Prentice Hall, 1997.

58. M. Medjoub, H. Maher, C. Ladner, J. L. Courant, and G. Post, "Silicon Nitride Passivation of Double Channel InP HEMTs Using Inductively Coupled Plasma-Enhanced Chemical Vapor Deposition," Symposium on High Performance Electron Devices for Microwave and Optoelectronic Applications, pp. 33-36, 1999.

59. E. Kuffel, W. S. Zaengl, and J. Kuffel, "High Voltage Engineering: Fundamentals," Newnes, 2000.

60. S. M. Sze, "Current Transport and Maximum Dielectric Strength of Silicon Nitride Films", Journal of Applied Physics, vol. 38, no. 7, pp. 2951-2956, June 1967.

61. M. Williams, J. Smith, J. Mark, G. Matamis, and B. Gogoi, "Development of a Low Stress, Silicon-rich Nitride Film For Micromachined Sensor Applications," Micromachining and Microfabrication Process Technology VI, Proceedings of SPIE, vol. 4174, pp. 436-442, 2000.

62. P. J. French, P. M. Sarro, R. Mallée, E. J. M. Fakkeldij, and R. F. Wolffenbuttel, "Optimization of a Low-Stress Silicon Nitride Process for Surface-micromachining Applications," Sensors and Actuators, vol. A58, pp. 149-157, 1997.

63. S. Habermehl, and C. Carmignani, "Correlation of Charge Transport to Local Atomic Strain in Si-rich Silicon Nitride Films," Applied Physics Letters, vol. 80, no. 2, pp. 261-263, January 2002.

64. S. Habermehl, "Stress Relaxation in Si-rich Silicon Nitride Thin Films," Journal of Applied Physics, vol. 83, no. 9, pp. 4671-4677, May 1998.

65. Linear Technologies, "Precision, Rail-to-rail Input and Output, Zero-Drift Instrumentation Amplifier with Resistor Programmable Gain," http://www.linear.com, December 2001.

66. T. J. Brosnihan, "An SOI Based, Fully Integrated Fabrication Process For High-Aspect-Ratio Microelectromechanical Systems," Ph.D. thesis, University of California at Berkeley, Fall 1998.

67. Texas Instruments, "Ultra-low Noise Precision Amplifiers," Texas Instruments OPA627 Specifications Sheet.

68. M. A. Lemkin, "Micro Accelerometer Design with Digital Feedback Control," Ph.D. thesis, University of California at Berkeley, Fall 1997.

69. E. Sacristan, R. A. Peura, A. Shahnarian, R. Fiddian-Green, "Development of a Flexible $PCO_2$ Microsensor For Gastrointestinal pHi Monitoring," Proceedings of the 1991 IEEE Seventeenth Annual Northeast Bioengineering Conference, pp. 141-143, April 1991.